Long-wavelength radio observations of blazars with the Low-Frequency Array (LOFAR)

Dissertation zur Erlangung des
naturwissenschaftlichen Doktorgrades
der Julius-Maximilians-Universität Würzburg

vorgelegt von
Jonas Elias Trüstedt

aus München

Würzburg 2016

Eingereicht am: ....
bei der Fakultät für Physik und Astronomie

1. Gutachter: ....
2. Gutachter: ....
3. Gutachter: ....
der Dissertation

Vorsitzende(r): ....

1. Prüfer: ....
2. Prüfer: ....
3. Prüfer: ....
im Promotionskolloquium

Tag des Promotionskolloqiums: ....

Doktorurkunde ausgehändigt am: ....

Zusammenfassung

Aktive Galaxienkerne (AGN) gehören zu den hellsten Objekten in unserem Universum. Diese Galaxien werden als aktiv bezeichnet, da ihre Zentralregion heller ist als alle Sterne in einer Galaxie zusammen beitragen könnten. Das Zentrum besteht aus einem supermassiven schwarzen Loch, das von einer Akkretionsscheibe und weiter außerhalb von einem Torus aus Staub umgeben ist. Diese AGN können über das ganze elektromagnetische Spektrum verteilt gefunden werden, von Radiowellen über Wellenlängen im optischen und Röntgenbereich bis hin zur γ-Strahlung. Allerdings sind nicht alle Objekte bei jeder Wellenlänge detektierbar. In dieser Arbeit werden überwiegend Blazare bei niedrigen Radiofrequenzen untersucht. Blazare gehören zu den radio-lauten AGN, welche üblicherweise stark kollimierte Jets senkrecht zur Akkretionsscheibe aussenden. Bei Blazaren sind diese Jets in die Richtung des Beobachters gerichtet und ihre Emissionen sind stark variabel.

AGN werden anhand ihres Erscheinungsbildes verschiedenen Untergruppen zugeordnet. Diese Untergruppen werden in einem vereinheitlichen AGN Modell zusammengeführt, welches besagt, dass diese Objekte sich nur in ihrer Luminosität und ihrem Winkel zur Sichtlinie unterscheiden. Blazare sind diejenigen Objekte, deren Jets in unsere Sichtrichtung zeigen, während die Objekte deren Jets eher senkrecht zur Sichtlinie orientiert sind als Radiogalaxien bezeichnet werden. Daraus folgt, dass Blazare die Gegenstücke zu Radiogalaxien mit einem anderen Winkel zur Sichtlinie sind. Diese Beziehung soll unter anderem in dieser Arbeit untersucht werden.

Nach ihrer Entdeckung in den 1940er Jahren wurden die aktiven Galaxien bei allen zugänglichen Wellenlängen untersucht. Durch die Entwicklung von Interferometern aus Radioteleskopen, welche eine erhöhte Auflösung bieten, konnten die Beobachtungen stark verbessert werden. In den letzten 20 Jahren wurden viele AGN regelmäßig beobachtet. Dies erfolgte unter anderem durch Programme wie dem MOJAVE Programm, welches 274 AGNs regelmäßig mithilfe der Technik der “Very Long Baseline Interferometry"(VLBI) beobachtet. Durch diese Beobachtungen konnten Informationen zur Struktur und Entwicklung der AGN und Jets gesammelt werden. Allerdings sind die Prozesse zur Bildung von Jets und deren Kollimation noch nicht vollständig bekannt. Durch relativistische Effekte ist es schwierig die eigentlichen Größen der Jets anstelle der scheinbaren zu messen. Um die intrinsische Energie von Jets zu messen, sollen die ausgedehnten Emissionsregionen untersucht werden, in denen die Jets enden und mit dem Intergalaktischen Medium interagieren. Beobachtungen bei niedrigen Radiofrequenzen sind empfindlicher um solche ausgedehnte, diffuse Emissionsregionen zu detektieren.

Seit Dezember 2012 ist ein neues Radioteleskop für niedrige Frequenzen in Betrieb, dessen Stationen aus Dipolantennen besteht. Die meisten dieser Stationen sind in den Niederlanden verteilt (38 Stationen) und werden durch 12 internationale Stationen in Deutschland, Frankreich, Schweden, Polen und England ergänzt. Dieses Instrument trägt den Namen "Low Frequency Array" (LOFAR). LOFAR bietet die Möglichkeit bei Frequenzen von 30–250 MHz bei einer höheren Auflösung als bisherige Radioteleskope zu beobachten (Winkelauflösungen unter 1 arcsec für das gesamte Netzwerk aus Teleskopen).
Diese Arbeit behandelt die Ergebnisse von Blazaruntersuchungen mithilfe von LOFAR-Beobachtungen. Dafür wurden AGNs aus dem MOJAVE Programm verwendet um von den bisherigen Multiwellenlängen-Beobachtungen und Untersuchungen der Kinematik zu profitieren. Das "Multifrequency Snapshot Sky Survey" (MSSS) Projekt hat den gesamten Nordhimmel mit kurzen Beobachtungen abgerastert. Aus dem daraus resultierenden vorläufigen Katalog wurden die Flussdichten und Spektralindizes für MOJAVE-Blazare untersucht. In den kurzen Beobachtungen von MSSS sind nur die Stationen in den Niederlanden verwendet worden, wodurch Auflösung und Sensitivität begrenzt sind. Für die Erstellung des vorläufigen Kataloges wurde die Auflösung auf $\sim$120 arcsec beschränkt. Ein weiterer Vorteil der MOJAVE Objekte ist die regelmäßige Beobachtung der AGN mit dem "Owens Vally Radio Observatory" zur Erstellung von Lichtkurven bei 15 GHz. Dadurch ist es möglich nahezu zeitgleiche Flussdichtemessungen bei 15 GHz zu den entsprechenden MSSS-Beobachtungen zu bekommen. Da diese Beobachtungen zu ähnlichen Zeitpunkten durchgeführt wurden sind diese Flussdichten weniger von der Variabilität der Blazare beeinflusst. Die Spektralindizes berechnet aus den Flussdichten von MSSS und OVRO können verwendet werden um den Anteil an ausgedehnter Emission der AGNs abzuschätzen.
Im Vergleich der Flussdichten aus dem MSSS Katalog mit den Beobachtungen von OVRO fällt auf, dass die Flussdichten bei niedrigen Frequenzen tendenziell höher sind, was durch den höheren Anteil an ausgedehnter Struktur zu erwarten ist. Die Spektralindexverteilung zwischen MSSS und OVRO zeigt ihren höchsten Wert bei ~ -0.2. In der Verteilung existieren Objekte mit steilerem Spektralindex durch den höheren Anteil von ausgedehnter Emission in der Gesamtflussdichte, doch über die Hälfte der untersuchten Objekte besitzt flache Spektralindizes. Die flachen Spektralindizes bedeuten, dass die Emissionen dieser Objekte größtenteils von relativistischen Effekten beeinflusst sind, die schon aus Beobachtungen bei GHz-Frequenzen bekannt sind.
Durch neue Auswertung der MSSS Beobachtungsdaten konnten Bilder bei einer verbesserten Auflösung von $\sim$20–30 arcsec erstellt werden, wodurch bei einigen Blazaren ausgedehnte Struktur detektiert werden konnte. Diese höher aufgelösten Bilder sind allerdings nicht komplett kalibriert und können somit nur für strukturelle Informationen verwendet werden. Die Überarbeitung der Beobachtungsdaten konnte für 93 Objekte für ein Frequenzband durchgeführt werden. Für 45 der 93 Objekte konnten sogar alle vorhandenen Frequenzbänder überarbeitet werden und dadurch gemittelte Bilder erstellt werden. Diese Bilder werden in dieser Arbeit vorgestellt. Die resultierenden Bilder mit verbesserter

Auflösung wurden verwendet um Objekte auszuwählen, die mit allen LOFAR-Stationen beobachtet und auf ausgedehnte Struktur untersucht werden können.
Im zweiten Teil der Arbeit werden die Ergebnisse von internationalen LOFAR Beobachtungen von vier Blazaren präsentiert. Da sich die Auswertung und Kalibration von internationalen LOFAR Beobachtungen noch in der Entwicklung befindet, wurde ein Schwerpunkt auf die Kalibration und deren Beschreibung gelegt. Die Kalibration kann zwar noch verbessert werden, aber die Bilder aus der angewandten Kalibration erreichen eine Auflösung von unter 1 arcsec. Die Struktur der untersuchten vier Blazare entspricht den Erwartungen für Radiogalaxien unter einem anderen Sichtwinkel. Durch die gemessenen Flussdichten der ausgedehnten Struktur aus den Helligkeitsverteilungen konnte die Luminosität der ausgedehnten Emissionen berechnet werden. Im Vergleich mit den Luminositäten, die von Radiogalaxien bekannt sind, entsprechen auch diese Werte den Erwartungen des vereinheitlichten AGN Modells.
Durch die in dieser Arbeit vorgestellte Kalibration können noch mehr Blazare mit LOFAR inklusive den internationalen Stationen beobachtet werden und somit Bilder der Struktur bei ähnlicher Auflösung erstellt werden. Durch eine erhöhte Anzahl von untersuchten Blazaren könnten anschließend auch statistisch signifikante Ergebnisse erzielt werden.

Abstract

Active galactic nuclei (AGNs) are among the brightest sources in our universe. These galaxies are considered active because their central region is brighter than the luminosities of all stars in a galxies can provide. In their center is a supermassive black hole (SMBH) surrounded by an accretion disk and further out a dusty torus. AGN can be found with emission over the whole electromagnetic spectrum, starting at radio frequencies over optical and X-ray emission up to the γ-rays. Not all of these sources are detected in each frequency regime. In this work mainly blazars are examined at low radio frequencies. Blazars are a subclass of radio-loud AGN. These radio-loud sources usually exhibit highly collimated jets perpendicular to the accretion disk. For blazars these jets are pointed in the direction of the observer and their emission is highly variable.

AGN are classified in different subclasses based on their morphology. These different subclasses are combined in the AGN unification model, which explains the different morphologies by having sources only varying in their luminosities and their angle to the line of sight to the observer. Blazars are these targets, where the jet is pointing towards the observer, while the AGN observed edge on are called radio galaxies. This means that blazars should be the counterparts to radio galaxies seen from a different angle. Testing this is one of the goals in this work.

After the discovery of AGN in the 1940s these objects have been studied at all wavelengths. With the development of interferometry with radio telescopes the angular resolution for radio observations could be improved. In the last 20 years many AGN are regularly monitored. One of these monitoring programs is the MOJAVE program, monitoring 274 AGNs with using the Very Long Baseline Interferometry (VLBI) technique. The monitoring provides information on the evolution and structure of AGN and their jets. However, the mechanisms of the jet formation and their collimation are not fully understood. Due to relativistic effects it is difficult to obtain intrinsic instead of apparent parameters of these jets. One approach to get closer to the intrinsic jet power is by observing the regions, in which the jets end and interact with the intergalactic medium. Observations at lower radio frequencies are more sensitive for extended diffuse emission. Since December 2012 a new radio telescope for low frequencies is observing. It is a telescope with stations consisting of dipole antennas. The major part of the array located in the Netherlands (38 stations) with 12 additional international stations in Germany, France, Sweden, Poland and the United Kingdom. This instrument is called the Low Frequency Array (LOFAR). LOFAR offers the possibility to observe at frequencies between 30–250 MHz in combination with angular resolution (below 1 arcsec for the full

array), which was not available with previous telescopes.
In this work results of blazar studies with LOFAR observations are presented. To take advantage of a large database with multi-wavelength observations and kinematic studies the MOJAVE 1.5 Jy flux limited sample was chosen. Based on the preliminary results of the LOFAR Multifrequency Snapshot Sky Survey (MSSS) the flux densities and spectral indices of blazars of the MOJAVE sample are examined. 125 counterparts of MOJAVE blazars were found in the MSSS catalog. Since the MSSS observations only contain the stations in the Netherlands and observes in snapshots, the angular resolution and the sensitivity is limited. The first MSSS catalog was produced with an angular resolution of ∼120 arcsec and a sensitivity of ∼50–100 mJy. Another advantage of the MOJAVE sample is the monitoring of these sources with the Owens Valley Radio Observatory (OVRO) at 15 GHz to produce radio lightcurves. With these observations it is possible to get quasi-simultaneous flux densities at 15 GHz for the corresponding MSSS observations. By having quasi-simultaneous observations the variability of the blazars affects the flux densities less than with the use of archival data. The spectral indices obtained by the combination of MSSS and OVRO flux densities can be used to estimate the contribution of the diffuse extended emission for these AGNs.
Comparing the MSSS catalog with the OVRO data points, the flux densities have a tendency to be higher at low frequencies. This is expected due to the higher contribution of extended emission. The broadband spectral index distribution shows a peak at ~ -0.2. While some sources seem to have steeper spectral indices meaning that extended emission contributes a large fraction of the total flux density, more than the half of the sample shows flat spectral indices. The flat spectral indices show that the total flux densities of these sources are dominated by their relativistic beamed emission regions, which is the same for the observations at GHz frequencies.
To obtain more detailed images of these sources the MSSS measurement sets including sources of the sample were reprocessed to improve the angular resolution to ∼30 arcsec. The higher angular resolution reveals extended diffuse emission of several blazars. Since the reimaging results were not fully calibrated only the morphology at this resolution could be examined. However, with the short snapshot observations the images obtained with this strategy are affected from artifacts. The reimaging could be successfully performed for 93 sources in one frequency band. For 45 of these sources all availabe frequency bands could be reprocessed and used to created averaged images. These images are presented in this work. As a results of the reimaging process a pilot sample was defined to observe targets with diffuse extended emission using the whole LOFAR array including the international stations.
The second part of this work presents the results of a pilot sample consisting of four blazars observed with the LOFAR international array. Since the calibration of this kind of LOFAR observation is still in development, the main focus was the description of the used calibration strategy. The calibration strategies still has some limitation but resulted in images with angular resolutions of less than 1 arcsec. The morphology of all

four blazars show features confirming the expectations of their counterpart radio galaxies. With the flux densities of the extended emission found in these brightness distributions the extended radio luminosities are calculated. Comparing these to the radio galaxy classifications also confirm the expectations from the unification model.
By extending the sample of observed blazars with LOFAR international in future the calibration strategy can be used to create similar high resolution images. A larger sample can be used to test the unification model with statistical significant results.

Contents

1. Introduction

Compared to optical astronomy performed with a telescope since the 17th century, the radio astronomy is a relatively new possibility to study the sky available since ~ 60 years. The atmosphere from Earth has only two frequency ranges where astronomical observations can take place: in the optical range and for longer wavelengths corresponding to the radio frequencies.
When Karl Guthe Jansky was assigned to search for interference sources for radio transmissions from the Bell Labs, he built an antenna for radio waves at 20.5 MHz. 1931 he discovered different static sources: thunderstorms and a signal following the sidereal day cycle. This signal turned out to come from the center of the Milky Way (Jansky 1933). After this first discovery, Grote Reber built his own telescope with a parabolic dish in his backyard in 1937. One year later he could confirm the findings of Karl Jansky and chart and track the radio waves from our galaxy.
This started the time of radio astronomy and led to more discoveries like the detection of the Sun at radio wavelengths in 1942. In 1944 Jan Oort and Hendrik C. van de Hulst predicted the existence of the 21-cm hydrogen line, which was then found 1951 by Edward Mills Purcell and Harold Irving Ewen (Ewen & Purcell 1951). For their studies on the 21-cm hydrogen line van de Hulst et al. (1954) used an old German radar dish from Würzburg, which was surplus after World War II. 1964 Arno Penzias and Robert Woodrow Wilson accidentally discovered the 3 Kelvin cosmic microwave background while testing an antenna horn (Penzias & Wilson 1965), which awarded with the Nobel Prize of Physics in 1978.
In the 1940s also the first interferometers of radio telescopes were used to obtain higher angular resolutions. The first dedicated Very Long Baseline Interferometry (VLBI) project started in 1967 by Canadian and US researchers. The VLBI technique led to great progress in radio astronomy by improving the resolution with growing radio telescope networks (Kellermann & Moran 2001). Observations at 21 cm wavelength (Adgie et al. 1965; Barber 1966) and later at 11 and 6 cm (Palmer et al. 1967) radio sources with a size of 0.05 arcsec were found. Due to the success of the linked radio telescope interferometer a dedicated multi-element radio-linked interferometer was developed. This project was later known as the Multi-Element-Radio-Linked-Interferometer-Network (MERLIN) (Davies et al. 1980).
The sources for radio emission are different than what can be observed in the optical. Besides the cosmic microwave emission new objects found with radio telescopes are pulsars, active galaxies, supernova remnants, merging galaxy clusters, the Sun and gas clouds.

Some sources like the Sun have a continuum spectrum from black body radiation, others show certain emission lines like the hydrogen lines of gas clouds orbiting the center of the galaxy or the synchrotron emission of the powerful jets of active galactic nuclei (AGN). In the last years radio astronomy mostly used radio receivers at GHz frequencies from cm-wavelengths down to sub-mm-wavelenghts. The combination of the smaller wavelenghts with the VLBI techniques provides the highest possible resolutions. However new projects want to cover also the low frequencies in the MHz regimes. The coming Square Kilometre Array (SKA) (Carilli & Rawlings 2004) will provide an instrument to observe the Southern Hemisphere with extremely high sensitivity at low frequencies like 50-350 MHz but will also cover the frequency bands up to 14 GHz. These low frequencies are sensible to very old and diffuse radio emissions and highly shifted emission lines from distant sources and give us the possibility to learn more about the dark ages of the universe and galaxy evolution.
One of the precursors for the SKA covering the Northern Hemisphere is the Low Frequency Array (LOFAR) which started regular observations in December 2012. This thesis will present observational results of AGN in the catalog of the first LOFAR all sky survey and the first-ever high resolution observations of some of these AGN at frequencies between 120-160 MHz.

2. Active Galactic Nuclei (AGN)

For the following chapter the main information was taken from textbooks if no additional reference is given. For the AGN properties these textbooks are Schneider (2008) and Krolik (1999), while for the radiation processes the textbooks are Rybicki & Lightman (1979) and Longair (2011).

An active galaxy is characterized as active when the luminosity of the central region is much brighter than the stellar emission of the host galaxy can contribute. The name active galactic nucleus (AGN) refers only to the inner central region of a galaxy. The luminosities of AGN are about 10^3 times greater than the radiation of ordinary galaxies and ranges from 10^{42} up to 10^{48} erg s^{-1}. The emission of various processes of AGN can be observed over the whole electromagnetic spectrum from the longest radiowavelengths up to the γ-rays at TeV-energies. To observe these objects we use many instruments: for example the *Fermi Gamma-ray Space Telescope* (Atwood et al. 2009) in the γ-rays, *Chandra* (Weisskopf et al. 2002), *Swift* (Burrows et al. 2005) and *XMM-Newton* (Jansen et al. 2001) in the X-rays, *HST* (Williams et al. 1996) in the optical and *VLBI* networks in the radio regime.
A typical AGN consists of a supermassive black hole (SMBH) of 10^6 - 10^9 $M_\odot$ (Peterson 1997) in the center surrounded by an accretion disk to gain energy and further outside a dusty donut-shaped torus. Some AGN also exhibit bright jets in both directions perpendicular to the accretion disk ending in big lobes, best observed at radio frequencies. Since these sources appeared as luminous and still compact sources at their discovery at radio or optical wavelengths , they were also called "quasi-stellar radio sources" (Quasars) or "quasi-stellar sources" (QSO).
Only $\sim$ 10% of the AGN show the powerful jets perpendicular to their accretion disk. If a jet is detected at radio frequencies, the AGN is considered radio-loud corresponding when the radio-to-optical fluy density ratio R is $10 < R < 1000$, while radio-quiet AGN have $0.1 < R < 1$ (Kellermann et al. 1989). The other classification parameter for AGN is their inclination angle and the corresponding emission lines. The Unification Model (Antonucci 1993; Urry & Padovani 1995) merges the different types of AGN classified after observation properties in one model with dependency on the angle of the line of sight.
The **supermassive black hole** in the center is the power plant of an AGN. The assumption of constant observed luminosities over the lifetime of the object leads to an estimation of the total produced energy to $E \sim 3 \times 10^{61}$ erg using the luminosity and

the minimum age. The Schwarzschild-Radius should be $r_S \sim 6 \times 10^{14}$ cm considering thermonuclear processes and a maximal efficiency the burnt-out matter. This size is the same magnitude of the estimated radius of the whole central source. The large energy output and the gravitational processes can only be explained with a black hole in the center of these galaxies (Shakura & Sunyaev 1973). Using the *Eddington-limit* ($L < L_{\text{Edd}} = 1.3 \times 10^{38} \frac{M}{M_\odot}$) the mass of such a black hole can be estimated from its luminosity. An AGN with a luminosity of 10^{46} erg s^{-1} has therefore a mass of approximately 10^8 M$_\odot$ (Longair 2011).
Another hint for black holes in the center is the observation of apparent superluminal motion in jets, which will be explained in the section for the jet physics (Sect. 2.3). The outflow of particles in these jets has high relativistic velocities near the speed of light. To reach these high velocities the producing regions need to have escape velocities of the same magnitude. The only candidates with a compact size needed for these escape velocities are black holes and neutron stars. Using again the Eddington-limit rules out the neutron stars, since these objects cannot reach the high masses required for these processes. These processes also explain, that the jets have to arise very close to the Schwarzschild-Radius to get the needed acceleration.
However not only AGN have SMBH in their center, but also other galaxies like our galaxy have them. The center of the Milky Way known as Sagittarius A* (Sgr A*) is a black hole with the mass of 4.31×10^6 M$_\odot$ (Gillessen et al. 2009) and object to many studies (Eckart & Genzel 1996; Doeleman 2008).
The accretion disk surrounding the SMBH at a distance of r $\sim 10^{-3}$ pc can cause thermal emission, which can be observed as a peak in the ultraviolet and optical wavelengths. This peak is also known as the *big blue bump*. In the more distant regions between the dusty torus (r $\sim$ 1 - 10 pc) and the black hole gas clouds are found. These gas clouds build the the *broad line region* and the *narrow line region*. Since the torus is made of cold dust and of a donut-shape, it can absorb the light from the central region if it is in the line of sight.
The **broad line region** consists of very dense clouds at high temperatures. The widths of the observed broad lines leads to the assumption that this region is in close proximity to the accretion disk (r $\sim$ 0.01 - 0.1 pc). The turbulent motion of the clouds Doppler broadens the detected emission lines. The width of the broad lines correspond to velocities of $v \sim 10^3$ - 10^4 km s^{-1} (Osterbrock & Mathews 1986; Sulentic et al. 2000). Would this emission come from thermal broadening, it would correspond to temperatures of T $\sim 10^{10}$ K. At these temperatures atoms are completely ionized and could not produce emission lines. To reach the high temperatures and velocities the gas clouds have to be very dense ($n_e > 10^9$ cm^{-3}; Sulentic et al. 2000).
Further out (r $\sim$ 100 - 1000 pc) the gas clouds are less dense ($n_e \sim 10^3$ cm^{-3}), colder and referred to as **narrow line region** (Sulentic et al. 2000). In this region also forbidden lines with widths of a few hundreds km s^{-1} can be observed (Osterbrock & Mathews

1986).
The **jets** observed perpendicular to the accretion disk in both directions are a collimated, highly relativistic outflow of particles (Bridle & Perley 1984). Due to *relativistic beaming* (explained in Sect. 2.3) in most cases only one jet direction can be observed. If both jets are visible the jet moving away from the observer is fainter and referred to as *counterjet*. The jets have been observed so far in radio, optical and x-ray observations and can extend up to $\sim$ Mpc away from the central black hole. With the radio VLBI technique these jets are observed even on sub-pc scales. Tracking jet features at these scales often shows the already mentioned apparent superluminal motion of velocities up to $\sim 50c$. The interaction of these outflows with the intergalactic medium on kpc and Mpc scales results in lobes on either side, which can be detected best at radio frequencies.

2.1. The AGN zoo

Historically and based on their observed properties AGN are divided into different classes (Lawrence 1987). Features from optical observations like the emission lines are the main classification criterion. A similar criterion is the radio-loudness (Peacock et al. 1986) and their morphology in radio observations. The morphology for these sources is highly dependent on the inclination angle.

Radio-quiet AGN

For completeness the radio-quiet AGN are shortly presented. They build the larger fraction of AGN, since only about 10% of the AGN are radio-loud (Kellermann et al. 1989). The radio-quiet AGN are commonly Seyfert galaxies or radio-quiet Quasars.
The Seyfert galaxies were discovered by Carl Seyfert (1943) are the most common class of AGN. He observed several galaxies with an extrordinarily bright compact nucleus at optical wavelengths. The Seyfert galaxies are divided due to their optical properties (Khachikyan & Weedman 1971) into Seyfert 1 galaxies, which show mainly broad emission lines, and Seyfert 2 galaxies with only the narrow (forbidden) lines. However there are some more subclasses like the narrow-line Seyfert 1 (NLS1) galaxies. In these galaxies the broad emission lines are narrower than in the typical Seyfert 1 galaxies. Additional to the NLS1 also some intermediate types like Seyfert 1.5 or Seyfert 1.8 have been defined, since these did not fit into the established model.
The quasi-stellar radio objects (QSO) are AGN, which have been identified as blue star-like objects in surveys. Sandage (1965) found that these objects show similar properties like the quasi-stellar radio sources, which have later been known as quasars. Commonly both are named quasar with distinguishing them into radio-loud and radio-quiet (Kellermann et al. 1989). This class was found to have most of the brightest objects in the sky.

They were first taken as bright stars, but they are far more distant (higher redshifts) and show different emission lines than stars. Compared to Seyfert galaxies this radio-quiet type of AGN has weaker absorption, weaker narrow lines and higher bolometric brightness values. Often it is difficult to distinguish between the radio-quiet quasars (quasi-stellar object = QSO) and Seyfert 1 galaxies. In most cases the host galaxy is the criterion: if the host galaxy is not identified as a spiral galaxy, it is a QSO.

Radio-loud AGN

Since this work is based on radio observation the targets of these observations are all radio-loud. The common radio-loud AGN types are radio galaxies and blazars. A relatively new small subsample of AGN build the more uncommon group of radio-loud narrow line Seyfert 1 galaxies (NLS1).

Radio galaxies

Like the Seyfert galaxies, the radio-loud radio galaxies can be subdivided based on their optical properties into broad-line radio galaxies (BLRG) and narrow-line radio galaxies (NLRG). The difference to Seyfert galaxies is the radio-loudness. Typical radio galaxies have a radio flux at least 10 times higher than their optical flux. The optical luminosity and the extended radio emission are the classification features to distinguish them from quasars.
The inclination angle of radio galaxies are on the edge, which means that often not only one jet but both jets are detected. In most cases radio galaxies are subdivided after their radio morphology into Fanaroff-Riley I and II (FRI & FRII) galaxies. FR I radio galaxies have a bright core and prominent two-sided jets coming from the compact central region of the AGN. FR II show bright hot spots and luminous lobes while usually only a one-sided jet and a less dominating core can be detected. The observation of these jets show that AGN can have highly collimated jets extending their structure from kpc to Mpc away from the central region.
Comparing the luminosities of FRI and FRII radio galaxies, the FRII galaxies have much more powerful jets and lobes with luminosities of $\log(L_{\mathrm{ext}}[\mathrm{W\ Hz^{-1}})$=26 and higher, while the jet-dominated FRIs are less powerful with usually less than $\log(L_{\mathrm{ext}}[\mathrm{W\ Hz^{-1}}])$=24 (Ledlow & Owen 1996; Baum et al. 1995). However also radio galaxies with intermediate luminosities have been found. These luminosity may also be dependent on the black hole mass and the accretion rate, which can also create the radio galaxies with intermediate jet luminosities (Ghisellini & Celotti 2001).

Blazars

Blazars are the most luminous AGN and show highly variable emission. The optical as well as the radio emission of these sources is strong polarized. This class is again subdivided into BL Lac objects, named after BL Lacertae (Hoffmeister 1929), and flat spectrum radio quasars (FSRQ). FSRQs show broad emission lines, while BL Lac objects usually show no or only very weak emission lines.
Hoffmeister (1929) found the object Bl Lacertae to have highly variable emission in the optical wavelengths on the timescale of a few days. Schmitt (1968) found this source also to be bright and variable in radio observations. Based on the properties of this objects the subclass BL Lac objects of the radio-loud AGN has been formed and several similar sources were detected (Stein et al. 1976).
The radio-loud quasars were discovered by Schmidt (1963) with 3C 273 as the first of these objects. With more observation on 3C 273 and 3C 48 (Greenstein & Schmidt 1964) these quasi-stellar radio sources were defined. Quasars are among the brightest sources in the sky. Based on their radio appearance and their spectral indices, the radio-loud quasars are often subdivided into flat spectrum radio quasars (FSRQ) and compact steep sources (CSS).
Compared to the radio galaxies these sources are often compact or show only a one-sided jet. This is caused by their different orientation than radio galaxies. While radio galaxies are observed on the edge, making it possible to detect both jets, for blazars the observer looks into the jet at a very small inclination angle. This strongly boosts the jet in the direction of the observer while deboosting the counterjet at the same time.
The catalog of FERMI/LAT reveals, that most of the γ-detected sources are blazars (Abdo et al. 2010; Nolan et al. 2012; Acero et al. 2015). Taking into account the emission of these sources over the electromagnetic spectrum, blazars usually show a spectral energy distribution of two humps. The peak of the synchrotron radiation is often used to further subdivide the blazars into low-, high-frequency and intermediate synchrotron peaked sources.
Looking into the relativistic jets of these AGN results in highly beamed emission, causing this bright emission. The inner regions of blazars are well studied with VLBI, revealing that these sources possess jets with apparent superluminal speeds (Kellermann et al. 2007; Lister et al. 2013).

Radio-loud narrow line Seyfert 1 galaxies (NLS1)

Even if Seyfert galaxies are usually radio-quiet, also some radio-loud ones have been found (Komossa et al. 2006). Especially the NLS1 show a small subsample of radio-loud narrow-line Seyfert 1 galaxies with slightly lower black hole masses. These AGN have usually shorter and fainter jets. In their emission lines and their variability these objects have blazar-like features. For this the NLS1 are a candidate for young blazars (Foschini et al. 2015).

2.2. The unification model

Table 2.1.: Summary of unification scheme

	Type 1	**Type 2**
radio-quiet	Seyfert 1 radio-quiet quasar	Seyfert 2 radio-quiet quasar
radio-loud	Blazars (BL Lac, FSRQ) radio-loud quasar	radio galaxies (FR1 + FR2) radio-loud quasar
	increasing angle to the line of sight $\longrightarrow$	

The different properties (Lawrence 1987) leading to the various AGN classifications can be combined to a unification model. This model has been introduced by Antonucci (1993), Miller (1994) and Urry & Padovani (1995). An AGN is defined as described in the beginning of Section 2. The unification model aims to explain the different AGN classes with a rather simple model. Most observed differences of the classes can originate from the observing angle to the target.
A view edge on results in an obscured core region by the dusty torus. The torus also hides the broad line region, changing the observed emission lines. This is also confirmed in the observations of NGC 1068, where Antonucci & Miller (1985) found that the nuclei of Seyfert 2 galaxies have the same properties as Seyfert 1 nuclei. This means that the broad and narrow lines come from different regions seen under different observing angles. On the other side for the radio galaxies the counterjet can be detected, while viewing almost into the jet the boost of the jet and deboost of the counterjet at the same time result in a one-sided observed morphology.
While the observing angle explains the differences of Seyfert 1 versus Seyfert 2 and radio galaxies versus blazars, the radio loudness is a criterion to further distinguish AGN (see Table 2.1). Additional the luminosity plays a role at further subclassification like the Fanaroff-Riley classification (Fanaroff & Riley 1974a) for radio galaxies.
With the luminosity subclassification the unification model assumes that blazars are the counterparts to radio galaxies, only observing them with a different inclination angle. In this case BL Lac objects should be the counterparts to FRI radio galaxies and the FSRQs correspond to the FRII radio galaxies. This leads to the expectation that their

radio morphology should fit to this classification, meaning that BL Lac objects should have a prominent jet structure, however due to relativistic boosting effects only a one sided jet can be seen, and quasars should show the more diffuse counterparts of the bright lobes. Also a similar behaviour of the jet luminosities is expected. However the measurement of the luminosities is more difficult for blazars since there jets are highly boosted by relativistic effects. Even if there are many observations where the unification model fits rather well, some sources were found behaving different from the expectation. These observations challenge the simple unification model for AGN.

Challenges to the unification model

This unification model is tested in several studies. Many results confirm the expected features, however some studies also found AGN which fit not into the model. This indicates that the unification model might fit for many sources but is an oversimplification to unite all AGN classes. The following list shows some examples on AGN sample studies in which most samples show deviations from the expected unification behavior:

- Cooper et al. (2007) and Kharb et al. (2010): VLA study on MOJAVE sample (135 sources, mainly blazars); many sources confirm expected morphologies for the BL Lac/FR I and FSRQ/FR II counterpart theory; luminosities show blazars with intermediate luminosities corresponding to the FR I/II division line
- Antonucci & Ulvestad (1985): sample study on blazars confirming the expectation for the morphology to fit for the counterpart theory
- Gopal-Krishna & Wiita (2000): sample study on hybrid radio galaxies, several objects show different features in their lobes being candidates for an intermediate FR I/II class
- Landt et al. (2006): FSRQ sample study finding morphological features for FR I and FR II counterparts; most extended emission is FR II-like but the host galaxies are FR I-like
- Heywood et al. (2007): quasar sample study; morphological counterparts for both FR I and FR II radio galaxies; also luminosities in the intermediate range
- Chen et al. (2015): study on mixed sample confirming the expected luminosity division for BL Lacs and quasars to be the counterparts of FR I and FR II radio galaxies
- Rector & Stocke (2001): BL Lac sample multiwavelength study (radio and X-ray) detecting several BL Lac objects in deep VLA observations showing higher extended luminosities than expected for FR I counterparts

- Giroletti et al. (2004): BL Lac sample in which no target shows evidence to have FR II properties; thus confirming the unification model
- more sample studies finding intermediate luminosities by Sambruna et al. (2007) and Ghisellini et al. (2011)
- Massaro et al. (2013): large sample study on blazars with several BL Lacs with spectral indices indicating missing extended emission (might also be caused by the variability)

The main deviations are the indication of intermediate subclassifications for AGN (e.g. Seyfert 1.5 or intermediate luminosities of FR I/FR II), which is strengthened by the finding of blazars with luminosities intermediate to the corresponding FR I/II division and the finding of sources with different morphological features.
For the blazars several sources match not with the morphological expectation like BL Lac objects with hot spots in their extended emission (Cooper et al. 2007; Kharb et al. 2010; Heywood et al. 2007; Landt et al. 2006). In most cases the extended luminosities do not match the expectation. This expectation is calculated following Ledlow & Owen (1996) based on the observational division line between FR I and FR II found by Fanaroff & Riley (1974a) for the corresponding blazar counterparts (Giroletti et al. 2006). In the studies mostly BL Lac objects are found to have higher luminosities than expected (Chen et al. 2015; Rector & Stocke 2001), but also some quasars show less extended luminosities (Sambruna et al. 2007; Heywood et al. 2007; Landt et al. 2006) than the calculation expects. The radio luminosity of AGN seems also to be connected to the optical luminosity and the black hole mass of the SMBH in the center of the galaxy.

Now these studies can be improved by adding observational data covering new frequencies. Using the capabilities of the current and future telescopes like the Low Frequency Array (LOFAR) and the Square Kilometer Array (SKA) several studied can be enhanced. The key to this improvement are the low frequencies in combination with the resolution these telescope arrays offer. Observations at low frequencies are more sensitive to the diffuse extended emission, which will be explained further in the following sections and the next chapter. With higher sensitivity for extended diffuse emission it will be possible to uncover the structure of lobes and diffuse emission in blazars.
Massaro et al. (2013) was tackling the extended emission at lower frequencies by calculating spectral indices of the sources. Their data is based on different catalogs of surveys at different frequencies however with an angular resolution which is not sufficient to resolve structures. The spectral indices for several BL Lacs indicate that the extended emission is missing, but since these sources are known for the high variability and the catalog observations are not simultaneous the flux densities can deviate and thus change the spectral index. The new telescopes offer higher angular resolution, which will result in resolved structures of the extended emission. Additional these observations can be used

to obtain extended radio luminosities at low resolutions. These should be similar to the already known extended radio luminosities if the observations at higher frequencies were sensitive enough to detect the diffuse extended emission.
With low frequency observations of blazars at arcsec-resolution the unification model can be tested by examining the morphology of the resolved extended emission and by calculating the radio luminosity of extended emission, which has to be separated from the bright core region.

2.3. Jet physics

AGN are detected over the whole electromagnetic spectrum starting at low radio frequencies up to γ-rays at TeV-energies. The AGN jets (Bridle & Perley 1984) are observed by radio telescopes as well detected in the optical and X-rays are not fully understood. Due to the increase of angular resolution by connecting radio telescopes into a network it is possible to resolve them on different scales. The highest angular resolution images show the radio jets on sub-pc scales, however these features extend to structures of Mpc. To study the structural evolution of the jets many AGN are monitored over decades. Since these jets are very powerful and yet collimated on pc-scales (Müller et al. 2011), many theories have been formed to explain the jet formation using magnetohydrodynamics, general relativity and electrodynamics. Even if some mechanisms seem to be understood, parts of the jet formation are still open questions with theories but no unique favored explanation. For this the jets are still a subject to study their features and evolution with multiwavelength observations to confirm or rule out certain theories. An idealized jet is modeled by Blandford & Königl (1979) describing it with a conical geometry with a given opening angle where plasma is ejected into a stream. In this stream shock fronts are built if the a higher density plasma compared to the underlying jet is injected. The shock-fronts can then be acceleration and collimation regions due to their magnetic fields (Fermi 1949).
To explain the powerful and highly collimated outflows mainly two models for the process of jet formationare commonly used. The first model was developed by Blandford & Znajek (1977) and is based on a rotating SMBH with an accretion disk. The accretion disk provides a magnetic field which accelerates the plasma created in the combination with the rotating SMBH. The rotating black hole extracts energy from the accretion disk and accelerates parts of that as a jet perdendicular to the accretion disk building the jet and the counterjet. By minor modificating the model this process also works for highly rotating black holes (Tchekhovskoy et al. 2010), since these were not included in the first model.
The other model was developed by Blandford & Payne (1982). In this model the plasma is accelerated by a toroidal magnetic field component coming from the rotation of the

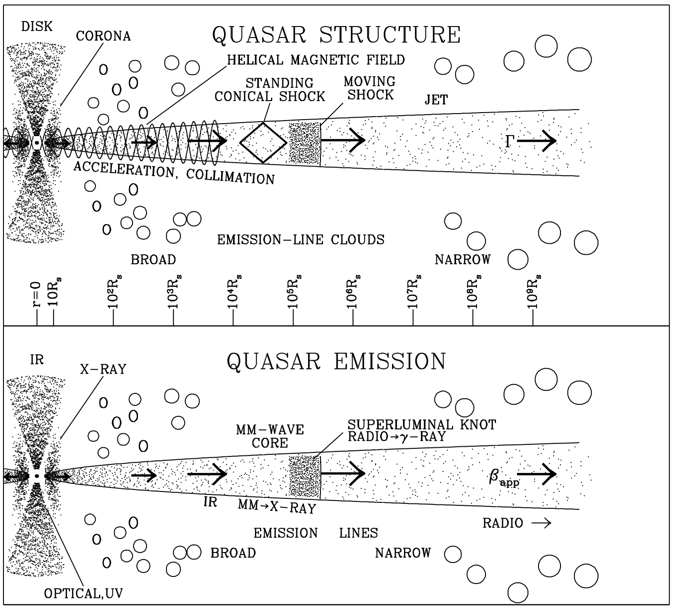

Figure 2.1.: Jet model of AGN showing the physical jet structure in the top part and the origin of various radiation in the lower part of the figure. Image from Marscher (2009)

accretion disk. By winding up the magnetic field lines a cone-shaped field is developed in which the plasma is moving as a jet. So in both models the magnetic fields and acceleration of particles is due to rotating magnetic field lines.
There are strong pressure gradients needed to push out matter in a highly collimated outflow at relativistic velocities. This can be explained using gas dynamics. Marscher (2009) argued that jets with Lorentz factors > 10 and a collimation $< 1°$ cannot be formed through gas dynamics. Considering this, only magnetic forces have enough power to be the driving force to launch such jets. Magnetic forces of this required strength can be created by a spinning black hole and/or the accretion disk. Through spinning the magnetic field lines wind up into a helix. The decreasing magnetic pressure in the distance of the black hole creates a strong pressure gradient which can accelerate the matter. Both theories, the magnetic fields and the gas dynamics, lead to a gradual acceleration with an opening angle inverse proportional to the final Lorentz factor. This leads to the expectation that the highest intensity of observed emission is found at the launching point and the close regions. Changes in the magnetic field can be observed studying the polarization of jets (e.g. Hovatta et al. 2010; Homan & Lister 2006; Lister & Homan 2005)
The point close to the launching point where the radio emission changes from optically thick to optically thin ($\tau = 1$) is usually referred to as the core. The position of the core is frequency dependent stationary feature, which is also used as reference when looking at the kinematics of moving features. Even with the high collimation of the jets, some

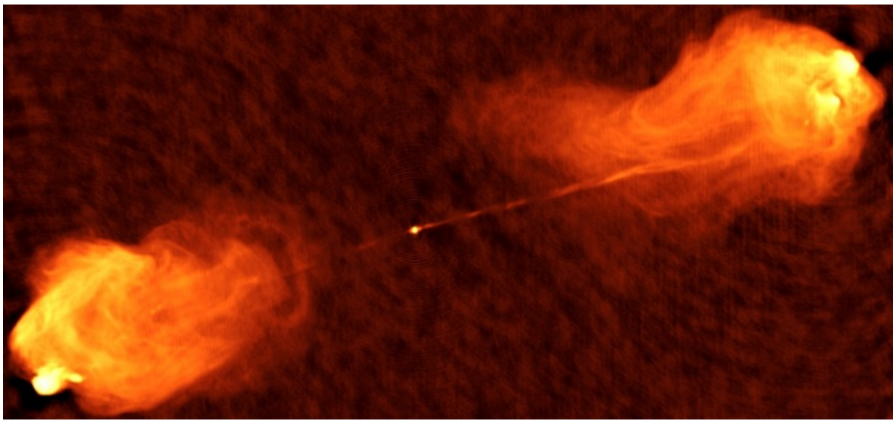

Figure 2.2.: A VLA observation of CygnusA at 6 GHz shows the bright core in the center. The jet moves in west direction and ends in a big lobe with a hot spot where the particles are decelerated due to the interaction with the intergalactic medium. In the east direction the lobe of the counterjet is seen while the counterjet itself is weaker and hardly detected. Image from Perley et al. (1984) with image courtesy of NRAO/AUI.

sources have been found where the jet shows disruptions or bends (e.g. Kellermann et al. 2004).

The shock waves are usually detected as bright knots in the resolved jet on pc-scales (see Figure 2.1). These knots can move along the jet axis or be stationary. The shocks inside the jet are created by differences in the jet pressure. One kind of shock are the recollimation shocks where the jet is over-pressured in respect to the ambient pressure (Agudo et al. 2012). The increased pressure magnifies the intensity and polarization of this feature, making it brighter in appearance. In further distance of the black hole the gas dynamic model becomes valid and differences in the magnetic field can lead to Kelvin-Helmholtz instabilities building shocks due to differences in the plasma velocities. In the jet quasi-stationary features and moving knots can be found (e.g. Lister et al. 2009). While the recollimation shocks keep the jet collimated, all shocks may travel along the jet axis allowing the plasma particles to be reflected. Multiple reflection at a wave front can also lead to acceleration. In several kinematic studies this kind of acceleration was detected (e.g. Kellermann et al. 2004; Homan et al. 2009; Lister et al. 2013; Bloom et al. 2013; Homan et al. 2015).

At larger distances away from the core the jet can interact with the intergalactic medium and create the radio lobes. The interaction with the intergalactic medium leads to instabilities in the jet and deceleration of the particles. These lobes are usually seen in radio observations at larger scale and lower resolution than the observations to study the jet kinematics. As example a radio observation at 6 GHz with the Very Large Array (VLA) is shown in Figure 2.2.

To be able to study the jet evolution and kinematics as well as other AGN properties, it is important to understand where and through which processes the observed emission is produced. The main processes, the synchrotron radiation for the low-energy emission and the inverse Compton effect for the high-energy emission, will be explained briefly in the following.

Synchrotron radiation

The synchrotron radiation is also called magnetobremsstrahlung and is the relativistic version of cyclotron radiation. Any kind of bremsstrahlung is radiation caused by the deceleration or acceleration of charged particles. The deceleration can happen through interaction like scattering with other particles resulting in emission of photons due to the energy loss. Synchrotron emission is the radiation from the acceleration of relativistic particles in magnetic fields.
The Lorentz force influences relativistic charged particles e with mass m_e moving on a helical path with velocity $\vec{v}$ in a magnetic field $\vec{B}$:

$$m_e \gamma \dot{\vec{v}} = \frac{e}{c} \vec{v} \times \vec{B} \tag{2.3.1}$$

with the Lorentz factor $\gamma = (1-\beta^2)^{-0.5}$, $\beta = v/c$ and c is the speed of light. The acceleration leads to emission of photons in a cone on the helical path through the magnetic field. For relativistic particles the cone has an opening angle $\propto \gamma^{-1}$ if $\gamma \gg 1$ and the emitted energy of a single charged particle can be calculated with

$$-\frac{\mathrm{d}E}{\mathrm{d}t} = \frac{4}{3} \sigma_T c \beta^2 \gamma^2 \frac{B^2}{8\pi} \tag{2.3.2}$$

where σ_T is the Thomson cross section. Using the relation $E = \gamma m_e c^2$ it can be shown, that the energy per time is $\propto m_e^{-2}$ and for this reason the synchrotron radiation of more massive particles is low and negligible.
Considering a non-thermal electron distribution $n(\gamma)$, leads to

$$S_\nu = -\frac{\mathrm{d}E}{\mathrm{d}t} = \int_1^\infty S_\nu(\gamma) n(\gamma) d\gamma \tag{2.3.3}$$

$$\Rightarrow n(\gamma) d\gamma = n_0 \gamma^{-p} d\gamma \tag{2.3.4}$$

where p is the *particle distribution index* and describes the power law of the particle distribution. Integrating over the corresponding critical frequency ν_c shows that the

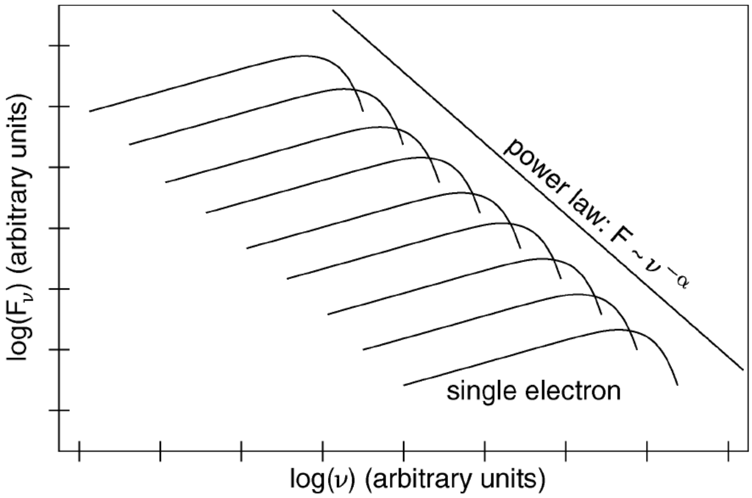

Figure 2.3.: The combination of the synchrotron radiation of a charged particle distribution to a power law spectrum $S_\nu \propto \nu^\alpha$. Taken from Schneider (2008)

spectrum can be described again with a power law with the spectral index α, see Figure2.3

$$S_\nu \propto \nu^{-\frac{p-1}{2}} \tag{2.3.5}$$

$$\text{where}\alpha = \frac{1-p}{2} \tag{2.3.6}$$

The photons of the synchrotron radiation can be absorbed by electrons which is called synchrotron self-absorption. The self-absorption alters the photon spectrum with a self-absorption coefficient a_S

$$a_S \propto \nu^{-\frac{p+4}{2}} \tag{2.3.7}$$

The self-absorption coefficient is used to calculate the optical depth τ_ν

$$\tau_\nu = \int_{s_0}^{s} a_S(s')\mathrm{d}s' \tag{2.3.8}$$

where ds is the distance the photons travels corresponding to the loss of intensity. If $\tau_\nu < 1$ the medium is called *optically thin* or *transparent*, while $\tau_\nu > 1$ means the medium is *optically thick* or *opaque*. The frequency near $\tau_\nu = 1$ is called turnover frequency ν_t

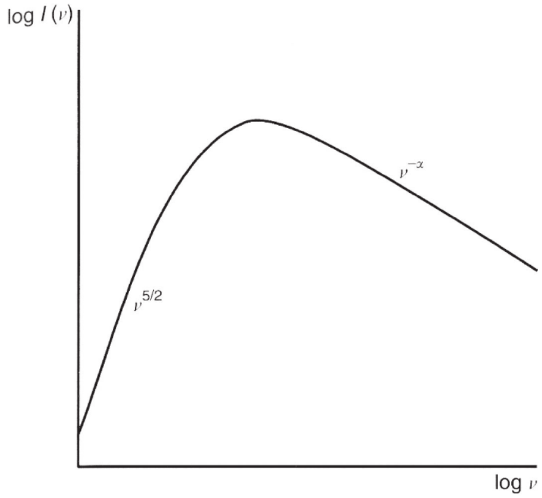

Figure 2.4.: Typical synchrotron spectrum: broken power-law with synchrotron self absorption which turns into a power spectrum $\propto \nu^{-\alpha}$. Taken from Longair (2011)

which leads to a broken power-law of the spectrum, like in Fig. 2.4:

$$S_\nu \propto \nu^{\frac{5}{2}} \quad \text{for } \nu < \nu_t \tag{2.3.9}$$

$$S_\nu \propto \nu^{\frac{1-p}{2}} \quad \text{for } \nu > \nu_t \tag{2.3.10}$$

For the discussion of spectral indices α with $S_\nu \propto \nu^{-\alpha}$ spectral indices with $\alpha < 0$ corresponding to optical thin emission regions and in case of absorption inverted spectral indices of $\alpha > 0$ are found.

Inverse Compton effect

To reach the high energies at which AGN are detected in the X-rays and γ-rays, low-frequency photons scatter off relativistic electrons to obtain higher energies. This process is called Inverse Compton scattering. Similar to the Compton scattering a photon is inelastically scattered at a charged particle however instead of transferring energy from the photon to the particle, in the inverse Compton effect the photon gains energy. The particle looses energy, which is important for cooling an electron gas.
This effect is also dependent on the particle density, their energy density and the magnetic fields. Similar to the synchrotron radiation the inverse Compton scattering can be described by a power-law. Since this thesis is focused on radio observations, where the high energy processes are less important, this effect will not be discussed in greater detail.

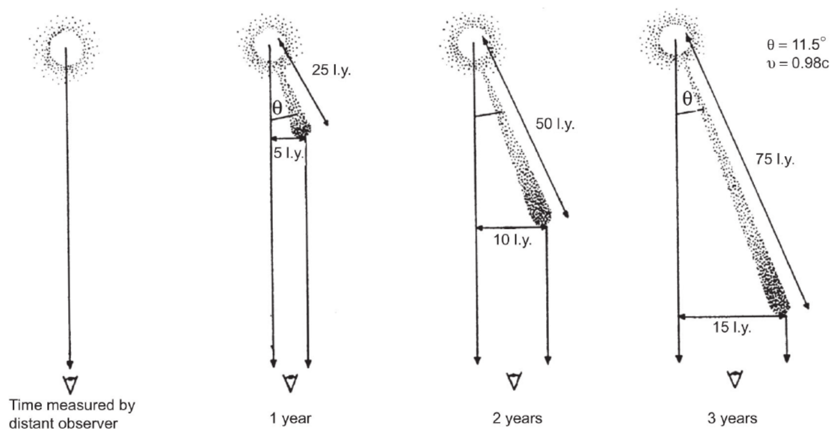

Figure 2.5.: Projection effect leading to apparent velocities faster than the speed of light, here $\sim 5c$ at an angle $\theta = 11.5°$ to the line of sight and $\beta = 0.98$. Taken from Longair (2011)

Apparent superluminal motion

Studying AGN jets on pc-scale with observations obtained with Very Long Baseline Interferometry (VLBI), which will be explained in detail in the next chapter (Section 3.2), revealed that some jet knots reach apparent superluminal speeds. The kinematics can only be calculated after monitoring the jet with several observations over time. The timescale between those observations is dependent on the speeds of the target. With the brightness distributions of several observations the distance of certain knots in the jet from the core can be measured. Combining the distances with the timeintervals between the observations their jet speeds can be calculated. For this at least five observations should be used. In large samples jets often show the superluminal speeds (Lister et al. 2009). However the apparent superluminal velocities are caused by a projection effect.

This effect of superluminal motion can be explained with the geometrical connection between jet axis and the line of sight, see Fig. 2.5. In two observations within a time difference of Δt a jet feature traveling along the jet axis shows only a projected distance of between both positions of $\beta \Delta t \sin\theta$. The angle between the jet axis and the line of sight is θ. Assuming high relativistic jet speeds with $\beta \approx 1$ and small angles θ between the jet axis and the line of sight the apparent speeds v_{app} can be faster than the speed of light c:

$$v_{\text{app}} = \frac{v \sin\theta}{1 - \beta \cos\theta} \tag{2.3.11}$$

If the angle to the line of sight is known, the intrinsic jet speed can be calculated. The intrinsic speeds can reach velocities very close to the speed of light.

Doppler boosting

Additional to the projection effect creating apparent superluminal motion another relativistic effect called Doppler boosting occurs. The relativistic moving plasma particles undergo a Doppler shift between the observed frequency ν_{obs} and the intrinsic emitted frequency ν_{em}:

$$\nu_{\text{obs}} = \frac{\nu_{em}}{\gamma(1-\beta\cos\theta)} \tag{2.3.12}$$

The Doppler factor D is a measure how strongly the emission is boosted or deboosted and can be calculated with

$$D = \frac{\nu_{\text{obs}}}{\nu_{em}} = \frac{\sqrt{1-\beta^2}}{1-\beta\cos\theta} \tag{2.3.13}$$

With small angles between observer and jet axis the emission can be boosted by a large fraction. Since the flux density is also dependent of the frequency ($S_\nu \propto \nu^{-\alpha}$) the Doppler boosting has a strong influence on the intensity of the emission and the spectrum. A jet in the direction of observer gets boosted and shows higher flux ($S_{\nu 1}$) while the counterjet which moves in the direction away from the observer gets deboosted ($S_{\nu 2}$).

$$R = \frac{S_{\nu 1}}{S_{\nu 2}} = \left(\frac{1+\beta\cos\theta}{1-\beta\cos\theta}\right)^{3+\alpha} \tag{2.3.14}$$

If the ratio R between both jets is >1 the boosting explains why many observations can only detect one jet. The counterjet is deboosted and the flux density is often below the sensitivity limit of the telescopes.

2.4. Search for intrinsic jet power

For the understanding of AGN and their jets it is difficult to verify models when boosting effects influence the measurable quantities. Even with the knowledge of the boosting processes it is very difficult to disentangle these relations. Besides the velocities the power of the jet could help to understand the needed magnetic fields to form a jet and keep it collimated. However the jet power, which can be measured as luminosity suffers also from boosting effects making it difficult to obtain the intrinsic jet powers. To calculate the intrinsic jet power from the apparent jet luminosity, the Doppler factor D and the angle to the line of sight has to be known. Together with the apparent jet velocity β_{app} these quantities have the following relations (Cohen et al. 2007b; Lister 2003; Cara &

Lister 2008):

$$D = \gamma^{-1}(1-\beta\cos\theta)^{-1} \quad (2.4.1)$$

$$\beta_{\text{app}} = \frac{\beta\sin\theta}{1-\beta\cos\theta} \quad (2.4.2)$$

$$L = D^n L_0 \quad (2.4.3)$$

where $n = \alpha + p$ with p being the Doppler boost exponent, α the spectral index ($S \propto \nu^{\alpha}$), $\beta = (1-\gamma^{-2})^{-1/2}$ the speed of the jet in units of c, γ the Lorentz factor and θ the angle to the line of sight. Usually $p = 2$ for continuous jet emission and $p = 3$ for discrete emitting regions is used (Lind & Blandford 1985).
The radio luminosity L can be calculated from the flux density S, the distance d and the redshift z of the target. For the spectral index assumptions can be made if it is not measured. To measure the spectral index at least comparable observations at different frequencies have to be made. The formula to calculate the radio luminosity is:

$$L = 4\pi S d^2 (1+z)^{1+\alpha} \quad (2.4.4)$$

For blazars looking almost into the jet it is even more difficult to disentangle because small differences in their inclination angle can cause large deviations in their Doppler factor. In many cases the apparent speed β_{app} and apparaent luminosity L are measured but the desired values are the Lorentz factor γ and the intrinsic luminosity L_0, which is also known as the inversion problem (Cohen et al. 2007b). Knowing the angle to the line of sight of these objects allows only to estimate a range for the desired values, but it is also difficult to get the angle to the line of sight for most objects. One way to calculate the angle to the line of sight is by using the jet (S_{jet}) to counterjet (S_{cjet}) ratio R of their flux densities in combination with the apparent jet speed, for which a detection of the counterjet is needed or only limits can be obtained (Kadler et al. 2012):

$$R = \frac{S_{\text{jet}}}{S_{\text{cjet}}} = \left(\frac{1+\beta\cos\theta}{1-\beta\cos\theta}\right)^n = (\beta_{\text{app}}^2 + D^2)^n \quad (2.4.5)$$

Kharb et al. (2010) calculated the luminosities for blazars using their extended emission at 1.4 GHz and subtracting the beamed central and jet regions to study the relation between the extended emission and the apparent jet speeds and found a significant correlation, where "the most powerful sources possess faster jets" (Kharb et al. 2010). The conclusion of this correlation was that the kinetic power of the jet is closely related to the extended unbeamed emission.
The emission of a single particle becomes less energetic with time, this means that the wavelengths become larger. Observing at lower frequencies can show the emission of older particle populations, while still having the emission of the particle population where new particles are injected into the stream constantly with a continuous emission spectrum.

This leads to a frequency dependence of the boosting effects. For the region without new injections of particles the emission is less beamed with decreasing observing frequencies. Thus looking at the extended jet emission at low frequencies is a way to get closer to the measurement of intrinsic jet powers. The extended emission consists mainly of particles coming from the jet but interacting with the galactic medium creating the lobes at the end of the jet. For this particle population it can be assumed that the emission if coming from older particles which are not beamed any more by relativistic effects. The behaviour of the particle populations are also reflected in the spectral index. The core and the close jet regions with constantly new injected particles show flat spectral indices of $\alpha \sim 0$. The steep spectral indices of the lobes with $\alpha \sim -0.7$ indicate that the particle population is different in these regions (Kellermann & Pauliny-Toth 1969; Burbidge & Burbidge 1957). Because of this the approach to observe at lower frequencies can help to measure intrinsic jet luminosities, which can help to estimate the Doppler factor and thus improve the models and the understanding of the jet formation and evolution.
To use the advantage of lower frequencies than the usual observations in the GHz-regime with less beaming effects was already subject to studies like Arshakian et al. (2010). For this archival flux densities for a blazar sample was used to interpolate the low frequency flux densities at 151 MHz. The interpolated flux densities were then used to calculate luminosities to use them for further estimations on intrinsic jet powers. However these flux densities correspond to the flux density of all emission of the source. The emission of the core region and at least the inner jet is still beamed. It was assumed that the extended emission would dominate the emission however it was not able to be tested. For the case that the core emission is still a large fraction of the total flux density, these luminosities can not be used for estimation of intrinsic jet power.
With the new telescopes like LOFAR and the future SKA it is possible not only to measure the total flux densities but also observe these sources with a resolution to see the structure. By observing at different frequencies the spectral indices of certain regions can be measured, to determine if there are still indications for beamed emission. With this possibility the extended flux densities can be measured and only the extended radio luminosities can be calculated. This will improve the possibility to estimate the Doppler factors and the intrinsic jet powers.

3. Observations with radio telescopes

Observations of AGN are crucial to improve the understanding of the processes of the jet formation and evolution. This thesis is based on radio observations to examine the extended emission of AGN jets. Using radio telescopes connected as an interferometer greatly improve the resolution and resolution, which helps to get view on the detailed structure of AGNs at radio wavelengths. The following chapter will introduce how a radio telescope and how an interferometer of radio telescope work. This part is mainly based on Burke & Graham-Smith (2010), Thompson et al. (2001) and Taylor et al. (1999). After the introduction to radio telescopes, the basics of data reduction, the telescope LOFAR, which is used for the observations of this work and two popular AGN monitoring programs are presented.

3.1. Principles of a radio telescope

The main parts of a radio telescope are: the antenna, a receiver and a recording system. The design depends on the observed wavelengths (see Fig. 3.1). While the antennas for observation at cm and mm-wavelengths have a parabolic dish shape to reflect the incoming waves into the receiver, the long wavelength designs are often only dipole antennas. Based on the wavelength the reflector dishes can often consist of a mesh while small wavelengths need solid dishes. The flux density of the radiation measured with a radio telescope usually has the unit *Jansky* (Jy) and is defined as:

$$1 \text{ Jy} = 10^{-26} \text{J s}^{-1} \text{ m}^{-2} \text{ Hz}^{-1} \tag{3.1.1}$$

To get a detailed view on the structure of the observed objects a high resolution is needed. The angular resolution of a radio telescope is defined by the Rayleigh criterion, which can be approximated by

$$\sin(\alpha) \approx 1.22 \frac{\lambda}{D} \tag{3.1.2}$$

where α is the angular resolution, λ the observed wavelength and D the diameter of the reflector. This means that the resolution is highly dependent on the observed wavelength and to achieve similar resolution as optical telescopes large reflectors are needed.
To measure the brightness distribution of a target the radio telescopes effective area and the beam characteristic of the telescope and the flux density has to be taken into account.

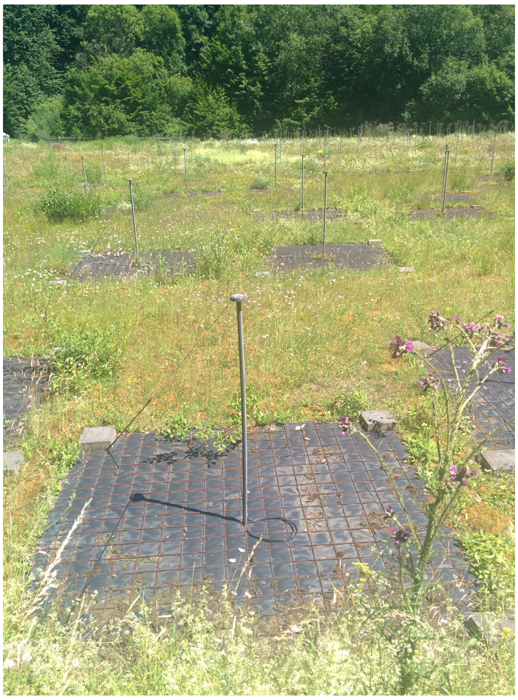

Figure 3.1.: Example images for radio telescopes using different designs:
Left: the SRT (Sardinia Radio Telescope) in Sardinia (Italy) with a diameter of 64 m covering frequencies from 0.3 to 115 GHz. Picture taken in October 2014. Website for the telescope: http://www.srt.inaf.it
Right: low band antennas (LBA) of the Effelsberg LOFAR station near Bonn (Germany) observing at frequencies from 10 to 90 MHz. Picture taken in June 2015.

The receiver has a beam characteristic, which is the same as if the telescope would be an emitter. The receiving pattern consists of a main lobe which is commonly named beam and some smaller sidelobes which can affect the observation allowing signals from sources apart from the target field to be received. Hence, the design of a radio telescope aims at reducing the sidelobes and the impact of radio interference as much as possible. The full-width at half maximum of the main lobe defines the resolution of the radio telescope. The power P measured at a frequency ν by the telescope is then a convolution of the brightness distribution $B(\nu, \theta, \phi)$ of the target and the characteristic of the antenna:

$$P(\theta, \phi) = \int_0^\infty \mathrm{d}\nu A_{\mathrm{eff}}(\nu) \int \mathrm{d}\Omega B(\nu, \theta, \phi) \Pi_{\mathrm{Ant}}(\nu, \theta, \phi) \tag{3.1.3}$$

where $\Omega = (\theta, \phi)$ is the solid angle of the direction the telescope is pointing, $\Pi_{\mathrm{Ant}}(\nu, \theta, \phi)$ is the reception pattern and $A_{\mathrm{eff}}(\nu)$ is the effective area of the telescope.

3.2. Radio Interferometry

Achieving high resolution at radio wavelengths with only one dish requires very large telescopes. Connecting several radio telescopes to a network is another way to improve the resolution. When two radio telescopes are connected and point in the same direction, like in Fig. 3.2, the signal reaches one of the telescopes with a time delay since the path is longer. This delay τ_g can be calculates geometrically using the angle θ to the direction of the source and the baseline distance b_λ between both telescopes:

$$\tau_g = \frac{b_\lambda}{c} \sin\theta \tag{3.2.1}$$

The correlator corrects for the geometrical delay τ_g by inserting an instrumental delay τ_i for the other telescope ($\tau_g = \tau_i$). The signal of both telescopes is integrated and combined by a correlator, which creates the time-averaged product known as cross power product. By combining the telescope the resolution is improved as if the telescope has a dishsize of $D = b_\lambda$, which is the longest baseline b_λ of an interferometer.
The cross power product of the signals are the convolution of the brightness distribution and the characteristics of the antenna array. The source $\vec{s}(l, m, n)$ is related to the phase-tracking center $\vec{s_0}$ as $\vec{s} = \vec{s_0} + \vec{\sigma}$. The baseline vector $\vec{b}(u, v, w)$ is a right-handed rectilinear coordinate system usually in the units of the observed wavelength. The phase-tracking center $\vec{s_0}$ is defined in the w-direction and is perpendicular to the (u, v)-plane. The complex visibility function $V(u, v, w)$ corresponds to the convolution of the brightness distribution of the sky $B_\nu(l, m)$ and the reception pattern of the array $A(l, m)$. With the Fourier Transformation of the visibilities the brightness distribution of the observed

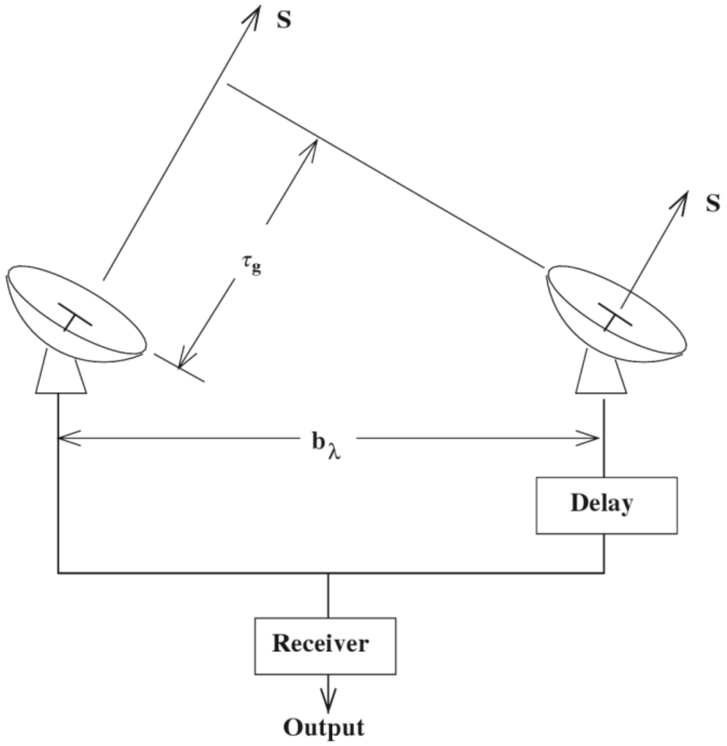

Figure 3.2.: Diagram of a two element interferometer. Through geometrical relations it is easy to define the geometrical delay. Image taken from Burke & Graham-Smith (2010)

target can be reconstructed.

$$V(u,v,w) = \int\int A(l,m)B_\nu(l,m)e^{(-i2\pi(ul+vm+w(\sqrt{1-l^2-m^2}-1))}\frac{\mathrm{d}l\mathrm{d}m}{\sqrt{1-l^2-m^2}} \tag{3.2.2}$$

In most cases the field of view is small and the third dimension w can be neglected and the visibility function $V(u,v)$ can be simplified to

$$V(u,v) = \int\int A(l,m)B_\nu(l,m)e^{-i2\pi(ul+vm)}\frac{\mathrm{d}l\mathrm{d}m}{\sqrt{1-l^2-m^2}} \tag{3.2.3}$$

For the widefield observations with the Dutch LOFAR array the w-term cannot be neglected. So the array of radio telescopes in the (u,v)-plane measures the visibilities, which are the Fourier transformation of the source brightness distribution convolved with the synthesized beam of the antenna array. The visibility function is complex and in most cases the visibilities are represented by the division into amplitude and phase instead of using the imaginary and real part of the complex numbers.

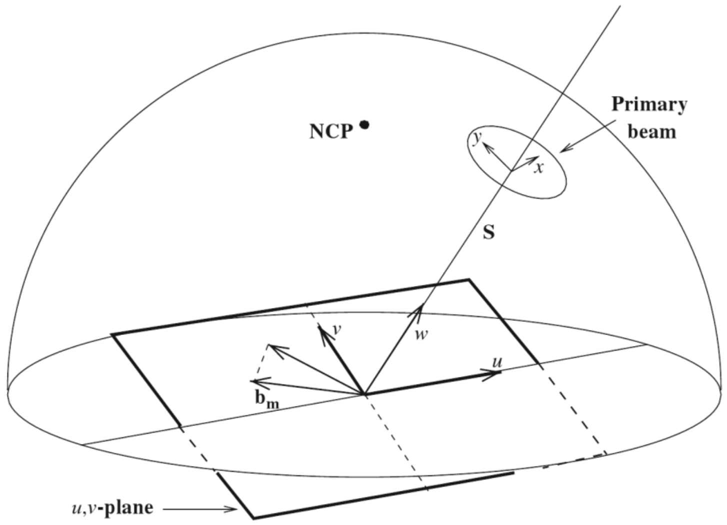

Figure 3.3.: Geometrical relation of the (u, v)-plane to the interferometer. x, y are used for the small-angle approximation of l, m parallel to u, v. Image taken from Burke & Graham-Smith (2010)

To reconstruct the brightness distribution of the source the visibilities from equation 3.2.3 are Fourier transformed and deconvolved with a model for the reception pattern of the array. Since the different baselines provide only coverage for parts of the (u, v)-plane the reconstructed image quality is highly dependent on a good (u, v)-coverage . The (u, v)-coverage can be improved by adding more telescopes and longer observation time. Since the position of the telescopes relative to the source change due to the Earths rotation, increasing the observation time improves the sampling of the visibilities in the (u, v)-plane. The (u, v)-coverage varies also with the angle of the array to the source in which the telescopes observe. This leads to elliptical beams with higher resolution in one direction. Adding more telescopes to the array increases the computational effort for the correlator since every added telescopes creates one baseline per existing telescope, which has to be correlated and corrected.

Besides the rather simple corrections for the geometrical delay, radio observations can be influenced by effects like the weather or the ionosphere of the atmosphere. Thunderstorms can cause interference, while the ionospheric effects are small at short wavelengths. For long wavelengths of the order of meters the ionosphere can influence the measurements. However, the ionospheric effects are difficult to measure and change with time, so that it is difficult to correct for these influences. Additional to atmospheric and weather effects radio interference signals detected by the sidelobes can affect the quality of the reconstructed images.

3.3. The Low Frequency Array (LOFAR)

LOFAR (**LO**w-**F**requency **AR**ray) is the new radio interferometer to explore the radio sky of the Northern Hemisphere at long wavelengths (van Haarlem et al. 2013). The array consists of 50 stations of fields with dipole antennas. 38 of these stations are located in the Netherlands, while the 12 international stations are distributed in Europe with 1 in France, 1 in the United Kingdom, 1 in Sweden, 6 in Germany and 3 new constructed ones in Poland (see Figure 3.4 for a map with all station locations). The polish stations joined the LOFAR network in Spring 2016 and are not included in any observation of this work. The 38 Stations in the Netherlands are divided into core stations and remote stations. The core stations form the central region of the array and consists of 24 stations within a radius of 2 km. The remaining 14 remote stations are located further away from the center. The core, remote and international stations have different composition of their arrays, which is explained in the next part of this section. The array distributed over Europe gives LOFAR a (u, v)-coverage providing a high angular resolution. The great sensitivity provides the possibility to image faint, diffuse objects and extended structures (de Gasperin et al. 2012; van Weeren et al. 2012).
LOFAR faces some challenges of the new generation of radio interferometers. The low frequencies are used for other services like radio broadcasts between 90-110 MHz which have to be avoided. The main technical challenge is the data amount created which has to be transferred from the station to the correlator (network bandwidth), the correlation of the data (computational performance) as well as the storage of the observation in an archive available for the users (long term archive). LOFAR (van Haarlem et al. 2013) is a pathfinder of the next generation large-scale radio telescope, the Square Kilometer Array (SKA, Carilli & Rawlings 2004; Aharonian et al. 2013). The long term archive (LTA) of LOFAR is distributed at the state of April 2016 on three different server sites holding about 22.5 PB of data. Currently LOFAR is one of three low frequency arrays consisting of dipole antennas. The other two are the Long Wavelength Array (LWA) in the US (Ellingson et al. 2009, 2013) and the Murchinson Widefield Array (MWA, Lonsdale et al. 2009; Tingay et al. 2013) in Australia.
Another challenge for LOFAR is the development of software to calibrate and reduce the data. The data calibration has to take care of effects like phase shifts of the ionosphere or smearing effects when calibrating observations with large frequency bandwidth. Since the data sets are also large in size, the data reduction is also a computational challenge creating the need of large computing clusters for the use of pipelines as well as individual user requests.
While the technical information of the station can be found in van Haarlem et al. (2013), updated descriptions after extensions of the array and new observing modes can be found on the website of ASTRON[1].

[1] http://astron.nl/radio-observatory/astronomers/technical-information/lofar-technical-information

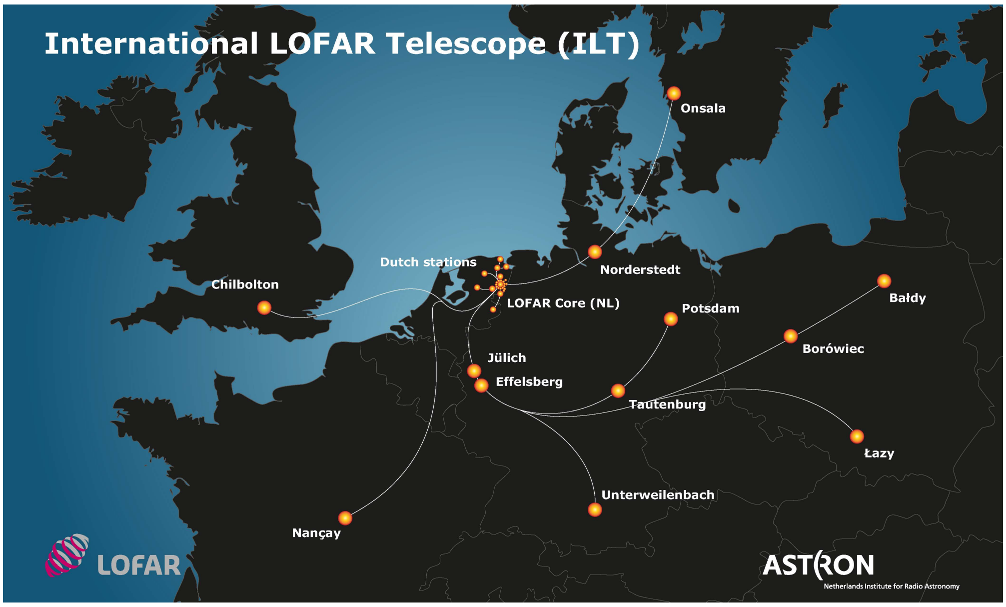

Figure 3.4.: Geographical location of all current LOFAR stations. Credit: ASTRON NL

Array

The LOFAR stations consist of fields of dipole antennas of two designs. One antenna type is for the low frequencies between 10-90 MHz called LBA (low band antenna) and the other one for the higher frequencies between 120-240 MHz called HBA (high band antenna). Each station consists of multiple antennas used as interferometer which are then connected with the other stations making it an interferometric array of interferometers of antennas. The antenna fields have station processing boards (Wijnholds & van der Veen 2009; Wijnholds et al. 2010; Wijnholds & van der Veen 2009) at their location which are used to correlate the antennas and to adapt the weightings of their signals to form the station beam (Thompson et al. 2001). Since the dipole antennas are solid the desired observing direction is created with the weighting and calculation of the delays for each antenna. The digital beamforming has the advantage, that the pointing direction can be changed fast and it is possible to observe in more than one direction by calculating multiple different beams from the signals. The beamsize for the Dutch array provides a large field view, making LOFAR a suitable telescope for surveys. The amount of beams is determined by the bandwidth the network is able to transfer and the computational performance of the computers involved. The amount of bandwidth used in the network is depends on the frequency bandwidth at which the observation is performed. Overall the idea behind the antenna design is to have cheap antennas which can easily be changed if broken to keep the maintenance efforts low.

Low band antennas (LBA)

Figure 3.5.: Image of a low band antenna field (LBA) at the inner core station (superterp) in the Netherlands taken in November 2014.

The low band antennas optimized for frequencies between 10-90 MHz consist of a PVC pipe with a low noise amplifier on the top. From the top 4 wires are connected with the ground in an angle of 45°. The wires form dipoles for linear polarization (X and Y) to detect the polarized signals. By combining the polarizations the total intensity can be measured. On the ground a mesh of steel concrete reinforcement rods and a foil to reduce vegetation growth take care that the antenna stays solid on the ground. Inside the PVC pipe two coaxial cables are connected with the low noise amplifier for power supply and to transfer the signal.
Core and remote stations consist of LBA fields with 96 antennas over an area with a diameter of 87 m together with 48 receiver units. International stations also have 96 antennas in each LBA field distributed over an area with a diameter of 70 m with 96 receiver units. This means that core and remote stations are limited to use only 48 dual polarization signal paths or 96 single polarization signal paths, while the international station are not limited in this way. Because of the lower number of receiver units than antennas the user has to choose the configuration for the observation:

- using only the outer antennas in both polarizations
- using only the inner antennas in both polarizations
- using half of the antennas distributed for the whole field in both polarizations
- using all antennas with only single polarization

The calibration for LBA observations is still a challenge since good models of the sky are needed, which are not available yet, and very bright sources close to certain regions like CygA, PerA and others can create strong interference.

High band antennas (HBA)

The high band antennas for observations in the frequency range between 120-240 MHz have a different design to minimize contributions of the system noise due to the electronics. HBA antennas are bow tie shaped dipole antennas combining 16 antennas in a 4x4 grid to one HBA "tile". A tile measures 5x5 m with a spacing of 1.25 m between each dipole and is covered in styrofoam and a plane to protect the electronics from weather influences. With an analogue radio frequency beamformer each tile beam is calculated for each of these 16 antennas. Compared to the LBA which can observe the whole visible sky, the beamforming of each HBA tile limits the field of view for the HBA to about 30° at a frequency of 150 MHz.
For the core stations two fields with 24 HBA tiles with a diameter of 30.8 m each are used. The remote station use 48 HBA tiles but combined into one field with 41 m diameter. International stations use fields with 96 HBA tiles with a diameter of 56.5 m. Different configurations are available for HBA observations:

- both antenna fields of the core station are correlated as two separate stations
- both antenna fields of the core station are correlated as one station
- using only one antenna field of the core station
- not including the HBA antennas of the core stations

3.4. Data reduction and processing

To obtain an image from radio observations the data has to be calibrated and imaged. For this purpose different software is available. Several examples for software packages are presented and explained in the next section. Some of the calibration concepts are very common and can be performed with almost every software package.
The first step on the way from detected radio signals with the interferometer to an image

Figure 3.6.: Image of an example high band antenna field (HBA) usually packed under black planes with 4x4 antennas at the inner core station (superterp) in the Netherlands taken in November 2014.

of the brightness distribution is the correlation. The correlater combines the telescopes to baseline to generate the visibilities of each baseline with their amplitude and phase (see Section 3.2). For the correlation it is crucial to have good knowledge of the antenna characteristics like precise positions and exact time measurements for each datapoint. To get the time usually each station has an oscillator with a stable atomic frequency as a clock providing the necessary high precision to accurately measure phases of each baseline. Some interferometeres store their data for each telescope and correlate it after the observation. LOFAR transfers all data via network to the correlator and only the correlated data is stored on disk.

After the correlation of each baseline the amplitude has to be calibrated. Usually this is done by including a calibrator source with known brightness. Amplitude calibrators are ideally compact based on the resolution the used array can achieve. The calibrator should also have a bright radio emission without variability. However it is not always possible to find compact calibrators. In this case a detailed model of the calibrators source structure is needed in order to calibrate the amplitudes. Most amplitude calibrator sources are quasars or radio galaxies, which show no variability in their spectrum. Using the model of the calibrator the amplitude can be corrected to fit to the calibrator model. Then the correction factors for the amplitude can be transferred to the target. To reduce other effects in the calibration, the amplitude calibrator source should be in appropriate close distance of the target field.

The next step is the phase calibration. This can be done with different strategies and depends on the observation type and telescope array. The atmospheres opacity changes with time during the observation, introducing phase deviations depending on the observing frequency. At low frequencies like the LOFAR frequency range the ionospheres changes over time affect the phases. Since the atmosphere is not homogeneous over large areas, the phases of large arrays with long baselines are stronger affected. Additional to the weather effects also instrumental phase errors are introduced. The instrumental errors can be calibrated with a bandpass calibration for which the bandpass of each antenna has to be known.

Due to atmospheric effects and limitations of the array model the correlator uses, deviations in delay and rate are occurring. In the measured phases the delay is the slope in frequency, the rate the slope in time. The calibration of delay and rate is called *fringe fitting*. Fringe fitting was developed (Schwab & Cotton 1983; Diamond 1995; Cotton 1995) in which the sum of the visibility phases for triangles of telescopes are called *closure phases*. Since closure phases are from triangles of telescopes, they are independent from errors of individual stations. So the closure phases have only the information of the brightness distribution without atmospheric deviations. Combining all baselines to triangles the errors of individual stations can be found and corrected or flagged. Using a global fringe fit can correct delay and rate from atmospheric deviations. To reduce the amount of triangles used for this, usually one station known to be good calibrated is taken as reference station together with two others. However, if all baselines are used to

correct the phases with fringe fitting, the absolute position of the source is lost.
For compact arrays like the Very Large Array (VLA) the atmosphere changes are weaker and it is not needed to correct the phases with fringe fitting. It may also be the case that the target is very faint and thus it is difficult to detect the brightness distribution of the source. For those cases a phase calibrator can be used. A phase calibrator should be compact and has to be very close to the target that the phase corrections can be transferred to the target similar to the amplitude calibration.
For less computational effort the phase calibration can also be performed by using a model of the brightness distribution of the sky to correct for phase errors. But for this procedure a sufficient model of the brightness distribution has to be used. For observations with a large field of view these models can be obtained by various sky surveys. The dataset can be calibrated with a lower resolution model and then the phase calibration can be improved in an iterative way using *selfcalibration*. This strategy is used for the Dutch LOFAR array. The model used can be either extrapolated by other surveys like NVSS (Condon et al. 1998) or VLSS (Cohen et al. 2007a). In future probably the MSSS catalog can be also used as calibration model.
Based on the sampling of the (u, v)-coverage of the observation these calibration steps may be sufficient to deconvolve the visibilities to obtain the brightness distribution (see equation 3.2.3). Högbom (1974) developed a CLEAN algorithm modelling the visibilities with δ-functions based on *difference mapping*. The brightness distribution deconvolved with the *dirty beam*, the beam calculated from the reception pattern, is called *dirty image*. The CLEAN-algorithm creates δ-peak model components with a fraction of the peak flux density at the brightest pixel in the map. The added δ-components are subtracted from the dirty map and a *residual map* is created. The residual map is the map where the next model components are added at the brightest pixel. In an iterative way this creates a model describing the brightness distribution. However since errors in the phase and uncovered areas in the (u, v)-plane can create artificial structures, which want to be avoided, it is possible to create a mask to limit in which regions the CLEAN-process is allowed to place model components also helping the algorithm to converge faster. Some extensions have been developed to the simple CLEAN of Högbom (1974) like a multiscale CLEAN deconvolution for extended structures (Cornwell 2008).
For the imaging process different weightings can be applied. The most commonly used weightings are natural weighting, uniform weighting and briggs weighting. While natural weighting treats each visibility with the same weight, uniform weighting applies a weighting based on the number density of the visibilities in the corresponding region of the (u, v)-plane. This way uniform weighting has a decreased signal-to-noise ratio (SNR) but higher angular resolution compared to natural weighting because the sparser visibilities of the long baselines get higher weightings. Natural weighting results in the best possible SNR. The briggs weighting (Briggs 1995) is a combination of both weightings using a robust-parameter. This parameter corresponds to something close to natural weighting at a value of 2.0, while corresponding to something like uniform weighting

at a value of -2.0. With values in between -2.0 to 2.0 intermediate weightings between uniform and natural are possible.
If there are large gaps in the (u, v)-coverage the images might still appear noisy and fainter structures are not clear detected. To further improve the image quality the *selfcalibration* can be used (Cornwell & Wilkinson 1981). Using the model from the CLEAN-process in combination with the closure relations the phases and amplitudes of the visibilities are calibrated. This is done for the model averaged over a given timerange. Often only the phases are calibrated and improved before also calibrating the amplitudes. By using clean and selfcalibration iteratively with a decreasing timerange for the selfcalibration, the image quality can be improved. During the clean and selfcalibration process often some visibilities are deviating to much to correct them and should be flagged.
However using inapproriate masks, models with artificial features or too many iterations of selfcalibration can create too large changes in the visibility data in both amplitude and phase. To make sure that the selfcalibration-process still reflects the brightness distribution of the target, the model of the final image should be compared to the original data before selfcalibration. Large deviations in this comparison would mean that the total flux density distribution or the structure is wrong.
The strategy applied to the datasets is different for the both parts in the results. For the data of the Multifrequency Snapshot Sky Survey (MSSS) the calibration strategy is explained in Section 3.6. For the international LOFAR observations of the second part in this work, the calibration strategy had to be developed and is also part of the results and described in detail in Section 5.1.

3.5. Calibration and imaging software

In the following part the main software which was used to achieve the calibration and imaging are shortly described. Most of the programs are standard software for the processing of radio observations. The functionality of each program has its limits and minor differences which is why in this work different programs are used. For the calibration of the international LOFAR data similar strategies with different software were used and compared. This section is meant to describe shortly the different software packages. The strategy for calibration and programs used for calibration and imaging are decribed in the corresponding results sections.

LOFAR software and pipeline packages

For LOFAR observations the signals of each station are transferred via network to the correlator. After the observation is performed and correlated the data sets can be further processed by pipelines. These pipelines have to be requested and specified in the proposal for the observation. The pipelines are able to average the observation in time

and/or frequency to reduce the size of the data files, as well as performing the amplitude calibration and first phase calibration for all stations in the Netherlands (for the setup of LOFAR stations see Sect. 3.3). For the use of the Dutch array also a first imaging can be done.
As data format the LOFAR software uses measurement sets (.MS-files). The frequency range of the observation is divided into several subbands each with its own MS and a bandwidth of 195.3 kHz. The MS can be combined in a larger MS with broader bandwidth.
Users can also apply for computing time on the LOFAR clusters on which software specifically developed for LOFAR data reduction is available. One main program is *BlackBoard Selfcal* (BBS), the other one is called *Default Pre-Processing Pipeline* (DPPP). Currently efforts are ongoing to include the functions of BBS in DPPP and to improve the performance and to unite the functionalities of both in one program. For the imaging *AW imager*, for source detection and sky model manipulation mainly *PyBDSM* is available. To manipulate the MS themselves *TaQL* can be used. All these programs are mostly terminal based without a graphical interface and are designed to use them in a scripted way. To specify the processes a parameter file is given, where all tasks and their parameters are passed. Both tools can make use of multiple processor core for parallel computing.
BBS is designed for the calibration and simulation of LOFAR data based on the Hamaker-Bregman-Sault measurement equation (Hamaker et al. 1996; Sault et al. 1996; Hamaker & Bregman 1996; Hamaker 2000, 2006; Smirnov 2011). The calibration is done using a sky model. This model contains information on the brightest targets in the field of view for at least one target. For the first phase calibration this model usually contains all known sources in the field of view. To create a sky model often models from other radio surveys are used with given spectral indices to extrapolate them to the frequency of the observation. The quality of the calibration is dependent on the model and its resolution. With the images of an observation a sky model can be created and used to improve the calibration iteratively. Also the solutions of another fields calibration can be transferred to apply for example the amplitude calibration of a calibrator source to the target field.
DPPP is the main tool, which already has included most functions of BBS. It can be used for example for flagging, averaging in time and/or frequency, phase shifts to other phase centers, combining measurement sets, demixing of interfering bright sources, phasing up stations to a tied station, filtering out stations or baselines, prediction of a sky model, applying a beam model and gain calibration.
The **AW imager** (Tasse et al. 2013) is based on the libraries of CASA, which will be explained later in this section. It has been modified and improved to use the LOFAR beam models and ionospheric correction, which is needed to correct for direction dependent atmopheric effects varying in time and frequency. It includes the possibility to image data produced by non-coplanar arrays, where the w-term ((u, v, w)-coverage) in the measured visibilities is not negligible and has an improved functionality in imaging wide fields (Cornwell et al. 2008; Bhatnagar et al. 2008).

PyBDSM (Python Blob Detection and Source Measurement) is a source-finding software based on python. It can process images (in FITS as well as MS) to fit Gaussian model components to sources. The output can be used to generate catalogs or can be used for the phase calibration of future datasets.
TaQL (Table Query Language) is a SQL-like language to edit MS with all kind of selections. This can be used to change the polarization from linear to circular polarization components. In this work it is also used in the process of amplitude calibration and to change the sorting of the data tables to improve their processing performance.
DPPP, BBS and AW imager can be used to calibrate, selfcalibrate and image LOFAR datasets. However the LOFAR software can only do this for observations of the Dutch array at the current stage. When including the international baselines the calibration is more complicated. The necessary calibration steps are still in development and currently not included in the standard pipelines. At the current state of the pipelines mostly using DPPP can perform the pre-processing, amplitude calibration of the Dutch array. Another crucial step where DPPP is needed for the international baseline observations is to combine the core stations to a tied central station, which will be explained in detail in the section for the calibration of these observations.

Standard software for radio astronomy

AIPS (Astronomical Image Processing System) is a program for calibration and imaging of radio observations (Greisen 2003). It is the only program in the software section which offers fringe-fitting (Schwab & Cotton 1983; Diamond 1995; Cotton 1995) to correct the phases in delay and rate using the closure phases and a model or a reference station. AIPS was initially developed for the VLA (Very Large Array) but became a general tool for calibration and imaging of radio interferometer observations. Some of the functionalities are to calculate the amplitude calibration correction with a given model, to apply the solutions or transfer them to other targets. With a known bandpass of the antenna receivers the visibilities can be corrected.
AIPS also has its own system for storing the data and the corresponding tables after importing the data from the UVFITS-files. This has the disadvantage that the AIPS storage needs lots of disk space. The advantage on the other side is that all calculated corrections are stored in separate tables. When a calibration table is applied to the visibilities, both are stored in a new dataset and can be exported as UVFITS-file. This way the original data is never changed and calibration steps can be easily changed or reverted. The output of calibrated AIPS datasets is again in the UVFITS-format.
The tasks in AIPS can be scripted to perform automatic pipelines. With an extension named ParselTongue (Kettenis et al. 2006) the scripting part became more userfriendly and python-compatible. ParselTongue has the advantage that python scripts can modify the datasets in a scripted way before they are used inside AIPS combining these processes

into one script.
When working on LOFAR observations in AIPS some limits have to be taken into account. AIPS has difficulties with the amount of baselines if more than 30 stations are included in the observation. This is why usually for observations with the international LOFAR array the core stations are combined into one tied station as reference station. The polarization of LOFAR observations is usually stored in linear polarization parameters, while for AIPS circular polarization should be used. For this the polarization should be converted before importing the observation in AIPS. Regarding the performance AIPS does not support multi-core processing, why the calibration of LOFAR observations can be very time-consuming.
The hybrid-imaging program **difmap** was developed to be able to create selfcalibrated images of VLBI observations in an interactive way (Shepherd 1997). It was designed to be user friendly with the ability to inspect and edit the datasets of radio observations. For imaging the CLEAN-algorithm by Högbom (1974) is used. The creation of masks for CLEANing is limited to rectangular windows which are applied interactively in the dirty image, to guide the algorithm where to put model components.
Similar to AIPS the dataformat of difmap is UVFITS. Since the original data is not saved the user should save the progress often to have the ability to recover the data of a previous step. Saving the data results in several files: a UVFITS-file with the data, a FITS-file with the deconvolved brightness distribution, a model-file and a par-file with the information which files have to be combined to load the saved data again. The FITS-file of the image includes information like the beamsize, the coordinates, the observation date, the used telescope array and some additional calculated values like the rms-noiselevel (root mean square).
Difmap offers a limited way to script processes by defining chains of commands which can be performed after each other. However the design of the program is more intended to be used interactively by editing the visibilities by hand and to create the images.
CASA (McMullin et al. 2007) is a python-based software with regular updates. It was developed as the successor of AIPS. The interface is also similar to AIPS, however functions like the fringe-fitting are not fully included so far. Compared to AIPS and difmap CASA supports new features like multifrequency-spectral cleaning. Compared to difmap it is not only possibile to create masks of rectangular shape but also use ellipses and irregular shapes. The masks are stored separately and can be imported instead of creating a new one for each calibration.
Compared to AIPS and difmap it supports multi-core processing, which can improve the performance and makes it suitable to use on computing clusters. Another difference is the memory management. AIPS and difmap create temporary data files on the hard disk for the data currently in use, while CASA can load the data in the memory, which improves the performance in respect of the computing time needed.
During the calibration outliers or visibilities, which cannot be adjusted to the model, can occur. In difmap most of these datapoints have to be found and flagged by hand.

CASA and AIPS offer automatic ways of doing the flagging. Even though the automatic flagging usually works quite well, the user should be careful and inspect the model and the results.
The dataformat CASA uses are measurement sets. CASA can import UVFITS to create a measurement set from it as well as export measurement sets to UVFITS-format. Since the imaging software of the LOFAR software package is based on CASA, it uses the same data format. In these measurement sets the visibilities are organized in three columns: the DATA-column where the original data is stored, the MODEL-column which is filled when creating or importing a first model and the CORRECTED-DATA-column storing the visibilities after calibration steps have been applied. With this structure it is possible to check for differences before and after a calibration step and to compare it with the used model. In a second calibration step the CORRECTED-DATA-column is overwritten if the default options are used. This means only the last step and the original data can be compared. The user can choose in which column the data should be written, which means that it is the choice of the user which data are kept and which are overwritten.
Since CASA is python-based it is easy to create scripts, but it also offers a userfriendly interface with a similar usage to AIPS.

3.6. Multifrequency Snapshot Sky Survey (MSSS)

One important ongoing project of LOFAR is the Multifrequency Snapshot Sky Survey (MSSS, Heald et al. 2015). It is the first Northern hemisphere sky survey performed with LOFAR. The aim of the survey is to provide spectral properties of the detected sources in 8 frequency bands between 30-75 MHz and in another 8 frequency bands between 120-160 MHz. The multi-beam capabilities and the snapshot observation yield a high survey speed. After calibration the fields are combined into mosaics from multiple observations to cover the complete sky.
After the MSSS project has finalized the catalog it can also be used to calibrate future LOFAR observation. Existing catalogs at low radio frequencies have less sensitivity, angular resolution and in most cases only one frequency band, which makes studies on the spectral behaviour difficult. Comparable catalogs to the future MSSS catalog are: the Eigth Cambridge Survey of Radio Sources at 38 MHz (8C; Rees 1990; Hales et al. 1995), the VLA Low-Frequency Sky Survey at 74 MHz(VLSS & VLSSr; Cohen et al. 2007a; Lane et al. 2012), the Seventh Cambridge Survey of Radio Sources at 151 MHz (7C; Hales et al. 2007), the Westerbork Northern Sky Survey at 330 MHz (WENSS; Rengelink et al. 1997), the Murchison Widefield Array Commissioning Survey between 104–196 MHz (MWACS; Hurley-Walker et al. 2014), the TIFR GMRT Sky Survey at 150 MHz (TGSS; Intema et al. 2016) and the Galactic and Extragalactic MWA Survey between 72-231 MHz (GLEAM; Wayth et al. 2015).

The LBA observations will use the inner 48 antenna elements of the dutch station and have the 96 antennas of each international station included. The 9 snapshots of 11 min each are separated by 1 hour to create a good (u, v)-coverage. To observe the complete Northern Hemisphere 660 fields are needed which will create about 130 TB raw visibility data and require a survey time of approximately 297 hours (Heald et al. 2015). The aim of the first LBA catalog is to have a resolution of $\sim$ 120" with a sensitivity of $\sim$50 mJy beam^{-1}. The sensitivity can vary if bright sources are in the field which are difficult to calibrate. However, the observations of this part of MSSS will take place in the future and this work only uses HBA data. For this reason future references of MSSS are referring to the MSSS HBA catalog if no additional details are given.

The HBA observations use the dutch stations with the core HBA fields as two separate antennas. For the remote stations only the inner 24 tiles are used to get an identical view for each station with losing slightly in sensitivity for the long baselines (van Haarlem et al. 2013). Since the sensitivity of the HBA frequencies is higher only 2 snapshots of 7 min each separated by 4 hours have been made. To observe the full Northern Hemisphere with the HBA 3616 fields are needed, creating about 470 TB raw visibility data and consuming 201 hours observation time (Heald et al. 2015). Because the (u, v)-coverage is sparse for the long baselines and the calibration and imaging would take a lot of computational resources, the HBA MSSS catalog only uses the inner baselines to a range of 2 kλ. This corresponds to a resolution of $\sim$120" and the images should reach a sensitivity of $\sim$10–15 mJy beam^{-1}.

The commissioning project MSSS was also the driver for the first version of a standard imaging pipeline (Heald et al. 2010). The data undergoes pre-processing, calibration, combining the snapshots, imaging and one step of selfcalibration. The pre-processing also includes demixing for those fields close to the brightest sources creating radio frequency interference (RFI), which are called "A-team": Cygnus A, Cassiopeia A, Virgo A, Taurus A and Perseus A. The demixing works in the way that a model for the bright sources is made which is then subtracted to be able to image the field without the bright source. This process needs lots of computational resources hence it is only applied if needed. For the imaging part Briggs weighting (Briggs 1995) with a robustness of 0 is used.

After the final images are combined to mosaics (in total 216 for MSSS HBA) and an averaged map over all frequency bands was created, two complementary source extraction software packages are used: PyBDSM[2] and PySE[3]. Both packages analyze images to identify sources in the MSSS images using either a false detection rate method (Hopkins et al. 2002) or a technique to locate emission regions above a threshold of the noise in the image. The found emission regions are then fitted with Gaussian model components. With the use of both source finders a reliable catalog with the multifrequency information from every frequency band can be created.

[2]http://tinyurl.com/pYBDSM-doc

[3]http://docs.transientskp.org/tkp/master/tools/pyse.html

To estimate errors in calibration and source location, the source list is compared similar to the VLA Low-Frequency Sky Survey (VLSS; Cohen et al. 2007a) and the NRAO/VLA Sky Survey (NVSS; Condon et al. 1998), because it has higher resolution, higher SNR and lower calibration errors due to the higher frequency of 1.4 GHz. To ensure the flux scale and to describe the spectral behaviour of the source the flux densities of each frequency band are fitted with the functional form (Scaife & Heald 2012):

$$S_\nu(\nu) = A_0 10^{A_1 \log(\nu/150\mathrm{MHz})} \tag{3.6.1}$$

To find the best fit for the spectral flux density at 150 MHz A_0 and the spectral index A_1 a linear least-squares fit to a polynomial in log S_ν space with the Levenberg-Marquardt χ^2-algorithm (Levenberg 1944) is used. These values are also added to the catalog. After publication the catalog and the images will be available in virtual observatory[4]. First checks and comparison of HBA data with the 7C survey at 151 MHz (Hales et al. 2007) resulted in the estimation that the MSSS HBA catalog should be 90% complete above 100 mJy and 99% complete by around 200 mJy at a mid-band reference frequency of 135 MHz. Combining all frequency bands leads to a brightness distribution which is $\sqrt{8}$ times more sensitive then the single frequency band maps.

3.7. The MOJAVE program

This work uses AGNs of the MOJAVE sample. MOJAVE (**M**onitoring **O**f **J**ets in **A**ctive galactic nuclei with **V**LBA **E**xperiments)[5] is a monitoring program of AGN observing since 1994 (Kellermann et al. 1998; Zensus et al. 2002). The aim of MOJAVE is to study the polarization and structural evolution of jets in the northern sky. It is one of the largest ongoing monitoring programs with a large database with the observations since 1994.
The first MOJAVE sample was selected after the criteria, that the sources have to show a spectral index flatter than $\alpha = -0.5$ at any frequency above 500 MHz and a flux density of more than 1.5 Jy at 15 GHz is measured for sources north of the equator. For sources between -20° and the equator the flux density has to be more that 2.0 Jy (Kellermann et al. 1998). The first sample of 132 sources has then been extended by 39 sources which did not match with the criteria at the decision on the first sample but after that matched the flux density limit (Zensus et al. 2002). After the release of the 11-month Fermi catalog the sample was again extended with sources detected by *Fermi* (Atwood et al. 2009; Abdo et al. 2010; Ackermann et al. 2011, 2015) in the γ-rays, defining a *Fermi*-MOJAVE sample of 116 sources of which 56 are common with the radio-selected MOJAVE 1.5 Jy

[4]http://vo.astron.nl
[5]http://www.physics.purdue.edu/astro/MOJAVE/index.html

sample (Lister et al. 2011). With the development of the sample by adding individual sources fitting in the selection criteria, the sample contains 274 AGNs with at least 5 VLBA observations (Lister et al. 2016). In this work the radio-selected 1.5 Jy sample of MOJAVE with 183 sources will be the sample referred to as the MOJAVE sample. This sample is considered to be statistically complete on the basis of compact emission at 15 GHz, which is important for statistical results (Lister et al. 2009).
With the VLBA monitoring of these AGN the kinematics with mas-resolution (Lister et al. 2009; Kellermann et al. 2004), the acceleration and deceleration of the jet (Homan et al. 2009), curvature of the jet (Lister et al. 2013), spectral behaviour (Hovatta et al. 2014), polarization (Hovatta et al. 2012; Homan & Lister 2006) and more have been studied. Besides the radio VLBA observations for high-resolution images of the jet also VLA observations have been performed to study the extended larger scale emission (Cooper et al. 2007; Kharb et al. 2010), multiwavelength connections have been investigated with *Fermi*-LAT (Lister et al. 2011) and statistical theoretical examinations on the sample or subsamples are published (Arshakian et al. 2010; Cara & Lister 2008; Cohen et al. 2007b; Lister 2003).
A large fraction of the radio-selected MOJAVE sample is additionally monitored at 15 GHz by the Owens Valley Radio Observatory (OVRO) (Richards et al. 2014, 2011). With the single-dish telescope the blazars can be monitored more frequently than with VLBI observations but limited to a resolution of 157 arcsec (Richards et al. 2011). The monitoring is used to create lightcurves to study the variability of blazars at radio frequencies. This makes it possible to determine at which time a certain blazar is in a high or low state of its variability. Due to the frequent monitoring flux densities from OVRO for almost each MSSS detected blazar of our sample can be used in a timerange of two weeks, in most cases only one week, apart from the MSSS snapshot.
Cooper et al. (2007) and Kharb et al. (2010) have studied the kpc-scale emission of blazars with the VLA at 1.4 GHz in the MOJAVE1 sample consisting of 135 AGN. The aim was to test the prediction of the AGN unification model that BL Lacs and quasars are the beamed counterparts to FRI and FRII radio galaxies. In about 93% of all sources, significant extended emission was detected. However, more than 25% of the quasars have powers intermediate between FRI and FRII confirming the studies of smaller samples (Landt & Bignall 2008; Rector & Stocke 2001). Moreover, many BL Lac objects show morphologies typical for more powerful FRII-like jets. These results challenge the unification model.
In addition a strong correlation was found between the apparent parsec-scale jet speeds measured with VLBI and the 1.4 GHz kpc-scale extended luminosity: *"the more radio powerful sources possess faster jets"* (Kharb et al. 2010). Such a correlation was well known and intensively studied for the beamed core luminosity (Cohen et al. 2007b), but its analytic power was strongly limited by the "inversion problem": Both, the beamed core luminosity and the apparent VLBI jet speed, are affected by Doppler boosting. It is difficult to derive the source-intrinsic jet speeds and luminosities from it, because the

former cannot be determined independently from the inclination angle of the jet in one-sided jets (which dominate the MOJAVE sample). By applying probabilistic arguments, however, it was possible to derive unique information about the distribution of Lorentz factors in a sample of AGN. These studies show that not only the beamed core luminosity from the inner jet but also the extended lobe emission is correlated with the apparent jet speeds on parsec scales. Therefore, the extended emission is considered to be a good proxy for the jet kinetic power (Kharb et al. 2010). The low frequencies of LOFAR are more sensitive to the unbeamed lobe emission and the high resolution due to the international baselines provide a similar resolution to the previous studies. This improves the constraints on the intrinsic jet power.

Similar to the MOJAVE program but covering the Southern Hemisphere the TANAMI project observes a sample of AGN. However TANAMI is designed to approach their sample with multi-wavelength observations. As I am also involved in the reduction of radio observation of TANAMI images, in the appendix A the TANAMI project is shortly described together with some of the results with my contributions over the last years.

4. Blazar studies with the Multifrequency Snapshot Sky Survey (MSSS)

In this part of the thesis the results of the MOJAVE blazars are presented using the preliminary MSSS catalog version 0.1, which is available for MSSS members for testing and to obtain first scientific results. However this catalog is not released at the current date. At the moment the aim for the first public version of the catalog is set to Autumn 2016. The version used in this work still misses some final tweaks on the flux calibration since the beam-models for each station used are not implemented correctly in the pipelines so far. The current flux densities are expected to be in a good shape however the spectral indices interpolated between the 8 frequency bands can change with the final correction. After applying a correction it is also planned to perform one step of self-calibration with a slight improvement of the resolution, which is currently at $\sim$120 arcsec.

4.1. Results

Using the MSSS catalog I found counterparts to 125 from the 183 MOJAVE 1.5 Jy sample. From the missing 58 sources, 48 are too low in declination since the MSSS observations only go to declination $0°$ with their snapshot pointings. Additional to the declination limit, regions may be cut off due to very strong sources in the low frequencies which cause so much interference that these regions are difficult to calibrate. One of these regions is the region around Cygnus A. In this region two sources of the MOJAVE sample are located, which are are not missing in the list of detected sources. The 8 remaining sources missing in the catalog are probably too faint in this frequency range to be detected in the MSSS snapshot observations. In the list of detected sources one source is only detected in two of eight frequency bands and has no spectral index fit (2013+370) and another one is with data points in each frequency band but no spectral index fit (1606+106) due to be picked up by only one of the two source finders. In this one case it is the source finder which is not used to fit the spectral indices.
For this work the IAU B1950 naming convention is used for the sources following the MOJAVE publications. For the common name of the sources in this paper see table B.1, where all sources are listed with their spectral indices. Only two sources are missing in

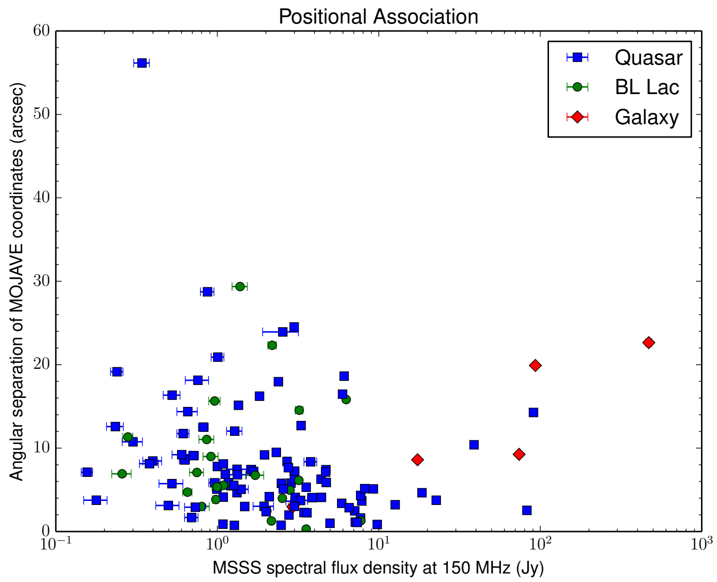

Figure 4.1.: For the association of the counterparts of the MOJAVE sample with the MSSS catalog, their angular separation from each other was calculated and plotted versus the spectral flux density at 150 MHz from the MSSS catalog.

this table: 1606+106 (common name: 4C +10.45) and 2013+370 (common name: MG2 J201534+3710) since both sources have no spectral index fit in the current MSSS catalog as mentioned before.

To find the counterparts of the MOJAVE sources in the preliminary MSSS catalog a cone-search with radius of 2 arcmin (corresponding to the beamsize of MSSS) around the J2000 coordinates was performed. In Figure 4.1 I present the deviation from the MOJAVE source coordinates compared to MSSS catalog coordinates. In all but one case this deviation is below 30 arcsec, which corresponds to 25% of the beamsize of MSSS. Since the only exception (0955+476) is still inside the beamsize and it is expected that it should be one the brightest sources in this region, it can be assumed that all targets are correct associated.

4.1.1. Spectral indices of the MOJAVE sample in MSSS

The spectral indices are fitted to the 8 frequency bands between 120–160 MHz as described in Section 3.3 ($S_\nu \propto \nu^\alpha$) using the flux densities measured with the PyBDSM source finding tool. The distribution of these spectral indices from the MSSS catalog are shown in Figure 4.2. As mentioned in the beginning of this chapter the current MSSS

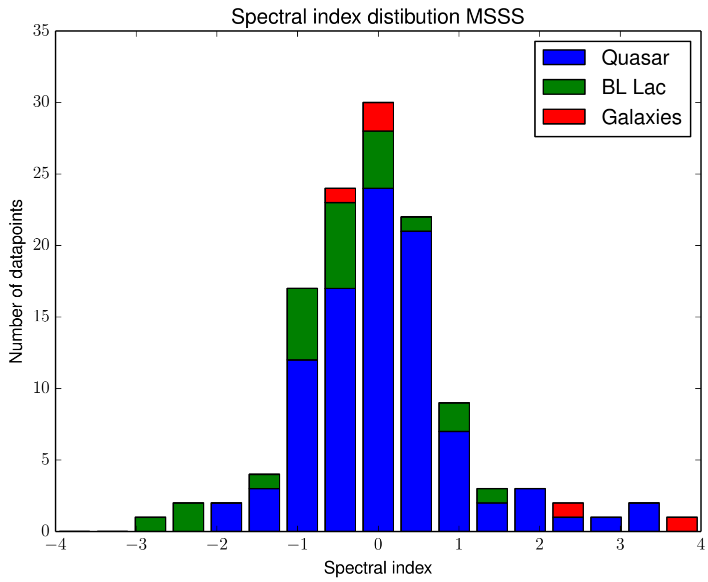

Figure 4.2.: Distribution of the low frequency spectral indices in the MOJAVE sample. The spectral indices are obtained by fitting the spectral index to the 8 frequency bands of MSSS. This fit is also part of the MSSS catalog. However this distribution probably will change with the final MSSS catalog since slight corrections in the flux densities can strongly affect the spectral index fitted to them in the 8 adjacent frequency bands.

catalog will receive a slight flux correction. This flux currection will not affect the overall flux densities very much. However slight changes in the flux densities over the different frequency bands can strongly affect the fit of the spectral index. So some changes in the spectral index distribution of the spectral indices between the different frequency bands of the MSSS catalog is expected.
The distribution shows that most spectral indices are between -1 and 0.5, which is expected. However, there are some sources showing much steeper or inverted spectra in ranges which are very unlikely. These spectral indices might be fixed with the correction of the flux calibration. Only minor changes in the flux densities can improve the spectral indices, so that less extreme spectral indices are found.

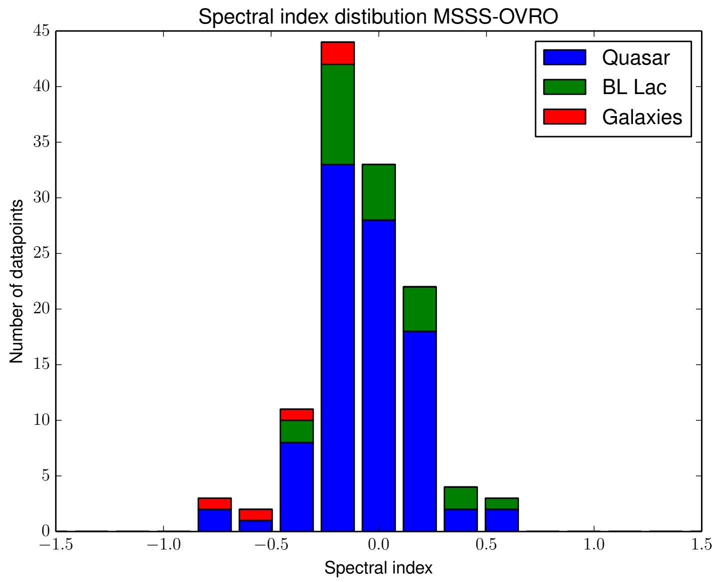

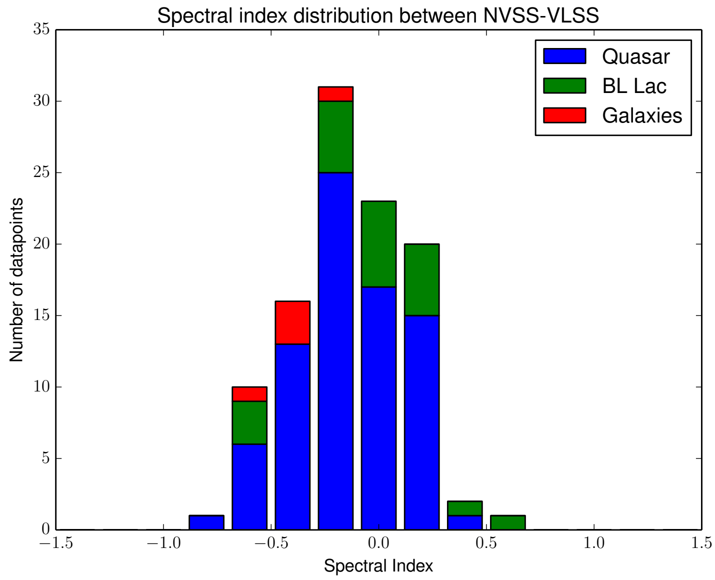

Figure 4.3.: Top: Broadband spectral index distribution of the MOJAVE sample between 150 MHz and 15 GHz. For 150 MHz the spectral flux density of the spectral index fit in the MSSS catalog is used. For the 15 GHz flux density the data point closest to the MSSS observation of the quasi-simultaneous OVRO monitoring is used.
Bottom: Broadband spectral index distribution as comparison calculated between the archival datapoints of the radio surveys NVSS (1.4 GHz; Condon et al. 1998) and VLSS (74 MHz; Cohen et al. 2007a; Lane et al. 2012).

4.1.2. Broadband spectral indices of the MOJAVE sample

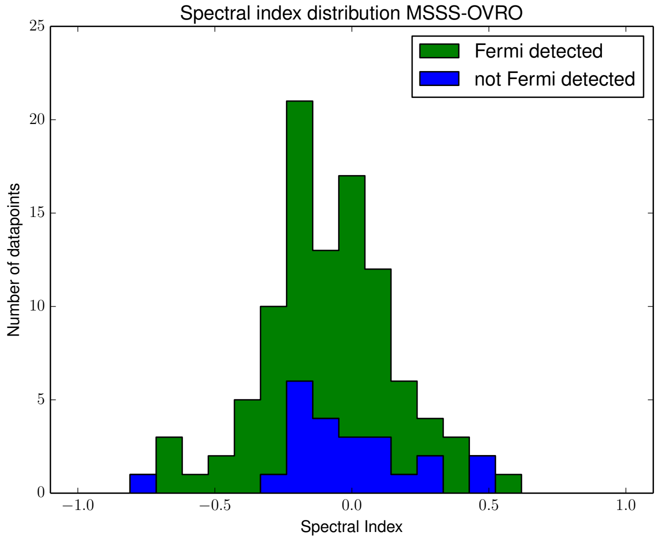

Figure 4.4.: Broadband spectral index distribution between 150 MHz and 15 GHz divided by their detection by *Fermi* (Lister et al. 2011).

To calculate spectral indices for the broadband spectral indices I used flux densities obtained by the OVRO monitoring (Richards et al. 2011, 2014). The flux densities used are from the single-dish observations in a timerange of about two weeks, in most cases only one week, apart from the MSSS observation. The beamsize of OVRO with 157 arcsec (Richards et al. 2011) should also be comparable to the ∼120 arcsec resolution of MSSS.
With these flux densities the broadband spectral index between MSSS and OVRO was calculated. For the MSSS flux density the spectral flux density at 150 MHz was used. This value is calculated from the spectral index fit and included in the catalog. For OVRO the flux density closest to the observation of MSSS at 15 GHz was used. Since both instruments have a beamsize of ∼2 arcmin, the flux densities should be comparable. Because of the two orders of magnitude difference in frequency of both instruments, it is possible that some other effects occur in between which deviate from the simple powerlaw assumed by the spectral index calculation.
The distribution of the spectral indices between MSSS (150 MHz) and OVRO (15 GHz) is shown in Figure 4.3 on the top. The the same figure on the bottom the spectral index distribution of the same sources is shown, but in this case the spectral index was calculated with the flux densities from VLSS (74 MHz) and NVSS (1.4 GHz). Neglecting the variability, which is typical for blazars, the spectral indices of these two surveys

performed with the VLA should be comparable. Both distributions are very similar with their largest bins between −0.4 and 0.2. However the spectral index between NVSS and VLSS are expected to have some deviations to broaden the distribution since the archival flux densities are not simultaneos, thus affected by variability.
To look for differences in the spectral index distribution of the γ-ray emitting sources, in Figure 4.4 only the AGN detected by *Fermi* are shown. However the spectral index distribution of this sample is very similar to the distribution of all detected sources.

4.1.3. Flux densities of MOJAVE blazars at 150 MHz

In Figure 4.5 the flux density distribution of the blazar sample in this work is shown. On the top the MSSS and on the bottom the corresponding OVRO distribution are plotted. The MSSS flux densities are the spectral flux densities at 150 MHz obtained by the spectral index fits. Since the sample is based on a flux density selection (above 1.5 Jy at 15 GHz) the lower flux densities are not well represented. However, due to higher extended emission also seen in steep spectral indices slightly higher flux densities at 150 MHz compared to the 15 GHz values are expected. For the flux density limit the target has to be only above the limit in one observation, which can be caused by the high variability of blazars. In the MSSS catalog about 26% of the sample (33/125) show flux densities below 1 Jy.
Comparing the flux density distributions of MSSS (top) and OVRO (bottom) (see Figure 4.5) the MSSS distribution is broader than the distribution of the OVRO flux densities. In Figure 4.6 on the top the flux densities of MSSS versus OVRO are plotted. Since flat spectral indices are observed, it is expected that the flux densities should be at the same level. However it is also expected that the low frequencies of MSSS are more sensitive to the extended emission from lobes of the jets, which should shift sources with extended emission to a higher flux density in the MSSS bands. In the plot on the top it appears that the major fraction is shifted towards higher MSSS flux densities, but it is difficult to estimate how strong this shift is on average. To look for such a shift, the relative deviation of the flux densities between MSSS and OVRO was calculated.
To examine the broadening in the MSSS distribution the relative deviation of the MSSS flux density from the corresponding OVRO flux density was calculated. The distribution of this deviation is shown in Figure 4.6 on the bottom. The plot shows that most sources have only weak deviations and some sources are shifted towards higher flux densities at low frequencies. The broadening is in the higher flux density direction as expected for the extended emission with the spectral steepening. Also the few radio galaxies included in the sample, where lobes and jets are found, contributing to the extended emission, show much higher flux densities at low frequencies. Three of four of these sources are too bright, that their relative deviations from OVRO lie outside the plotrange of Figure 4.6 (bottom). The shift indicates that the blazars with higher flux densities should have extended emission at the low radio frequencies. A few sources are brighter in the OVRO

observations than in the MSSS catalog. This could be explained by short time variability, in which the source is in a higher state in the GHz frequencies and the flare is not visible in the low frequencies at that point. Another explanation could be that a source may have its synchrotron peak frequency between 150 MHz and 15 GHz and their flux densities are lower in the low frequencies due to synchrotron self-absorption.

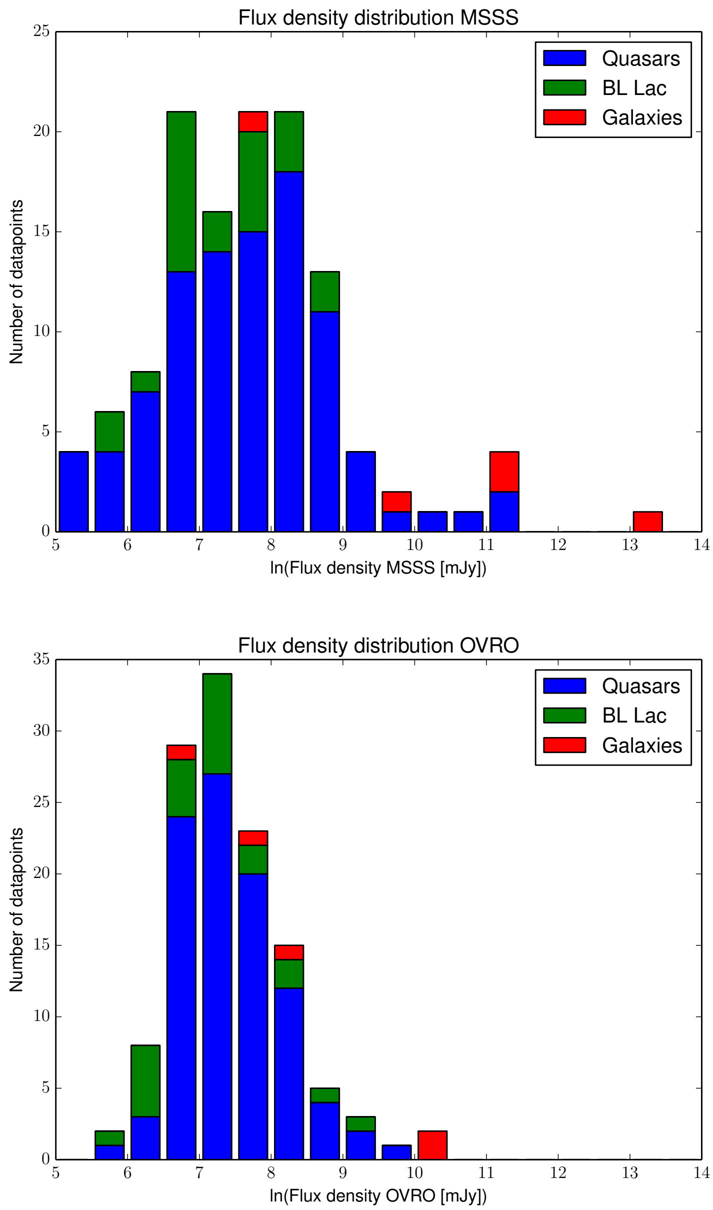

Figure 4.5.: Top: Logarithmic distribution of the spectral flux densities at 150 MHz in the MSSS catalog.
Bottom: Distribution of the used flux densities at 15 GHz from the OVRO monitoring.

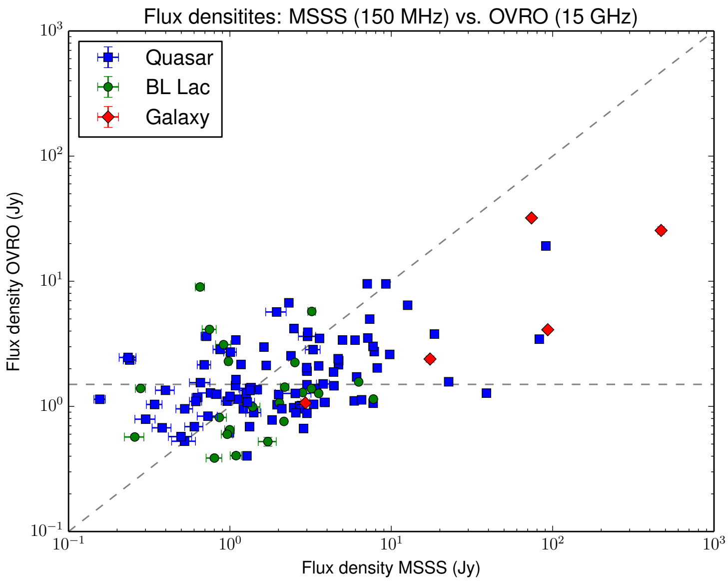

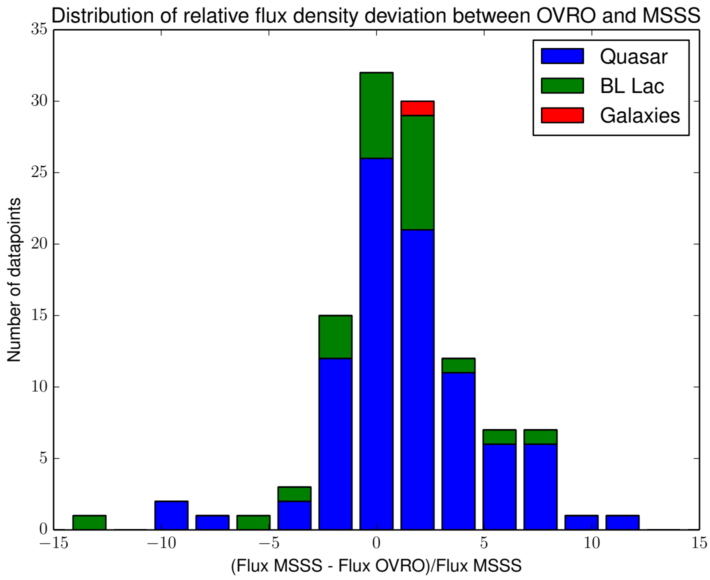

Figure 4.6.: Top: Comparison of the spectral flux density at 150 MHz from MSSS and the flux density at 15 GHz from the OVRO monitoring. The dashed lines are the line to the origin and the 1.5 Jy flux density limit, which was one of the selection criteria of the MOJAVE sample. Bottom: Relative deviation of the flux density between MSSS at 150 MHz and OVRO at 15 GHz calculated with $(S_{MSSS} - S_{OVRO})/S_{MSSS}$. The distribution shows that most sources have only weak deviations but some show higher flux densities at low frequencies. This is expected due to the steep spectral index of the extended emission in these sources.

4.1.4. Reimaging MSSS data sets of MOJAVE blazars

Since the MSSS catalog resolution is decreased to increase computational performance speed and to use the visibilities with good (u, v)-coverage, the visibilities of longer baselines are ignored in the catalog. The longest baselines are very sparse since the measurement sets only contain from two 7 min snapshot observation each. However I started a reimaging of certain MSSS fields containing MOJAVE sources with increased resolution. To do this I used an early version of the LOFAR selfcalibration pipeline available for testing on the LOFAR computing cluster.
The selfcalibration pipeline needed much memory and took days to reach the final stage. The strategy this pipeline uses is as follows:

1. use the VLSS catalog as low resolution model for the target field with BBS
2. calibrate the phases of the measurement set using this model with BBS and DPPP
3. create image using CLEAN using a (u, v)-range slightly higher than the VLSS resolution with AWImager
4. extract sources with PyBDSM
5. use the results of PyBDSM as model for next phase calibration (BBS & DPPP)
6. make image again with CLEAN (AWImager) further increasing the resolution by using a larger (u, v) range
7. extract sources with PyBDSM and continue the steps from 4. until the maximal resolution is reached after 10 iterations

This pipeline can only compute measurements with the Dutch LOFAR array. For this array the highest resolution is ∼5 arcsec. In this early version of the pipeline the final resolution could not be changed as well as the number of iteration steps in which the resolution is increased. The pipeline received several updates since my use on the MSSS measurements sets, but without having computing time on the cluster, the newer version has not been tested with these observations.
Since the longest baselines in the (u, v)-plane do not provide many visibilities to the (u, v)-plane the selfcal pipeline usually failed at the last iteration steps. The crash was caused by the source finder (PyBDSM) because it could not identify sources due to too many artifacts coming from sidelobes in the image. However, the images of earlier iteration steps with the resolution of ∼24 arcsec show good results. These images were affected by artificial features, thus I performed the selfcalibration pipeline to each MSSS-frequency band available and used the images to average them with the same script as for the averages maps in the MSSS catalog.
In the appendix B.3 the images of 93 sources are shown, which could be reimaged. To get

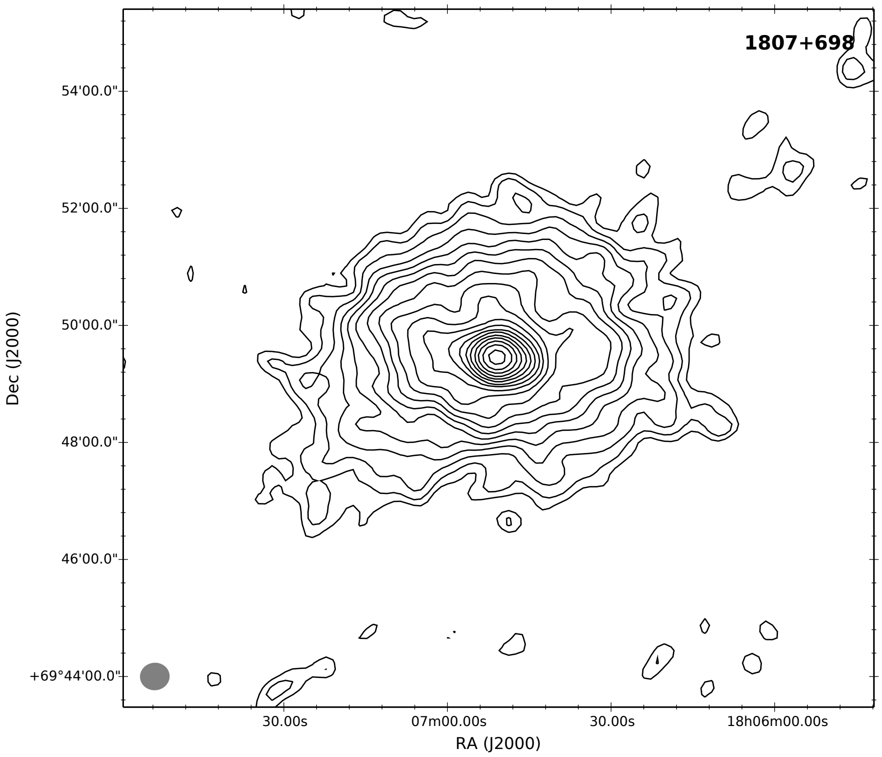

Figure 4.7.: The BL Lac object 1807+698 (3C 371) in the averaged map of the reimaged MSSS fields at a resolution of ~ 27 arcsec.

an overview over all sources first the frequency band centered at 143.3 MHz was reimaged, corresponding to an intermediate frequency band of the MSSS frequency range between 120–160 MHz. Some fields had to many sidelobes and the reimaging of the 143.3 MHz band failed. This was the case for two sources failing at the 143.3 MHz but the reimaging was successful for a higher frequency band (0119+115 and 2200+420).
Due to temporal limitation of the LOFAR cluster access it was not possible to reimage the target fields for all MOJAVE blazars. 45 sources could be reprocessed at all or most frequency bands. For those targets the resulting images were used to create an averaged image in which the sensitivity is increased by $\sqrt{n}$ with n being the number of frequency bands. The priority of each source was based on the indication of extended emission in the brightness distribution of their first frequency band. The averaged brightness distributions for these sources are shown in Figure B.4 in the appendix.

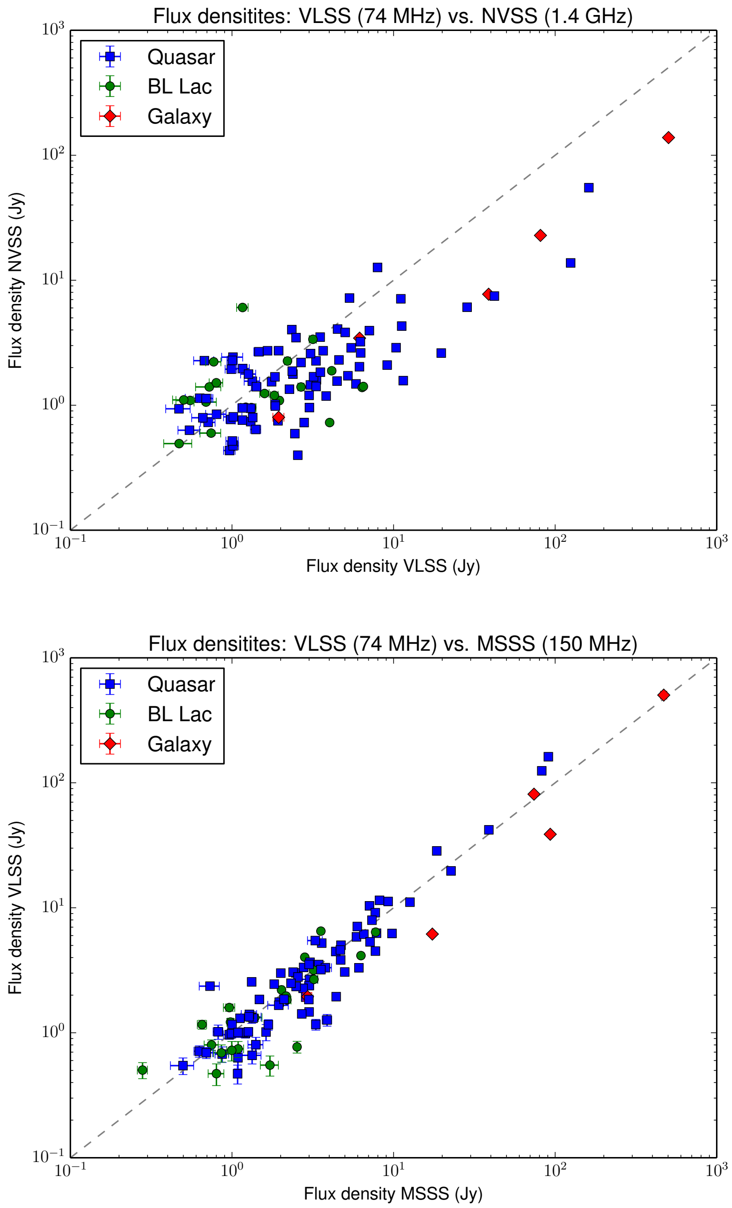

Figure 4.8.: Top: Comparison of the flux densities of NVSS at 1.4 GHz (Condon et al. 1998) and the flux densities of VLSS at 74 MHz (Cohen et al. 2007a).
Bottom: Comparison of the spectral flux densities of the MSSS catalog at 150 MHz and the flux densities of VLSS at 74 MHz (Cohen et al. 2007a).

4.2. Discussion

4.2.1. MOJAVE blazars in the MSSS catalog

A previous performed blazar study of Massaro et al. (2013) at low frequencies offers the possibility to compare their results with the MSSS catalog in combination with OVRO. The sample of Massaro et al. (2013) is much larger selected by finding counterparts to known blazars in the VLSS catalog (Cohen et al. 2007a). The flux densities of VLSS are combined with the flux densities of their counterparts in NVSS (Condon et al. 1998) to calculate spectral indices. While this sample is much larger, the MOJAVE sample is smaller and selected to include only the brightest blazars. This means that the sample of Massaro et al. (2013) has a flux density cutoff based on the sensitivity of VLSS, while MOJAVE sources are only included if their flux densities have reached 1.5 Jy in an observation at 15 GHz.
To compare the results of Massaro et al. (2013) and MSSS-OVRO reduced to sample in this work, the spectral indices between NVSS and VLSS can be are similar (see Figure 4.3 on the bottom) to the broadband spectral index distribution between MSSS and OVRO (see Figure 4.3 on the top). Since NVSS and VLSS are not simultaneous and observed several years before the MSSS observations, some differences due to different variability states of the sources are expected. This variability broadens the distribution in the NVSS-VLSS spectral index distribution. The peak around a spectral index of 0 demonstrates that the targets are still dominated by the beamed emission components even at low frequencies. The slight shift towards optical thinner ($\alpha < 0$) spectral indices indicates that the lower frequencies pick up more extended emission due to higher sensitivity, while some sources with inverted spectra $\alpha > 0$) could be included which have their synchrotron peak somewhere between 150 MHz and GHz frequencies or are in a flaring state at GHz frequencies. To exclude the variability more simultaneous observations are needed.
To compare the flux density correlation with Massaro et al. (2013), the NVSS and VLSS flux densities are presented in Figure 4.8 on the top. The archival data of radio surveys are affected from long term variability influencing the correlation more than the quasi-simultaneous data points in Figure 4.6 (top). However the data points are very similar distributed as the MSSS-OVRO flux densities. Most of the datapoints are located in a cloud with a slight shift towards the higher flux densities at lower frequencies. The brightest sources and especially the few radio galaxies confirm this shift in both plots.
The flux densities of MSSS and VLSS, which are both surveys at low radio frequencies, are plotted in Figure 4.8 on the bottom. The observing frequencies of 74 MHz (VLSS) and 150 MHz (MSSS) are close to each other so it is expected that the flux densities have only small differences due to variability. With the small difference in the observing frequency the extended emission does not affect the flux densities very much. In fact the flux densities seem to fit very good to each other, while the scattering in both directions

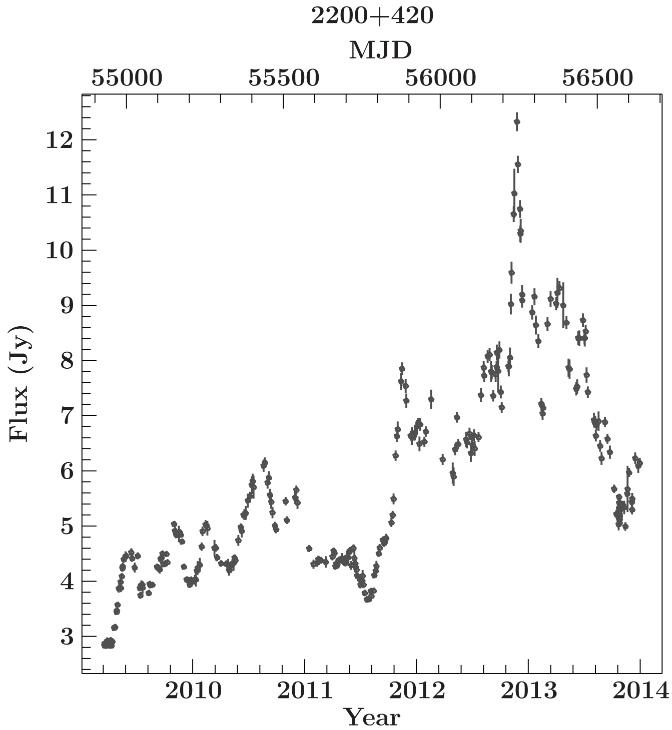

Figure 4.9.: The light curve of 2200+420 (common name: BL Lac) from the OVRO single-dish monitoring at 15 GHz.

can be caused by variability since the observations were not simultaneous.

In the plot of the flux densities of MSSS versus OVRO (Figure 4.6 on the top) as well as the plot of the flux densities of VLSS versus NVSS (Figure 4.8 on the top) one BL Lac object lies offside (green filled circle) which shows significantly higher flux densities at high radio frequencies than at lower frequencies. In both plots it is the same source: 2200+420 (common name: BL Lac). Since this source is highly variable one possibility is that the source shows a flare in the high frequencies which is not present at the low frequencies in the observations. Figure 4.9 shows the lightcurve of 2200+420 of the OVRO monitoring. The data point for the OVRO flux density is from May 5th, 2013. The MSSS observation is from April 20th, 2013 and 15 days before the measurement of the 15 GHz flux density. However since it is the same case in the archival data points of NVSS and VLSS, it is unlikely that a flare is causing the same effect in both cases. The other possibility is that the source has its synchrotron peak above 150 MHz and the flux densities of MSSS as well as the VLSS are fainter because the emission is already self-absorbed.

The initial MOJAVE sample consisting of 135 AGN has be also studied at lower fre-

quencies by Arshakian et al. (2010). In his study archival data was used to interpolate the flux densities of each to 151 MHz. Since the archival data is not simultaneous variability can affect these interpolations. However interpolating the flux densities to 151 MHz only using spectral index between the NVSS and VLSS catalog similar results like the flux densities of Arshakian et al. (2010) are obtained. Both versions of interpolated flux densities are plotted in Figure 4.10 on the top. Since only the NVSS and VLSS catalog is used, the fit is more affected of problems like variability calculating with only two data points. With more than two data points outlier can be averaged out making the fit more reliable. Most of the data points with larger deviation are BL Lac objects and those sources are typical for high variability. However, it shows that the flux densities interpolated by Arshakian et al. (2010) can be used as good reference to compare them with the MSSS flux densities. In the spectra in shown in Appendix B.2 the flux densities of Arshakian et al. (2010) are plotted as orange triangle as reference. Since not all sources of the sample in this work were interpolated by Arshakian et al. (2010) not every spectrum has these data points included.
To compare the results of the interpolation by Arshakian et al. (2010) with the spectral flux densities of MSSS at 150 MHz, the relative deviation of both flux densities is calculated like it was done for the flux densities between MSSS and OVRO in Figure 4.6 on the bottom. The distribution of the relative deviations are shown in the bottom plot in Figure 4.10. The distribution shows a shift of the peak towards higher flux densities in the MSSS catalog. Since the archival data used by Arshakian et al. (2010) probably contained more flux densities at higher frequencies and the spectra for those sources are mostly flat, the interpolation could miss some of the extended emission which adds more to the flux densities at lower frequencies underestimating the true flux densities. However, for the radio luminosities to estimate intrinsic jet power Arshakian et al. (2010) assumed that the flux densities at low frequencies should be dominated by the extended emission and the contribution of the beamed core and jet flux can be neglected. This assumption is contradictory to the flat spectral indices obtained in this work, indicating that the core and jet emission is still beamed and still contributes a large fraction to the total flux density. To get the ability to measure the radio luminosities of the jets needed for the estimation of the intrinsic jet power, higher resolution is needed. With higher angular resolution it is possible to subtract the flux density of the beamed emission regions with flat spectral indices to get the extended emission.

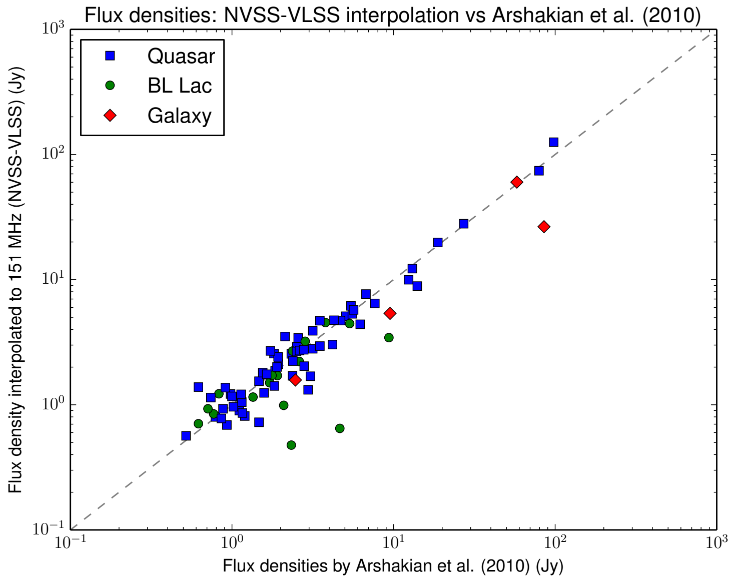

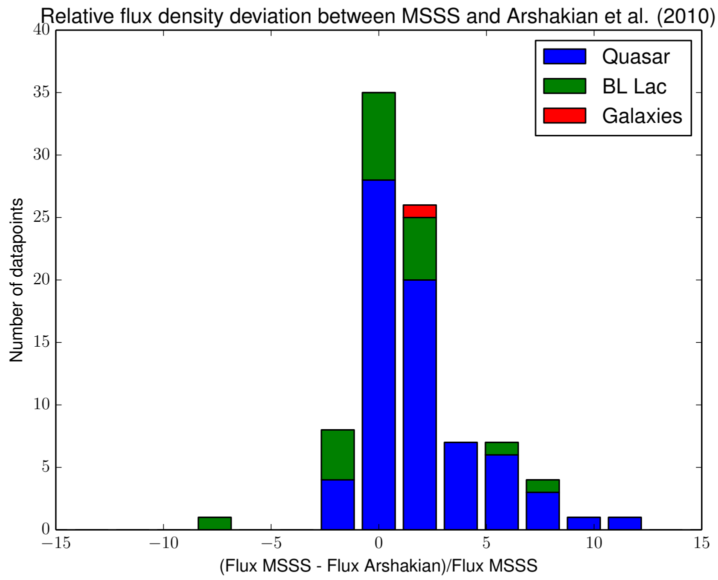

Figure 4.10.: Top: Flux densities interpolated to 151 MHz by Arshakian et al. (2010) versus the interpolated flux densities to 151 MHz using the spectral index from NVSS and VLSS. The dashed line is the line to the origin.
Bottom: Relative deviation of the flux density between MSSS at 150 MHz and the interpolation to 151 MHz from Arshakian et al. (2010).

4.2.2. Extended emission of reimaged blazars

In the images obtained by the reimaging process several blazars of the sample show extended emission. However, due to the lack of a correct absolute flux scale calibration only morphological information can be gained from these images. The original calibration results in wrong flux densities since the beam models of several stations were not correct. The flux densities of the catalog used for the spectral indices and flux densities already received a correction, which could not be applied to the reimaged measurement sets. For this the flux densities in the images of the reimaging process are not reliable and not used in this work.
Even the averaged images with the higher angular resolution (mostly ∼20-30 arcsec) are affected by sidelobes creating artifacts, which are not disappearing through the averaging. For some of the sources artifacts can be identified by comparing the images to the NVSS observations (Condon et al. 1998) with the VLA at 1.4 GHz. These images have a lower angular resolution of 45 arcsec, but features in the MSSS images not close to a bright source in NVSS are unlikely to be real. Besides most sources fit to the morphological structures seen in the NVSS images.
Examples from the reimaged fields of my work are also used in the first MSSS paper (Heald et al. 2015) for future possibilities, which was one of my contributions to that paper (see Figure 18 of that paper, where 0415+379 (3C 111) and two other double lobed sources are presented). Another example of this reimaging results was shown at conferences and is published in the corresponding proceedings (Trüstedt et al. 2014).
However, the main result of these images were the possibility to identify good candidates for LOFAR observations with international stations. To demonstrate the capabilities of these observations, a pilot sample, consisting of two BL Lacs and two FSRQs, was chosen based on these images. The results of the observations of this sample build the second chapter of results in this work (see Chapter 5.
One of the most promising candidates is the BL Lac 1807+698 which already shows a halo of extended emission over a large area in the corresponding reimaged MSSS field at all frequencies. The averaged map is presented in Fig. 4.7. The morphology of this source is very similar to the results of VLA observations at 1.4 GHz by Giroletti et al. (2004). For showing clearly extended emission this source also chosen to be one of the sources of the pilot sample.
The FSRQ 2201+315 shows extensions for a double sided structure with lobes. Compared to the radio galaxy 0415+379 the core is dominating the emission. The image of this source is found in Figure B.40 on the right side at the top.
The other two objects chosen to be included in the pilot sample are the FSRQ 1222+216 and the BL Lac 0716+714. Both images are found in Figure B.34 with 0716+714 on the left side in the mid and 1222+216 on the right side at the bottom. Both images of these sources show features, where it is not clear if they are artifacts or real. However, both are very bright core dominated sources, which helps with the calibration strategy of the

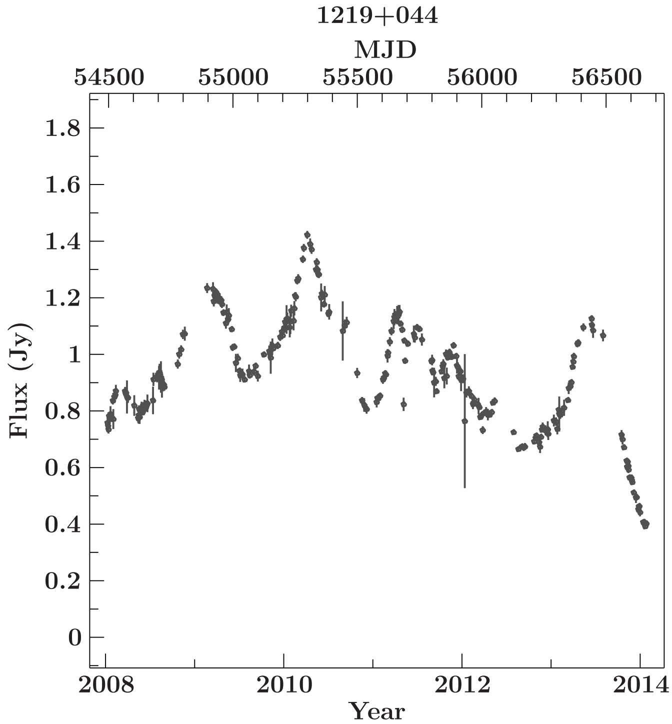

Figure 4.11.: The light curve of 1219+044 (common name: 4C +04.42) from the OVRO single-dish monitoring at 15 GHz.

international baselines because the targets can also be used as phase calibrators.

4.2.3. Radio-loud narrowline Seyfert1 galaxies (NLS1)

The main focus of this thesis is set on the blazars of the MOJAVE sample at low frequencies, however during the extensive study of the MOJAVE sample for one source a reference received a new classification. The AGN 1219+044 was previously classified as a quasar but is now classified as a radio-loud narrowline Seyfert 1 galaxy (NLS1) according to Yao et al. (2015). Only a handful of these sources with this classification are known currently. This class of AGN is thought to be a population of young AGN and show blazarlike features like variability, however even detected they are faint objects at radio frequencies. The mentioned NLS1 of the MOJAVE sample also shows variability in the OVRO monitoring at 15 GHz seen in Fig. 4.11.

To compare this subclass of AGN with the results on the MOJAVE blazar sample, I searched the MSSS preliminary catalog for counterparts of the radio-loud NLS1 sample from Foschini et al. (2015) containing 42 sources. However only for 5 of the 42 sources counterparts in the MSSS catalog are found, which are not enough sources to study their properties with a statistical significance. To explain this the flux densities and spectral indices given by Foschini et al. (2015) are used to extrapolate their expected flux density at 150 MHz for those sources with a spectral index given. Of the sample with 42 objects only 21 have given a spectral index for radio frequencies of which 3 sources are on the southern hemisphere. The remaining 18 sources are presented in Table 4.1 with their spectral index and flux density from Foschini et al. (2015) as well as the extrapolated and measured flux density at 150 MHz. The table shows that all sources with expected flux densities above 200 mJy were detected. Additional to this the source J1644+2619 was found where the extrapolation only led to a flux density of $S_{150\mathrm{MHz}} = 76.5$ mJy with a more than twice as high value. However this could be due to the variability of NLS1 or the source has some extended emission while most NLS1 show only very few features of jets or extended emission. Since most of these sources show rather flat spectral indices it is not expected that they appear much brighter at lower frequencies due to the low amount extended emission compared to the blazars of the MOJAVE sample.

Table 4.1.: Part of the radio-loud NLS1 sample by Foschini et al. (2015). The column with the flux densities at 1.4 GHz and the spectral indices are taken from the tables of the paper by Foschini et al. (2015). The column with S_{150MHz} are the extrapolated flux densities expected at 150 MHz. The last column shows the flux densities for those sources detected in the MSSS snapshot observations.

J2000 IAU name	$S_{1.4\mathrm{GHz}}$ (mJy)	α	$S_{150\mathrm{MHz}}$ (mJy)	S_{MSSS} (mJy)
J0324+3410	614.3 [b]	-0.26 ± 0.03 [a]	1098.0	1010.7
J0713+3820	10.4	-0.58 ± 0.12 [a]	38.0	
J0814+5609	69.2	-0.38 ± 0.01 [a]	161.7	
J0849+5108	344.1	-0.21 ± 0.01 [a]	550.0	301.1
J0902+0443	156.6	-0.07 ± 0.01	183.1	
J0948+0022	107.5	0.28 ± 0.01	57.5	
J1031+4234	16.6	0.40 ± 0.06 [a]	6.8	
J1047+4725	734	-0.33 ± 0.01 [a]	1533.9	2026.1
J1138+3653	12.5	-0.50 ± 0.09 [a]	38.2	
J1146+3236	14.7	-0.38 ± 0.09 [a]	34.4	
J1227+3214	6.5	1.04 ± 0.07	0.6	
J1246+0238	37	-0.55 ± 0.06	126.4	
J1421+2824	46.8	0.21 ± 0.01	29.3	
J1505+0326	365.4	0.31 ± 0.01	182.8	
J1548+3511	140.9	-0.26 ± 0.01 [a]	251.8	244.7
J1629+4007	12	0.68 ± 0.02	2.6	
J1633+4718	62.6	-0.42 ± 0.01	160.0	
J1644+2619	87.5	0.06 ± 0.01	76.5	167.6

The spectral index was calculated with flux densities at 1.4 and 5 GHz, for those sources with [a] the spectral index was calculated with 1.4 GHz and a lower frequency (mostly 325 MHz). The spectral indices are adapted to match the convention used in this work with $S \propto \nu^{\alpha}$.
The flux densities are the peak flux densities of the VLA FIRST survey (Becker et al. 1995) close to or at 1.4 GHz; flux densities with [b] are from the NVSS survey at 1.4 GHz (Condon et al. 1998).

5. LOFAR international observations

The MSSS reimaging results showed that LOFAR easily can detect extended emission of blazars even in snapshots (see Fig. 4.7). To study the structure of blazars in greater detail we proposed for longer LOFAR observations including the international baselines to get the best resolution possible at those low radio frequencies. For the first proposal a pilot sample of 4 sources was choosen based on the results of the MSSS reimaging. The sources are bright and show clearly extended emission. Another point was to have a small sample and to have equally representatives of the BL Lacs and the FSRQs. The pilot sample studied in this work consists of two BL Lacs: 1807+698 and 0716+714 and two FSRQs: 2201+315 and 1222+216 (MSSS bilder einfügen oder drauf verlinken).
After the accepted proposal for the pilot sample (PI: Trüstedt) in the following cycles more proposals were submitted and accepted. Two followup proposals (PI: Trüstedt) to observe more sources from the MOJAVE sample have been accepted in the two following cycles. Besides of the MOJAVE-LOFAR proposals a proposal two observe high redshift blazars searching for extended emission (PI: Trüstedt) and a complementary proposal for observations with the GMRT (Giant Metrewave Radio Telescope) in India to observe 3 of the pilot sample targets (PI: Trüstedt) were submitted and accepted as well. 0716+714 was not included since there is also an archival GMRT observation available.

5.1. The calibration of international LOFAR observations

The calibration of LOFAR observations with international stations is a difficult process because the strategies to calibrate the international stations are still in development, the software has still limitations regarding the high number of baselines and the requirement of computing clusters for optimal processing. So the current calibration process uses mainly the LOFAR pipeline, AIPS for fringefitting and an imaging tool such as CASA or difmap. This section will describe the calibration applied for the results of this work. At the end of the section improvements to the calibration resulting from newer insights of the LOFAR long baseline working group are suggested. However these improvements require more computing time and a computing cluster. The following steps give an overview over the applied calibration steps in this work:

1. After the observation the observatory pipeline processes the data including:
   - Averaging the visibilities into 4 s time steps
   - Calibration of the Dutch array in amplitude and phase using the amplitude calibrator observation and a simple sky model
   - Phasing up the core stations to combine them in a tied station with the virtual size of the combined core station area
2. Combination of the subbands to frequency bands with larger bandwidth resulting in 13 frequency bands of 3.1 MHz bandwidth
3. Transformation of the linear polarization coefficients into circular polarization
4. Filtering the core stations from the measurement sets to reduce the file size
5. Applying a rough correction to the amplitudes of the international stations to put them in the expected order of magnitude
6. Fringefitting the international stations in AIPS using the tied station as reference
7. Selfcalibration with amplitude and phase calibration using decreasing time intervals
8. Correction of the amplitudes using the calibrated Dutch array
9. Creation of the final images and tapered images

The LOFAR pipeline from step 1 is able to perform the calibration for the Dutch LOFAR array. This is possible since the phase calibration can be done by using a sky model obtained by interpolating a model from previous survey observations like NVSS (Condon et al. 1998) and VLSS (Cohen et al. 2007a) due to the large field of view of LOFAR. The amplitude calibration is done by observing an amplitude calibrator with a good model. However this strategy does not work for the international LOFAR stations. The field of view is much smaller and the (u, v)-coverage is sparse at the longer baselines. Because of this the international stations cannot be calibrated in an automatic way at the current stage of software development.
In the observations the 24 core stations used the dual mode available for the HBA tiles, resulting in 48 core stations in the measurement sets. Together with the remote and international stations a total station number of 74 stations can be found in measurement sets obtained from the LOFAR pipeline for the observations of this work. This results in a 2701 baselines which are too many baselines to process them in AIPS. To make a calibration via AIPS possible, the core stations are phased up to a tied stations combining 48 stations in one big virtual station. Due to the large virtual size this station is an ideal reference station. However the success of the calibration is dependent on the good previous calibration of the core array. In table 5.1 the participating stations in each

Table 5.1.: All participating stations in the observations of the 4 targets in the pilot sample. The ○ mark the stations, which had to be flagged completely.

Station	2201+315	1807+698	1222+216	0716+714
Tied Station	X	X	X	X
RS106HBA	X	X	X	X
RS205HBA	X	X	X	X
RS208HBA	X	X	X	X
RS210HBA	X	X	X	○
RS305HBA	X	X	X	X
RS306HBA	X	X	X	X
RS307HBA	X	X	X	X
RS310HBA	X	X	○	X
RS406HBA	X	X	X	X
RS407HBA	X	X	X	X
RS409HBA	X	X	X	X
RS503HBA	X	X	X	X
RS508HBA	X	X	X	○
RS509HBA	X	X	X	○
DE601HBA	X	X	X	X
DE602HBA	X	X	X	X
DE603HBA	X	X	X	X
DE604HBA	X			
DE605HBA	X	X		X
FR606HBA	X	X	X	X
SE607HBA	X	X	X	X
UK608HBA	X		X	
DE609HBA*			X	
Obs. date	2015, Jan 22	2014, Dec 16	2015, Mar 12	2014, Dec 17
Calibrator	3C48	3C196	3C295	3C196

* This station was included in the LOFAR array since February 2015

observation is listed. To reduce the file size but keeping a good time resolution in the pipeline the visibilities are averaged into 4 s time steps.

To cover the bandwidth between 120-160 MHz the bandwidth is distributed over 216 subbands. These subbands are combined into 13 frequency bands with 3.1 MHz bandwidth consisting of 16 subbands each. The larger bandwidth provides a larger amount of visibilities to find better solutions in the fringe fitting but keeping the bandwidth low enough to avoid frequency smearing effects. Since AIPS does not calculate correctly with linear polarization coeffients, which are the standard form for the polarization in LOFAR observations, the coefficients are transformed to circular polarization before importing the visibilities in AIPS.

Since the amplitudes of the international stations received no correction in the pipeline,

the amplitudes are at a random scale. Usually the amplitudes are higher than their expected range by a factor between 10-1000. To adjust the amplitudes the task CLCOR is performed with the multiplication of a factor between 0.01-0.1. After correcting the amplitudes, the weightings of all visibilities are calculated over a time interval of 5 minutes. The fringefitting is performed without using a model, e.g. a bright point source is anticipated, and only visibilities from baselines larger than 10 kλ are taken into a account. The tied station is taken as the reference station. The solutions of the fringe fitting were only used if the fraction of bad solutions was less than 10%. To reduce outliers the solutions were smoothed with the task SNSMO before applying them to the visibilities and exporting the calibrated visibilities to a new UVFITS-file. After testing the strategy the fringefitting was done using a script like in the example in Appendix C.3. To further calibrate the resulting UVFITS-files a selfcalibration strategy was applied.
The selfcalibration was tested with different approaches. In total 4 strategies were tested using CASA for two of them and difmap for the other two. Each of the strategies was tested and developed in an interactive way and then adapted to use scripts for a large fraction. The differences in the strategies can be summarized as following versions:

1. Selfcalibration using CASA without a mask for the cleaning
2. Selfcalibration using CASA with a mask for the cleaning
3. Selfcalibration using difmap without a mask for the cleaning
4. Selfcalibration using difmap with a mask for the cleaning

The results are shown on one frequency band for each source in the Figures 5.1, 5.2, 5.3 and 5.4. The examples show that the results can make a change in the resulting brightness distributions. Each of the strategy includes similar steps to do the selfcalibration:

1. Iterative use of CLEAN and phase SELFCAL to obtain a suitable model describing the visibilities
2. Applying an amplitude and phase selfcalibration over a certain time-interval
3. Repeat steps 1 and 2 with a decrease in the time-interval of step 2
4. Use of CLEAN with less gain over the whole map to smooth the final brightness distribution

For all strategies these steps were performed only on the visibilities with a (u, v)-range $>$60kλ to do a first calibration on the international baselines. Usually the decreasing time intervals were 10 min $\rightarrow$ 1 min $\rightarrow$ 30 s $\rightarrow$ 16 s $\rightarrow$ 4 s. For the strategies 1 - 3 after the first calibration of the longest baseline followed the selfcalibration for all visibilities with decreasing timeintervals of $\infty \rightarrow 10$ min $\rightarrow 1$ min $\rightarrow 30$ s $\rightarrow 16$ s $\rightarrow 4$ s. For strategy 4 after the selfcalibration for baselines $>$60kλ followed a selfcalibration over all visibilities excluding the tied station. This model was used for an amplitude selfcalibration of the tied station while freezing all other stations. After this step again a selfcalibration over all visibilities was performed. For these two selfcalibrations the timeintervals were: $\infty \rightarrow 30$ min $\rightarrow 5$ min $\rightarrow 1$ min $\rightarrow 4$ s. The strategy was changed in this way because of the tied station having such a huge virtual dishsize the high sensitivity reduces the weightings of this station in a way that it was always used as an almost perfect reference station ignoring possible errors for the tied station. Apart from causing problems by the creating of such a phased array as one station, calibration errors have a much higher impact in the selfcalibration. The change in the selfcalibration strategy was an attempt to further improve the calibration of this station.

Besides this difference the use of a mask (or several masks) makes a large difference. The results without using a mask showed much lower RMS values. This was caused by including all artifacts in the model during the CLEAN-process. With the mask the CLEAN is restricted only to build a model in those areas where a mask is put. This way only trusted features are included in the mask and the artifacts may disappear or get weaker during the selfcalibration. For strategy 4 the initial mask included only the brightest features to reduce the noise and a higher stage of the selfcalibration (usually after the amplitude selfcalibration over a time interval of 5 min) a larger area was included inside the mask to cover also fainter features of the source.

The last major difference between the strategies 1 and 2 compared to 3 and 4 is the way of flagging data. While most of the visibilities have to be flagged manually in difmap, CASA uses an automated version of flagging during each selfcalibration task. With this the CASA strategies flag much more visibilities (up to 60% of the visibilities), while in difmap problematic stations were flagged at the beginning and a manual flagging of each frequency band was performed after the selfcalibration of the international stations ($>$60kλ).

Finally strategy 4 turned out to produce the best images regarding less artifacts and a good model representing the source structure. Thus the two strategies with CASA were not further used and are not completely calibrated with a final flux scale correction.

Since the amplitude selfcalibration not only changes the international baselines but also the remote stations and the tied station, the final model is consistent but may deviate from the calibrated amplitude scale. Thus the flux densities measured from these images are not correct. To improve the flux calibration the Dutch array calibrated by the observatory pipeline is used. The measurement sets after the fringefitting and before selfcalibration is used to create a wide-field image with low angular resolution (~ 1 arcmin) excluding the international stations. The same procedure is performed on the measurement sets after the selfcalibration. By measuring and comparing the bright sources in the field a correction factor can be calculated, which corresponds to the deviation in amplitude of the selfcalibrated visibilities compared with the calibrated Dutch array from the

pipeline. For the four targets in this work the targets themself are by far the brightest sources in the field and the linear regression between all measured sources is dominated by this bright source. The correction factor is multiplied to the amplitude of each visibility using TaQL. The results show that the flux calibration obtained this way result in a good amplitude calibration.
After the correction of the flux scale the final images are produced by CLEANing with a mask followed by clean with lower gain over the complete map. Additional to the final high resolution images tapered images are created. For this all visibilities with a (u, v)-range $>$200kλ are downweighted. The resulting images have lower angular resolution but the larger beamsize improves the detection of diffuse fainter emission regions.
Because the tapered images might be affected by only using the taper for the cleaning on the final selfcalibrated visibilities one frequency band was fully selfcalibrated using a taper of 100kλ to look for differences. The result is shown in Figure 5.5. Since the resulting image showed no major differences, the tapered images were made starting at the final calibrated visibilities.
The final images of each frequency band are stacked and averaged to create an averaged image. For the stacking all images were convolved with a common beam slightly larger than the largest beam axis of the image with lowest resoltion. The averaged image has the advantage that features appearing only in one image disappear, which increases the sensitivity on the emission regions detected in every image. For this the averaged images are a good reference which features are real emission regions and can be used to search for weaker diffuse emission. For all sources except 1222+216 the averaged images contain all 13 single frequency bands. 1222+216 shows a phase shift in the first two frequency bands which is difficult to correct. Due to this shift for 1222+216 only the remaining 11 frequency bands were used.

To measure the flux densities of a target the total flux density included in the final model of the difmap image is used as total flux density for the source. These values vary only slightly comparing the high resolution and tapered images. To obtain a value for the core region a circular Gaussian model component is fitted to the region in difmap and the flux density of this component is used. The core is the region close to the supermassive black hole, where the jet emission changes from optically thick to optically thin and can be detected with radio observations. This fit has been performed on the high resolution and tapered images however due to having the same visibilities the fit results in the same components in size and flux density for almost every frequency band. For this the model component of the fits to the high resolution brightness distributions is used for those measurements.
Comparing the final flux densities of the sources show that the deviations from a spectral index fit to the flux densities is lower than 10% for the targets 2201+315 and 1222+216. For 1807+698 the calibration was not as good as for the previous two targets resulting in deviations in single bands up to 20%. Additionally to the larger deviations the amplitude calibration on the frequency band at 124 MHz failed for 1807+698. For this the correc-

tion factor for the flux scale was interpolated using the flux densities of the frequency bands at 121 and 127 MHz.
The observation of 0716+714 has more severe problems. The visibilities of the first 2 observation hours and the last 2 hours are completely different. This results in many errors during the calibration and in strange visibilities. Even with flagging several stations the data seems not to be usable. Using CASA it even fails to calculate a beam to deconvolve the visibilities for some frequency bands. The best obtainable results from this observation are presented however it is highly affected by calibration problems and artifacts. Due to these problems the results of this observation are not very trustworthy even when some of the results seem to fit to the expectations.
All brightness distributions obtained this way suffer from artifacts circular around the bright central region and large scale waveshaped structure. These artifacts are weak enough to disappear in most images, based on the selection of their lowest contourlevel. The large scale effects lead to a non-gaussian distributed noise in the images, which makes it difficult to calculate the true signal to noise ratio. In the images presented in this work the rms is calculated over the whole mapsize of the images ignoring the bright central source. Since this value does not represent the RMS well in all areas, the lowest contourlevel is chosen individually for the different targets and images. The lowest contourlevel was chosen in a way that most of the images show already artificial features. With this the lowest contourlevels show the emission from features, which are not very reliable and it is easier to estimate at which levels the features become significant.
The cause for these artifacts is most probable a problem with the amplitude calibration mainly the tied station. Due to its large virtual size it is weighted so sensitive that the selfcalibration steps basically ignore it. However not only problems in the calibration of the core stations can cause amplitude calibration of the tied station but also deviations occur from the process phasing up all core stations into one virtual station. Recent attempts of other LOFAR users revealed that the better strategy for the calibration is to use only the tied stations as reference in fringe fitting and to keep the core stations in the measurement sets. After the fringe fitting the tied station is filtered out and the selfcalibration is done with each individual core station. This strategy improves the image quality but on the other side increases the size of measurement sets by a factor of 10-100. With the large amount of baselines the calibration needs much more computational resources like memory and disk space. The calculation is slowed down much more and currently it is difficult to obtain time on a suitable computing cluster. For this the improved strategy could not be tested with these observations.

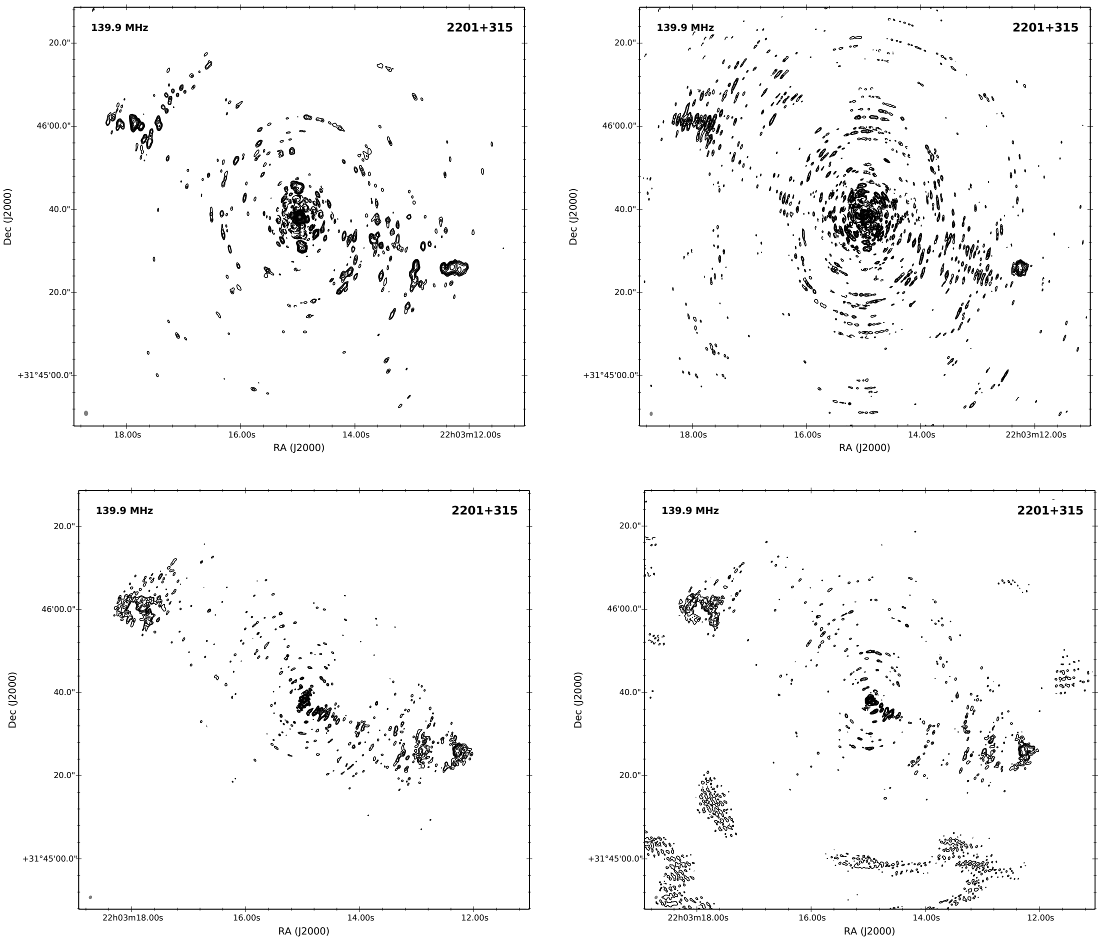

Figure 5.1.: Examples of the different selfcalibration strategies on the frequency band of 139.9 MHz for 2201+315. None of the examples is fully calibrated for absolute flux scales. Lowest contour for all maps is at 6.0 mJy beam^{-1}.
Top Left: Using CASA without a mask. Beamsize: 1.1" x 0.8"
Top Right: Using CASA with a mask. Beamsize: 0.8" x 0.5"
Bottom Left: Using difmap without a mask. Beamsize: 0.7" x 0.5"
Bottom Right: Using difmap a mask. Beamsize: 0.7" x 0.5"

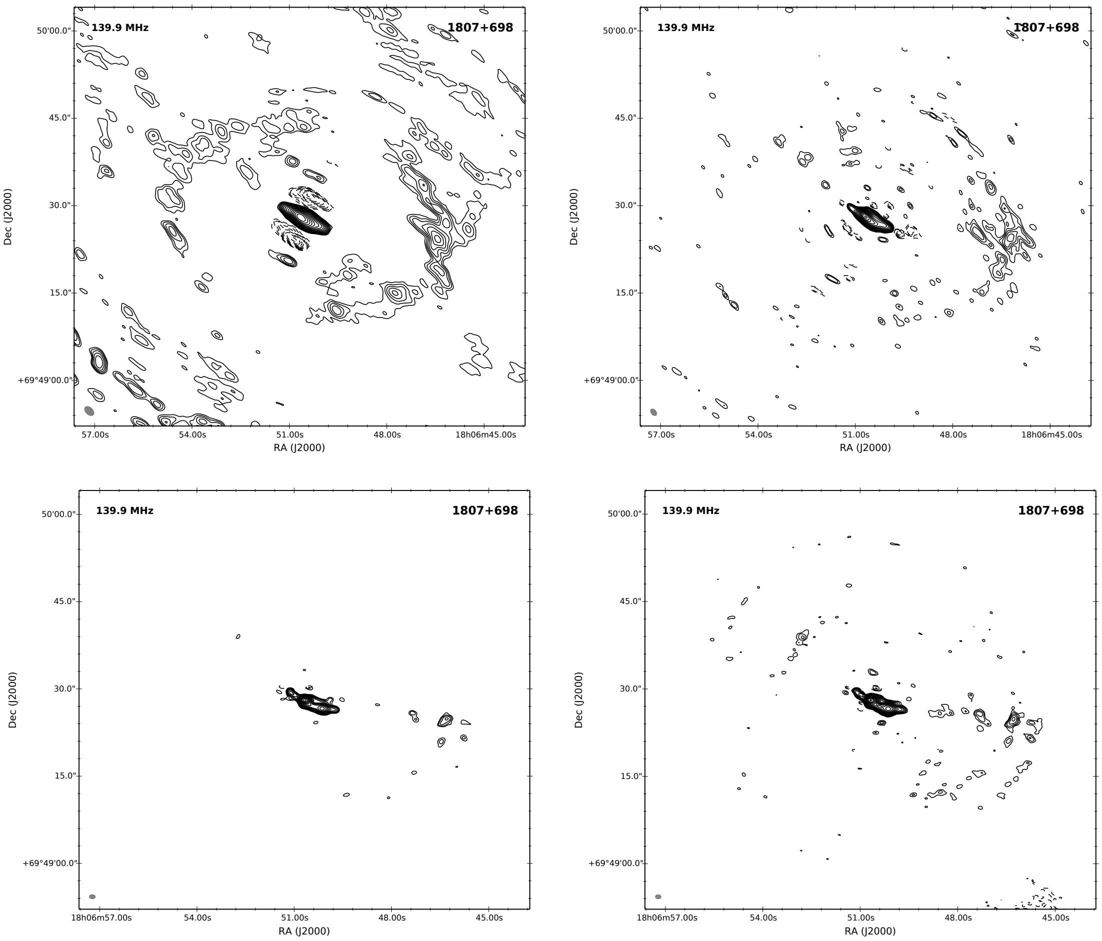

Figure 5.2.: Examples of the different selfcalibration strategies on the frequency band of 139.9 MHz for 1807+698. None of the examples is fully calibrated for absolute flux scales. Lowest contour for all maps is at 6.0 mJy beam^{-1}.
Top Left: Using CASA without a mask. Beamsize: 1.8" x 1.1"
Top Right: Using CASA with a mask. Beamsize: 1.3" x 0.8"
Bottom Left: Using difmap without a mask. Beamsize: 0.9" x 0.7"
Bottom Right: Using difmap a mask. Beamsize: 0.9" x 0.7"

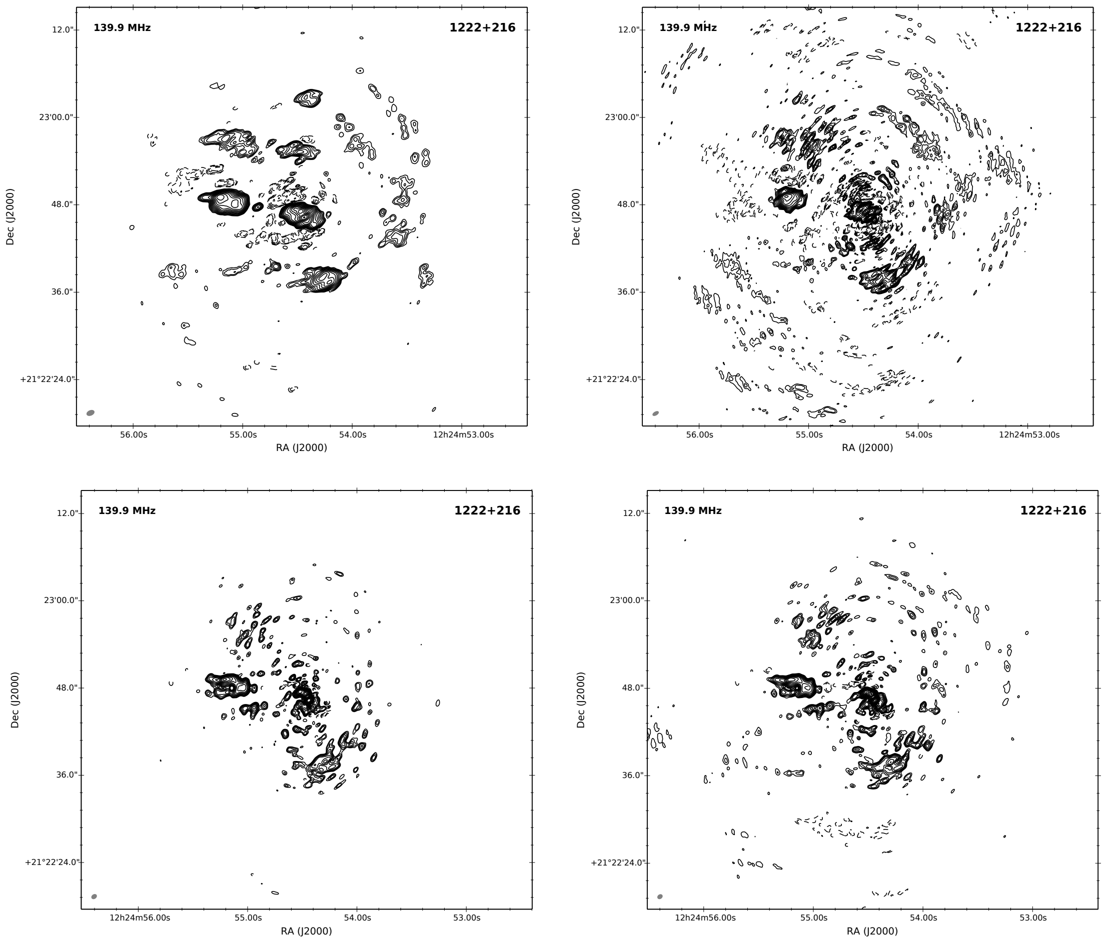

Figure 5.3.: Examples of the different selfcalibration strategies on the frequency band of 139.9 MHz for 1222+216. None of the examples is fully calibrated for absolute flux scales. Lowest contour for all maps is at 6.0 mJy beam^{-1}.
Top Left: Using CASA without a mask. Beamsize: 1.7" x 1.0"
Top Right: Using CASA with a mask. Beamsize: 1.3" x 0.8"
Bottom Left: Using difmap without a mask. Beamsize: 1.0" x 0.7"
Bottom Right: Using difmap a mask. Beamsize: 0.6" x 0.5"

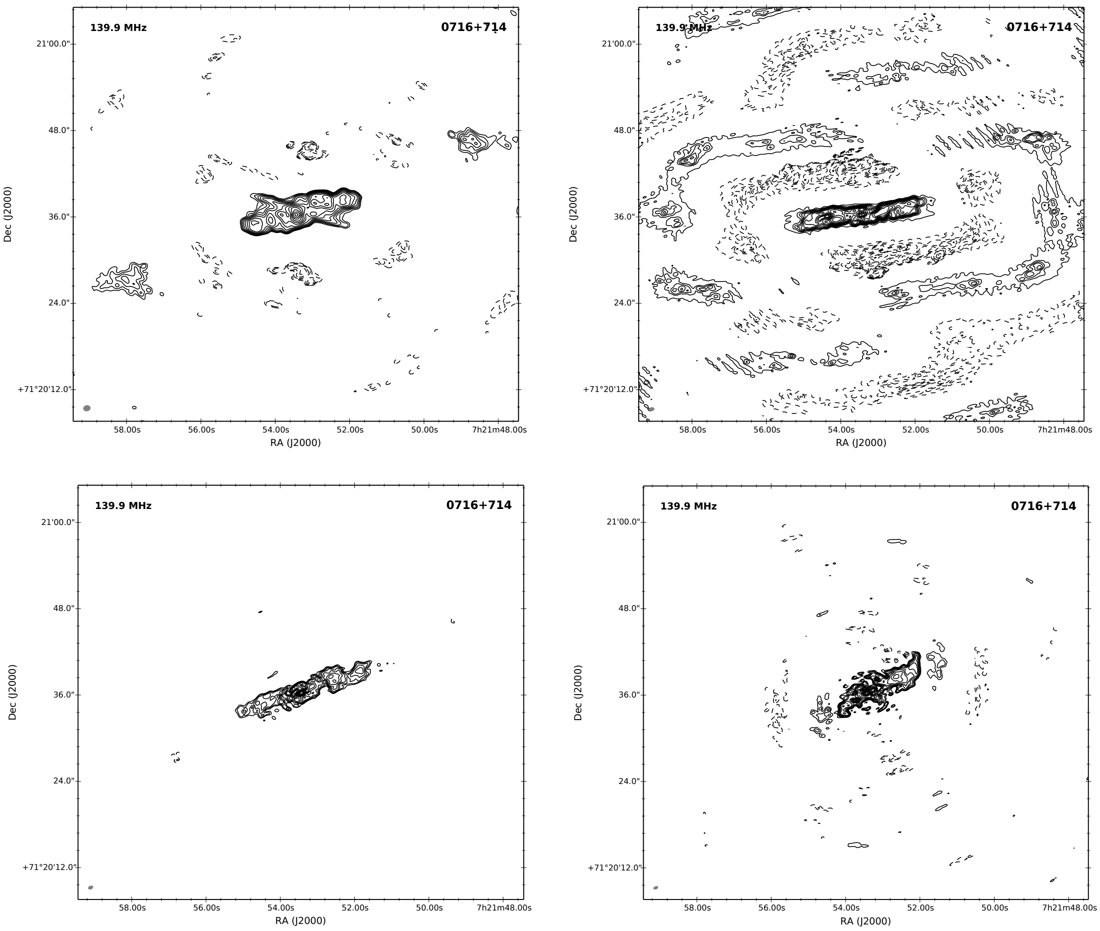

Figure 5.4.: Examples of the different selfcalibration strategies on the frequency band of 139.9 MHz for 0716+714. None of the examples is calibrated for absolute flux scales. Lowest contour for all maps is at 5.0 mJy beam^{-1}.
Top Left: Using CASA without a mask. Beamsize: 0.9" x 0.7"
Top Right: Using CASA with a mask. Beamsize: 0.7" x 0.4"
Bottom Left: Using difmap without a mask. Beamsize: 0.6" x 0.4"
Bottom Right: Using difmap a mask. Beamsize: 0.6" x 0.3"

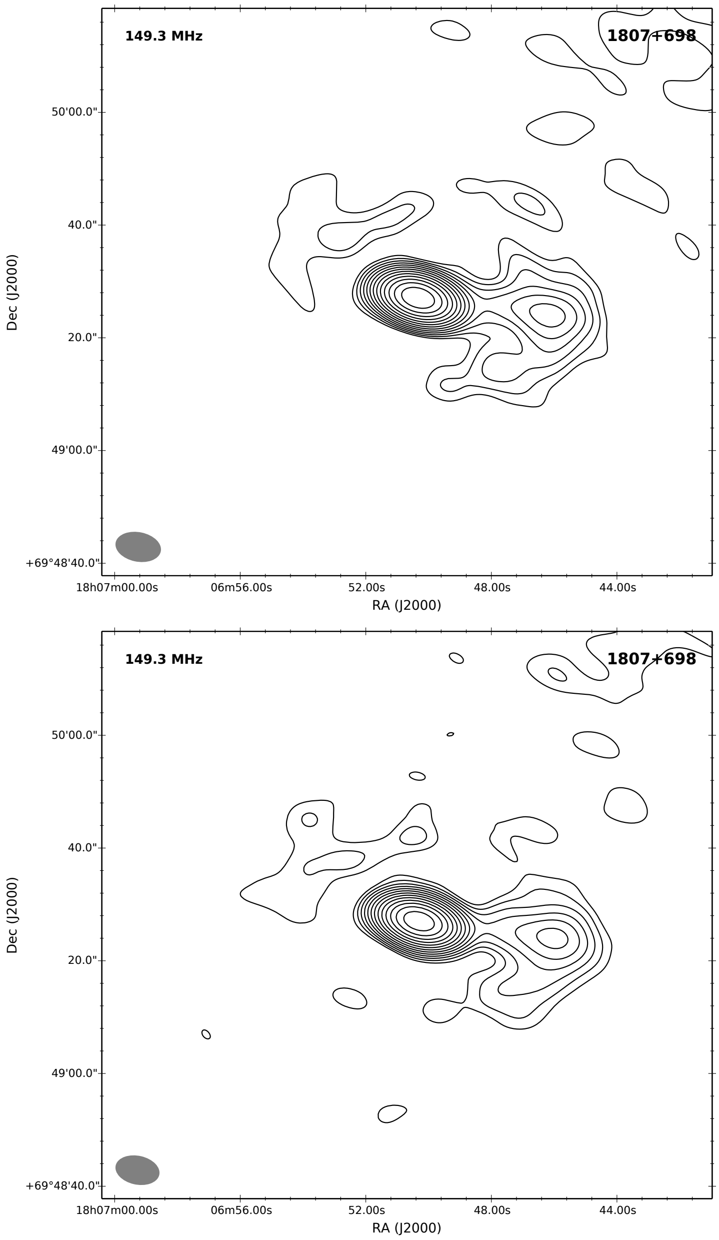

Figure 5.5.: The results of two strategies using a taper weighting down the visibilities at (u, v)-ranges higher than 100 kλ to 1%.
Top: Completely selfcalibration the dataset from scratch using the taper. S_{peak}=1.66 Jy beam^{-1}, S_{RMS}=7.85 mJy beam^{-1}, beam: 7.4" x 5.0" p.a. 77°
Bottom: Cleaning the already calibrated data set selfcalibrated at highest resolution with the taper. S_{peak}=1.50 Jy beam^{-1}, S_{RMS}=7.38 mJy beam^{-1}, beam: 7.2" x 4.9" p.a. 76°

5.2. Results

Using the selfcalibration strategy with difmap explained in Section 5.1 all four targets were imaged in their 13 frequency bands with a bandwidth of 3.1 MHz aiming for the highest resolution possible with a natural weighting and making tapered images to get a better impression on the distribution of weaker diffuse extended emission. Due to different flagging of each frequency band and differences in the participating international stations, each image has different image parameters. With the increase of the observing frequency the beam becomes smaller which increases the angular resolution.

5.2.1. Observation of 2201+315 (common name: 4C +31.63)

High resolution images

Table 5.2.: Parameters of the final brightness distribution maps of 2201+315 imaged with natural weighting. The images are shown in Fig. C.1 and the following.
In the last line the parameters of the averaged data set are given.

Frequency (MHz)	Bandwidth (MHz)	S_{peak} (Jy beam^{-1})	S_{RMS} (mJy beam^{-1})	beam$_{\mathrm{maj}}$ (arcsec)	beam$_{\mathrm{min}}$ (arcsec)	beam$_{\mathrm{p.a.}}$ (°)
121.2	3.1	0.885	1.774	0.71	0.55	-29.84
124.3	3.1	0.826	1.482	0.73	0.55	-29.75
127.4	3.1	0.903	1.582	0.73	0.55	-25.87
130.6	3.1	0.893	1.162	0.71	0.53	-27.34
133.7	3.1	0.952	1.483	0.69	0.51	-32.47
136.8	3.1	0.976	1.572	0.68	0.51	-32.70
139.9	3.1	0.978	1.092	0.67	0.49	-32.00
143.1	3.1	0.923	1.282	0.65	0.48	-33.12
146.2	3.1	0.857	1.361	0.64	0.47	-32.45
149.3	3.1	0.879	1.620	0.64	0.46	-31.89
152.4	3.1	0.926	1.148	0.66	0.51	-46.38
155.6	3.1	0.897	1.183	0.62	0.44	-32.81
158.7	3.1	0.866	1.492	0.61	0.43	-31.74
139.9	40.6	0.956	1.930	0.75	0.75	0.00

The observation of the target 2201+315 from January 22, 2015 all available stations were included besides the Hamburg station (DE609HBA), which was still in the building/testing phase. In Figure 5.6 the image of the frequency centered at 139.9 MHz with a bandwidth of 3.1 MHz is shown. This band corresponds to the central frequency of the observed frequency range between 120–160 MHz. The other 12 frequency bands are shown in Figure C.1 and C.2 in the appendix. The imaging parameters of the images from all frequency bands of this target are shown in Table 5.2.

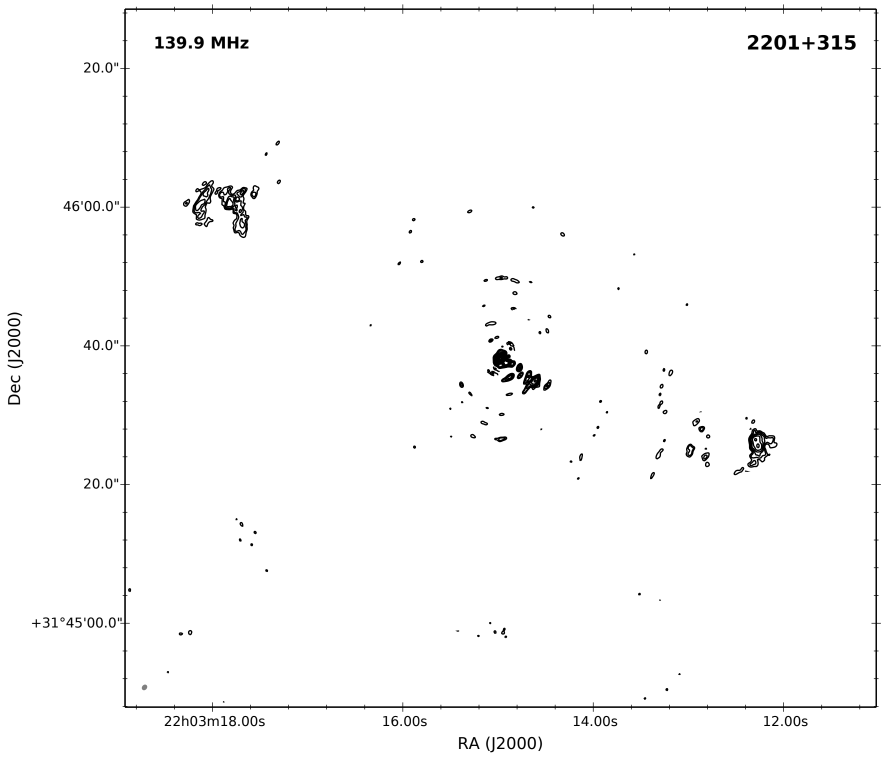

Figure 5.6.: Brightness distribution of 2201+315 of the frequency band centered at 139.9 MHz with a bandwidth of 3.1 MHz. The image parameters are listed in table 5.2. The images of the other 12 frequency bands are shown in Fig. C.1 and C.2. The contours indicate the flux density level and are scaled logarithmically and separated by a factor of $\sqrt{2}$. The lowest contourlevel is set to 3.5 mJy beam^{-1}.

All images of this source show the same morphology. A bright core in the center with a jet in the south-west direction. Further out in the south-west direction is a hot spot with some diffuse extended emission. In the counter-jet direction also a bright hot spot with diffuse extended emission is found. A counter-jet is not detected, which is typical for blazars. The lowest contourlevels show the circular artifacts around the core region, which were mentioned in Section 5.1.

Combining all single frequency bands into one stacked image to average over all frequencies increases the sensitivity by $\sqrt{13}$. The resulting image is shown in Figure 5.7. Since artifacts due to noise and also some of the artificial features from calibration errors are much weaker in the averaged image, this shows very clear the morphology of the source. In this image the two hot spots are clearly to see as well as a one sided jet to the south-west of the core. Additional to the already detected hot spots in the other images, the averaged image shows a halo of more diffuse fainter emission around the hot spots.

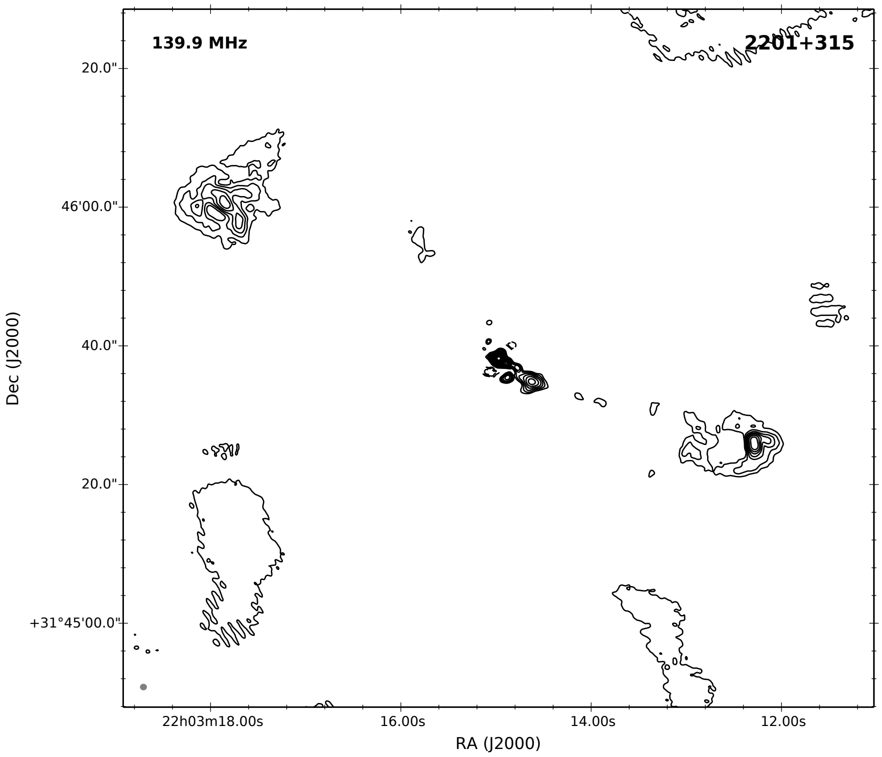

Figure 5.7.: Brightness distribution of 2201+315 using an averaged map over 13 frequency bands with a central frequency of 139.9 MHz, a bandwidth of 40.6 MHz and a common circular beam with diameter of 0.75 arcsec. The averaged map has a peak flux of $S_{peak} = 0.956$ Jy beam^{-1}. The contours indicate the flux density level and are scaled logarithmically and separated by a factor of $\sqrt{2}$. The lowest contourlevel is set to 3.0 mJy beam^{-1}.

The lowest two contourlevels in this image already show larger areas of artifacts. For this features with two or less contourlevels might not be real structure. On the other side the large weaker emission around the lobes seems reasonable. These emission regions can be studied better with the tapered images.

Tapered Images

To have a better view on the diffuse extended emission the tapered images are used. For these tapered images the (u, v)-range is reduced to 200 kλ which means that most of the international stations are ignored in these images. Figure 5.8 shows the frequency band at 139.9 MHz with the use of the taper. The other 12 frequency bands are shown in Figure C.9 and C.10. The imaging parameters of all frequency bands are listed in Table

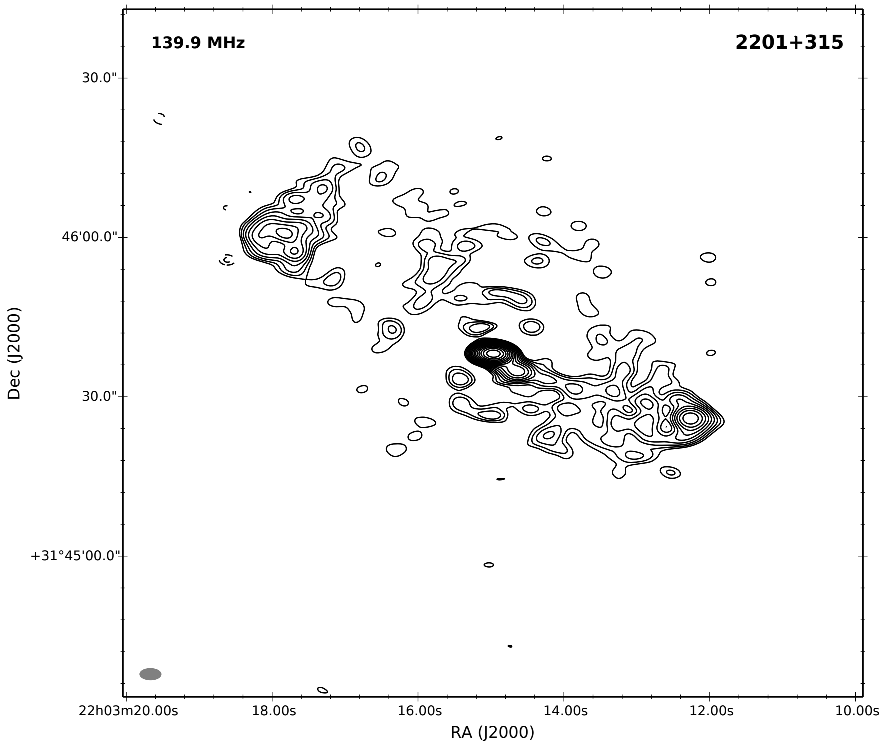

Figure 5.8.: Brightness distribution of 2201+315 of the frequency band centered at 139.9 MHz with a bandwidth of 3.1 MHz using a taper with a (u, v)-range of 200 kλ. The image parameters are listed in table 5.3. The images of the other 12 frequency bands are shown in Fig. C.9 and C.10. The contours indicate the flux density level and are scaled logarithmically and separated by a factor of $\sqrt{2}$. The lowest contourlevel is set to 7.0 mJy beam^{-1}.

5.3. The images show even more diffuse extended emission than detected in the averaged image of the high resolution maps (see Figure 5.7. Again the brightest features are the core and the two hot spots. Also the jet to the south-west is clearly to see in this image as well as additional diffuse emission around the jet axis towards the lobe. Between the core and the lobe in the north-east some extended weak emission regions are found.

Combining and averaging over all frequency bands results in an averaged brightness distribution presented in Figure 5.9. The tapered averaged image shows that between the north-east hot spot and the core is diffuse extended emission as well as a weak halo around the core region. Also around the jet from the core to the south-west hot spot diffuse extended emission is detected. The brightness distribution shows the source surrounded by a halo of diffuse weak emission connecting the core with both lobes. However also the artifacts in the north and south show that the emission with up to two contourlevels might be artificial.

Table 5.3.: Parameters of the final brightness distribution maps of 2201+315 imaged with natural weighting and a taper of 200 kλ. The images are shown in Fig. C.9 and the following.

Frequency (MHz)	Bandwidth (MHz)	S_{peak} (Jy beam^{-1})	S_{RMS} (mJy beam^{-1})	beam$_{maj}$ (arcsec)	beam$_{min}$ (arcsec)	beam$_{p.a.}$ (°)
121.2	3.1	1.210	3.990	2.72	1.87	83.95
124.3	3.1	1.048	3.192	3.02	1.99	86.07
127.4	3.1	1.101	3.445	3.16	2.02	86.84
130.6	3.1	1.077	2.496	3.24	2.01	87.63
133.7	3.1	1.103	3.170	3.38	2.02	88.42
136.8	3.1	1.124	3.406	3.51	2.05	88.93
139.9	3.1	1.135	2.429	3.63	2.05	89.43
143.1	3.1	1.141	2.801	3.72	2.06	89.95
146.2	3.1	1.132	2.916	3.82	2.07	-89.67
149.3	3.1	1.144	3.487	3.94	2.08	-89.39
152.4	3.1	1.135	2.253	4.02	2.10	-89.31
155.6	3.1	1.152	2.408	4.17	2.11	-89.00
158.7	3.1	1.107	3.287	4.21	2.11	-88.48
139.9	40.6	1.163	6.535	4.50	4.50	0.00

Flux densities & luminosities

To study the flux density distribution across all bands and to obtain the luminosities of extended emission, the total flux densities of the final models of each image are used. To obtain the flux density of the core regions a circular Gaussian model component is fitted to the high resolution images. The resulting flux densities and extended radio luminosities calculated with equation 2.4.4 are listed in Table 5.4. The flux density for the extended emission was calculated by subtracting the core from the total flux density. Following to the other flux densities in Table 5.4 a powerlaw was fitted to the flux density of the extended emission to obtain a spectral index. This spectral index is used in equation 2.4.4 for the luminosity together with the redshift and luminosity distance, listed in Table 5.14.

Comparing the flux densities of tapered and high resolution images the tapered images usually show a slightly higher flux density. However this is only 50–100 mJy more in each frequency band, which is still in the uncertainty range. To obtain an estimate on the uncertainty the deviations of the spectral index fit are calculated. For this observation the deviations are below 10% for all bands. Since the spectral index fit may not be perfect a relative error of 10% was used for this observation. Looking at the spectral indices in Table tab-flux-2201 the core region shows a flat spectral index while the total flux densities are optically thin.

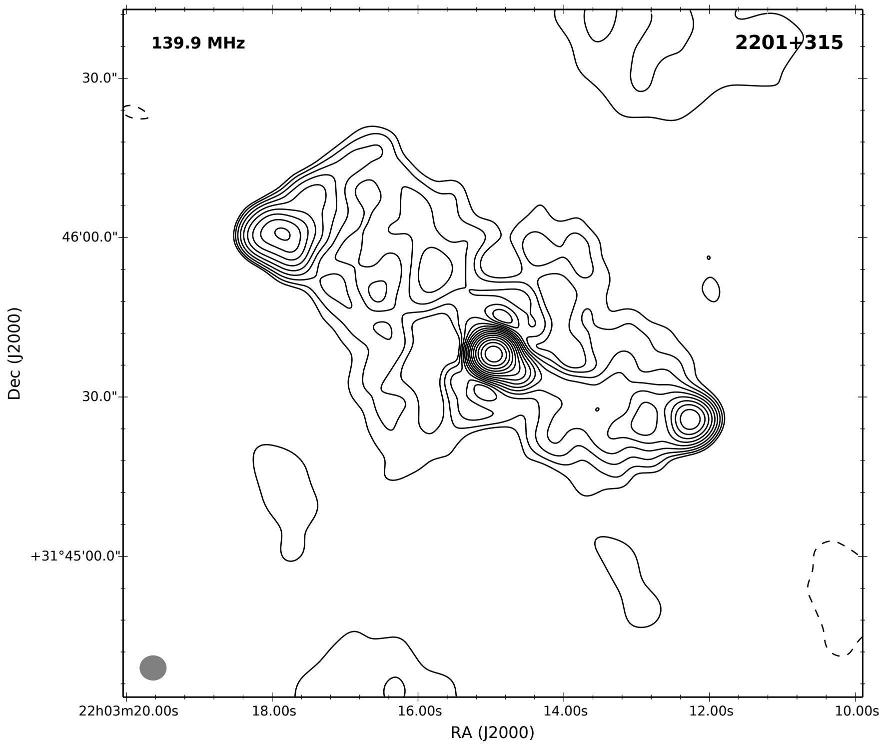

Figure 5.9.: Brightness distribution of 2201+315 using an averaged map over 13 frequency bands obtained using a taper of 200 kλ with a central frequency of 139.9 MHz, a bandwidth of 40.6 MHz and a common circular beam with diameter of 4.50 arcsec. The averaged map has a peak flux of $S_{peak} = 1.163$ Jy beam^{-1}. The contours indicate the flux density level and are scaled logarithmically and separated by a factor of $\sqrt{2}$. The lowest contourlevel is set to 10.0 mJy beam^{-1}.

In Figure 5.10 the flux densities are plotted with errorbars corresponding to a relative error of 10%. The plots show that the absolute flux calibration of these datasets has performed very well since the differences between the adjacent frequency bands are very small like expected. Overall all regions in all frequency bands follow the trend fitting to their expected spectral indices.

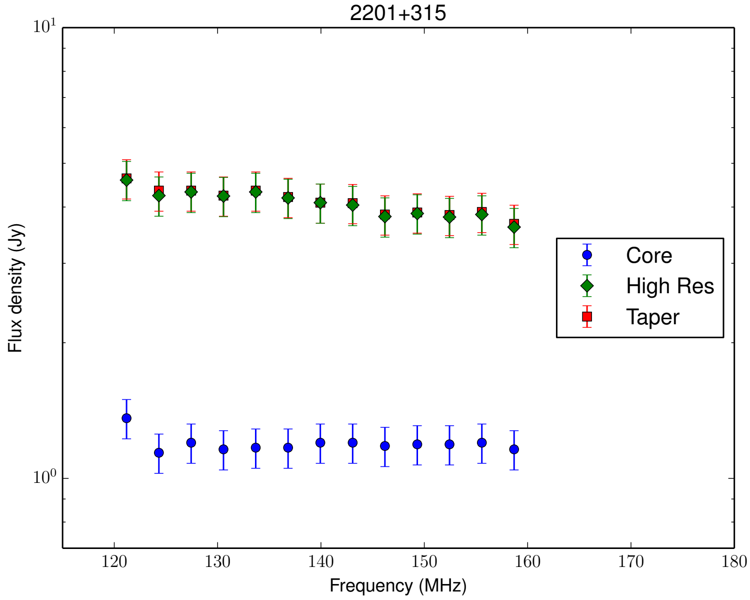

Figure 5.10.: Plot of all flux densities of 2201+315 given in Table 5.4 with an estimated uncertainty of 10%.

Table 5.4.: Flux densities of 2201+315 of the core by fitting a circular Gaussian model component to this region, the total flux density of the model for the high resolution images (HR) and the total flux density of the tapered images. By subtracting the core from the total flux density the extended emission was calculated, which was used with the spectral index of the extended flux density to calculate the luminosity of the extended emission.

Frequency (MHz)	Core S_{Core} (Jy)	$Total_{HR}$ S_{HR} (Jy)	$Total_{Taper}$ S_{Taper} (Jy)	Ext. luminosity L_{HR} (10^{26} W Hz^{-1})	Ext. luminosity L_{Taper} (10^{26} W Hz^{-1})
121.19	1.355	4.594	4.629	8.71	8.74
124.32	1.144	4.243	4.353	8.33	8.42
127.44	1.200	4.319	4.353	8.39	8.42
130.57	1.155	4.226	4.242	8.26	8.24
133.69	1.165	4.322	4.351	8.49	8.51
136.82	1.169	4.192	4.210	8.13	8.12
139.94	1.199	4.091	4.090	7.78	7.72
143.07	1.195	4.043	4.082	7.66	7.71
146.19	1.180	3.813	3.851	7.08	7.13
149.32	1.191	3.873	3.888	7.21	7.20
152.44	1.191	3.800	3.837	7.01	7.06
155.57	1.203	3.846	3.895	7.11	7.19
158.69	1.162	3.611	3.668	6.58	6.69
α	-0.15	-0.73	-0.73		

5.2.2. Observation of 1807+698 (common name: 3C 371)

High resolution images

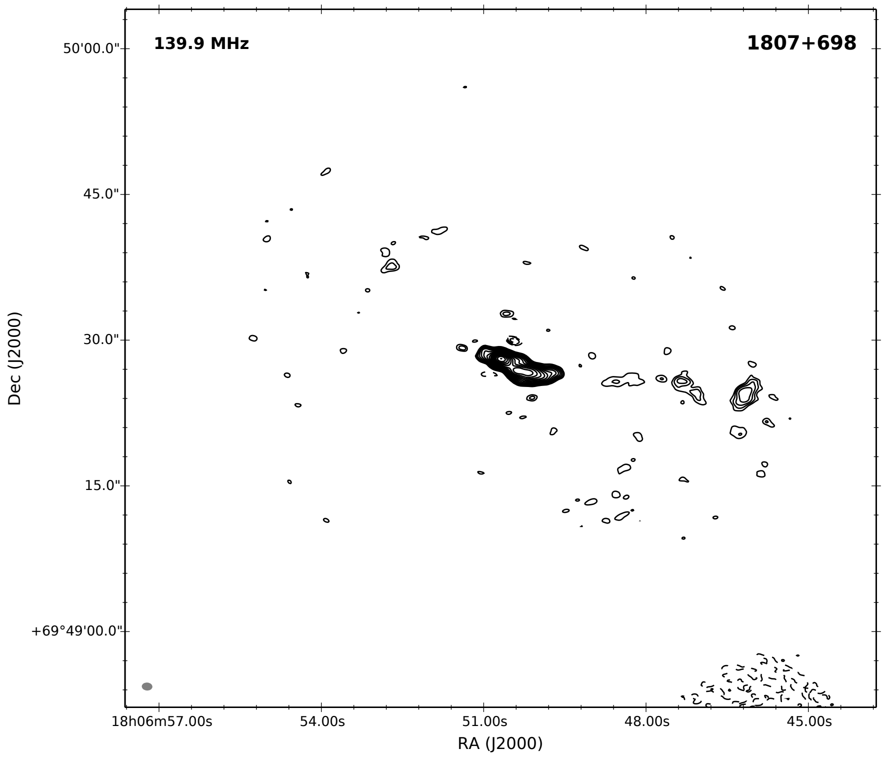

Figure 5.11.: Brightness distribution of 1807+698 of the frequency band centered at 139.9 MHz with a bandwidth of 3.1 MHz. The image parameters are listed in table 5.5. The images of the other 12 frequency bands are shown in Fig. C.3 and C.4. The contours indicate the flux density level and are scaled logarithmically and separated by a factor of $\sqrt{2}$. The lowest contourlevel is set to 3.0 mJy beam^{-1}.

The target 1807+698 was observed December 16, 2014. In this observation the station UK608HBA failed to produce any data and the station DE604HBA (Potsdam) was not in use due to not working air conditioner at the station cabin with the processing boards. As for the observation of 2201+315 the station DE609HBA (Hamburg) was still in the building phase and could not participate in this observation.

In Figure 5.11 the image of the frequency band at 139.9 MHz with 3.1 MHz bandwidth is shown as example. The other 12 frequency band images are shown in Figure C.3 and C.4. The parameters of all images are listed in Table 5.5. In all images of this source the brightest feature is the core. From the core a jet is pointing into west south-west direction. In the west direction a cloud of diffuse extended emission is found. This

Table 5.5.: Parameters of the final brightness distribution maps of 1807+698 imaged with natural weighting. The images are shown in Fig. C.3 and the following.
In the last line the parameters of the averaged data set are given. For this data set the frequency bands of 121.2 and 124.3 were not used due to calibration issues.

Frequency (MHz)	Bandwidth (MHz)	S_{peak} (Jy beam^{-1})	S_{RMS} (mJy beam^{-1})	$beam_{maj}$ (arcsec)	$beam_{min}$ (arcsec)	$beam_{p.a.}$ (°)
121.2	3.1	0.318	1.525	0.91	0.64	84.76
124.3	3.1	0.279	1.592	0.83	0.55	86.60
127.4	3.1	0.435	1.662	0.90	0.65	82.88
130.6	3.1	0.432	1.782	0.92	0.67	80.47
133.7	3.1	0.472	1.714	0.90	0.67	83.69
136.8	3.1	0.472	1.827	0.86	0.66	86.33
139.9	3.1	0.522	1.559	0.89	0.68	85.05
143.1	3.1	0.533	1.344	0.89	0.76	68.51
146.2	3.1	0.574	1.591	0.92	0.73	83.21
149.3	3.1	0.581	2.254	0.90	0.67	89.15
152.4	3.1	0.662	1.911	1.00	0.76	87.46
155.6	3.1	0.625	1.418	1.00	0.73	-86.13
158.7	3.1	0.651	1.752	1.04	0.72	-84.39
139.9	40.6	0.573	1.427	1.15	1.15	0.00

cloud could also be a weak hot spot. Around the target some faint spots with only one contourlevel are found. In the south-western corner some artifacts with negative flux densities (dashed lines) are found. The weak features around the source are not very trustworthy even if some diffuse extended emission is expected to be in those areas.
Combining the 13 frequency bands an averaged map is made, which is shown in Figure 5.12. The averaged brightness distribution shows again the core as the brightest feature with a very bright jet in west direction. Further out a feature shows a hot spot with diffuse extended emission around it. In the counter-jet direction a weak cloud-like feature of diffuse extended emission can be found. Considering the artifacts at the borders of the images the weak cloud in the counterjet-direction might even be due to artifacts. For a better view on these weak diffuse emission regions the tapered images can be studied.

Tapered images

To obtain a view on the diffuse extended emission the tapered images (taper with a (u, v)-range of 200 kλ) are used. The tapered brightness distribution for the frequency band of 139.9 MHz with 3.1 MHz bandwidth is shown in Figure 5.13. The images of the other 12 frequency bands are shown in Figure C.11 and C.12. The parameters of the corresponding images are listed in Table 5.6.
Similar to the structures seen in the higher resolution images a hot spot can be found in

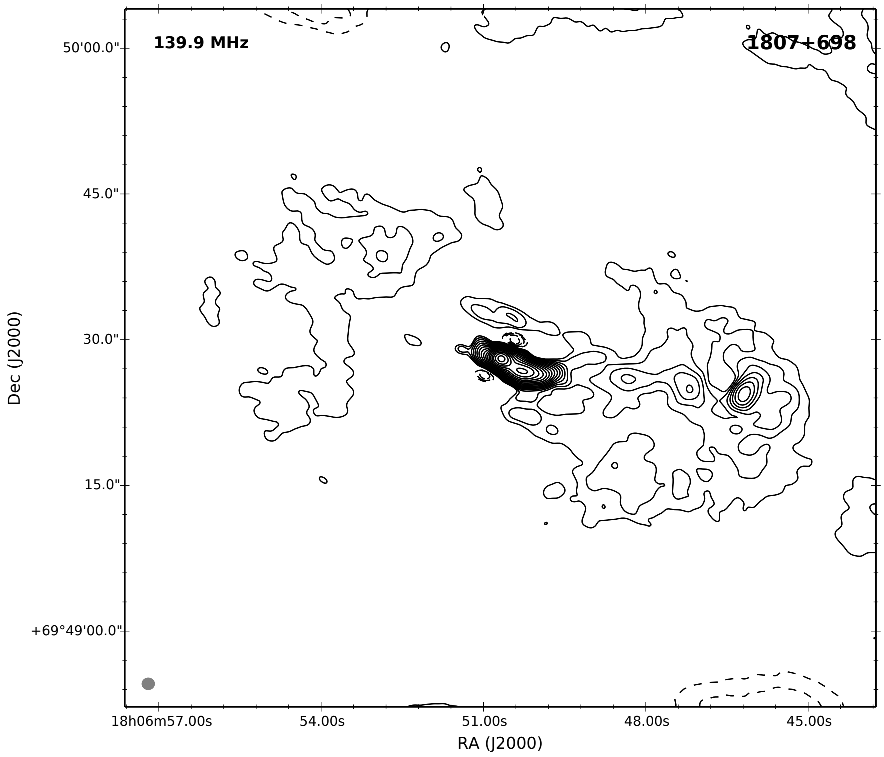

Figure 5.12.: Brightness distribution of 1807+698 using an averaged map over 13 frequency bands with a central frequency of 139.9 MHz, a bandwidth of 40.6 MHz and a common circular beam with diameter of 1.15 arcsec. The averaged map has a peak flux of $S_{\mathrm{peak}} = 0.573$ Jy beam^{-1}. The contours indicate the flux density level and are scaled logarithmically and separated by a factor of $\sqrt{2}$. The lowest contourlevel is set to 2.0 mJy beam^{-1}.

the west. Similar to the averaged image it is surrounded by diffuse extended emission. The bright core and the close bright jet features are merged into one feature at the lower resolution images. In the north-east where a small weak feature already indicated some emission in the averaged image in Figure 5.12, more diffuse emission is detected with two contourlevels while the artifacts in the image have only the lowest contourlevel. This feature could originate from the counterjet lobe.
In the combined average map of the 13 tapered images shown in Figure 5.14 the features are also detected. The weak fainter emission in the north-east direction and the hotspot with extended emission around it in the west. However the counterjet lobe is still mostly with three contourlevels only one level above the artifacts seen at the border of the image.

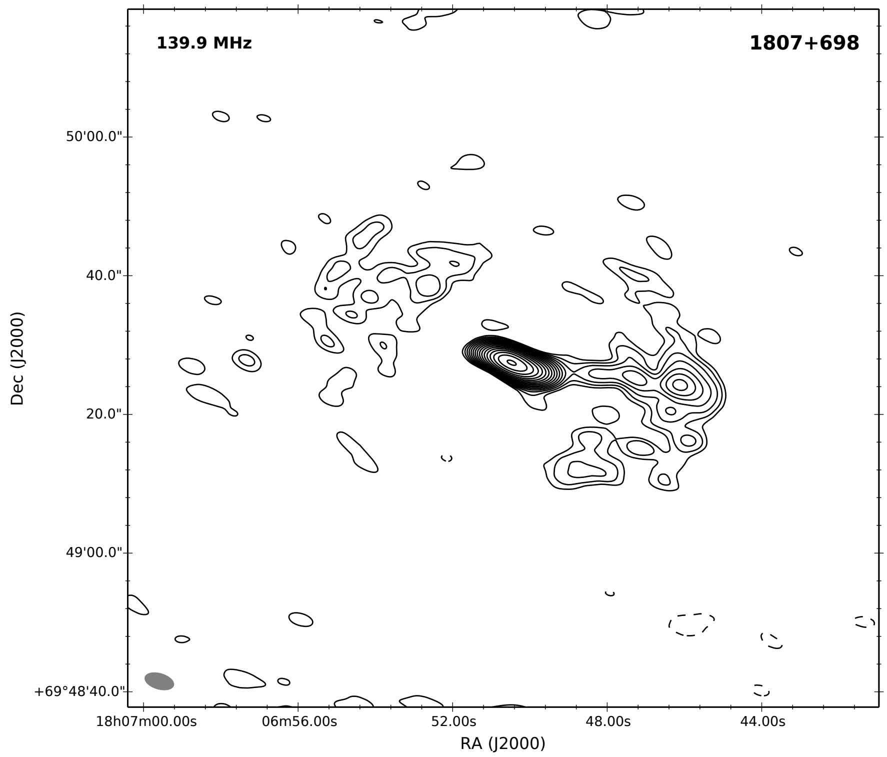

Figure 5.13.: Brightness distribution of 1807+698 of the frequency band centered at 139.9 MHz with a bandwidth of 3.1 MHz using a taper with a (u, v)-range of 200 kλ. The image parameters are listed in table 5.6. The images of the other 12 frequency bands are shown in Fig. C.11 and C.12. The contours indicate the flux density level and are scaled logarithmically and separated by a factor of $\sqrt{2}$. The lowest contourlevel is set to 6.0 mJy beam^{-1}.

Flux densities & luminosities

The total flux densities of the tapered and high resolution images are listed in Table 5.7 as well as the flux density for the core fitted with a circular Gaussian model component. In the last lines the spectral indices are calculated.

The extended flux density for the luminosity calculation was obtained by subtracting the core from the total flux density. The extended luminosities are also listed in table 5.7 calculated with the redshift, luminosity distance and the spectral index of the extended flux density from Table 5.14.

The flux densities are plotted in Figure 5.15. The evolution over the frequency bands shows that the flux densities increase with increasing frequency. For the error estimation the deviations from the spectral index fits are used. Most frequency bands deviate less than 10% but some are slightly higher. To account for the higher deviations the flux

Table 5.6.: Parameters of the final brightness distribution maps of 1807+698 imaged with natural weighting and a taper of 200 kλ. The images are shown in Fig. C.11 and the following.

Frequency (MHz)	Bandwidth (MHz)	S_{peak} (Jy beam^{-1})	S_{RMS} (mJy beam^{-1})	beam$_{maj}$ (arcsec)	beam$_{min}$ (arcsec)	beam$_{p.a.}$ (°)
121.2	3.1	0.720	2.817	3.35	2.25	64.19
124.3	3.1	0.730	3.299	3.07	1.95	67.83
127.4	3.1	0.924	3.031	3.53	2.17	69.18
130.6	3.1	0.899	3.159	3.66	2.14	70.34
133.7	3.1	1.001	3.047	3.73	2.15	70.93
136.8	3.1	1.019	3.330	3.75	2.14	71.55
139.9	3.1	1.080	2.780	3.93	2.16	71.65
143.1	3.1	1.087	2.301	4.01	2.17	72.37
146.2	3.1	1.159	2.711	4.21	2.16	73.04
149.3	3.1	1.189	3.978	4.32	2.18	73.88
152.4	3.1	1.283	3.202	4.51	2.20	74.53
155.6	3.1	1.280	2.389	4.50	2.20	74.33
158.7	3.1	1.309	2.979	4.68	2.23	75.30
139.9	40.6	1.230	3.304	5.00	5.00	0.00

uncertainty is estimated with 15%. Comparing the total flux densities of high-resolution and tapered images only very low deviations are found. However the spectral indices and the slight deviations show that the calibration is probably still not perfect for all bands. The inverted spectral indices for this observation indicate that the lowest frequencies are already selfabsorbed, which means that the synchrotron peak of 1807+698 should be between 160 MHz and 1.4 GHz. This indication can be seen in the plots of the flux densities as well (see Figure 5.15).

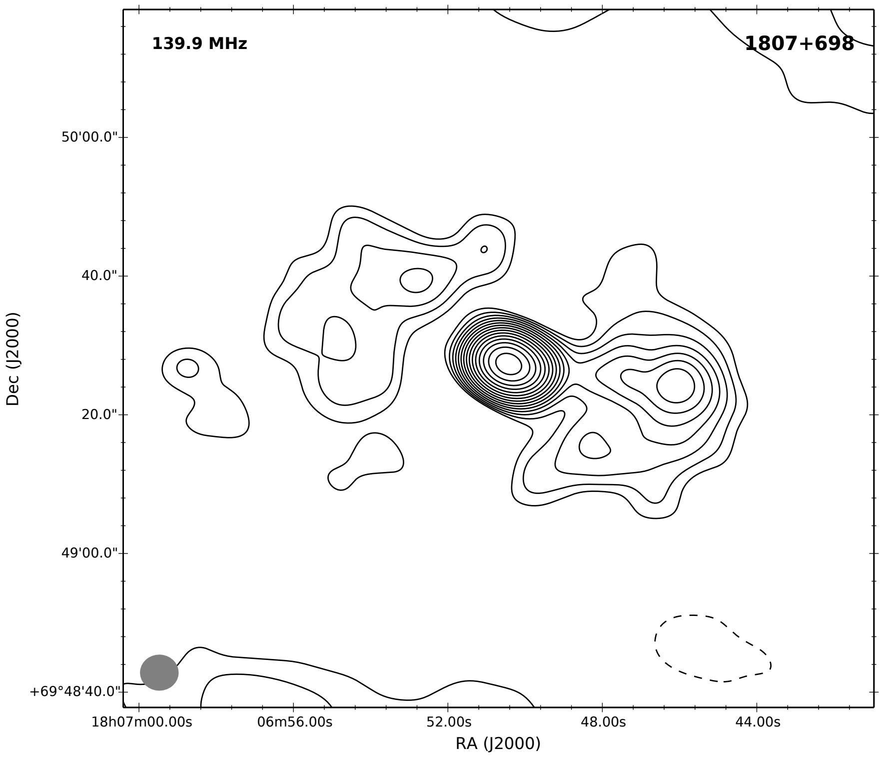

Figure 5.14.: Brightness distribution of 1807+698 using an averaged map over 13 frequency bands obtained using a taper of 200 kλ with a central frequency of 139.9 MHz, a bandwidth of 40.6 MHz and a common circular beam with diameter of 5.00 arcsec. The averaged map has a peak flux of $S_{\mathrm{peak}} = 1.230$ Jy beam^{-1}. The contours indicate the flux density level and are scaled logarithmically and separated by a factor of $\sqrt{2}$. The lowest contourlevel is set to 8.0 mJy beam^{-1}.

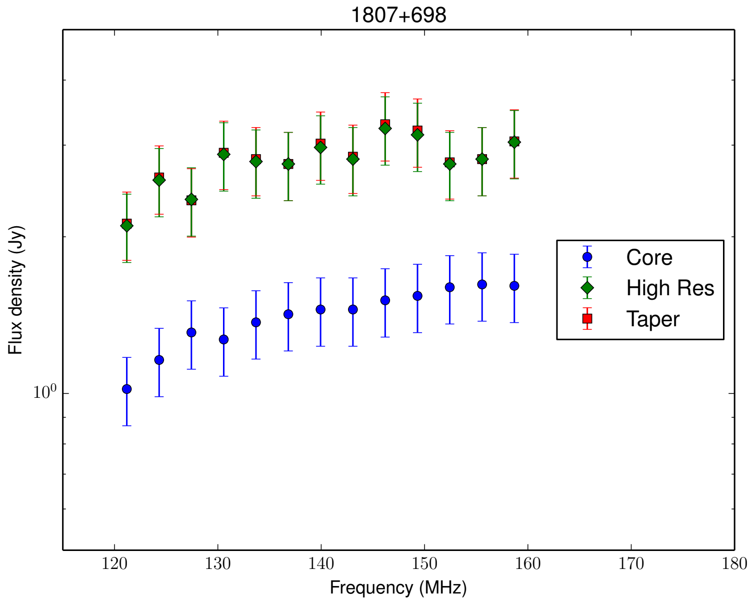

Figure 5.15.: Plot of all flux densities of 1807+698 given in Table 5.7 with an estimated uncertainty of 15%.

Table 5.7.: Flux densities of 1807+698 of the core by fitting a circular Gaussian model component to this region, the total flux density of the model for the high resolution images (HR) and the total flux density of the tapered images. By subtracting the core from the total flux density the extended emission was calculated, which was used with the spectral index of the extended flux density to calculate the luminosity of the extended emission.

Frequency (MHz)	Core S_{Core} (Jy)	$\mathrm{Total}_{\mathrm{HR}}$ S_{HR} (Jy)	$\mathrm{Total}_{\mathrm{Taper}}$ S_{Taper} (Jy)	Ext. luminosity L_{HR} (10^{24} W Hz^{-1})	Ext. luminosity L_{Taper} (10^{24} W Hz^{-1})
121.19	1.016	2.104	2.122	6.03	6.12
124.32	1.157	2.571	2.600	7.83	7.99
127.44	1.305	2.355	2.351	5.82	5.79
130.57	1.265	2.882	2.897	8.96	9.04
133.69	1.367	2.793	2.816	7.90	8.03
136.82	1.415	2.760	2.763	7.45	7.47
139.94	1.448	2.974	3.018	8.46	8.69
143.07	1.454	2.819	2.846	7.57	7.71
146.19	1.512	3.233	3.291	9.54	9.85
149.32	1.536	3.141	3.198	8.90	9.21
152.44	1.600	2.764	2.776	6.45	6.52
155.57	1.618	2.817	2.824	6.65	6.68
158.69	1.607	3.042	3.049	7.95	7.99
α	1.50	0.97	0.98		

5.2.3. Observation of 1222+216 (common name: 4C +21.35)

High resolution images

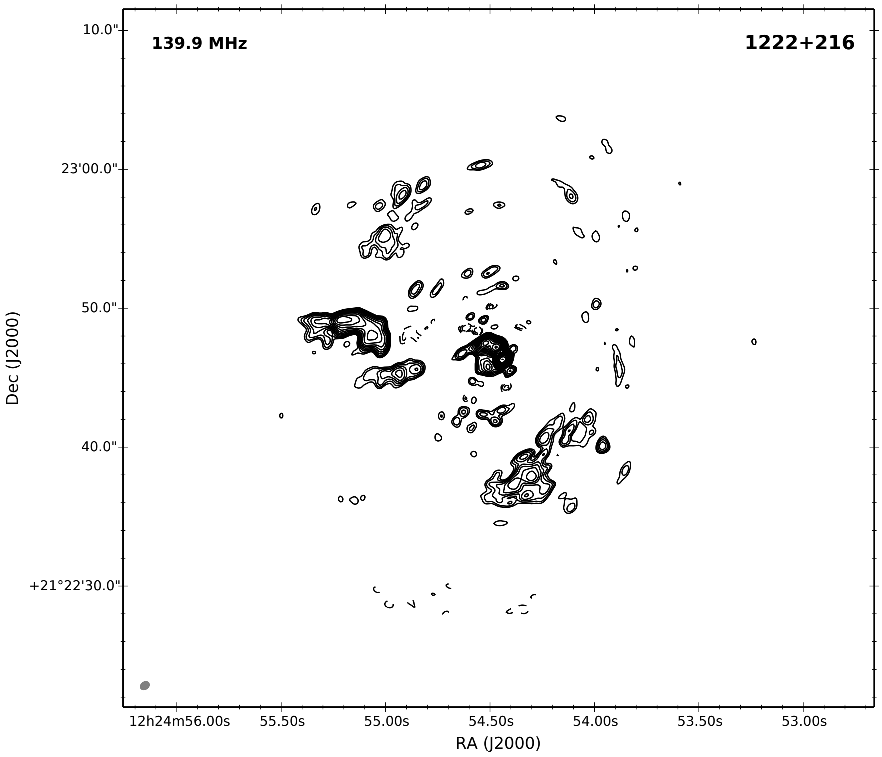

Figure 5.16.: Brightness distribution of 1222+216 of the frequency band centered at 139.9 MHz with a bandwidth of 3.1 MHz. The image parameters are listed in table 5.8. The images of the other 12 frequency bands are shown in Fig. C.5 and C.6. The contours indicate the flux density level and are scaled logarithmically and separated by a factor of $\sqrt{2}$. The lowest contourlevel is set to 6.0 mJy beam^{-1}.

The observation of 1222+216 was performed on March 12, 2015. In this observation the new built station DE609HBA participated but the stations DE604HBA and DE605HBA are were not included in the observation due to network problems.
Figure 5.16 shows the resulting image of the selfcalibration process for the frequency band of 139.9 MHz with 3.1 MHz bandwidth. The other 12 frequency bands are found in Figure C.5 and C.6. The parameters of each frequency band are listed in Table 5.8. By looking at all frequency bands the first two bands show a phase shift. In those two bands the complete image is shifted about 2 arcsec towards south south-west. For the averaged image these two bands were skipped.
The images of this observation show some circular features around the core, however, from

Table 5.8.: Parameters of the final brightness distribution maps of 1222+216 imaged with natural weighting. The images are shown in Fig. C.5 and the following.
In the last line the parameters of the averaged data set are given. For this data set the frequency bands of 121.2 and 124.3 were not used due to phase shifts.

Frequency (MHz)	Bandwidth (MHz)	S_{peak} (Jy beam^{-1})	S_{RMS} (mJy beam^{-1})	$beam_{maj}$ (arcsec)	$beam_{min}$ (arcsec)	$beam_{p.a.}$ (°)
121.2	3.1	1.065	2.663	0.72	0.63	-39.40
124.3	3.1	1.140	4.196	0.70	0.60	-37.17
127.4	3.1	1.152	3.337	0.69	0.58	-36.66
130.6	3.1	1.087	2.520	0.67	0.55	-38.07
133.7	3.1	1.106	2.755	0.66	0.53	-39.76
136.8	3.1	1.087	2.509	0.65	0.51	-42.10
139.9	3.1	1.053	1.967	0.64	0.50	-46.68
143.1	3.1	1.055	2.314	0.63	0.48	-41.45
146.2	3.1	1.018	2.407	0.61	0.45	-37.23
149.3	3.1	1.122	2.110	0.63	0.46	-37.74
152.4	3.1	0.775	1.715	0.61	0.44	-57.10
155.6	3.1	0.997	1.516	0.60	0.43	-38.67
158.7	3.1	0.979	2.257	0.56	0.43	-39.05
143.1	34.4	1.048	2.020	0.80	0.80	0.00

other observations it is expected detecting a faint extended emission covering this source in a halo - corresponding to the regions where these weaker circular features are found. But since the other observations show similar features coming from calibration problems this might be the case in this observation as well. Besides the extended emission the brightness distribution shows a strong emitting core with a jet consisting of two features starting in north direction bending to the east. In the east a hot spot is found with some weaker features around it. South-west from this hot spot some other features are detected. Combining these features with the jet from the core, they indicate a S-shaped jet from the core to the eastern hot spot. A second hot spot is found in the south of the core with a halo of extended emission surrounding it. Additional to the two hot spots a cloud of extended emission shows up north of the eastern hot spot.
The averaged map over 11 frequency bands is presented in Figure 5.17. In this image the core is the brightest feature again. Also the eastern hot spot is very bright and the jet from the core still suggests the S-shape starting towards the north, bending to the south-east with another bend to the north-east ending in the hot spot. Also the hot spot in the south of the core is more prominent with some extended emission around it. The extended emission cloud north of the eastern hot spot is detected. In the north and west of the core several weaker diffuse emission features are found mostly with only one or two contourlevels which makes their emission similar to the artifacts. Even in the averaged image an artifact with negative flux density is found in the south with two

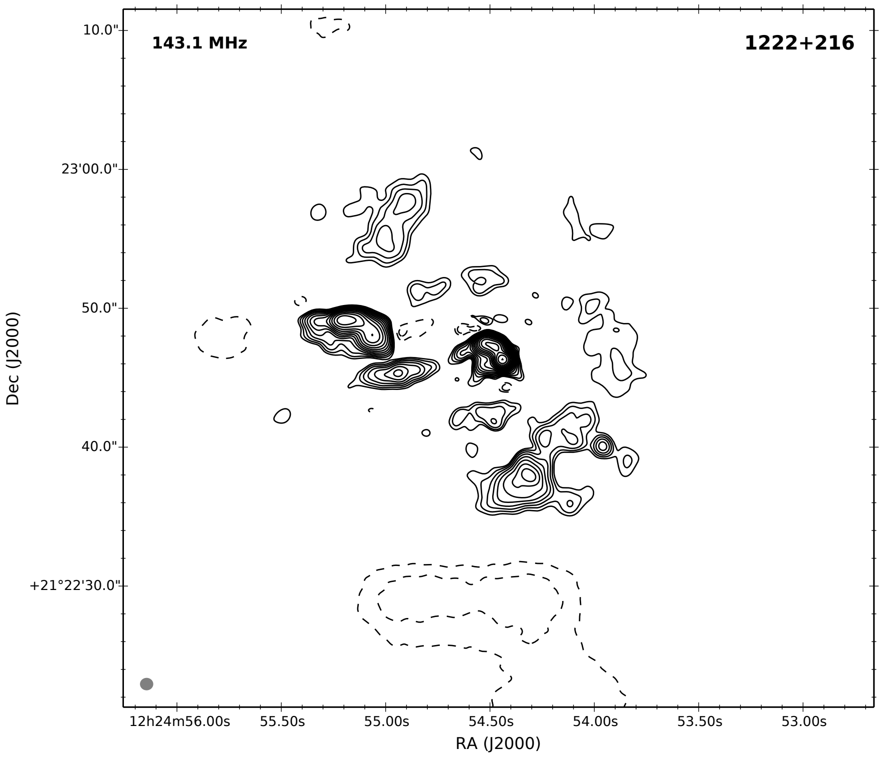

Figure 5.17.: Brightness distribution of 1222+216 using an averaged map over 11 frequency bands (ignoring the first two due to phaseshifts) with a central frequency of 143.1 MHz, a bandwidth of 34.4 MHz and a common circular beam with diameter of 0.80 arcsec. The averaged map has a peak flux of $S_{peak} = 1.048$ Jy beam^{-1}. The contours indicate the flux density level and are scaled logarithmically and separated by a factor of $\sqrt{2}$. The lowest contourlevel is set to 6.0 mJy beam^{-1}.

negative contourlevels (dashed lines).

Tapered images

As example for a tapered image of 1222+216 the frequency band of 139.9 MHz with 3.1 MHz bandwidth is shown in Figure 5.18. The other 12 frequency bands are shown in Figure C.13 and C.14. The parameters for all images are listed in Table 5.9. In the tapered images the resolution is to low to resolve the jet and its features. The bright core and the two bright hot spots are easily spotted and the extended emission around the whole structure looks very similar to the expectations from previous images. The cloud north of the eastern hot spot is more prominent than the remaining diffuse extended

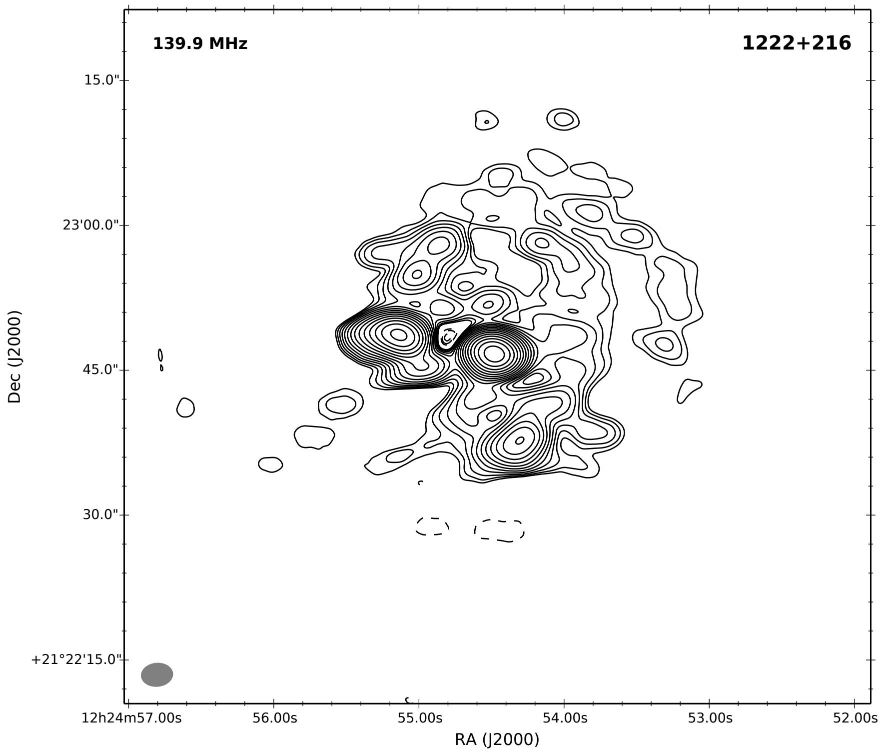

Figure 5.18.: Brightness distribution of 1222+216 of the frequency band centered at 139.9 MHz with a bandwidth of 3.1 MHz using a taper with a (u, v)-range of 200 kλ. The image parameters are listed in table 5.9. The images of the other 12 frequency bands are shown in Fig. C.13 and C.14. The contours indicate the flux density level and are scaled logarithmically and separated by a factor of $\sqrt{2}$. The lowest contourlevel is set to 12.0 mJy beam^{-1}.

emission. Compared to the high resolution maps the diffuse extended emission in the north, east and north-east is detected more clear in those images.

In the tapered average map shown in Figure 5.19 the resolution is slightly lower and again three very bright features are prominent: the core and the two hot spots. Also the cloud northern of the eastern hot spot is brighter than the rest of the extended emission covering the source in a halo-like structure. Towards south-east direction a weak feature is found looking like an outflow. Together with the islands of negative emission in the south with a similar amount of contourlevels this structure is most likely something artificial coming from calibration problems.

Table 5.9.: Parameters of the final brightness distribution maps of 1222+216 imaged with natural weighting and a taper of 200 kλ. The images are shown in Fig. C.13 and the following.

Frequency (MHz)	Bandwidth (MHz)	S_{peak} (Jy beam^{-1})	S_{RMS} (mJy beam^{-1})	$beam_{maj}$ (arcsec)	$beam_{min}$ (arcsec)	$beam_{p.a.}$ (°)
121.2	3.1	2.000	5.247	2.76	2.23	84.42
124.3	3.1	1.881	8.337	2.85	2.25	83.85
127.4	3.1	1.836	6.727	2.74	2.32	-88.79
130.6	3.1	1.843	5.392	2.74	2.31	-85.60
133.7	3.1	1.843	5.928	2.82	2.34	-83.35
136.8	3.1	1.835	5.404	2.89	2.34	-82.90
139.9	3.1	1.858	4.168	2.98	2.35	-83.23
143.1	3.1	1.851	4.950	3.13	2.41	-83.01
146.2	3.1	1.815	5.406	3.20	2.45	-83.50
149.3	3.1	1.774	4.397	3.42	2.55	-82.16
152.4	3.1	1.681	4.061	3.21	2.31	-84.48
155.6	3.1	1.730	3.145	3.85	2.60	-85.22
158.7	3.1	1.772	5.070	3.67	2.52	-84.17
143.1	34.4	2.069	4.311	4.00	4.00	0.00

Flux densities & luminosities

The core and the total flux densities are listed in Table 5.10. Calculating the flux density of the extended emission by subtracting the core from the total flux density can be used to calculate the extended radio luminosity with equation 2.4.4. The spectral index is fitted to the extended flux density, the luminosity distance and the redshift are given in Table 5.14.
Comparing the total flux densities of the high resolution and tapered images only very low differences are found. In the plots in Figure 5.20 it is shown that the flux densities for the complete source decrease with increasing frequency, while the core stays on a similar level with a slight increase. With the spectral index the deviations of the frequency bands can be determined. Using these deviations the relative error of the flux densities are estimated with 10%.
The spectral index for the core is flat as it is typical for beamed regions, while the total flux densities show optical thin spectra.

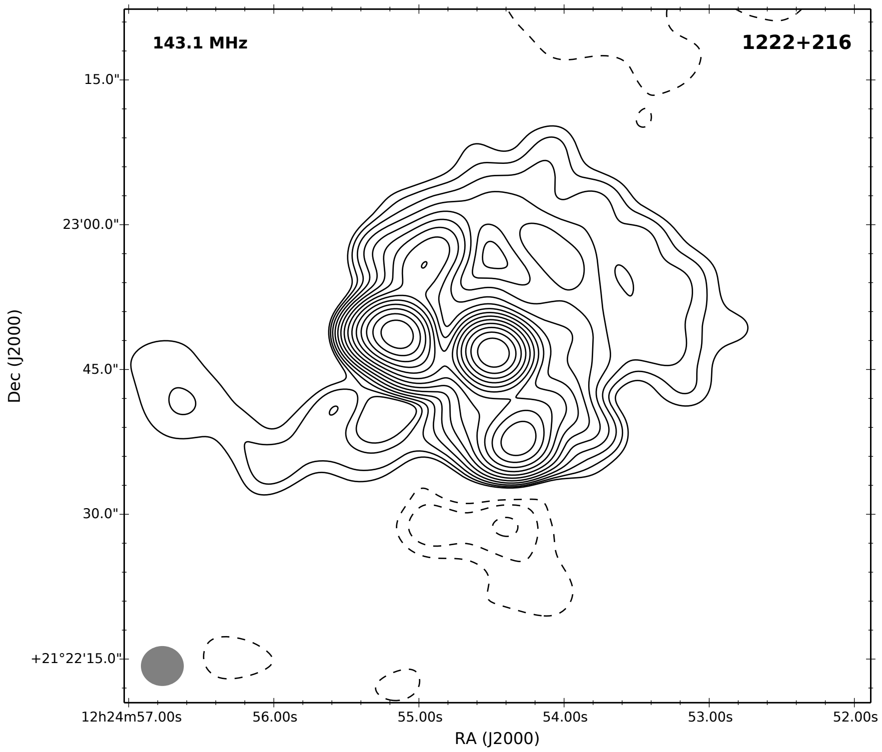

Figure 5.19.: Brightness distribution of 1222+216 using an averaged map over 11 frequency bands obtained using a taper of 200 kλ (ignoring the first two due to phaseshifts) with a central frequency of 143.1 MHz, a bandwidth of 34.4 MHz and a common circular beam with diameter of 4.00 arcsec. The averaged map has a peak flux of S_{peak} = 2.069 Jy beam^{-1}. The contours indicate the flux density level and are scaled logarithmically and separated by a factor of $\sqrt{2}$. The lowest contourlevel is set to 12.0 mJy beam^{-1}.

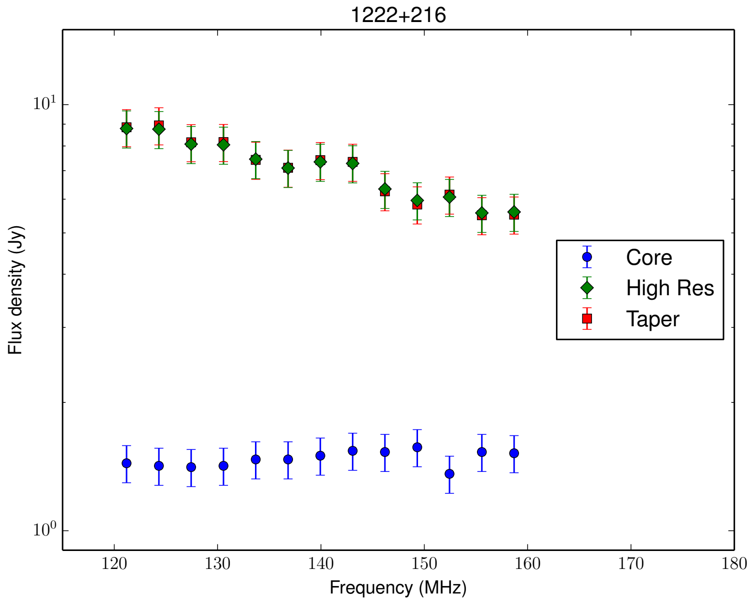

Figure 5.20.: Plot of the flux densities of 1222+216 given in table 5.10 with an estimated uncertainty of 10%.

Table 5.10.: Flux densities of 1222+216 of the core by fitting a circular Gaussian model component to this region, the total flux density of the model for the high resolution images (HR) and the total flux density of the tapered images. By subtracting the core from the total flux density the extended emission was calculated, which was used with the spectral index of the extended flux density to calculate the luminosity of the extended emission.

Frequency (MHz)	Core S_{Core} (Jy)	$Total_{HR}$ S_{HR} (Jy)	$Total_{Taper}$ S_{Taper} (Jy)	Ext. luminosity L_{HR} (10^{27} W Hz^{-1})	Ext. luminosity L_{Taper} (10^{27} W Hz^{-1})
121.19	1.439	8.788	8.854	8.07	8.52
124.32	1.421	8.760	8.937	8.06	8.63
127.44	1.410	8.081	8.162	7.33	7.76
130.57	1.418	8.052	8.165	7.29	7.75
133.69	1.465	7.447	7.421	6.57	6.84
136.82	1.468	7.105	7.114	6.19	6.48
139.94	1.502	7.341	7.411	6.41	6.79
143.07	1.537	7.278	7.339	6.30	6.66
146.19	1.528	6.344	6.262	5.29	5.44
149.32	1.570	5.959	5.831	4.82	4.89
152.44	1.357	6.066	6.150	5.17	5.50
155.57	1.534	5.572	5.505	4.43	4.56
158.69	1.518	5.601	5.520	4.48	4.50
α	0.25	-1.79	-1.88		

5.2.4. Observation of 0716+714 (common name: S5 0716+71)

High resolution images

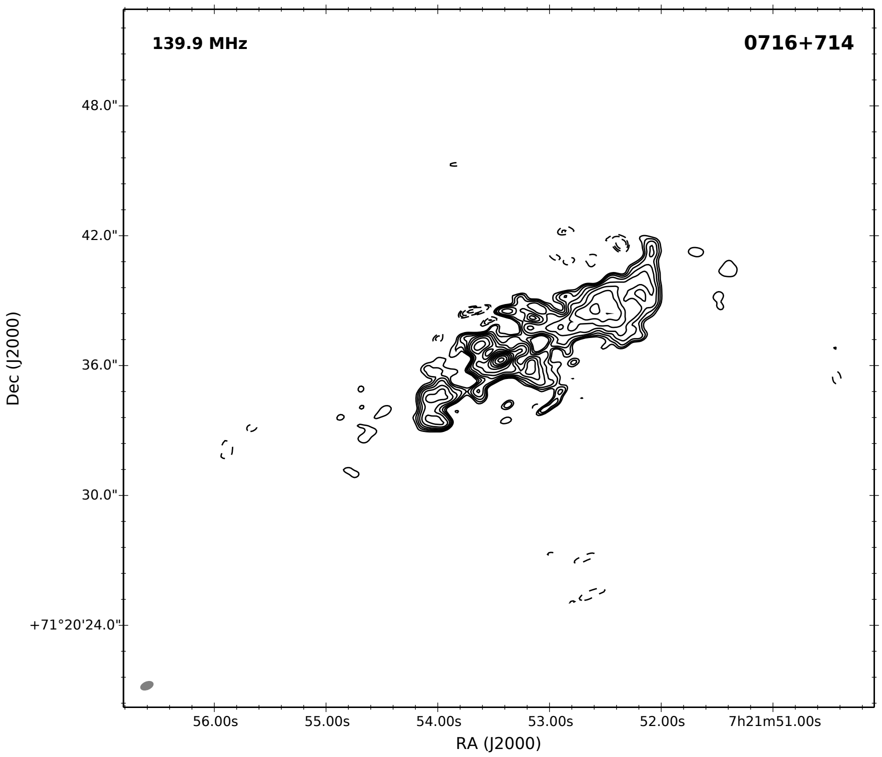

Figure 5.21.: Brightness distribution of 0716+714 of the frequency band centered at 139.9 MHz with a bandwidth of 3.1 MHz. The image parameters are listed in table 5.11. The images of the other 12 frequency bands are shown in Fig. C.7 and C.8. The contours indicate the flux density level and are scaled logarithmically and separated by a factor of $\sqrt{2}$. The lowest contourlevel is set to 4.0 mJy beam^{-1}.

The fourth target 0716+714 was observed on December 17, 2014 where DE604HBA suffered of broken air conditioning for the processing boards and could not participate in the observation. DE609HBA was not built and included in the array and the UK608HBA station lost the connection and produced no data. Additionally the complete observation was disturbed by some effects of unknown origin. For this reason 3 of 14 remote stations had to be flagged completely. The problems of the observation already affect the calibration of the Dutch array in the pipeline. For this reason it is difficult to reduce images of this observation.
The best results of the selfcalibration are shown here, but compared to the previous three targets this observation is considered less reliable. Figure 5.11 shows the brightness dis-

Table 5.11.: Parameters of the final brightness distribution maps of 0716+714 imaged with natural weighting. The images are shown in Fig. C.7 and the following.
In the last line the parameters of the averaged data set are given.

Frequency (MHz)	Bandwidth (MHz)	S_{peak} (Jy beam^{-1})	S_{RMS} (mJy beam^{-1})	beam$_{maj}$ (arcsec)	beam$_{min}$ (arcsec)	beam$_{p.a.}$ (°)
121.2	3.1	0.255	0.656	0.61	0.38	-66.10
124.3	3.1	0.325	0.939	0.60	0.38	-65.00
127.4	3.1	0.272	0.742	0.59	0.37	-64.51
130.6	3.1	0.183	0.804	0.57	0.36	-65.42
133.7	3.1	0.257	0.953	0.57	0.39	-66.21
136.8	3.1	0.202	0.721	0.56	0.36	-64.12
139.9	3.1	0.199	0.602	0.55	0.33	-64.29
143.1	3.1	0.261	0.764	0.55	0.32	-63.35
146.2	3.1	0.176	0.575	0.53	0.31	-64.03
149.3	3.1	0.201	0.545	0.53	0.31	-64.00
152.4	3.1	0.204	0.695	0.53	0.32	-65.78
155.6	3.1	0.267	0.849	0.53	0.32	-63.96
158.7	3.1	0.289	0.743	0.53	0.34	-63.48
139.9	40.6	0.298	0.546	0.70	0.70	0.00

tribution of the 139.9 MHz frequency band with a bandwidth of 40.6 MHz. The other frequency bands are included in Figure C.7 and C.8. The parameters to the corresponding images are listed in Table 5.11. The variations in the peak flux density already shows that the flux calibration did not perform well on this observation.
In the image the brightest feature is the core. A more diffuse but also bright feature is in north-west direction of the core. Some extended emission is found in the south-east direction of the core, which might be from the counterjet.
The averaged map in Figure 5.22 with a bandwidth of 40.6 MHz centered at 139.9 MHz shows a similar structure; a bright core, an extended bright region in the north-west and a weaker extended emission region in the south west. In both direction weak emission regions are found at only two contourlevels, which are followed by a region of negative flux. These features are most likely artifacts due to calibration problems.

Tapered images

The tapered images are presented in Figure 5.23 with the 139 MHz frequency band with 3.1 MHz bandwidth. The other frequency bands are shown in Figure C.15 and C.16. All brightness distributions show islands of negative flux densities with more than two contourlevels. This is another indicator that there are problems in the calibration. The image parameters are found in Table 5.12
The three prominent features from the high resolution maps are clear to identify in

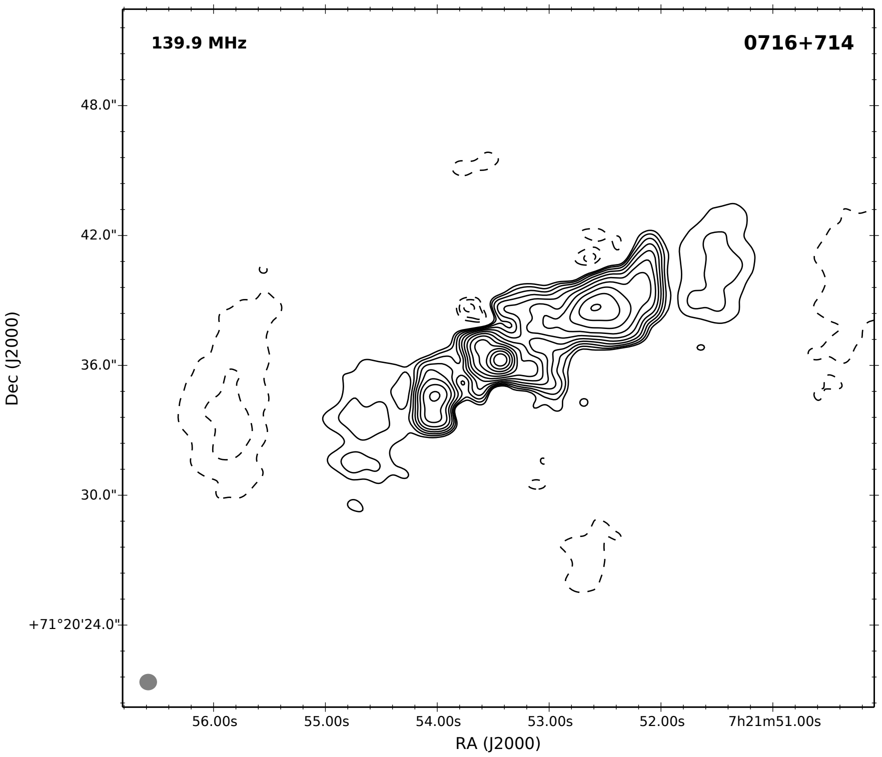

Figure 5.22.: Brightness distribution of 0716+714 using an averaged map over 13 frequency bands with a central frequency of 139.9 MHz, a bandwidth of 40.6 MHz and a common circular beam with diameter of 0.70 arcsec. The averaged map has a peak flux of $S_{peak} = 0.298$ Jy beam^{-1}. The contours indicate the flux density level and are scaled logarithmically and separated by a factor of $\sqrt{2}$. The lowest contourlevel is set to 5.0 mJy beam^{-1}.

these images. The bright core with the bright feature in the north-west, both at similar contourlevels. Also the feature in counter-jet direction to the south-east is detected.
The tapered average image in Figure 5.24 shows clearly the calibration problems with the symmetrical islands of positive and negative flux around the source. The core is still the brightest component. The north-west feature is almost as bright as the core region. The extended emission in counterjet direction is still visibile with an outflow from the core in this direction.

Flux densities & luminosities

The flux densities for 0716+714 are listed in table 5.13. Even if the spectral indices are not very representative for this observation due to the variations and calibration issues,

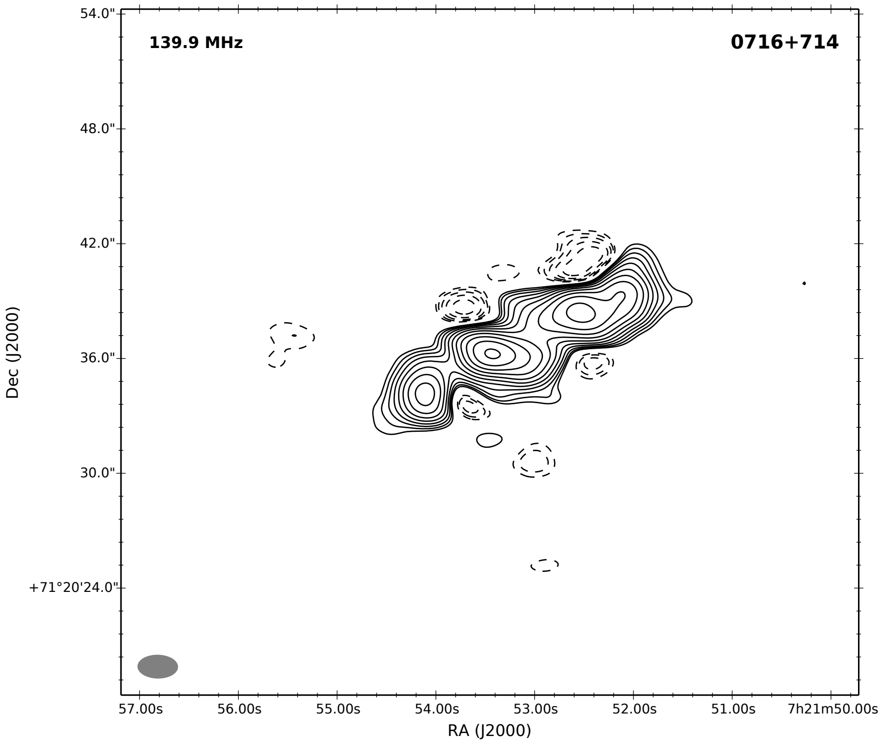

Figure 5.23.: Brightness distribution of 0716+714 of the frequency band centered at 139.9 MHz with a bandwidth of 3.1 MHz using a taper with a (u, v)-range of 200 kλ. The image parameters are listed in table 5.12. The images of the other 12 frequency bands are shown in Fig. C.15 and C.16. The contours indicate the flux density level and are scaled logarithmically and separated by a factor of $\sqrt{2}$. The lowest contourlevel is set to 15.0 mJy beam^{-1}.

the spectral behaviour is like expected: the core shows a flat spectrum while the total flux densities have a steep spectral index.
With luminosity distance, redshift and the spectral index for the extended flux density from Table 5.14 and the equation 2.4.4, the extended luminosities are calculated. For the extended flux density the total flux density was used and the core was subtracted. The resulting extended emission luminosities also vary but are all on a similar level.
Looking at the plots of the flux densities across the frequency bands for both, the high resolution and tapered images presented in Figure 5.25, the higher uncertainty of the absolute flux calibration can be seen. The variations of the flux density are not limited to the total flux densities but apply also to the core in the corresponding frequency band, which means that the flux scale is deviating systematically. To estimate the errors the deviation from the spectral index fit is determined and results in a relative error 20%. Even with the uncertainty of the spectral index, the plot in Figure 5.25 shows that the

Table 5.12.: Parameters of the final brightness distribution maps of 0716+714 imaged with natural weighting and a taper of 200 kλ. The images are shown in Fig. C.15 and the following.

Frequency (MHz)	Bandwidth (MHz)	S_{peak} (Jy beam^{-1})	S_{RMS} (mJy beam^{-1})	$beam_{maj}$ (arcsec)	$beam_{min}$ (arcsec)	$beam_{p.a.}$ (°)
121.2	3.1	0.515	3.409	1.55	1.13	82.46
124.3	3.1	0.629	5.013	1.62	1.15	83.74
127.4	3.1	0.565	3.597	1.68	1.15	85.49
130.6	3.1	0.439	4.388	1.67	1.15	84.63
133.7	3.1	0.493	3.886	1.84	1.19	87.42
136.8	3.1	0.428	3.108	1.87	1.18	88.33
139.9	3.1	0.496	2.870	1.91	1.18	88.88
143.1	3.1	0.643	3.238	2.03	1.20	89.74
146.2	3.1	0.445	2.976	2.10	1.21	89.83
149.3	3.1	0.477	2.404	2.19	1.21	-89.88
152.4	3.1	0.531	3.198	2.35	1.26	-89.59
155.6	3.1	0.662	3.619	2.48	1.28	-89.55
158.7	3.1	0.623	2.672	2.54	1.31	89.06
139.9	40.6	0.834	4.136	3.00	3.00	0.00

errors might be underestimated.
It was difficult to image all frequency bands of this observation run. In some bands CASA had problems or failed to convolve a beam model with the visibilities. Even with being able to create an image with difmap for each of the frequency bands, the absolute flux calibration did not work sufficiently in each band.

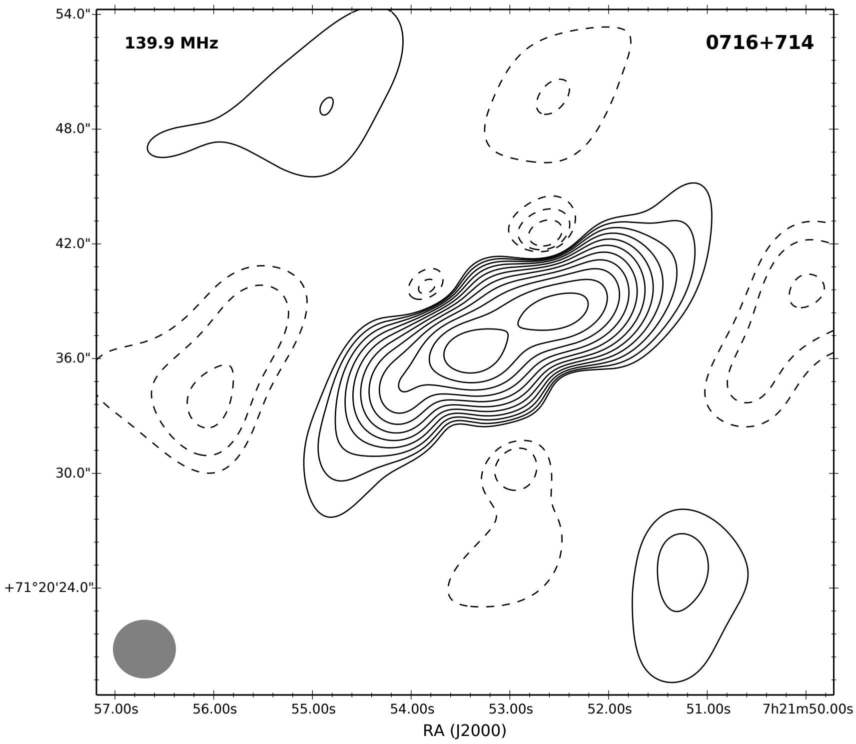

Figure 5.24.: Brightness distribution of 0716+714 using an averaged map over 13 frequency bands obtained using a taper of 200 kλ with a central frequency of 139.9 MHz, a bandwidth of 40.6 MHz and a common circular beam with diameter of 3.00 arcsec. The averaged map has a peak flux of $S_{\mathrm{peak}} = 0.834$ Jy beam^{-1}. The contours indicate the flux density level and are scaled logarithmically and separated by a factor of $\sqrt{2}$. The lowest contourlevel is set to 20.0 mJy beam^{-1}.

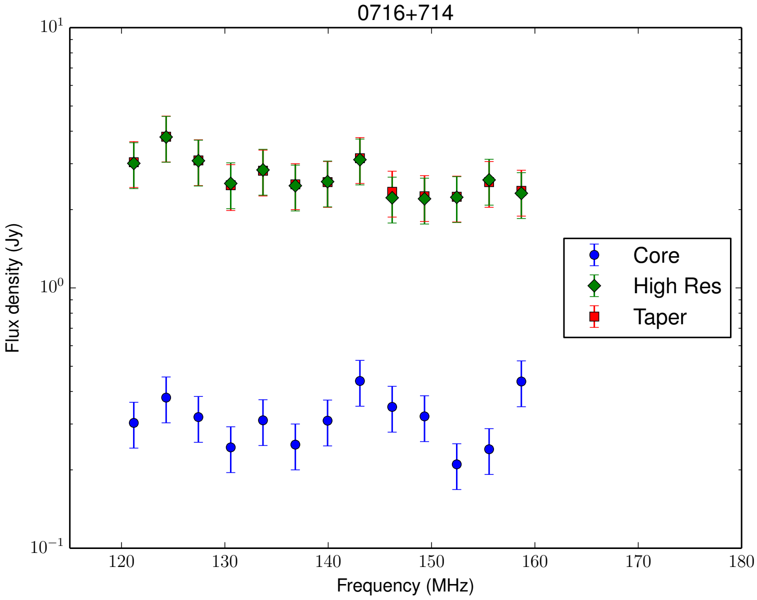

Figure 5.25.: Plot of all flux densities of 0716+714 given in table 5.13 with an estimated uncertainty of 20%.

Table 5.13.: Flux densities of 0716+714 of the core by fitting a circular Gaussian model component to this region, the total flux density of the model for the high resolution images (HR) and the total flux density of the tapered images. By subtracting the core from the total flux density the extended emission was calculated, which was used with the spectral index of the extended flux density to calculate the luminosity of the extended emission.

Frequency (MHz)	Core S_{Core} (Jy)	$Total_{HR}$ S_{HR} (Jy)	$Total_{Taper}$ S_{Taper} (Jy)	Ext. luminosity L_{HR} (10^{26} W Hz^{-1})	Ext. luminosity L_{Taper} (10^{26} W Hz^{-1})
121.19	0.303	3.013	3.041	1.20	1.20
124.32	0.379	3.798	3.812	1.51	1.51
127.44	0.319	3.079	3.094	1.22	1.22
130.57	0.244	2.517	2.483	1.00	0.98
133.69	0.310	2.836	2.822	1.12	1.10
136.82	0.250	2.474	2.497	0.98	0.99
139.94	0.309	2.558	2.546	0.99	0.98
143.07	0.439	3.115	3.152	1.18	1.19
146.19	0.349	2.224	2.343	0.83	0.88
149.32	0.321	2.201	2.254	0.83	0.85
152.44	0.210	2.228	2.239	0.89	0.89
155.57	0.240	2.603	2.550	1.04	1.01
158.69	0.437	2.312	2.358	0.83	0.84
α	-0.04	-1.34	-1.30		

5.3. Discussion

5.3.1. Morphology

2201+315

2201+315 (common name: 4C +31.63) is classified as FSRQ at a redshift of $z = 0.29474$ (Marziani et al. 1996). As described in the previous Section 5.2 the images of this source (see Fig. 5.7 for the averaged image) show an AGN with a bright core with a jet in the south west direction ending in a lobe with a hot spot. In the opposite direction a second lobe with a hot spot is present. Comparing this morphology with the radio galaxy scheme by Fanaroff & Riley (1974a) this source shows clearly the features of a counterpart to FRII radio galaxies.
The VLA image of Cooper et al. (2007) has the same features but with less diffuse extended emission. The lobes with the hotspots have similar flux densities and have a total flux only slightly lower than the bright core. However the spectral index fit to the flux density of the core region shows an inverted behavior while the lobes have steep spectral indices, like expected for extended emission. Also earlier VLA observations of Gower & Hutchings (1984) obtain a very similar morphology.
Already the MSSS reimaging results showed the two-sided jet morphology (see Fig. B.3 and B.4). However with the high resolution images not only the two hot spots can be detected and distinguished but also the kpc-scale jet is visible. Due to the low radio frequencies also the diffuse extended emission around the hot spots and the jet can be detected and seen at the lowest contour levels in the averaged image. This gives the possibility to measure the flux density of the source and the core to get only the extended emission for the calculation of the extended radio luminosity.
Compared to the MSSS observation the spectral index of total flux density is less steep in the LOFAR international observation (MSSS: -1.7 vs LOFAR int: -0.7). The extensions seen in the reimaged MSSS brightness distribution fits to the both bright lobes seen in the images of the international LOFAR observation. In the MSSS catalog the source has flux densities of $\sim$4 Jy, fitting to the total flux densities listed in Table 5.4.

1807+698

The BL Lac object 1807+698 (common name: 3C 371) at a redshift of $z = 0.051$ (de Grijp et al. 1992) shows a one sided jet to the west ending in a diffuse lobe region with a hot spot. In the opposite direction diffuse emission is detected. The averaged brightness distribution (see Fig. 5.12) shows diffuse emission, which indicates that also the extended diffuse halo observed already at the MSSS reimaging (see Fig. 4.7), is still in the image. The bright jet close to the core is also found in the VLA observation of Kharb et al. (2010) as well as the more diffuse lobe with the hot spot. However the VLA image seems not to show any emission in the counterjet direction, which is then probably also missed in the measurement of the extended emission of this source. Comparing the images to other published radio observations of this BL Lac they show very similar features. Similar to the reimaged result of the MSSS data (figure 4.7) the image of Giroletti et al. (2004) shows the diffuse halo with a brighter jet feature in the west direction. However these images have lower resolution. The images of Wrobel & Lind (1990) using the VLA at 5 GHz are similar in resolution and show the bright jet near the core and the diffuse lobe with the hot spot. The structure of the bright core with a jet to the west is also seen in the observations with the VLA at 1.4 GHz by Kharb et al. (2010). In the images of Wrobel & Lind (1990) the diffuse lobe emission of the counterjet is detected matching to the image presented in this work. This diffuse lobe emission is not found in the images by Kharb et al. (2010).

Even if the diffuse emission extends to a much larger area in the MSSS reimaging results (Figur 4.7), this emission is not picked up by the international array. This might come from phasing up all the core station to a tied station, the calibration or that the emission is too diffuse and too faint to be picked up at the high resolution. In the high resolution images as well as the tapered images mainly the brightest inner region is seen with much more details of the structure. The missing extended emission of the halo can also be seen in comparison of the flux densities. While the flux densities in the high resolution images are between ∼2–3 Jy the flux densities in the MSSS catalog are around ∼6–7 Jy. The spectral indices of the source is inverted ($\alpha \sim 1.0$) for the dedicated LOFAR observation with international baselines. For the MSSS catalog much more extended emission is picked up, making the spectral index steep ($\alpha \sim -0.4$).

As a BL Lac object it is expected to show the features of a counterpart to FRI radio galaxies. Since these radio galaxies have bright jets ending in a plume-like emission, it is expected that only one jet is detected due to looking inside the beamed jet in the direction towards the observer. So the image shows the bright jet in the direction towards the Earth with only a small angle to the line of sight, which can be seen in the images going to the west direction. The extended diffuse emission of the plumes can be seen as the halo around the hot spot in the west and the lobe on the side of the counterjet. The small angle also explains that the source appears to have a halo-like structure at lower resolutions since in these images the extended emission of the jet and the counterjet are merged. However the detected hot spot does not fit exactly in the expectation of a counterpart of a FRI radio galaxy, since those have prominent jets instead of lobes. Another possibility is that this emission is produced in a disruption of the jet. Taking into account the results of the MSSS reimaging (see Figure 4.7) the diffuse emission is much more extended than the detections of the international LOFAR observations. This means that the features in the west of the core is more likely a feature of the jet than the lobe where the jet ends. In this case the morphology fits nicely into the expectation of being a counterpart to a FR I radio galaxy in the unification model.

1222+216

The second FSRQ in this pilot sample is 1222+216 (common name: 4C +21.35) at a redshfit of $z = 0.432$ (Abazajian et al. 2009). The morphology on kpc-scale of this source is more complex than the other AGNs in this work. The images show a very bright core in the center of the brightness distributions. In the east direction a bright hot spot is detected. A second hotspot is found in the south of the core. Several features suggest a jet-like structure in a S-shape starting from the core in the north-east direction, bending down in the south east-direction with a second bend into the lobe with the hotspot in the east coming from the south-west direction. The S-shaped jet is also seen in the VLA observation by Cooper et al. (2007).
The kpc-jet with the two hot spots and the diffuse emission around the source besides the strange diffuse emission region in the south east are confirmed from the VLA observation by Cooper et al. (2007). The jet starting at the core and the hot spot in the eastern direction are also detected in snapshot observations at 4.8 GHz with the VLA by Price et al. (1993).
Detecting a bright core feature with two hot spots and a one-sided jet fits in the expectation of a FRII radio galaxy with a jet towards the observer. Due to the small angle of the line of sight of blazars the diffuse emission corresponds to the lobe emission of both jets.
Subtracting the core from the total flux density of this source, the extended emission still contains a large fraction of the total flux density. In the observed subsample of 57 sources by Cooper et al. (2007) this target was the only AGN, which showed more extended than core emission. In the LOFAR observations, however, all 4 sources of this pilot sample have more extended emission than the core region.
Compared to the averaged image of the MSSS reimaging, the extended emission covers a smaller area, which corresponds only to the bright inner region in the reimaged brightness distribution. This means that the features around the core in the MSSS reimaging have to be artifacts from sidelobes. The flux densities in the observation with international baselines are in the range of $\sim$5.5–9.0 Jy, while the flux densities of MSSS are in the range of $\sim$7.5–9.5 Jy. The small difference might come from some faint diffuse extended emission, which is not picked up by the longest baselines, but is included in the low resolution observations by MSSS. These differences also affect the spectral indices, which are much steeper for the international LOFAR observation ($\alpha \sim -1.8$) compared to the MSSS spectral index fit ($\alpha \sim -0.9$). However since the spectral indices might change in the MSSS catalog, it is difficult to decide which spectral index is more favored. The very steep spectral index of the international LOFAR observation is unlikely and could be affected by errors in the amplitude calibration.

0716+714

0716+714 (common name: S5 0716+71) is the second BL Lac object at a redshift of $z = 127$ (Stadnik & Romani 2014). Due to phase problems in large parts of the observational data the images show artificial regions of radio emission. While some positive regions with diffuse like emission are found, regions with negative flux densities around the source are detected as well. These negative regions are occuring due to imaging or calibration problems. Like discussed in Section 5.2 this observation had several problems in the data and calibration.
Besides the artificial features probably caused by phase calibration problems, the source shows an overall cigar-like shape. This shape is more elliptical in the VLA observations by Cooper et al. (2007) and Antonucci et al. (1986). The remaining morphology is very similar in all images, the LOFAR observations and the VLA observations by Cooper et al. (2007) and Antonucci et al. (1986).
The bright core seems to have a jet with very small angle towards the observer creating a bright lobe-like region in the north-east direction of the core. This region is again extended to the north-east corresponding perfectly to the expectation of the counterpart of the jet-plumes of FRI radio galaxies. The same feature with covering a similar region is observed in the south-west direction, corresponding to the counterjet-plume. This shows that also the fourth target of the pilot sample corresponds to the expectations of the blazars being counterparts to the FRI/FRII radio galaxies.
The structure of 0716+714 covers only a small area, which cannot be resolved in the reimaged MSSS brightness distributions. For this the features seen there are most likely artifacts coming from sidelobes. On the other side the calibration of the international LOFAR observation had several problems, which resulted in artifacts in the images. These problems are probably also causing the differences in the spectral indices, where the fit to the flux densities of the LOFAR international observation shows a steeper spectrum ($\alpha \sim -1.3$) than the MSSS spectral index ($\alpha \sim -0.6$). However, both spectral indices are steep and the flux densities of both observations result in total flux densities of $\sim$3 Jy.

5.3.2. Extended radio luminosities

In Section 5.2 the flux density of the model at the highest resolution and of the tapered images and a fit of the core region were used to study the spectrum. For all sources the extended radio emission was measured by taking the total flux density of the target and subtracting the core. With the spectral index fitted to this extended emission the radio luminosity of each target was calculated. The values for each frequency band are give in Section 5.2, the mean extended radio flux and the mean extended radio luminosity for each high resolution and tapered image are listed in table 5.14.

Fanaroff & Riley (1974b) found a dividing line for the luminosities between FR I and

Table 5.14.: Luminosities from extended emission measured in the images using the maximal resolution with natural weighting (see Section C.1) and the images using a taper to 200 kλ (see Section C.2). For the flux densities of each region in each frequency band see Section 5.2
Used cosmological constants: $H_0 = 71$ km s^{-1} Mpc^{-1}, $\Omega_{\mathrm{matter}} = 0.27$, $\Omega_{\mathrm{vacuum}} = 0.73$

Target	Type	Redshift z	Lum. Distance (Mpc)	Mean S_{ext} (Jy)	α_{ext}	Mean L_{ext} (W Hz^{-1})
2201+315	FSRQ	0.29474[1]	1503	2.91	-0.97	$7.8{\cdot}10^{26}$
1807+698	BL Lac	0.051[2]	223	1.40	0.44	$7.7{\cdot}10^{24}$
1222+216	FSRQ	0.434[3]	2381	5.64	-2.40	$6.3{\cdot}10^{27}$
0716+714	BL Lac	0.127[4]	588	2.38	-1.53	$1.1{\cdot}10^{26}$

References for redshifts: [1]Marziani et al. (1996), [2]de Grijp et al. (1992), [3]Abazajian et al. (2009), [4]Stadnik & Romani (2014)

FR II, where sources with luminosities above $L_{\mathrm{ext}-178} \sim 2.5 \cdot 10^{26}$ W Hz^{-1} at 178 MHz show almost exclusively FR II radio morphology while below this value the morphology usually fits to FRI radio galaxies. For this value a Hubble constant of $H_0 = 50$ km s^{-1} Mpc^{-1} was used and the luminosity is dependent of this constant by $\mathrm{L}_{\mathrm{ext}} \propto H_0^{-2}$. Ledlow & Owen (1996) found that this luminosity is not only dependent of the radio jet emission but also of the optical luminosity. This resulted in an intermediate region of radio luminosities where both types of radio galaxies can be found. This intermediate region was found to be between $10^{24.5}$-10^{26} W Hz^{-1}, which was used by Kharb et al. (2010) and others to compare the expectations of the blazar counterparts from the unification model with their luminosities. Extrapolating the intermediate region of radio luminosities to 150 MHz ($L_{ext} \propto \nu^{\alpha}$) and using the cosmological constant with $H_0 = 71$ km s^{-1} Mpc^{-1}, $\Omega_{\mathrm{matter}} = 0.27$, $\Omega_{\mathrm{vacuum}} = 0.73$ gives a region of $\sim 10^{25.5}$-$10^{26.8}$ W Hz^{-1}. This means that sources with luminosities below $\sim 3.7 \cdot 10^{25}$ W Hz^{-1} should be equivalent to FR I radio galaxies seen with a different angle to the line of sight, while the FR II counterparts should have luminosities higher than $\sim 5.7 \cdot 10^{26}$ W Hz^{-1}. For our pilot sample both FSRQs show extended luminosities in the luminosity region expected above $10^{26.8}$ W Hz^{-1}, while the BL Lac 1807+698 is below $\sim 10^{25.5}$ W Hz^{-1} corresponding to be a counterpart of a jet dominated FRI radio galaxy. The extended luminosity of 1807+698 is similar to the total intrinsic luminosity calculated by Giroletti et al. (2004) from 325 MHz WENSS data (Rengelink et al. 1997) assuming a Lorentz-Factor of $\gamma = 5$ and that the radio flux density is dominated by extended emission and the core is self-absorbed. Since in this work the target shows an inverted spectrum one possibility is that the emission is already self-absorbed and the synchrotron peak is at a higher frequency than 160 MHz. The other possibility would be a problem with the flux calibration. The second BL Lac 0716+714 has an extended luminosity in the intermediate range of luminosities however the morphology tends to fit to the FRI classification. These luminosities and their location in the FR I/FR II luminosity region is consistent with the finding of Kharb et al. (2010).

Table 5.15.: Luminosities calculated from the extended emission at 1.4 GHz by Kharb et al. (2010) and extrapolation to 150 MHz with the assumption of $\alpha = -0.8$ following Ledlow & Owen (1996).
Used cosmological constants: $H_0 = 71$ km s^{-1} Mpc^{-1}, $\Omega_{\mathrm{matter}} = 0.27$, $\Omega_{\mathrm{vacuum}} = 0.73$

Target	$S_{\mathrm{ext-1400}}$ (Jy)	$L_{\mathrm{ext-1400}}$ (W Hz^{-1})	$S_{\mathrm{ext-150}}$ (Jy)	$L_{\mathrm{ext-150}}$ (W Hz^{-1})
2201+315	0.378	$9.47 \cdot 10^{25}$	2.259	$5.65 \cdot 10^{26}$
1807+698	0.369	$2.16 \cdot 10^{24}$	2.201	$1.29 \cdot 10^{25}$
1222+216	0.956	$5.82 \cdot 10^{26}$	5.710	$3.48 \cdot 10^{27}$
0716+714	0.376	$1.50 \cdot 10^{25}$	2.247	$8.97 \cdot 10^{25}$

Using the flux density by Kharb et al. (2010) from the MOJAVE observations with the VLA at 1.4 GHz and assuming a spectral index of $\alpha = -0.8$ for the extended emission following Ledlow & Owen (1996) a flux density at 150 MHz can be extrapolated. With the same cosmological constants used for the previous luminosity calculation, the corresponding radio luminosities of the 1.4 GHz flux density as well as for the extrapolated 150 MHz flux density are calculated and listed in table 5.15. Compared to the results of the LOFAR images the extended flux densities and their luminosities are close to the extrapolated values. Only 1807+698 has less extended emission and the radio luminosity is lower by a factor of 2. For the other sources the extended flux densities are higher for 2201+315 and 0716+714, while 1222+216 is slightly lower. This is also reflected in the corresponding luminosities.

Despite of having four AGNs observed fitting into the expectations of the simple AGN unification model, this result is not very significant. To test the AGN unification model more sources are needed to be able to get statistical significant results. Cooper et al. (2007) and Kharb et al. (2010) found several sources in the intermediate luminosity regime and some AGN without extended emission or emission features, which do not match exactly the expectation of the simplified unification scheme. Most of these morphological features were hot spots in the observation of BL Lac objects, which are typical for FR II radio galaxies but not for FR Is.
On the other side a significant correlation of the extended radio luminosities with the apparent parsec-scale jet speeds is found. Since the low radio frequencies are more sensitive for this extended emission, this correlation should be tested for these frequencies as well. For this a larger sample like the full MOJAVE1 sample should be observed with international LOFAR observations.
With a larger sample the luminosities of the extended emission can be used to estimate Lorentz factors and the intrinsic luminosities taking into account the well studied kinematics and multi-wavelength information of these sources. Doing this with a large

fraction of the MOJAVE sample could improve the understanding of the jets by providing statistical significant results.
In this work the main focus was to develop a calibration and imaging strategy, testing the capabilities of the international LOFAR observations and to present the first images obtained with these methods. These methods can still be improved. The improvements of the calibration and the data reduction of more observations will be topic in near future.

6. Summary & Outlook

6.1. Summary

The first part of this work studies blazars of the MOJAVE 1.5 Jy sample in the preliminary MSSS catalog for the frequencies between 120–160 MHz combining the flux densities with the measurements of the OVRO single-dish monitoring at 1.4 GHz. 125 of 183 AGN of the MOJAVE 1.5 Jy sample were detected in the catalog. Most of the missing AGN are not detected because they are located too low in declination for the MSSS observations. The MSSS catalog was produced from two snapshot observations of 7 min each for each field using the Dutch array of LOFAR. The first catalog is limited to an angular resolution of $\sim$120 arcsec with a sensitivity of 50–100 mJy.
The MSSS flux densities for these 125 blazars are similar to the flux densities in the VLSS catalog (Cohen et al. 2007a) and match the interpolated flux densities of (Arshakian et al. 2010). The interpolation of Arshakian et al. (2010) using archival data is close to the measured flux densities in the MSSS catalog. However, the tendency is to underestimate the flux densities, which can be due to variability or the underestimation of the contribution coming from extended emission regions. Compared to measurements at higher frequencies around half of the sample shows higher flux densities in the MSSS observations. To reduce the influence of variability the quasi-simultaneous observations of the OVRO single-dish monitoring at 15 GHz are used for this comparison. The results indicate that these sources have extended emission due to having an increased sensitivity for diffuse extended emission at low frequency radio observations.
The flux densities of the OVRO monitoring at 15 GHz are used with the MSSS flux densities to calculate broadband spectral indices. Comparing the spectral index distribution of these quasi-simultaneous measurements with the spectral indices calculated with the flux densities of the VLSS (Cohen et al. 2007a) and NVSS (Condon et al. 1998) catalogs, the MSSS-OVRO distribution is less broadened. The broadening of the distribution of the VLSS-NVSS spectral indices is likely due to the variability differences, since those observations were timely independent. Both distributions show their peak at spectral indices between -0.5 and 0. A large fraction of the sample has flat spectral indices meaning that those sources are still dominated by the beamed emission. The sources with steep spectral indices ($\alpha < -0.3$) probably have a larger contribution of their extended emission to their total flux density, while also some sources show inverted spectral indices ($\alpha > 0$). The inverted spectral indices show that the synchrotron peak frequency of those sources has to be at higher frequencies than 150 MHz of the MSSS flux density or

that these sources are currently in a higher state (flaring) at the GHz frequencies, which has not arrived at the low frequencies at that time. The spectral index distribution of the sample in this work is similar to the results by Massaro et al. (2013) studying a much larger blazar sample with the use of the archival data coming from VLSS and NVSS.
Arshakian et al. (2010) used the interpolated flux densities to calculate luminosities. With the assumption that the extended emission is dominating and the contribution of the beamed emission can be neglected, these luminosities should be a good proxy for the intrinsic jet power of these sources. However, the flat spectral indices for most sources are contradictory indicating that the beamed emission coming from the core/jet region is still dominating. With observation at low angular resolution or interpolation using archival data it is not possible to obtain a correct value for the extended emission at low frequencies. The extended flux densities can only be measured if the angular resolution is high enough to separate the beamed core region of the extended emission. For this the angular resolution of the MSSS catalog is not sufficient.
To obtain more information on the morphology and the extended emission of the studied blazars the MSSS measurement sets were reimaged including all available baselines. The resulting images have an increased angular resolution of ∼20–30 arcsec. However due to the snapshot observations several field show strong artifacts coming from sidelobes. For 93 sources one MSSS frequency band was reimaged at a higher resolution. 45 of these 93 sources could also be reimaged in more frequency bands giving the possibility to create averaged images. The averaged images reduce influence of artifacts, which occur only in single band images. The images of the intermediate frequency band at 143.3 and the averaged images resulting of the reimaging process are presented in this work. Due to problems in the calibration these images do not have correct flux densities. For this they can only be used for the morphological details. Compared to images with lower resolution like the NVSS observations (Condon et al. 1998), the morphology of these sources is similar.
Combining the results of the reimaging process and the results coming of the preliminary MSSS catalog a sample of four blazars was chosen to be observed with international LOFAR observations. This pilot project was designed to develop a calibration strategy and test the capabilities of the LOFAR international observations for further blazar studies. Since one source of the MOJAVE sample was newly classified as radio-loud narrowline Seyfert 1 (NLS1) galaxy during this work, a short check on other radio-loud NLS1 was made. The number of detected radio-loud NLS1 is not very large currently, so the sample of 42 radio-loud NLS1 by Foschini et al. (2015) was used. However only 5 of these 42 sources were detected in the MSSS observations. 3 of the missing sources are located on the Southern Hemisphere and not inside the range. For 18 of the 42 targets spectral indices are given by Foschini et al. (2015), which were used to calculate their expected emission at 150 MHz. As result all sources with extrapolated flux densities above 200 mJy were detected with LOFAR in the MSSS observations. One source with an extrapolated flux density of 77 mJy was detected with 168 mJy making it twice as bright as expected.

Most of the radio-loud NLS1 not detected by MSSS have expected flux densities below the sensitivity. Additional the flux densities for the spectral indices were obtained at 1.4 and 5 GHz and might not perfectly fit into the spectrum at lower frequencies of these sources.

In the second part of the work the calibration of international LOFAR observations is explained. The calibration of these observation is still under development and can be improved. These improvements have much higher hardware requirements for the computers or improvements in the software. However the calibration used in this work already results in high resolution images with angular resolution below 1 arcsec. Additional to the high resolution images a taper was used to get the brightness distribution with more sensitivity on the diffuse larger scale emission regions at lower resolution.
With the images of 13 frequency bands covering the frequency range between 120–160 MHz the morphology of these sources could be studied. Compared to previous VLA observations the slightly higher resolution results in more details and the low frequencies are more sensitive to the extended emission. With the tapered images the diffuse emission is seen on a larger scale.
The morphology of the FSRQs 2201+315 (4C +31.63) and 1222+216 (4C +21.35) fits in the expectation for counterparts for FR II radio galaxies. Both show a bright core with a jet and two hot spots surrounded in diffuse extended emission. The spectral indices of both sources are flat for the core region and steep for the total and extended flux densities. By calculating the extended radio luminosities both AGN are above the dividing line for the FR I/FR II division for radio galaxies. This confirms both sources to be counterpart of a FR II radio galaxy with a different line of sight.
The observation of the BL Lac 0716+714 (S5 0716+71) already had several problems in the calibration resulting in many artifacts in the images. The morphology fits to the expectation as a FR I radio galaxy counterpart, but shows some differences to the morphology in VLA observations. The spectral indices fit to the typical expectation of a flat core spectrum and steep extended and total emission. These spectral indices have to be taken with care since the calibration was not perfect. The extended radio luminosities are below the dividing line for FR II radio galaxies but higher than the line for FR Is. The extended luminosity is in the intermediate range, which confirms the results from previous studies by Cooper et al. (2007) and Kharb et al. (2010).
The other BL Lac of this pilot sample 1807+698 (3C 371) has a large halo of diffuse extended emission in the reimaged MSSS images. The high resolution images show a bright core with a jet to the west. More distant in the west of the core an emission region is found, which could be a faint hot spot. A hot spot is not expected for FR I counterparts. However with the halo of the MSSS images covering a much larger area, the feature could also be a disruption of the jet. The other features fit in the expected morphology of a FR I counterpart. The spectral indices of the source are highly inverted for all features. This might be due to a calibration problem or that the emission is selfabsorbed and the source has its synchrotron peak frequency above the frequency

of 160 MHz. The extended luminosity of 1807+698 is below the dividing line for FR I radio galaxies. Taking all results combined this target fits into the FR I counterpart expectation.
Thus all four targets in the pilot sample fit in the AGN unification model. However, with only four targets this result is not statistically significant. With the calibration strategy of this work more sources can be studied to get a statistical significant result. Future LOFAR observations and result can test the unification model by studying the extended emission and the resulting luminosities.

6.2. Outlook

The results of this work shows the possibilities of blazar studies at low frequencies. This opens the possibility for several follow-up projects with similar aims and methods.
On the one hand the study on the MSSS study will be improved by using the catalog with final calibration and slightly enhanced resolution. Additional to the frequency range of 120-160 MHz, the efforts of MSSS will be extended to cover also the range of the LBA-antennas of LOFAR by observing the Northern Hemisphere at frequencies between 30-75 MHz. The outcome of these observation will add another catalog to perform a similar study. The results can then be compared and combined with the measurements of the final HBA-catalog.
For the second part of the project already follow-up proposals have been submitted and accepted. 26 of the MOJAVE blazars are already observed and available. With the results even more observations can be proposed with the long-term goal to get observations of the complete sample.
By combining the luminosities from LOFAR observations for a larger number of sources with their apparent velocities the next step would lead to estimate the jet powers and Doppler factors. Future observations will have improved resolution since LOFAR expands with 3 new stations in Poland and another new station in Ireland.
To cover the frequencies between the VLA 1.4 GHz observations and the low frequency observations at 120-160 MHz, a proposal to observe the pilot sample with the GMRT at 610 MHz was accepted and performed. The brightness distribution of these frequencies will add another data point for the flux densities to confirm the spectral index distribution as well as the extended radio luminosity at 610 MHz.
The project of observing blazars at low frequencies can be extended additionally by observing with the international stations of the LBA from LOFAR. This would add images of even lower frequencies while loosing a fraction of the angular resolution. For further extension the future SKA will be a new telescope to observe the blazars of the Southern Hemisphere. As starting point for SKA observations not only the Southern MOJAVE sources can be used as target but the TANAMI program, which was also mentioned has a sample with several candidate targets.

Appendices

A. The TANAMI project and personal contributions

A.1. The TANAMI project on the Southern Hemisphere

Similar to MOJAVE the TANAMI project (**T**racking **a**ctive galactic **n**uclei with **a**ustral **m**illiarcsecond **i**nterferometry)[1] is observing AGN on the southern hemisphere (Ojha et al. 2010; Kadler et al. 2015). This program is not designed to be just a radio monitoring of AGN at high resolutions but is designed to offer multi-wavelength information of the AGN.
To have high-resolution radio observation TANAMI uses various telescopes on the Southern part of the world, mainly located in Australia and New Zealand but also in the Antarctica, South Africa and South America. Unlike the VLBA used by MOJAVE, the VLBI array in TANAMI is a heterogeneous array of different radio telescopes. The radio observations take place at 8.4 and 22.3 GHz, though not all telescopes support the 22.3 GHz observations. Due to the geographical situation with much area covered by oceans south of the equator, the array lacks (u, v)-coverage on the intermediate baselines.
However in 2011 the radio observations of Cen A (Müller et al. 2011), which is the closest radio-loud AGN to us, offered sub-parsec resolution on the inner jet, which were the highest spatial resolution images of an AGN jet at that time. Since not all telescopes participate in each observation cycle the data vary in resolutions and sensitivity.
Apart from the radio observations the sample is observed in the X-ray regime using the *RXTE*, *Suzaku*, *INTEGRAL* and *SWIFT* (also UV and optical) satellites, at γ-ray energies using the *Fermi* satellite (Atwood et al. 2009; Abdo et al. 2010; Ackermann et al. 2011, 2015). Additional radio observations at low resolution are provided by the ATCA radio telescope in Australia.
The sources in the TANAMI sample are selected in anticipation of the launch of Fermi based on a subsample of known and candidate γ-ray sources from the results of *EGRET* observations (Hartman et al. 1992). Another selection criterion is based on radio flux density selection from the catalog of Stickel et al. (1994) of more than 2 Jy at 5 GHz and a flat readio spectrum ($\alpha > -0.5$). The so created initial sample was expanded by adding new detected bright γ-ray sources detected by *Fermi*.
In one the latest studies the results of the neutrino detector *IceCube* are used to combine

[1] http://pulsar.sternwarte.uni-erlangen.de/tanami/

them with the AGN information of the TANAMI sample (Krauß et al. 2014; Kadler et al. 2016). For the neutrino astronomy TANAMI is also collaborating with *ANTARES* (Ageron et al. 2011). The results of the TANAMI studies are based on the sample (Ojha et al. 2010) or on individual sources in a more detailed way. Since I also worked on TANAMI radio data in the last years, but it was not connected to the LOFAR specific work, in this section some published projects are highlighted. My contributions are mainly in the data reduction and development of scripts for improved data reduction and analysis. In the following listed papers I contributed with imaging milliarcsec-resolution VLBI data of different sources in multiple observations of the monitoring program of TANAMI:

- the radio-loud NLS1 PKS 2004-447 (Schulz et al. 2016; Kreikenbohm et al. 2016)
- the closest AGN to Earth Centaurus A (Müller et al. 2014b)
- the peculiar γ-ray source PMN J1603-4904 (Müller et al. 2014a)
- the search for the origin of the IceCube neutrino events (Krauß et al. 2014; Kadler et al. 2016)
- new sources of the TANAMI sample (Müller et al. in prep)

A.2. Contributions to publications

PKS 2004-447

PKS 2004-447 is a radio-loud narrow-line Seyfert1 galaxy detected at γ-rays with *Fermi*. The radio-loud NLS1 are also subject in Section 4.2.3, where counterparts of radio-loud NLS1 in MSSS are searched. Of this kind of AGN only few sources are known. The sample of (Foschini et al. 2015) consists of 42 radio-loud NLS1 and is one of the larger sample studies. Only two AGN of this sample are located in the Southern Hemisphere. As part of the TANAMI sample PKS 2004-447 was studied in the X-rays (Kreikenbohm et al. 2016) and at radio frequencies (Schulz et al. 2016).
In the X-rays moderate variability with flux changes of a factor of $\sim$3 between the minimum and maximum flux on timescales down to two months and a photon index typically for FSRQs was observed (Kreikenbohm et al. 2016). To study spectral variability more high signal-to-noise observations are required. The luminosity range of the few detected radio-loud NLS1 ranges over two orders of magnitude. The results of *XMM-Newton* and *Swift* observations confirm that radio-loud NLS1 show blazar-like features.
At radio frequencies not only the high-resolution monitoring observations from the TANAMI project, but also ATCA observations (project: C1730, related to TANAMI and archival observations) at different frequencies between 1.7 and 45 GHz were used. Compared

to other radio-loud NLS1 PKS 2004-447 seems to be the radio-loudest one. The multi-frequency observations with ATCA show that the source has a steep radio spectrum with moderate variability. The high resolution images of the source observed with the TANAMI array reveal a single-sided jet in north-west direction (Schulz et al. 2016).
Due to the location on the Southern Hemisphere this source would be an interesting target for the future *SKA*. The low frequencies and the high sensitivity could add information on the turn-over frequency. Additionally the ongoing TANAMI monitoring will add information on the jet speed and structural evolution with radio observations on milliarcsecond-scales.

Centaurus A

Centaurus A (Cen A) is the closest radio-loud AGN to Earth with a distance of only 3.8 Mpc (Harris et al. 2010). Using the high-resolution observations of TANAMI with milliarcsecond-resolution translates into sub-pc resolution (1 mas corresponds to 0.018 pc). This resolution makes the source a perfect target to study the inner details of a double-sided radio-jet with high details (Müller et al. 2011). The monitoring of TANAMI (Müller et al. 2014b) presents details on the structural evolution over a time span of 3.5 years.
With data of seven observations at 8.4 GHz several jet components could be identified and tracked over time. With this tracking apparent jet speeds between 0.1 c and 0.3 c were measured. Using the jet-to-counterjet ratio also the angle to the line of sight can be constrained to be in the range of $\sim 12°$-$45°$. However not all components are moving over time, some features seem to be stationary, which can be explained with a locally pressure maximum.
The jet shows a structure with the shape of a tuning-fork. This peculiar structure with an increase in the optical depth can be interpreted with an interaction of the jet with a star. The jet flow is redirected around the star, resulting in the "tuning-fork" shape. With the observational data it is unlikely, that this feature is a recollimation shock.
The X-ray monitoring of Cen A reveals several high flux states. Correlating the dates of these higher flux states with the jet activity it is found that the extrapolation of certain jet features correspond to the higher flux states observed in the X-rays. That means that the ejection of new jet components could be related to an increase of X-ray flux.

PMN J1603-4904

PMN J1603-4904 is located close to the galactic plane and has peculiar multiwavelength properties (Müller et al. 2014a). It is detected at γ-rays by *Fermi*-LAT and is a bright source with a hard spectrum. Due to its low synchrotron peak it was classified as BL Lac object (Nolan et al. 2012). The first VLBI images show a morphology which looks like a bright core with two jet features in both directions. A double-sided jet, however, is not

typical for BL Lac objects. Even if the bright γ-ray emission fits in the classification of a blazar, the broadband emission and VLBI morphology are unusual. It was suggested that the object could be a compact symmetric object (CSO), which also would be the first with these unusual properties, or a starburst galaxy (Müller et al. 2014a).
Studying the X-ray properties an emission line was found (Müller et al. 2015). If this emission line corresponds to a neutral Fe Kα line, the shift of this line would correspond to a redshift of $z = 0.18 \pm 0.01$. Using optical observations resulted in a redshift measurement of $z = 0.2321 \pm 0.0004$ (Goldoni et al. 2016).
With these multi-wavelength results the two scenarios for the classification are the CSO type, which would be the first one detected in the γ-rays or a strange blazar with obscured X-ray emission. For further clarification if it might be a Gigahertz-peaked source (GPS), low frequency radio observations could help.

Neutrino events from IceCube

When IceCube announced the detection of PeV neutrino events (Aartsen et al. 2013; IceCube Collaboration 2013; Aartsen et al. 2014), TANAMI sources were found in the regions of the IceCube events. It is not known where the neutrino emission comes from, but the blazars with the highly relativistic jets also producing γ-rays are the good candidates for this emission. For the events 14 and 20 (also known as "Bert" and "Ernie") detected between May 2010 and May 2012 six blazars of the TANAMI sample are located within the event regions (Krauß et al. 2014). The third detected event 35 (named "Big Bird") does not only positionally coincidence with the blazar PKS B1424-418 but does also temporally coincidence with a major outburst of this blazar (Kadler et al. 2016).
Assuming hadronic models and using the known high energy properties from X-ray and γ-ray observations, the neutrino flux can be estimated. In the case of the two events "Ernie" and "Bert" the contribution of all six blazars in their regions is almost sufficient to create the needed neutrino flux (Krauß et al. 2014). In the case of "Big Bird" the outburst of PKS B1424-418 alone is sufficient to create the neutrino excess measured by IceCube. However even if blazars are good candidates to produce neutrinos, probably also other neutrino sources exist and several neutrino events will not be explainable by only using blazars as candidates.
In both publications Krauß et al. (2014) and Kadler et al. (2016) new radio images are presented together with multi-wavelength data. These VLBI images are first published high resolution images for most of these sources. My contribution was mainly the imaging of these observations.

New TANAMI sources

The images of the first observations of the initial TANAMI sample were presented in Ojha et al. (2010). The initial sample has been extended over time. A paper on 30 sources extending the sample is in preparation, presenting the images of the first observation and analyzing their mas-scale properties. These results are quasi-simultaneous to the γ-ray properties discussed in Böck et al. (2016).
For this paper I imaged all observations of these new sources. These will be included partly in the paper or used as verification of the images produced by others.

B. Appendix: MOJAVE-blazars in MSSS observations

B.1. Flux densities and spectral indices

Table B.1.: Spectral indices of the counterparts of the 1.5 Jy selected radio sample of MOJAVE in the MSSS catalog version 0.1. Here the spectral indices of the MSSS catalog, the spectral index between MSSS and the single-dish OVRO monitoring at 15 GHZ and the spectral index between the archival flux densities of the radio surveys NVSS (Condon et al. 1998) and VLSS (Cohen et al. 2007a).

Source	Common name	Type	α_{MSSS}	$\alpha_{\mathrm{MSSS-OVRO}}$	$\alpha_{\mathrm{NVSS-VLSS}}$
0016+731	S5 0016+73	Q	-1.039 ± 0.670	0.496 ± 0.019	- ± -
0059+581	TXS 0059+581	Q	0.270 ± 0.732	0.354 ± 0.016	- ± -
0106+013	4C +01.02	Q	-0.906 ± 0.238	-0.228 ± 0.008	-0.296 ± 0.012
0109+224	S2 0109+22	B	-1.308 ± 1.156	0.173 ± 0.031	- ± -
0109+351	B2 0109+35	Q	-1.169 ± 0.202	-0.142 ± 0.012	-0.632 ± 0.014
0119+115	PKS 0119+11	Q	-0.210 ± 0.540	-0.170 ± 0.011	-0.399 ± 0.013
0133+476	DA 55	Q	1.855 ± 0.548	0.247 ± 0.012	0.200 ± 0.064
0202+149	4C +15.05	Q	0.259 ± 0.088	-0.431 ± 0.003	-0.035 ± 0.012
0202+319	B2 0202+31	Q	3.141 ± 1.308	0.186 ± 0.031	- ± -
0212+735	S5 0212+73	Q	0.552 ± 0.915	0.258 ± 0.021	0.413 ± 0.049
0215+015	OD 026	Q	-0.339 ± 0.191	-0.317 ± 0.006	-0.321 ± 0.023
0224+671	4C +67.05	Q	-0.061 ± 0.214	-0.139 ± 0.007	-0.045 ± 0.019
0229+131	4C +13.14	Q	-0.635 ± 0.211	-0.184 ± 0.006	-0.358 ± 0.012
0234+285	4C +28.07	Q	-0.147 ± 0.832	0.039 ± 0.027	-0.067 ± 0.016
0235+164	AO 0235+164	Q	-0.622 ± 0.448	-0.051 ± 0.011	0.229 ± 0.030
0241+622	7C 0241+6215	Q	-0.797 ± 1.161	0.264 ± 0.029	- ± -
0300+470	4C +47.08	B	-0.447 ± 0.334	0.185 ± 0.009	-0.080 ± 0.026
0316+413	3C 84	G	-0.409 ± 0.209	-0.181 ± 0.006	-0.431 ± 0.010
0333+321	NRAO 140	Q	0.928 ± 0.236	-0.152 ± 0.007	0.204 ± 0.026
0336-019	CTA 26	Q	-1.241 ± 0.266	0.132 ± 0.009	0.296 ± 0.052
0355+508	NRAO 150	Q	0.528 ± 0.073	0.006 ± 0.003	-0.327 ± 0.010
0400+258	CTD 026	Q	0.120 ± 0.340	0.066 ± 0.009	0.234 ± 0.059
0415+379	3C 111	G	-0.091 ± 0.114	-0.679 ± 0.004	-0.549 ± 0.011
0420-014	PKS 0420-01	Q	0.098 ± 1.029	0.233 ± 0.032	0.168 ± 0.022
0422+004	PKS 0422+00	B	-0.908 ± 0.760	-0.158 ± 0.026	0.015 ± 0.068
0430+052	3C 120	G	-0.183 ± 0.137	-0.431 ± 0.013	-0.198 ± 0.012
0440-003	NRAO 190	Q	-0.919 ± 0.542	-0.098 ± 0.015	-0.101 ± 0.018
0446+112	PKS 0446+11	Q	0.684 ± 0.897	-0.099 ± 0.024	0.018 ± 0.050
0458-020	S3 0458-02	Q	-0.117 ± 0.480	-0.275 ± 0.013	-0.129 ± 0.017

0528+134	PKS 0528+134	Q	-2.004 ± 0.935	0.011 ± 0.031	0.052 ± 0.039
0529+075	OG 050	Q	-0.237 ± 0.405	-0.240 ± 0.012	0.115 ± 0.023
0529+483	TXS 0529+483	Q	-0.091 ± 0.742	0.029 ± 0.018	-0.272 ± 0.030
0552+398	DA 193	Q	0.364 ± 1.626	- ± -	- ± -
0642+449	OH 471	Q	0.754 ± 1.827	0.511 ± 0.026	- ± -
0716+714	S5 0716+71	B	-0.550 ± 0.177	-0.170 ± 0.005	-0.582 ± 0.012
0723-008	PKS 0723-008	B	-0.890 ± 0.467	0.126 ± 0.012	-0.220 ± 0.018
0730+504	TXS 0730+504	Q	-0.010 ± 0.357	-0.104 ± 0.014	-0.084 ± 0.025
0735+178	OI 158	B	-0.598 ± 0.311	-0.139 ± 0.008	0.008 ± 0.017
0736+017	OI 061	Q	0.356 ± 0.494	-0.251 ± 0.012	0.178 ± 0.035
0738+313	OI 363	Q	-0.088 ± 0.400	0.133 ± 0.010	0.279 ± 0.027
0742+103	PKS B0742+103	Q	-0.321 ± 0.170	-0.198 ± 0.005	-0.001 ± 0.013
0745+241	S3 0745+24	Q	-0.867 ± 0.102	-0.203 ± 0.007	-0.390 ± 0.014
0748+126	OI 280	Q	-1.451 ± 0.121	0.013 ± 0.005	-0.253 ± 0.014
0754+100	PKS 0754+100	B	-2.857 ± 0.797	-0.073 ± 0.024	-0.110 ± 0.025
0804+499	OJ 508	Q	1.090 ± 1.243	0.124 ± 0.029	- ± -
0808+019	OJ 014	B	-1.008 ± 0.798	-0.216 ± 0.021	-0.074 ± 0.052
0814+425	OJ 425	B	0.179 ± 0.086	-0.227 ± 0.005	-0.200 ± 0.015
0821+033	4C +39.23	Q	0.353 ± 0.156	-0.363 ± 0.005	-0.467 ± 0.011
0823+033	PKS 0823+033	B	-2.274 ± 0.558	-0.093 ± 0.016	0.224 ± 0.061
0827+243	OJ 248	Q	-1.015 ± 0.283	0.004 ± 0.013	-0.194 ± 0.022
0829+046	OJ 049	B	-2.437 ± 0.626	-0.103 ± 0.018	-0.085 ± 0.025
0836+710	4C +71.07	Q	0.184 ± 0.135	-0.154 ± 0.004	-0.093 ± 0.012
0838+133	3C 207	Q	-0.916 ± 0.058	-0.579 ± 0.009	-0.688 ± 0.011
0851+202	OJ 287	B	0.620 ± 1.074	0.371 ± 0.023	0.216 ± 0.034
0906+015	4C +01.24	Q	-0.529 ± 0.309	0.051 ± 0.008	-0.144 ± 0.034
0917+449	S4 0917+44	Q	-0.025 ± 0.159	-0.018 ± 0.005	-0.203 ± 0.018
0917+624	OK 630	Q	0.441 ± 0.264	0.009 ± 0.007	-0.110 ± 0.021
0923+392	4C +39.25	Q	-0.378 ± 0.199	0.064 ± 0.005	-0.435 ± 0.011
0945+408	4C +40.24	Q	0.465 ± 0.215	-0.218 ± 0.007	-0.250 ± 0.013
0954+658	S4 0954+65	Q	0.306 ± 0.640	0.137 ± 0.016	0.008 ± 0.037
0955+476	OK 492	Q	-1.188 ± 0.746	0.241 ± 0.024	- ± -
1030+415	S4 1030+41	Q	0.950 ± 0.329	0.001 ± 0.009	-0.260 ± 0.029
1036+054	PKS 1036+054	Q	1.772 ± 1.148	-0.037 ± 0.024	-0.267 ± 0.027
1038+064	4C +06.41	Q	1.233 ± 0.481	-0.214 ± 0.012	-0.003 ± 0.025
1055+018	4C +01.28	Q	0.222 ± 0.223	-0.288 ± 0.008	-0.225 ± 0.013
1128+385	B2 1128+38	Q	-0.376 ± 1.259	0.114 ± 0.036	- ± -
1150+497	4C +49.22	Q	-0.054 ± 0.098	-0.303 ± 0.005	-0.676 ± 0.011
1150+812	S5 1150+81	Q	-0.376 ± 0.155	-0.230 ± 0.007	-0.178 ± 0.016
1156+295	4C +29.45	Q	-0.362 ± 0.154	-0.382 ± 0.005	-0.377 ± 0.015
1219+044	4C +04.42	G	3.726 ± 1.134	-0.220 ± 0.014	-0.302 ± 0.028
1222+216	4C +21.35	Q	-0.879 ± 0.133	-0.204 ± 0.005	-0.501 ± 0.014
1226+023	3C 273	Q	1.368 ± 0.331	-0.338 ± 0.006	-0.367 ± 0.012
1228+126	M87	G	2.238 ± 0.798	-0.633 ± 0.010	-0.439 ± 0.012
1308+326	OP 313	Q	-0.308 ± 0.110	-0.083 ± 0.005	-0.031 ± 0.022
1324+224	B2 1324+22	Q	0.336 ± 1.149	0.130 ± 0.026	- ± -
1413+135	PKS B1413+135	B	0.230 ± 1.059	-0.258 ± 0.033	0.233 ± 0.063
1417+385	B3 1417+385	Q	0.203 ± 1.346	0.210 ± 0.031	- ± -
1435+638	VIPS 0792	Q	-0.340 ± 0.309	0.040 ± 0.009	-0.069 ± 0.025
1458+718	3C 309.1	Q	0.009 ± 0.049	-0.742 ± 0.004	-0.588 ± 0.010

1502+106	OR 103	Q	0.927 ± 0.646	-0.278 ± 0.015	0.115 ± 0.038
1538+149	4C +14.60	B	0.110 ± 0.084	-0.415 ± 0.003	-0.519 ± 0.011
1546+027	PKS 1546+027	Q	-0.737 ± 1.594	-0.151 ± 0.054	- ± -
1548+056	4C +05.64	Q	-0.494 ± 0.522	-0.145 ± 0.013	-0.235 ± 0.014
1611+343	DA 406	Q	0.946 ± 0.338	0.113 ± 0.008	0.184 ± 0.015
1633+382	4C +38.41	Q	1.141 ± 0.291	0.055 ± 0.007	-0.101 ± 0.013
1637+574	OS 562	Q	-0.156 ± 0.187	-0.104 ± 0.005	-0.312 ± 0.012
1638+398	NRAO 512	Q	0.460 ± 0.697	0.126 ± 0.019	- ± -
1641+399	3C 345	Q	0.164 ± 0.132	-0.147 ± 0.005	-0.152 ± 0.012
1642+690	4C +69.21	Q	0.658 ± 0.113	-0.006 ± 0.003	-0.377 ± 0.011
1655+077	PKS 1655+077	Q	2.843 ± 1.222	-0.199 ± 0.021	-0.290 ± 0.019
1726+455	S4 1726+45	Q	0.314 ± 1.320	0.029 ± 0.030	- ± -
1739+522	4C +51.37	Q	0.371 ± 0.667	0.091 ± 0.015	-0.079 ± 0.046
1749+096	4C +09.57	B	1.429 ± 1.150	0.266 ± 0.023	- ± -
1800+440	S4 1800+44	Q	0.003 ± 0.271	-0.230 ± 0.008	-0.458 ± 0.015
1803+784	S5 1803+784	B	-0.246 ± 0.152	-0.026 ± 0.005	0.360 ± 0.038
1807+698	3C 371	B	-0.392 ± 0.101	-0.301 ± 0.005	-0.268 ± 0.014
1823+568	4C +56.27	B	-0.788 ± 0.100	-0.223 ± 0.003	-0.520 ± 0.011
1828+487	3C 380	Q	-0.585 ± 0.061	-0.690 ± 0.006	-0.750 ± 0.010
1842+681	S4 1842+68	Q	-0.124 ± 0.347	-0.250 ± 0.009	-0.177 ± 0.021
1849+670	S4 1849+67	Q	0.298 ± 0.236	0.089 ± 0.006	-0.226 ± 0.031
1923+210	PKS B1923+210	B	0.817 ± 0.547	-0.093 ± 0.014	-0.144 ± 0.022
1928+738	4C +73.18	Q	0.062 ± 0.154	-0.123 ± 0.005	-0.199 ± 0.011
2007+777	S5 2007+77	B	0.753 ± 0.975	-0.011 ± 0.023	0.145 ± 0.055
2021+317	4C +31.56	B	-0.115 ± 0.129	-0.181 ± 0.008	0.021 ± 0.020
2023+335	B2 2023+33	Q	2.401 ± 0.908	0.215 ± 0.020	- ± -
2029+121	PKS 2029+121	Q	-0.559 ± 0.419	-0.170 ± 0.011	-0.215 ± 0.023
2037+511	3C 418	Q	0.401 ± 0.060	-0.345 ± 0.004	-0.526 ± 0.010
2121+053	OX 036	Q	2.043 ± 1.219	0.002 ± 0.029	0.063 ± 0.051
2131-021	4C -02.81	Q	0.013 ± 0.398	-0.113 ± 0.011	-0.217 ± 0.015
2134+004	PKS 2134+004	Q	-0.653 ± 0.323	0.231 ± 0.009	0.113 ± 0.016
2136+141	OX 161	Q	-0.135 ± 0.829	0.246 ± 0.021	0.167 ± 0.036
2145+067	4C +06.69	Q	0.263 ± 0.189	-0.084 ± 0.006	-0.057 ± 0.015
2200+420	BL Lac	B	-0.966 ± 0.567	0.570 ± 0.017	0.561 ± 0.030
2201+171	PKS 2201+171	Q	-0.101 ± 0.359	-0.185 ± 0.015	-0.483 ± 0.014
2201+315	4C +31.63	Q	-1.711 ± 0.774	-0.031 ± 0.023	-0.218 ± 0.013
2209+236	PKS 2209+236	Q	0.674 ± 1.055	0.431 ± 0.018	- ± -
2223+210	DA 580	Q	3.174 ± 0.396	-0.266 ± 0.007	-0.222 ± 0.013
2230+114	CTA 102	Q	0.413 ± 0.242	-0.154 ± 0.010	0.102 ± 0.013
2234+282	CTD 135	B	-0.534 ± 0.608	0.348 ± 0.016	0.267 ± 0.051
2251+158	3C 454.3	Q	-0.007 ± 0.617	-0.084 ± 0.013	0.158 ± 0.012
2325+093	OZ 042	Q	-0.589 ± 1.616	0.001 ± 0.038	- ± -
2331+073	TXS 2331+073	Q	-0.913 ± 1.317	0.031 ± 0.036	0.049 ± 0.053
2351+456	4C +45.51	Q	-0.861 ± 0.951	0.029 ± 0.031	-0.079 ± 0.017

Table B.2.: Flux densities of the counterparts of the 1.5 Jy selected radio sample of MOJAVE in the MSSS catalog version 0.1. Here the flux density of the spectral index fit in the MSSS catalog, the flux density of the single-dish OVRO monitoring at 15 GHZ, the flux density of the radio survey NVSS (Condon et al. 1998) and the flux density of the radio survey VLSS (Cohen et al. 2007a).

Source	Type	$S_{\mathrm{MSSS150MHz}}$ (Jy)	S_{OVRO} (Jy)	S_{NVSS} (Jy)	S_{VLSS} (Jy)
0016+731	Q	0.239 ± 0.021	2.348 ± 0.037	1.136 ± 0.034	- ± -
0059+581	Q	0.713 ± 0.051	3.634 ± 0.053	0.848 ± 0.025	- ± -
0106+013	Q	7.846 ± 0.280	2.741 ± 0.037	2.621 ± 0.079	6.261 ± 0.108
0109+224	B	0.257 ± 0.035	0.570 ± 0.022	0.385 ± 0.012	- ± -
0109+351	Q	1.324 ± 0.036	0.689 ± 0.033	0.398 ± 0.012	2.555 ± 0.070
0119+115	Q	4.708 ± 0.232	2.153 ± 0.024	1.184 ± 0.035	3.827 ± 0.094
0133+476	Q	1.088 ± 0.057	3.392 ± 0.083	1.137 ± 0.034	0.631 ± 0.117
0202+149	Q	7.722 ± 0.067	1.060 ± 0.013	4.068 ± 0.122	4.504 ± 0.090
0202+319	Q	0.657 ± 0.095	1.548 ± 0.014	0.657 ± 0.020	- ± -
0212+735	Q	0.869 ± 0.084	2.853 ± 0.026	2.271 ± 0.068	0.675 ± 0.096
0215+015	Q	2.861 ± 0.060	0.666 ± 0.012	0.750 ± 0.022	1.927 ± 0.114
0224+671	Q	1.961 ± 0.046	1.032 ± 0.026	1.540 ± 0.046	1.759 ± 0.081
0229+131	Q	4.389 ± 0.103	1.882 ± 0.024	1.560 ± 0.047	4.471 ± 0.085
0234+285	Q	3.028 ± 0.370	3.629 ± 0.028	2.197 ± 0.066	2.676 ± 0.096
0235+164	Q	1.211 ± 0.059	0.956 ± 0.015	1.941 ± 0.058	0.990 ± 0.083
0241+622	Q	0.399 ± 0.053	1.346 ± 0.019	0.364 ± 0.011	- ± -
0300+470	B	0.979 ± 0.039	2.290 ± 0.019	0.963 ± 0.029	1.218 ± 0.084
0316+413	G	73.968 ± 1.876	32.069 ± 0.180	22.829 ± 0.685	81.108 ± 0.171
0333+321	Q	3.002 ± 0.079	1.490 ± 0.026	2.677 ± 0.080	1.468 ± 0.102
0336-019	Q	1.625 ± 0.050	2.979 ± 0.075	2.424 ± 0.073	1.014 ± 0.151
0355+508	Q	9.258 ± 0.091	9.530 ± 0.107	4.296 ± 0.129	11.233 ± 0.061
0400+258	Q	1.084 ± 0.041	1.465 ± 0.018	0.936 ± 0.028	0.470 ± 0.081
0415+379	G	93.254 ± 1.462	4.099 ± 0.048	7.726 ± 0.236	38.756 ± 0.209
0420-014	Q	1.948 ± 0.282	5.684 ± 0.081	2.726 ± 0.082	1.661 ± 0.093
0422+004	B	0.801 ± 0.089	0.387 ± 0.015	0.493 ± 0.015	0.471 ± 0.093
0430+052	G	17.381 ± 0.323	2.391 ± 0.135	3.439 ± 0.103	6.163 ± 0.111
0440-003	Q	3.007 ± 0.195	1.912 ± 0.034	1.773 ± 0.053	2.383 ± 0.106
0446+112	Q	1.405 ± 0.150	0.892 ± 0.022	0.847 ± 0.025	0.803 ± 0.116
0458-020	Q	6.102 ± 0.341	1.720 ± 0.033	2.264 ± 0.068	3.311 ± 0.132
0528+134	Q	1.325 ± 0.188	1.394 ± 0.023	1.556 ± 0.047	1.336 ± 0.146
0529+075	Q	4.415 ± 0.246	1.462 ± 0.009	2.729 ± 0.082	1.945 ± 0.118
0529+483	Q	0.962 ± 0.077	1.102 ± 0.020	0.434 ± 0.013	0.966 ± 0.079
0552+398	Q	0.178 ± 0.029	- ± -	1.516 ± 0.045	- ± -
0642+449	Q	0.234 ± 0.028	2.462 ± 0.017	0.452 ± 0.014	- ± -
0716+714	B	2.822 ± 0.063	1.291 ± 0.012	0.727 ± 0.022	4.023 ± 0.074
0723-008	B	3.216 ± 0.175	5.739 ± 0.106	1.399 ± 0.042	2.675 ± 0.117
0730+504	Q	0.993 ± 0.041	0.615 ± 0.032	0.770 ± 0.023	0.985 ± 0.067
0735+178	B	2.026 ± 0.066	1.069 ± 0.018	2.258 ± 0.068	2.206 ± 0.091
0736+017	Q	3.303 ± 0.179	1.039 ± 0.016	1.964 ± 0.059	1.165 ± 0.115
0738+313	Q	1.172 ± 0.049	2.163 ± 0.036	2.284 ± 0.069	1.005 ± 0.074
0742+103	Q	3.440 ± 0.066	1.383 ± 0.011	3.506 ± 0.105	3.514 ± 0.078
0745+241	Q	2.485 ± 0.028	0.976 ± 0.031	0.958 ± 0.029	3.014 ± 0.085

0748+126	Q	2.390 ± 0.034	2.537 ± 0.051	1.453 ± 0.044	3.056 ± 0.085
0754+100	B	1.384 ± 0.150	0.990 ± 0.021	0.956 ± 0.034	1.322 ± 0.087
0804+499	Q	0.380 ± 0.051	0.674 ± 0.011	1.115 ± 0.033	- ± -
0808+019	B	1.092 ± 0.088	0.404 ± 0.021	0.598 ± 0.024	0.743 ± 0.109
0814+425	B	2.163 ± 0.020	0.759 ± 0.016	1.091 ± 0.033	1.966 ± 0.062
0821+033	Q	5.893 ± 0.098	1.106 ± 0.014	1.481 ± 0.044	5.853 ± 0.069
0823+033	B	0.997 ± 0.069	0.651 ± 0.013	1.400 ± 0.042	0.724 ± 0.129
0827+243	Q	1.121 ± 0.035	1.141 ± 0.058	0.739 ± 0.022	1.306 ± 0.075
0829+046	B	0.963 ± 0.078	0.599 ± 0.015	1.241 ± 0.044	1.591 ± 0.105
0836+710	Q	4.727 ± 0.070	2.321 ± 0.018	3.823 ± 0.115	5.020 ± 0.100
0838+133	Q	22.685 ± 0.154	1.573 ± 0.064	2.613 ± 0.078	19.731 ± 0.172
0851+202	B	0.747 ± 0.075	4.122 ± 0.119	1.512 ± 0.045	0.800 ± 0.077
0906+015	Q	1.679 ± 0.057	2.125 ± 0.029	0.760 ± 0.023	1.160 ± 0.112
0917+449	Q	1.478 ± 0.027	1.360 ± 0.018	1.017 ± 0.030	1.848 ± 0.079
0917+624	Q	1.352 ± 0.040	1.412 ± 0.012	0.946 ± 0.028	1.308 ± 0.072
0923+392	Q	7.096 ± 0.161	9.541 ± 0.101	2.885 ± 0.086	10.369 ± 0.084
0945+408	Q	2.777 ± 0.063	1.016 ± 0.024	1.599 ± 0.048	3.334 ± 0.075
0954+658	Q	0.627 ± 0.046	1.176 ± 0.024	0.729 ± 0.022	0.712 ± 0.074
0955+476	Q	0.342 ± 0.038	1.036 ± 0.012	0.604 ± 0.018	- ± -
1030+415	Q	1.263 ± 0.046	1.270 ± 0.020	0.473 ± 0.014	1.017 ± 0.081
1036+054	Q	1.281 ± 0.140	1.081 ± 0.024	0.640 ± 0.019	1.403 ± 0.103
1038+064	Q	2.703 ± 0.139	1.007 ± 0.021	1.405 ± 0.042	1.416 ± 0.097
1055+018	Q	9.782 ± 0.238	2.602 ± 0.068	3.220 ± 0.097	6.231 ± 0.143
1128+385	Q	0.758 ± 0.125	1.281 ± 0.025	0.702 ± 0.021	- ± -
1150+497	Q	8.185 ± 0.101	2.030 ± 0.040	1.572 ± 0.047	11.482 ± 0.088
1150+812	Q	2.756 ± 0.052	0.956 ± 0.023	1.343 ± 0.040	2.269 ± 0.079
1156+295	Q	6.551 ± 0.121	1.128 ± 0.013	2.031 ± 0.072	6.149 ± 0.147
1219+044	G	2.936 ± 0.184	1.067 ± 0.021	0.800 ± 0.024	1.944 ± 0.152
1222+216	Q	7.707 ± 0.135	3.017 ± 0.041	2.094 ± 0.074	9.133 ± 0.171
1226+023	Q	90.774 ± 2.426	19.150 ± 0.117	54.991 ± 1.900	161.687 ± 0.189
1228+126	G	470.012 ± 20.792	25.464 ± 0.155	138.487 ± 4.859	503.208 ± 0.843
1308+326	Q	2.991 ± 0.037	2.041 ± 0.039	1.687 ± 0.051	1.845 ± 0.104
1324+224	Q	0.525 ± 0.063	0.956 ± 0.020	0.850 ± 0.025	- ± -
1413+135	B	1.718 ± 0.220	0.524 ± 0.042	1.092 ± 0.033	0.551 ± 0.101
1417+385	Q	0.301 ± 0.043	0.790 ± 0.005	0.612 ± 0.018	- ± -
1435+638	Q	1.001 ± 0.040	1.203 ± 0.013	0.951 ± 0.029	1.166 ± 0.080
1458+718	Q	38.888 ± 0.244	1.276 ± 0.020	7.468 ± 0.224	42.068 ± 0.102
1502+106	Q	3.878 ± 0.260	1.076 ± 0.013	1.774 ± 0.053	1.266 ± 0.136
1538+149	B	7.746 ± 0.076	1.145 ± 0.008	1.387 ± 0.042	6.386 ± 0.089
1546+027	Q	2.543 ± 0.635	1.270 ± 0.027	0.835 ± 0.029	- ± -
1548+056	Q	4.686 ± 0.261	2.402 ± 0.056	2.303 ± 0.069	4.594 ± 0.127
1611+343	Q	2.494 ± 0.094	4.190 ± 0.025	4.024 ± 0.121	2.346 ± 0.073
1633+382	Q	3.039 ± 0.100	3.912 ± 0.030	2.726 ± 0.082	3.667 ± 0.083
1637+574	Q	2.005 ± 0.044	1.244 ± 0.013	1.199 ± 0.036	3.002 ± 0.063
1638+398	Q	0.615 ± 0.053	1.096 ± 0.021	0.976 ± 0.034	- ± -
1641+399	Q	12.631 ± 0.221	6.432 ± 0.087	7.099 ± 0.213	11.095 ± 0.213
1642+690	Q	3.593 ± 0.045	3.495 ± 0.021	1.720 ± 0.052	5.217 ± 0.075
1655+077	Q	3.784 ± 0.344	1.512 ± 0.045	1.413 ± 0.042	3.317 ± 0.151
1726+455	Q	0.602 ± 0.078	0.689 ± 0.031	0.914 ± 0.027	- ± -
1739+522	Q	0.821 ± 0.057	1.251 ± 0.015	0.807 ± 0.024	1.019 ± 0.133

1749+096	B	0.914 ± 0.098	3.114 ± 0.031	0.623 ± 0.019	- ± -
1800+440	Q	2.562 ± 0.078	0.890 ± 0.019	0.727 ± 0.022	2.797 ± 0.090
1803+784	B	2.528 ± 0.044	2.242 ± 0.031	2.223 ± 0.067	0.771 ± 0.083
1807+698	B	6.283 ± 0.072	1.569 ± 0.030	1.886 ± 0.073	4.144 ± 0.064
1823+568	B	3.550 ± 0.031	1.270 ± 0.012	1.412 ± 0.042	6.505 ± 0.091
1828+487	Q	82.647 ± 0.762	3.447 ± 0.098	13.752 ± 0.413	124.719 ± 0.150
1842+681	Q	1.275 ± 0.045	0.403 ± 0.007	0.798 ± 0.024	1.344 ± 0.072
1849+670	Q	1.090 ± 0.025	1.639 ± 0.024	0.517 ± 0.015	1.005 ± 0.088
1923+210	B	2.187 ± 0.132	1.426 ± 0.034	1.199 ± 0.036	1.830 ± 0.102
1928+738	Q	5.964 ± 0.099	3.385 ± 0.045	3.950 ± 0.118	7.084 ± 0.090
2007+777	B	0.860 ± 0.091	0.816 ± 0.007	1.060 ± 0.037	0.691 ± 0.109
2021+317	B	3.199 ± 0.052	1.389 ± 0.046	3.368 ± 0.101	3.169 ± 0.162
2023+335	Q	1.007 ± 0.091	2.715 ± 0.037	1.268 ± 0.038	- ± -
2029+121	Q	2.099 ± 0.098	0.957 ± 0.020	0.985 ± 0.029	1.855 ± 0.113
2037+511	Q	18.507 ± 0.152	3.785 ± 0.053	6.081 ± 0.182	28.528 ± 0.120
2121+053	Q	1.333 ± 0.179	1.343 ± 0.021	0.793 ± 0.024	0.660 ± 0.097
2131-021	Q	3.551 ± 0.180	2.107 ± 0.029	1.690 ± 0.060	3.200 ± 0.077
2134+004	Q	2.320 ± 0.100	6.724 ± 0.044	3.473 ± 0.104	2.491 ± 0.086
2136+141	Q	0.693 ± 0.066	2.149 ± 0.040	1.131 ± 0.034	0.692 ± 0.070
2145+067	Q	4.988 ± 0.108	3.392 ± 0.047	2.589 ± 0.091	3.065 ± 0.083
2200+420	B	0.653 ± 0.043	9.000 ± 0.415	6.051 ± 0.181	1.163 ± 0.095
2201+171	Q	1.826 ± 0.077	0.779 ± 0.043	0.592 ± 0.018	2.450 ± 0.066
2201+315	Q	3.278 ± 0.344	2.842 ± 0.039	2.878 ± 0.099	5.466 ± 0.090
2209+236	Q	0.156 ± 0.013	1.140 ± 0.016	0.556 ± 0.017	- ± -
2223+210	Q	3.001 ± 0.085	0.881 ± 0.010	1.837 ± 0.055	3.524 ± 0.086
2230+114	Q	7.154 ± 0.233	3.519 ± 0.104	7.202 ± 0.216	5.340 ± 0.117
2234+282	B	0.280 ± 0.020	1.392 ± 0.031	1.103 ± 0.033	0.503 ± 0.074
2251+158	Q	7.351 ± 0.415	4.982 ± 0.093	12.657 ± 0.380	7.960 ± 0.131
2325+093	Q	0.524 ± 0.088	0.527 ± 0.023	0.741 ± 0.022	- ± -
2331+073	Q	0.498 ± 0.082	0.574 ± 0.008	0.631 ± 0.019	0.546 ± 0.083
2351+456	Q	0.731 ± 0.104	0.835 ± 0.019	1.872 ± 0.056	2.361 ± 0.091

B.2. Plots of MSSS spectra

All flux densities and the fit for the spectral index are based on the preliminary MSSS catalog version 0.1
The different colors represent the different source finders used in MSSS and the flux densities obtained with interpolation by Arshakian et al. (2010):

- black data points are used if both source finders of MSSS (PyBDSM and PySE) matched with the source fits
- blue data points are the results of the source finder PyBDSM which is also used for spectral index fits
- green data points are the result of source finder PySE which is used as consistency check of PyBDSM
- yellow triangles mark the flux density of the interpolated flux density at 151 by Arshakian et al. (2010)

The difference in the two source finders is, that PySE was developed for transients and is conceived to detect unresolved sources, while PyBDSM uses Gaussian elliptical components to fit sources with diffuse as well as compact emission. For this reason PySE is not best suited for extended sources and may miss some flux for those sources.

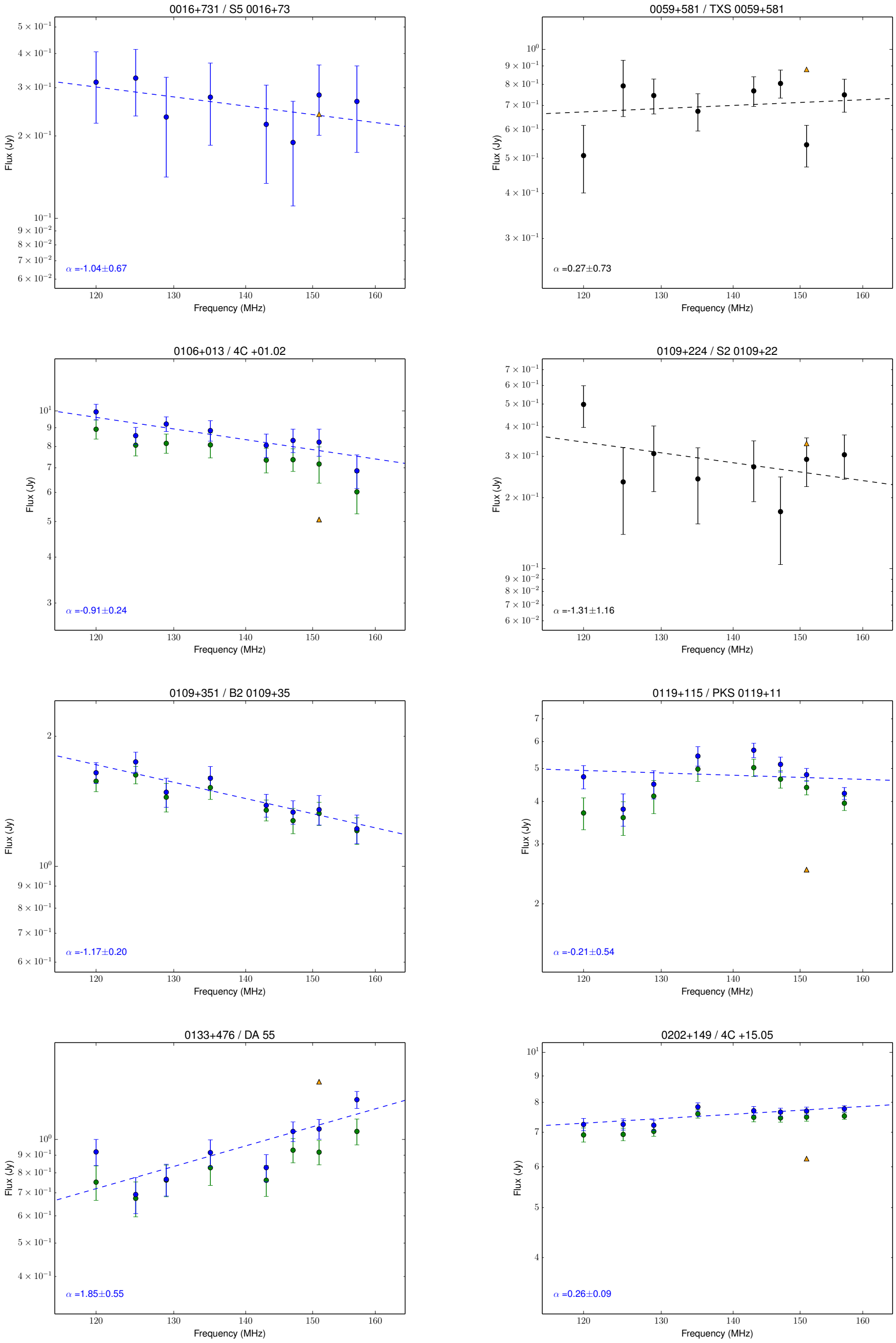

Figure B.1.: MSSS spectra for the sources: 0016+731, 0059+581, 0106+013, 0109+224, 0109+351, 0119+115, 0133+476 and 0202+149. The orange triangles correspond to the flux densities interpolated by Arshakian et al. (2010), the other colors represent different source finding tools: black for consisent results of both tools, blue for the results of PyBDSM, which was used for the spectral index fit and green for the results of PySE.

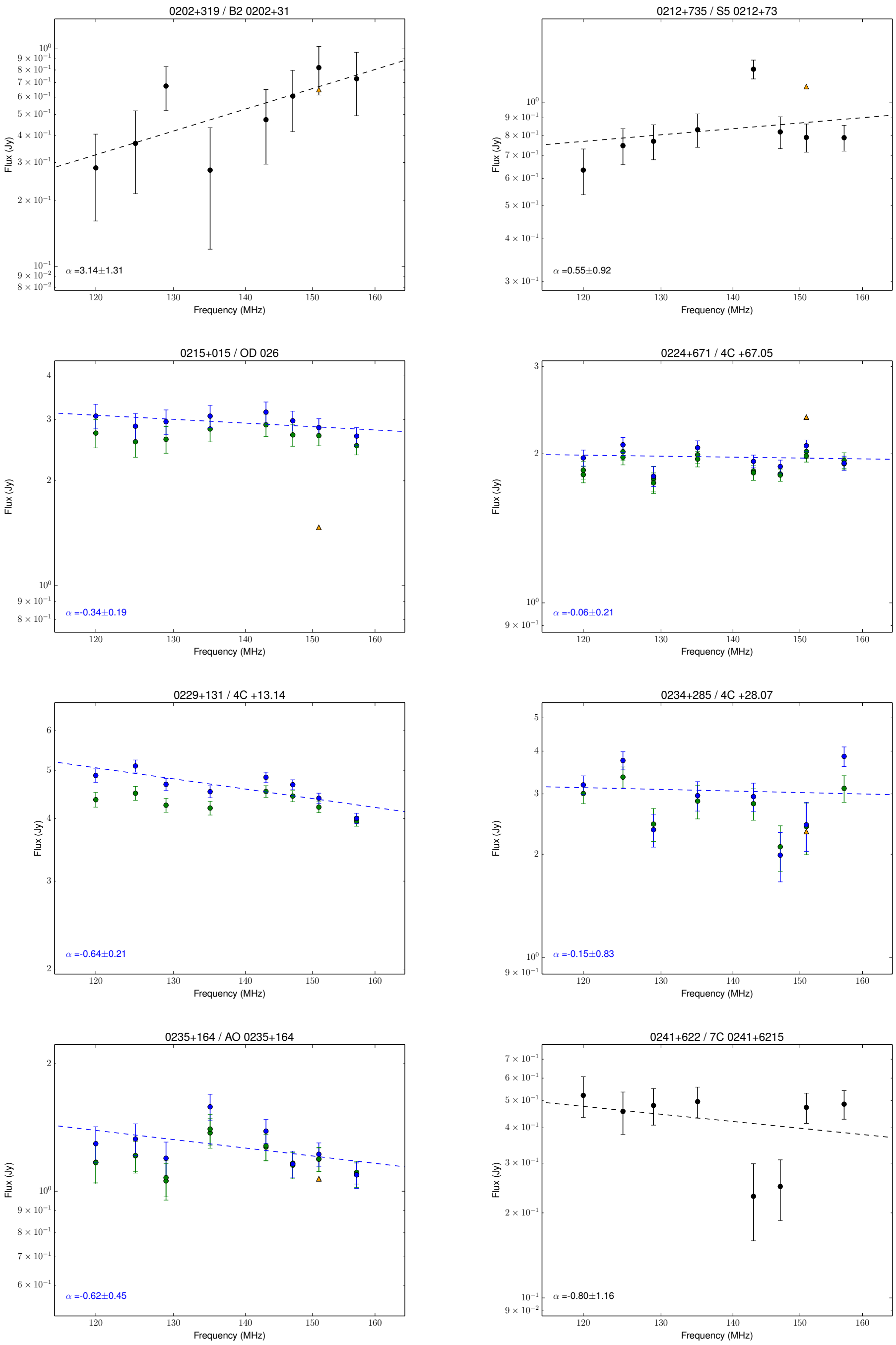

Figure B.2.: MSSS spectra for the sources: 0202+319, 0212+735, 0215+015, 0224+671, 0229+131, 0234+285, 0235+164 and 0241+622. The orange triangles correspond to the flux densities interpolated by Arshakian et al. (2010), the other colors represent different source finding tools: black for consisent results of both tools, blue for the results of PyBDSM, which was used for the spectral index fit and green for the results of PySE.

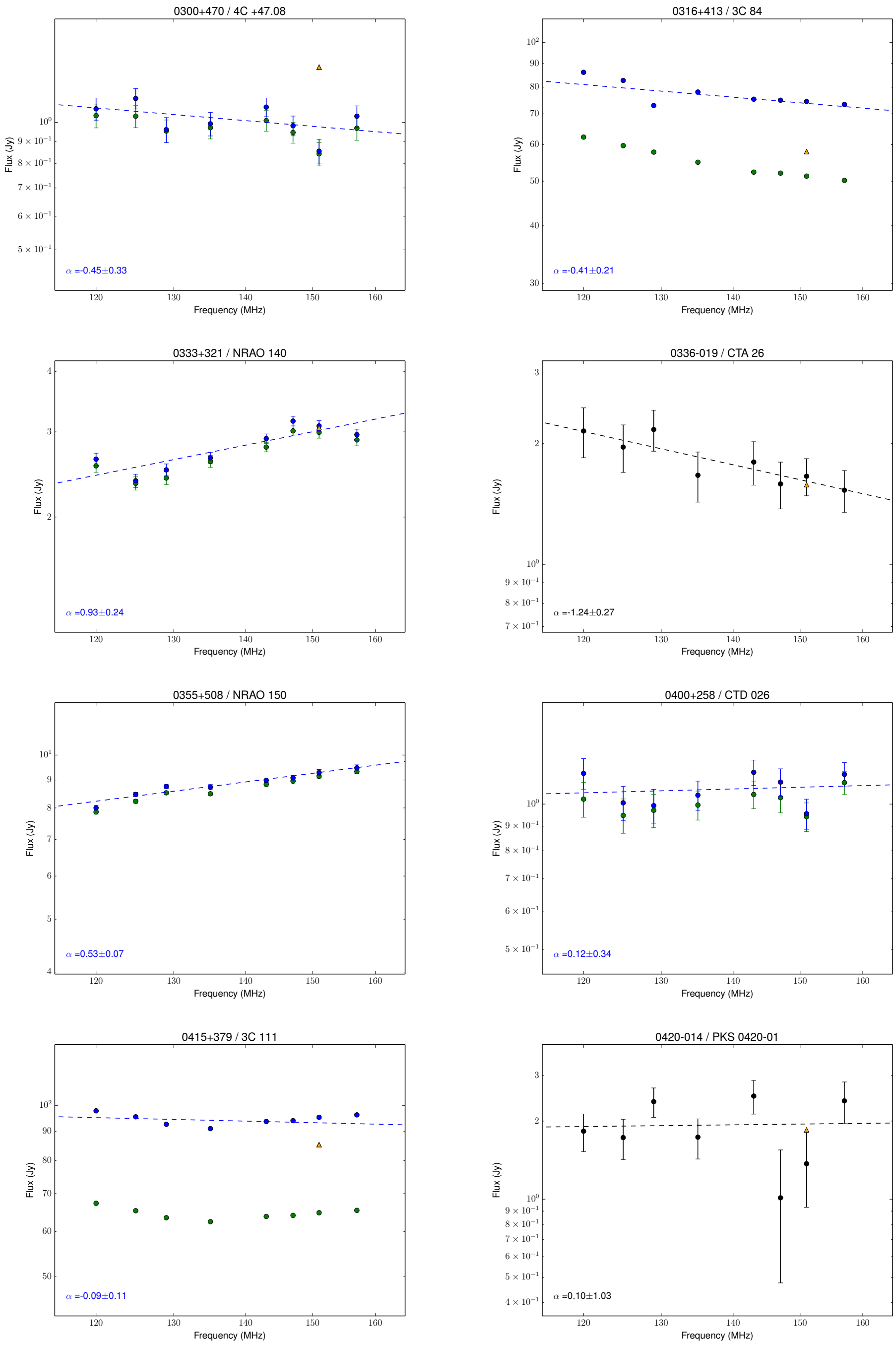

Figure B.3.: MSSS spectra for the sources: 0300+470, 0316+413, 0333+321, 0336-019, 0355+508, 0400+258, 0415+379 and 0420-014. The orange triangles correspond to the flux densities interpolated by Arshakian et al. (2010), the other colors represent different source finding tools: black for consisent results of both tools, blue for the results of PyBDSM, which was used for the spectral index fit and green for the results of PySE.

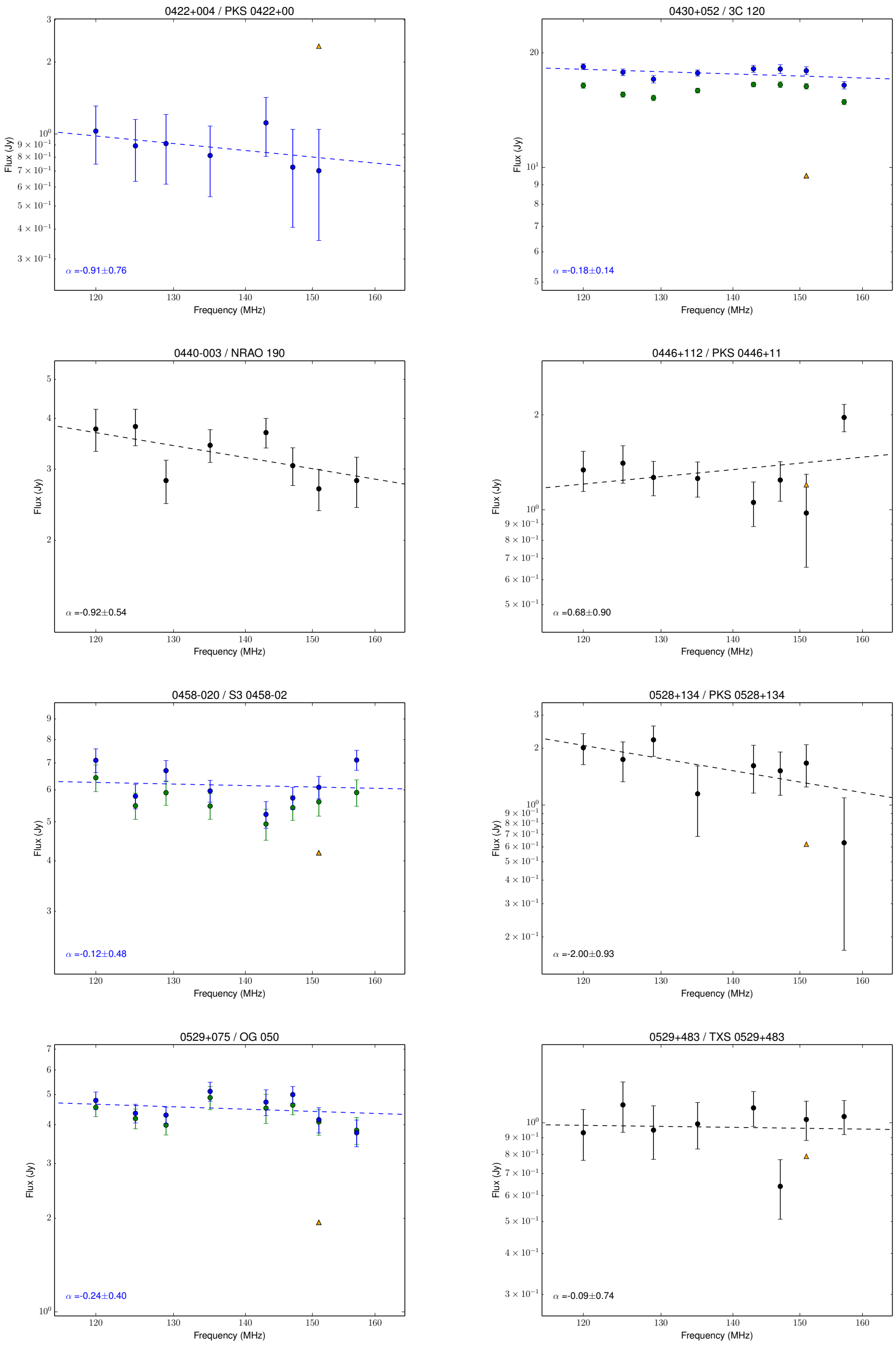

Figure B.4.: MSSS spectra for the sources: 0422+004, 0430+052, 0440-003, 0446+112, 0458-020, 0528+134, 0529+075 and 0529+483. The orange triangles correspond to the flux densities interpolated by Arshakian et al. (2010), the other colors represent different source finding tools: black for consisent results of both tools, blue for the results of PyBDSM, which was used for the spectral index fit and green for the results of PySE.

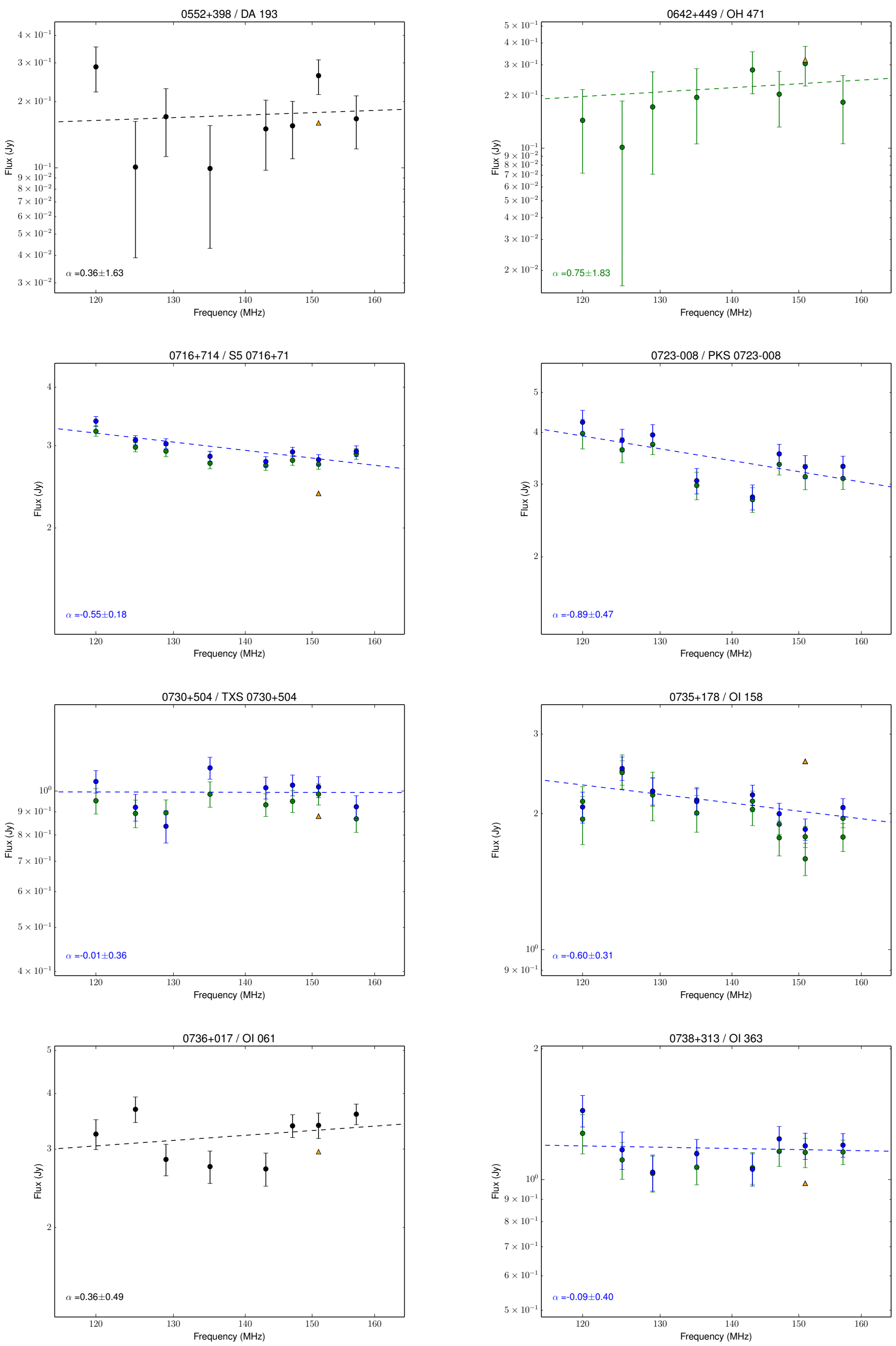

Figure B.5.: MSSS spectra for the sources: 0552+398, 0642+449, 0716+714, 0723-008, 0730+504, 0735+178, 0736+017 and 0738+313. The orange triangles correspond to the flux densities interpolated by Arshakian et al. (2010), the other colors represent different source finding tools: black for consisent results of both tools, blue for the results of PyBDSM, which was used for the spectral index fit and green for the results of PySE.

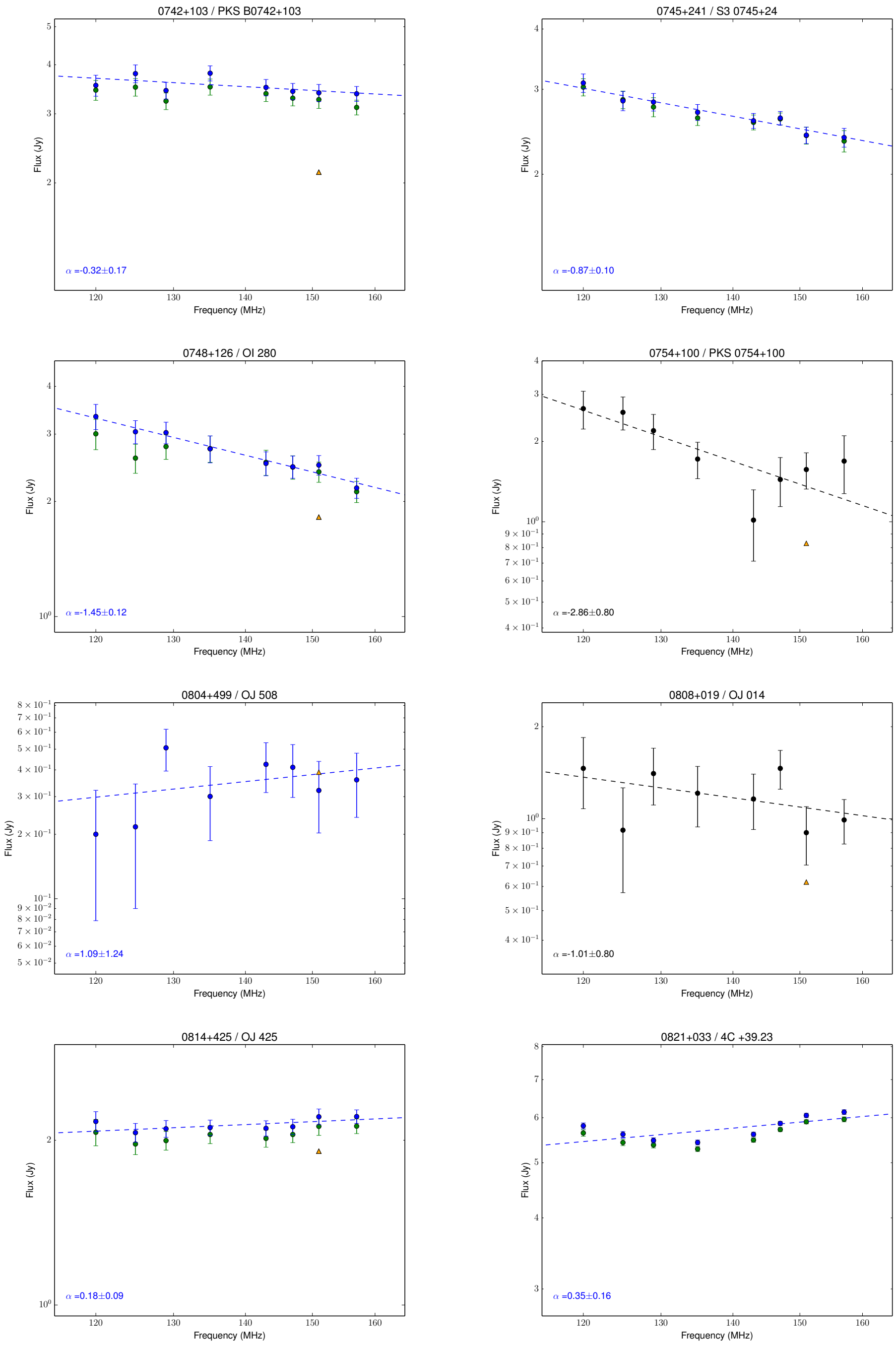

Figure B.6.: MSSS spectra for the sources: 0742+103, 0745+241, 0748+126, 0754+100, 0804+499, 0808+019, 0814+425 and 0821+033. The orange triangles correspond to the flux densities interpolated by Arshakian et al. (2010), the other colors represent different source finding tools: black for consisent results of both tools, blue for the results of PyBDSM, which was used for the spectral index fit and green for the results of PySE.

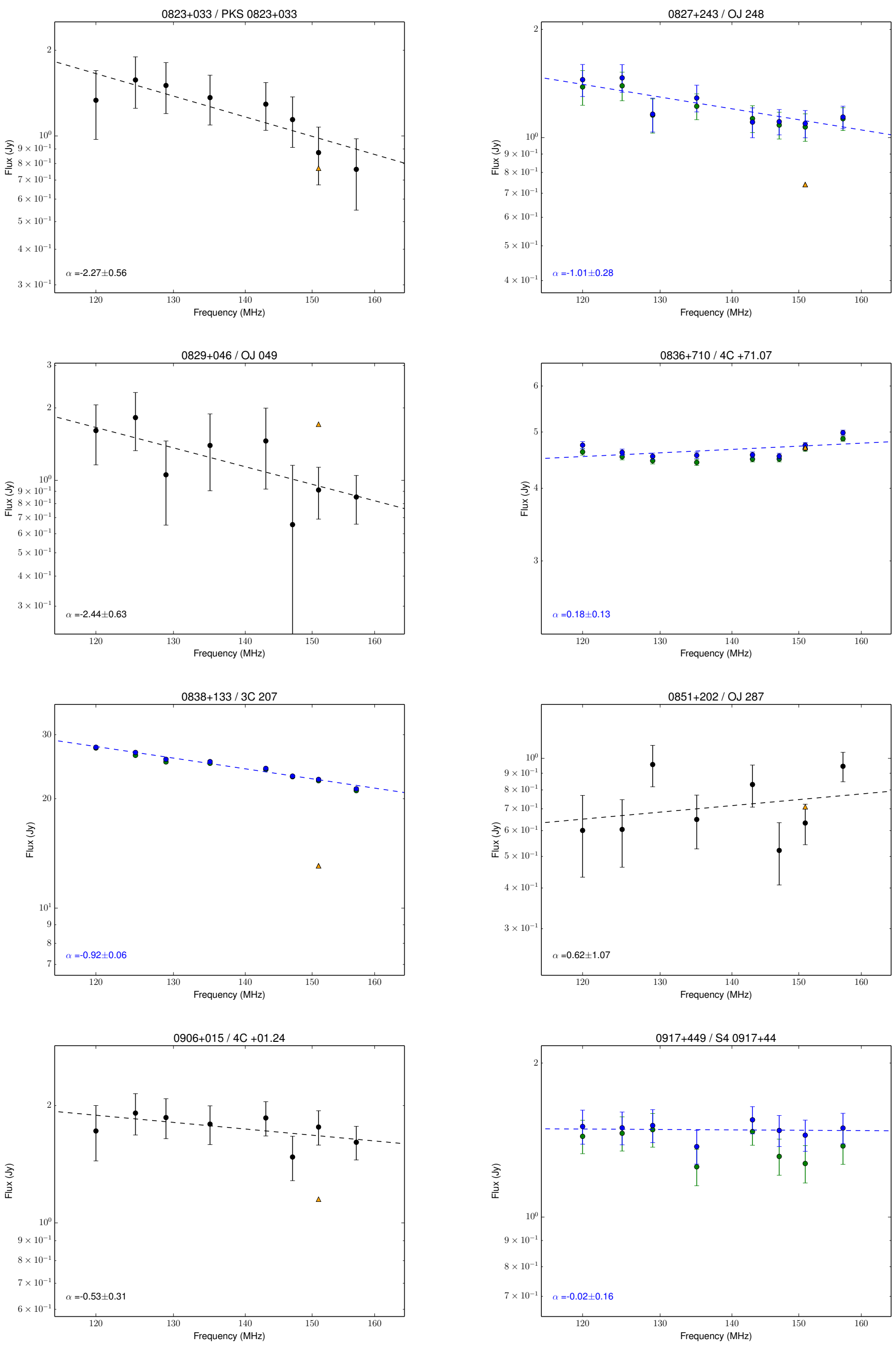

Figure B.7.: MSSS spectra for the sources: 0823+033, 0827+243, 0829+046, 0836+710, 0838+133, 0851+202, 0906+015 and 0917+449. The orange triangles correspond to the flux densities interpolated by Arshakian et al. (2010), the other colors represent different source finding tools: black for consisent results of both tools, blue for the results of PyBDSM, which was used for the spectral index fit and green for the results of PySE.

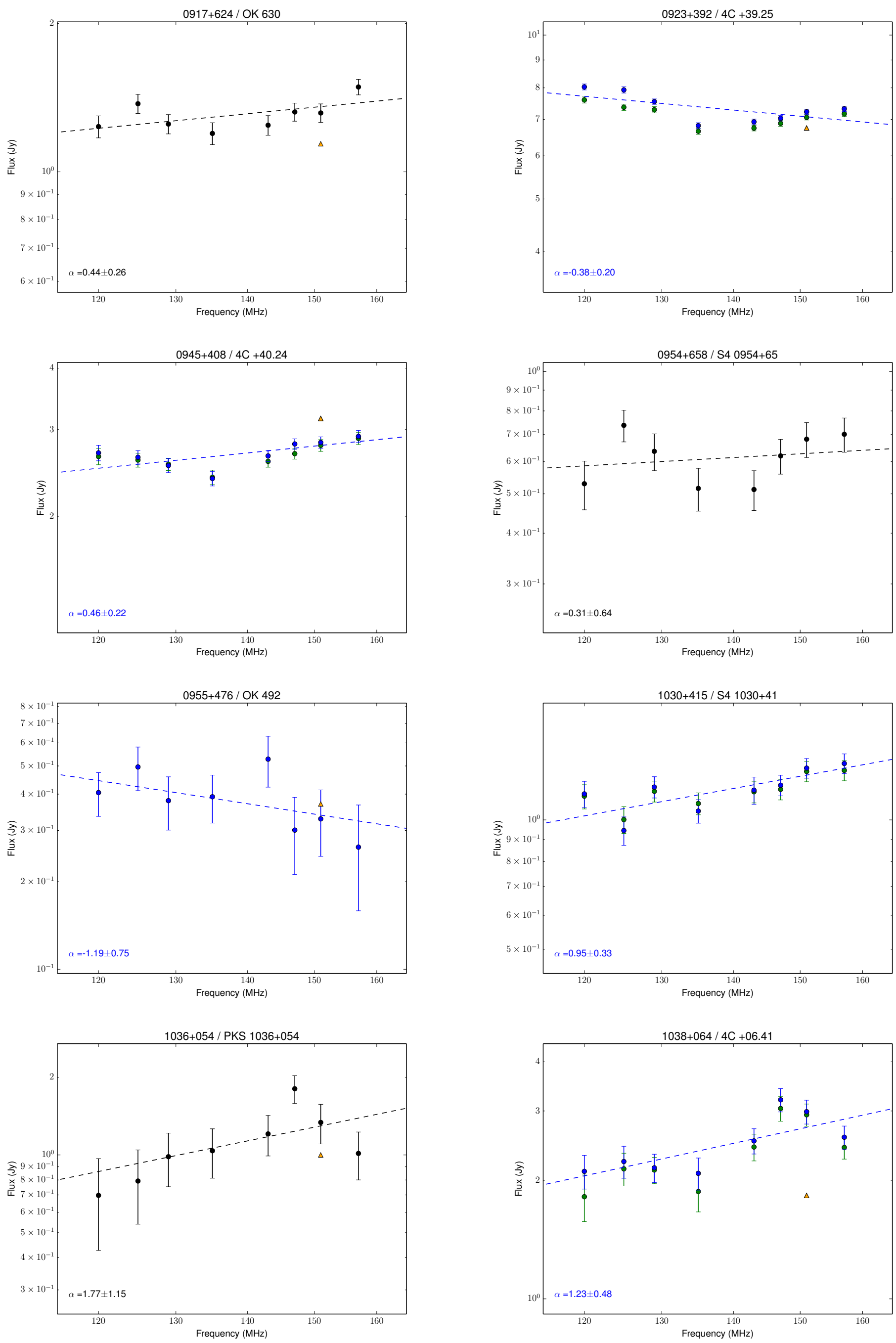

Figure B.8.: MSSS spectra for the sources: 0917+624, 0923+392, 0945+408, 0954+658, 0955+476, 1030+415, 1036+054 and 1038+064. The orange triangles correspond to the flux densities interpolated by Arshakian et al. (2010), the other colors represent different source finding tools: black for consisent results of both tools, blue for the results of PyBDSM, which was used for the spectral index fit and green for the results of PySE.

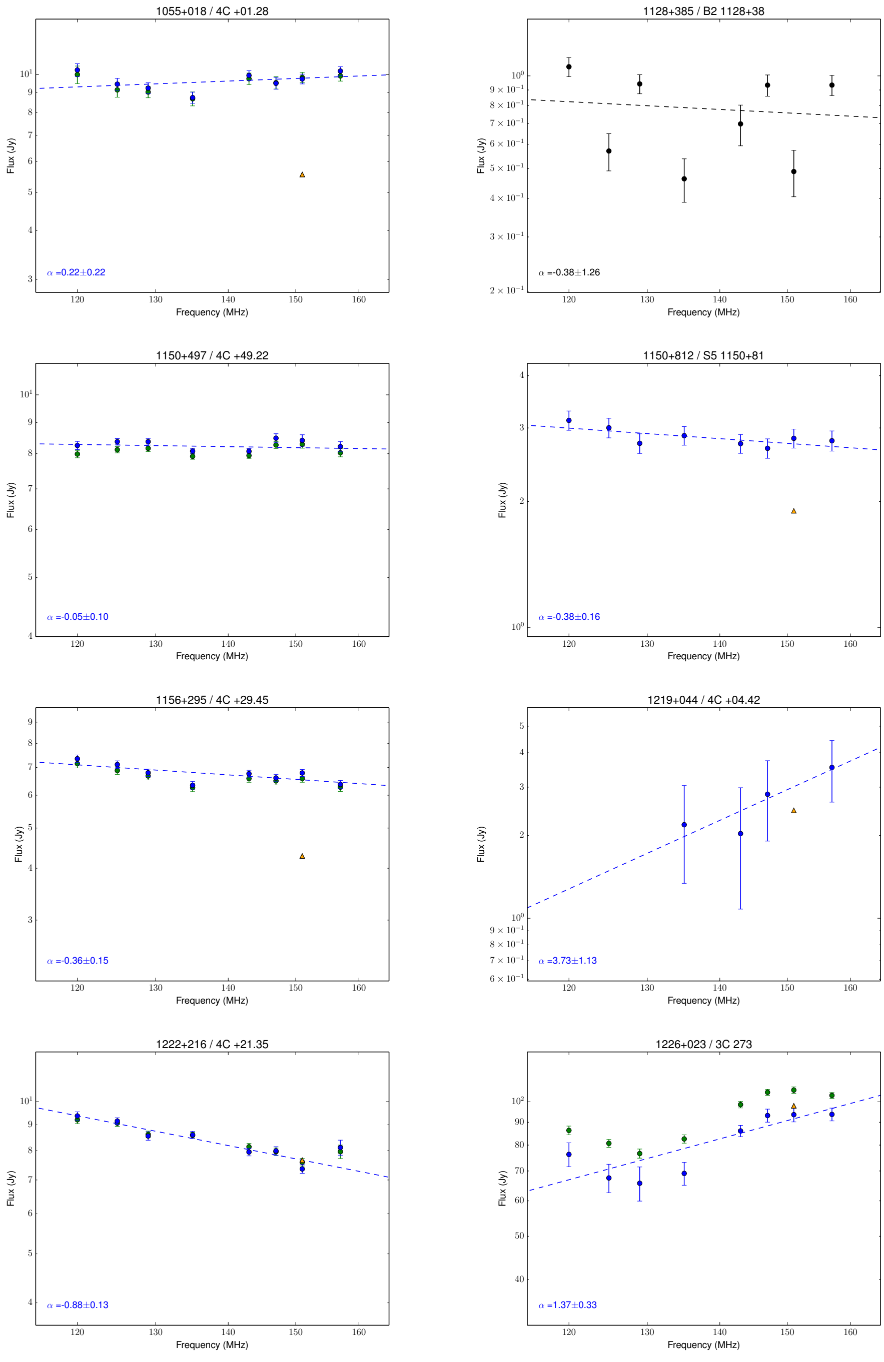

Figure B.9.: MSSS spectra for the sources: 1055+018, 1128+385, 1150+497, 1150+812, 1156+295, 1219+044, 1222+216, 1226+023. The orange triangles correspond to the flux densities interpolated by Arshakian et al. (2010), the other colors represent different source finding tools: black for consisent results of both tools, blue for the results of PyBDSM, which was used for the spectral index fit and green for the results of PySE.

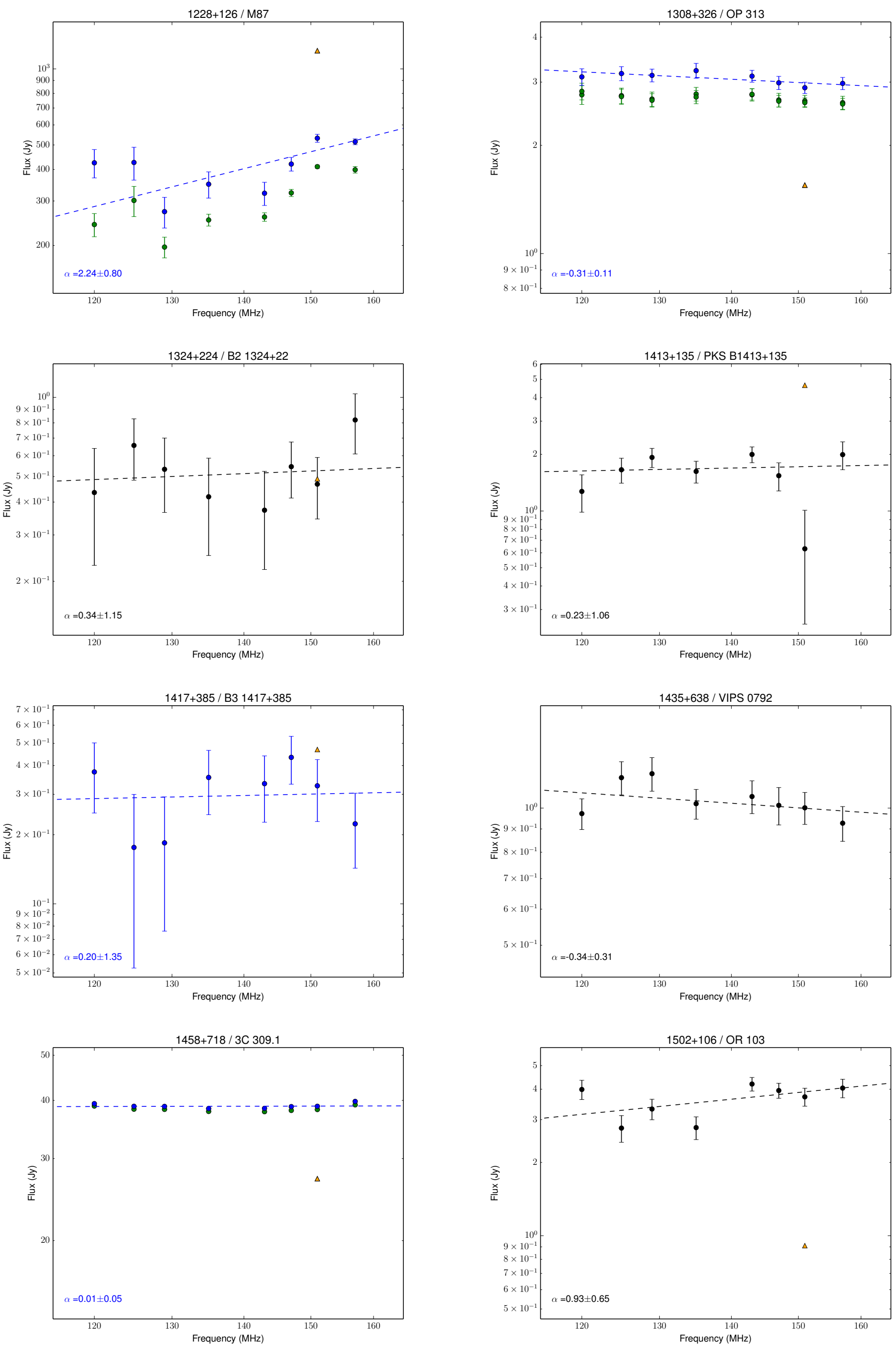

Figure B.10.: MSSS spectra for the sources: 1228+126, 1308+326, 1324+224, 1413+135, 1417+385, 1435+638, 1458+718 and 1502+106. The orange triangles correspond to the flux densities interpolated by Arshakian et al. (2010), the other colors represent different source finding tools: black for consisent results of both tools, blue for the results of PyBDSM, which was used for the spectral index fit and green for the results of PySE.

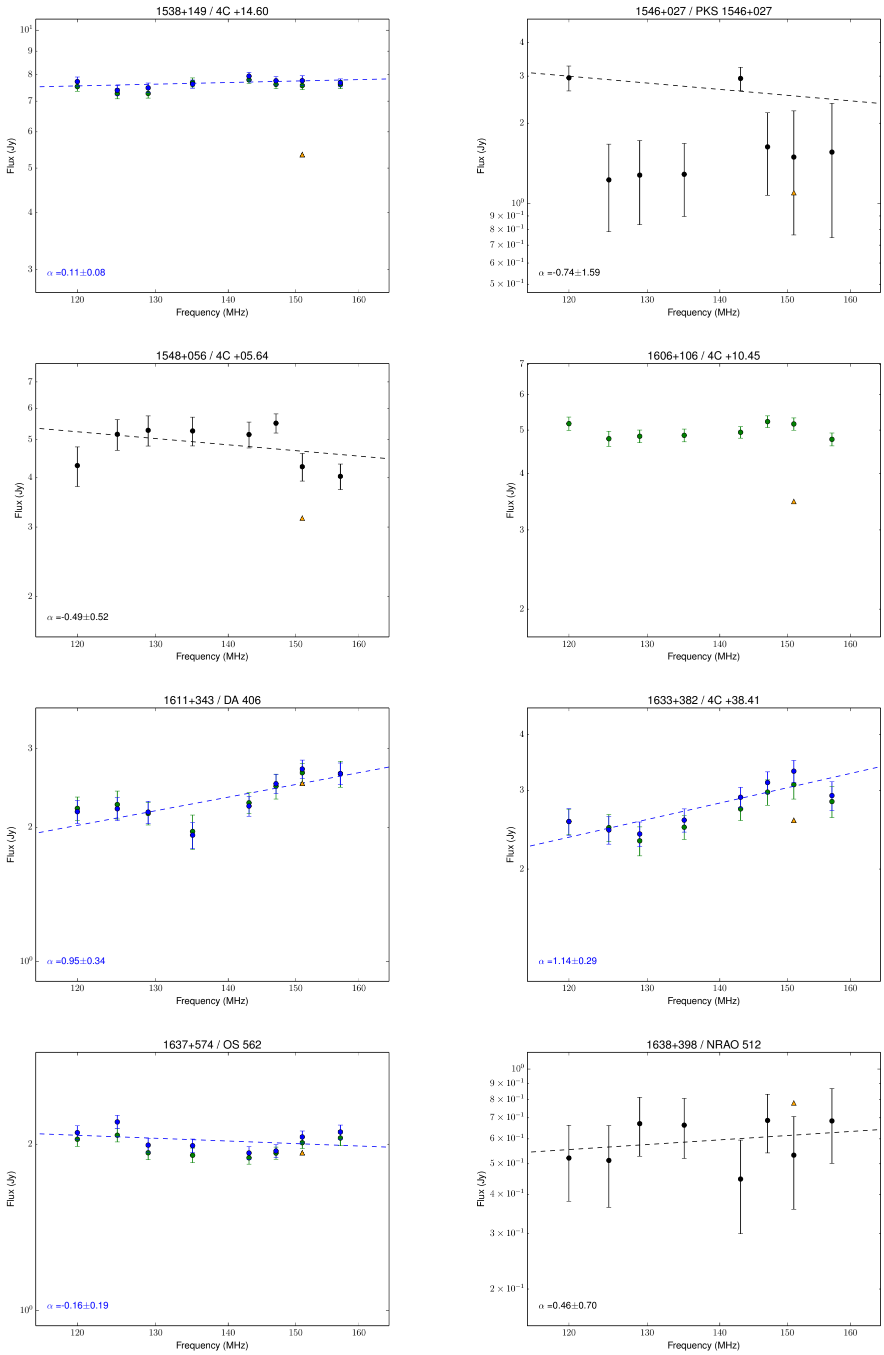

Figure B.11.: MSSS spectra for the sources: 1538+149, 1546+027, 1548+056, 1606+106, 1611+343, 1633+382, 1637+574 and 1638+398. The orange triangles correspond to the flux densities interpolated by Arshakian et al. (2010), the other colors represent different source finding tools: black for consisent results of both tools, blue for the results of PyBDSM, which was used for the spectral index fit and green for the results of PySE.

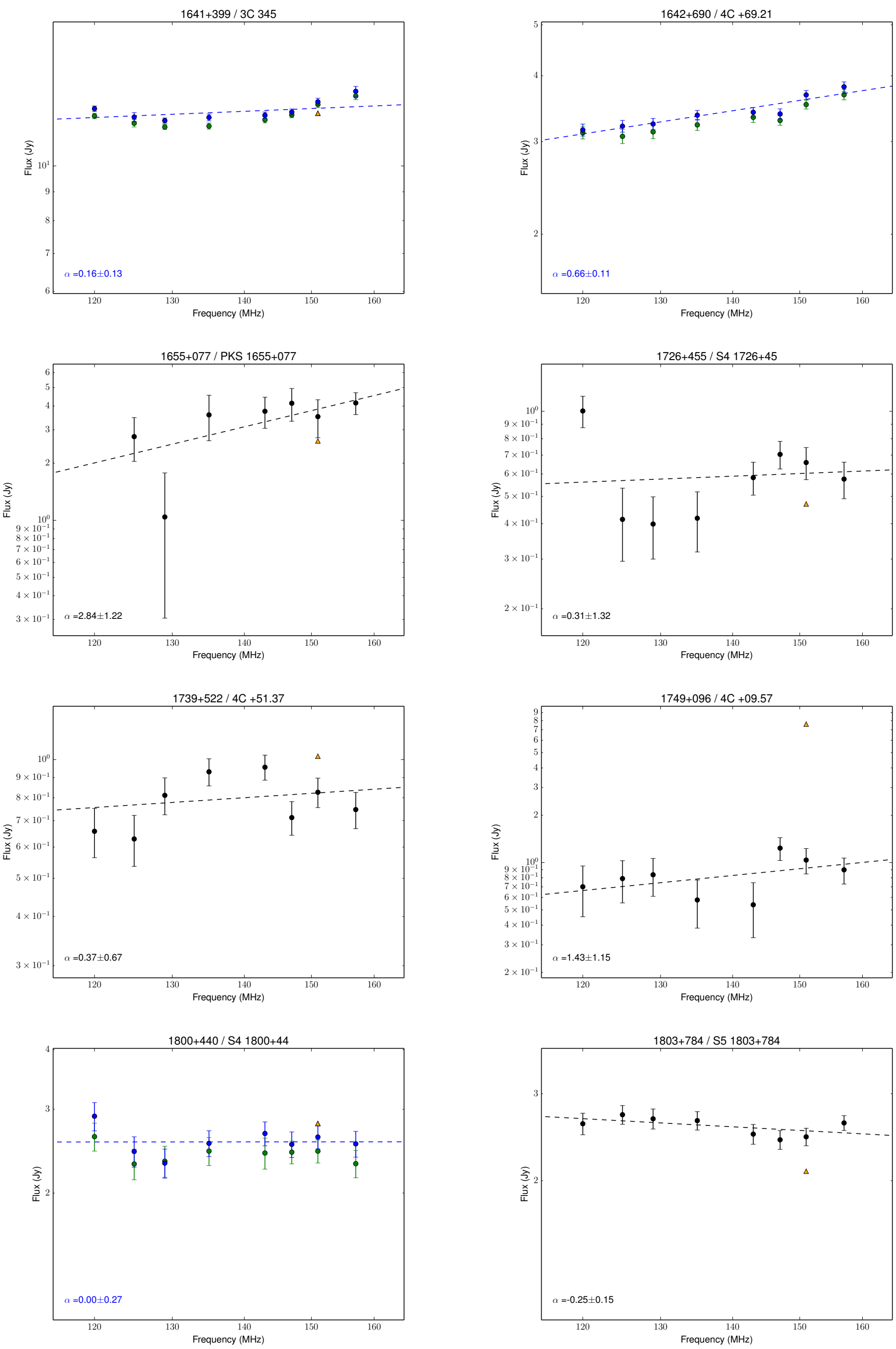

Figure B.12.: MSSS spectra for the sources: 1641+399, 1642+690, 1655+077, 1726+455, 1739+522, 1749+096, 1800+440 and 1803+784. The orange triangles correspond to the flux densities interpolated by Arshakian et al. (2010), the other colors represent different source finding tools: black for consisent results of both tools, blue for the results of PyBDSM, which was used for the spectral index fit and green for the results of PySE.

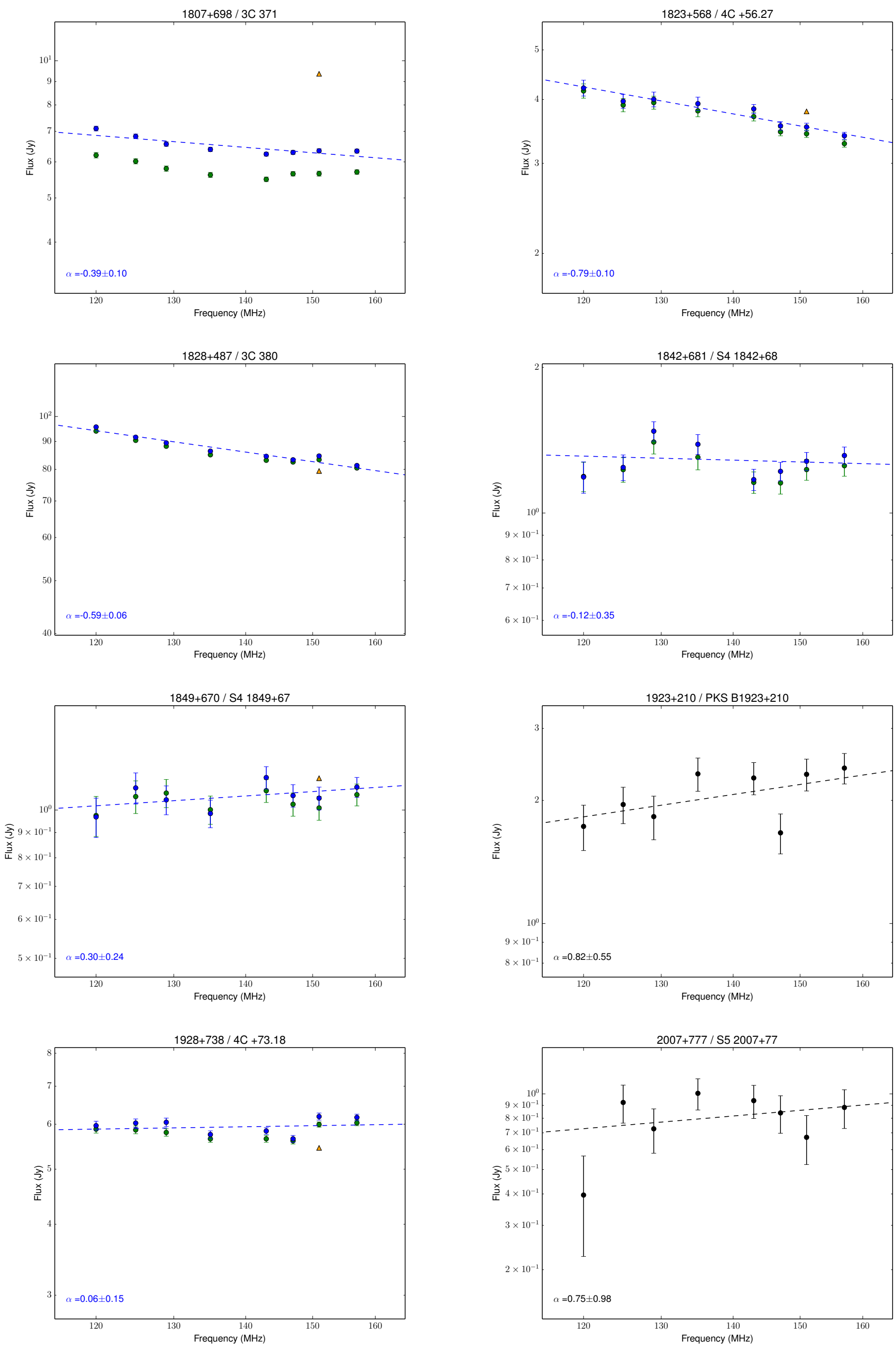

Figure B.13.: MSSS spectra for the sources: 1807+698, 1823+568, 1828+487, 1842+681, 1849+670, 1923+210, 1928+738 and 2007+777. The orange triangles correspond to the flux densities interpolated by Arshakian et al. (2010), the other colors represent different source finding tools: black for consisent results of both tools, blue for the results of PyBDSM, which was used for the spectral index fit and green for the results of PySE.

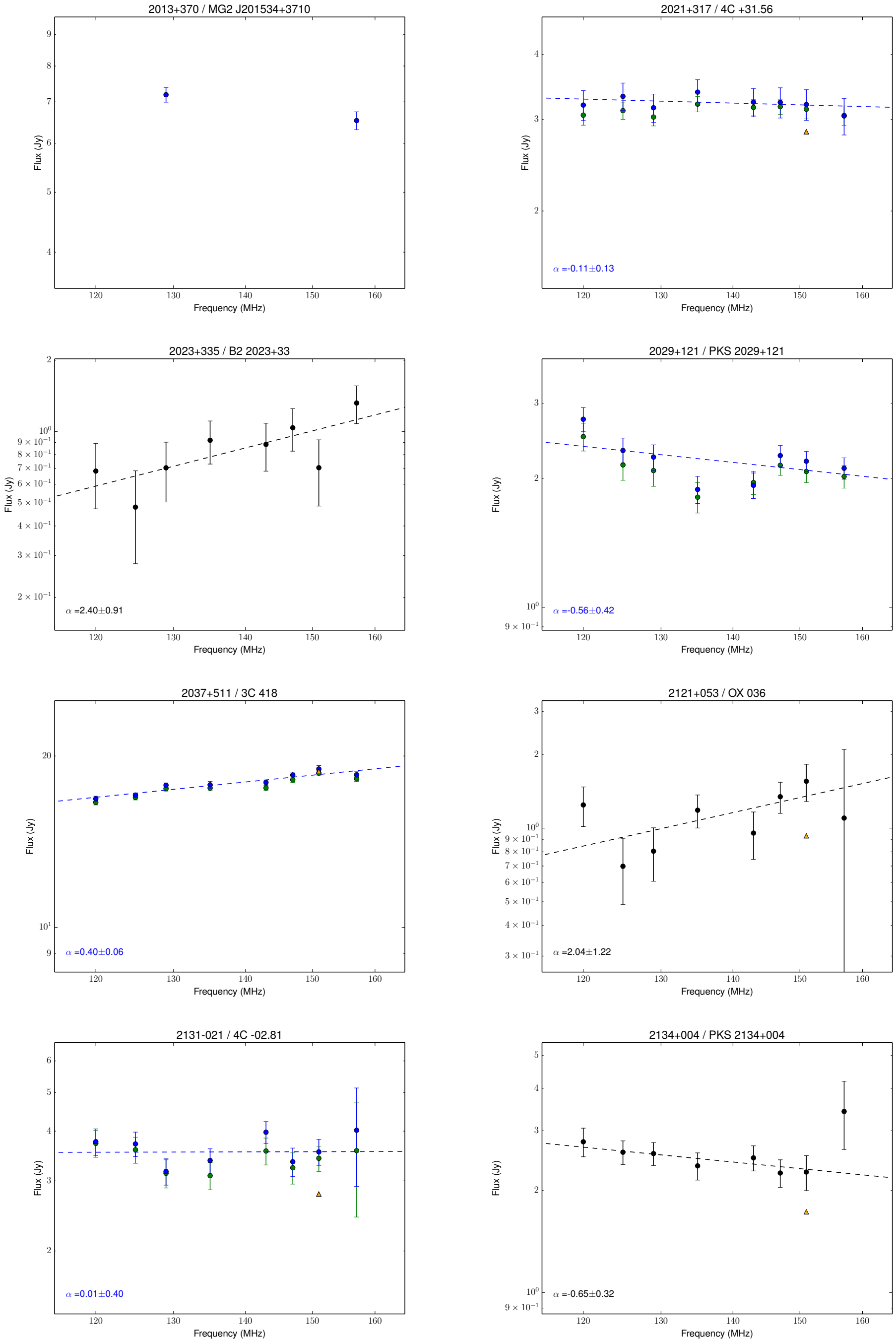

Figure B.14.: MSSS spectra for the sources: 2013+370, 2021+317, 2023+335, 2029+121, 2037+511, 2121+053, 2131-021 and 2134+004. The orange triangles correspond to the flux densities interpolated by Arshakian et al. (2010), the other colors represent different source finding tools: black for consisent results of both tools, blue for the results of PyBDSM, which was used for the spectral index fit and green for the results of PySE.

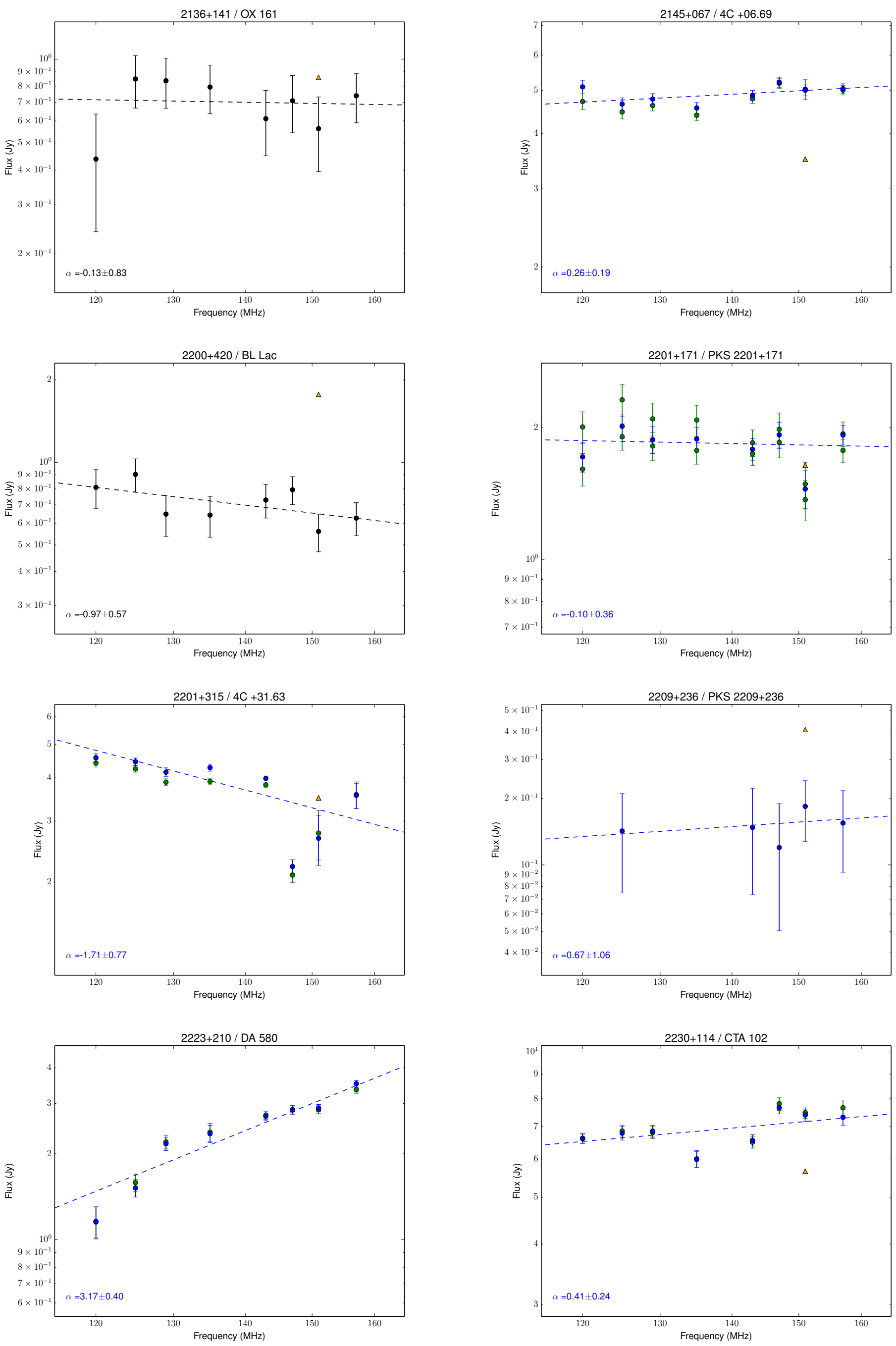

Figure B.15.: MSSS spectra for the sources: 2136+141, 2145+067, 2200+420, 2201+171, 2201+315, 2209+236, 2223+210 and 2230+114. The orange triangles correspond to the flux densities interpolated by Arshakian et al. (2010), the other colors represent different source finding tools: black for consisent results of both tools, blue for the results of PyBDSM, which was used for the spectral index fit and green for the results of PySE.

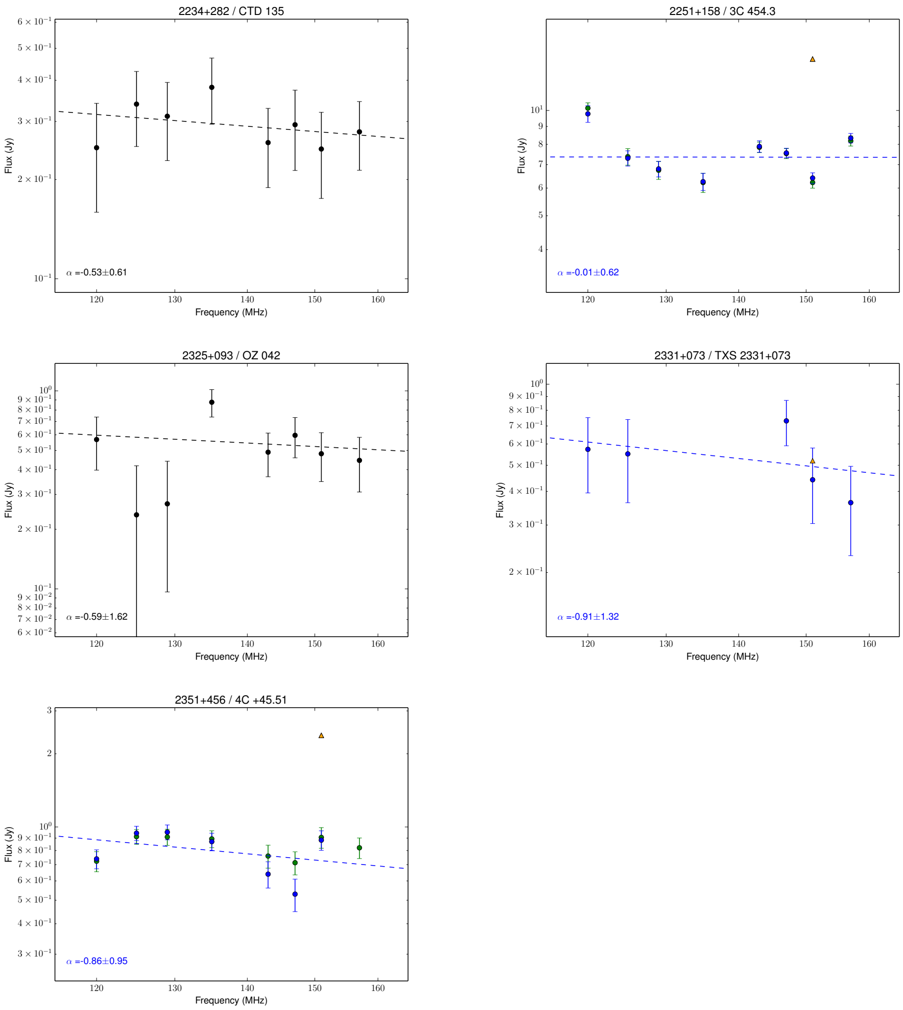

Figure B.16.: MSSS spectra for the sources: 2234+282, 2251+158, 2325+093, 2331+073 and 2351+456. The orange triangles correspond to the flux densities interpolated by Arshakian et al. (2010), the other colors represent different source finding tools: black for consisent results of both tools, blue for the results of PyBDSM, which was used for the spectral index fit and green for the results of PySE.

B.3. Single frequency band images of reprocessing

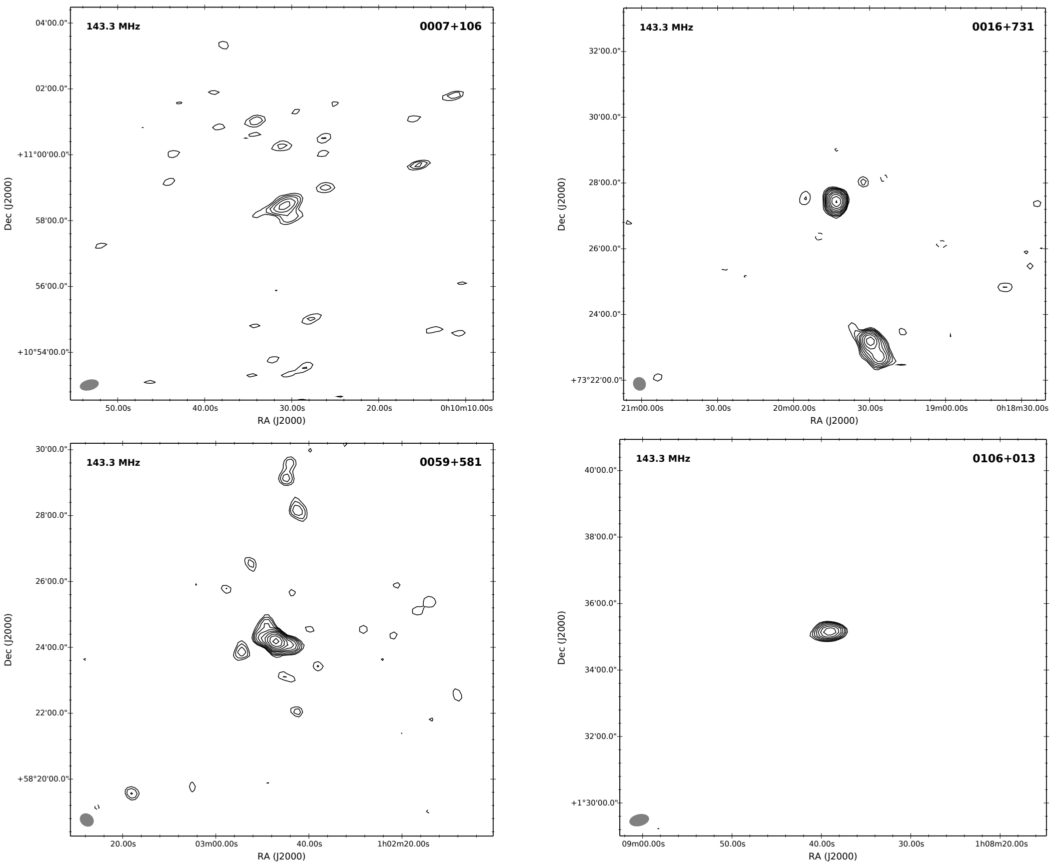

Figure B.17.: Single band reimaging result of 0007+106, 0016+731, 0059+581 and 0106+013. Imaging parameters are given in table B.3.

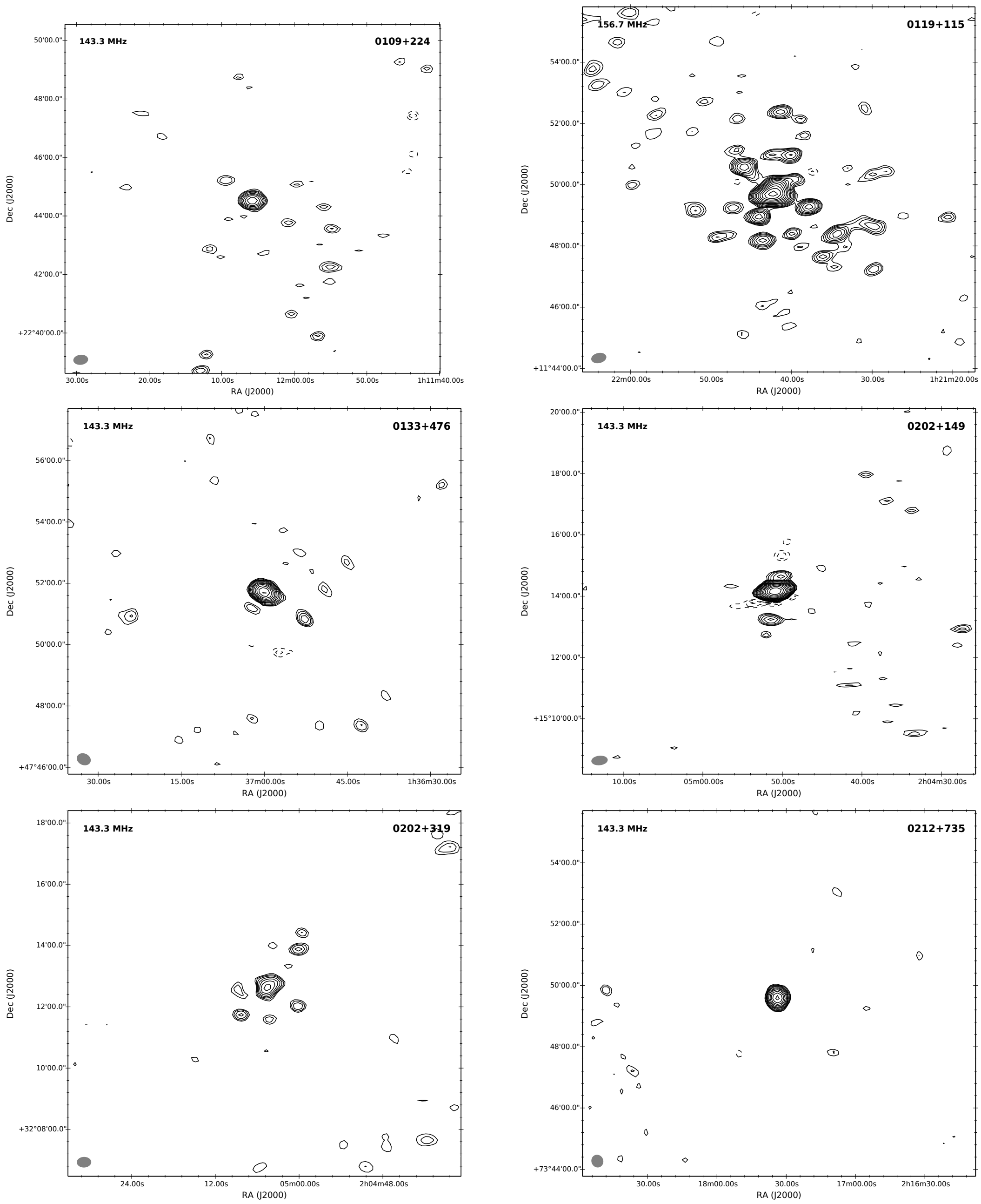

Figure B.18.: Single band reimaging result of 0109+224, 0119+115, 0133+476, 0202+149, 0202+319 and 0212+735. Imaging parameters are given in table B.3.

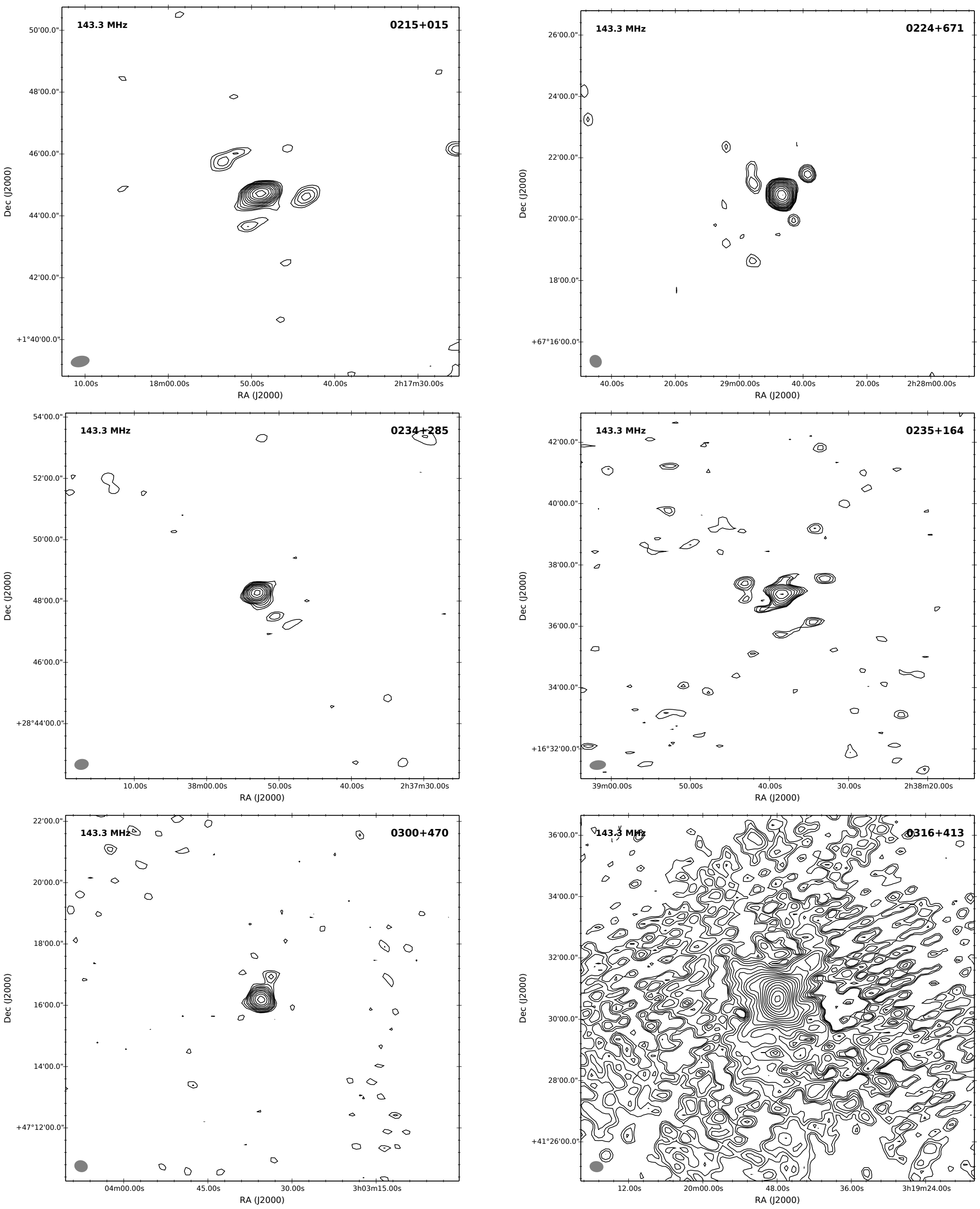

Figure B.19.: Single band reimaging result of 0212+015, 0224+671, 0234+285, 0235+164, 0300+470 and 0316+413. Imaging parameters are given in table B.3.

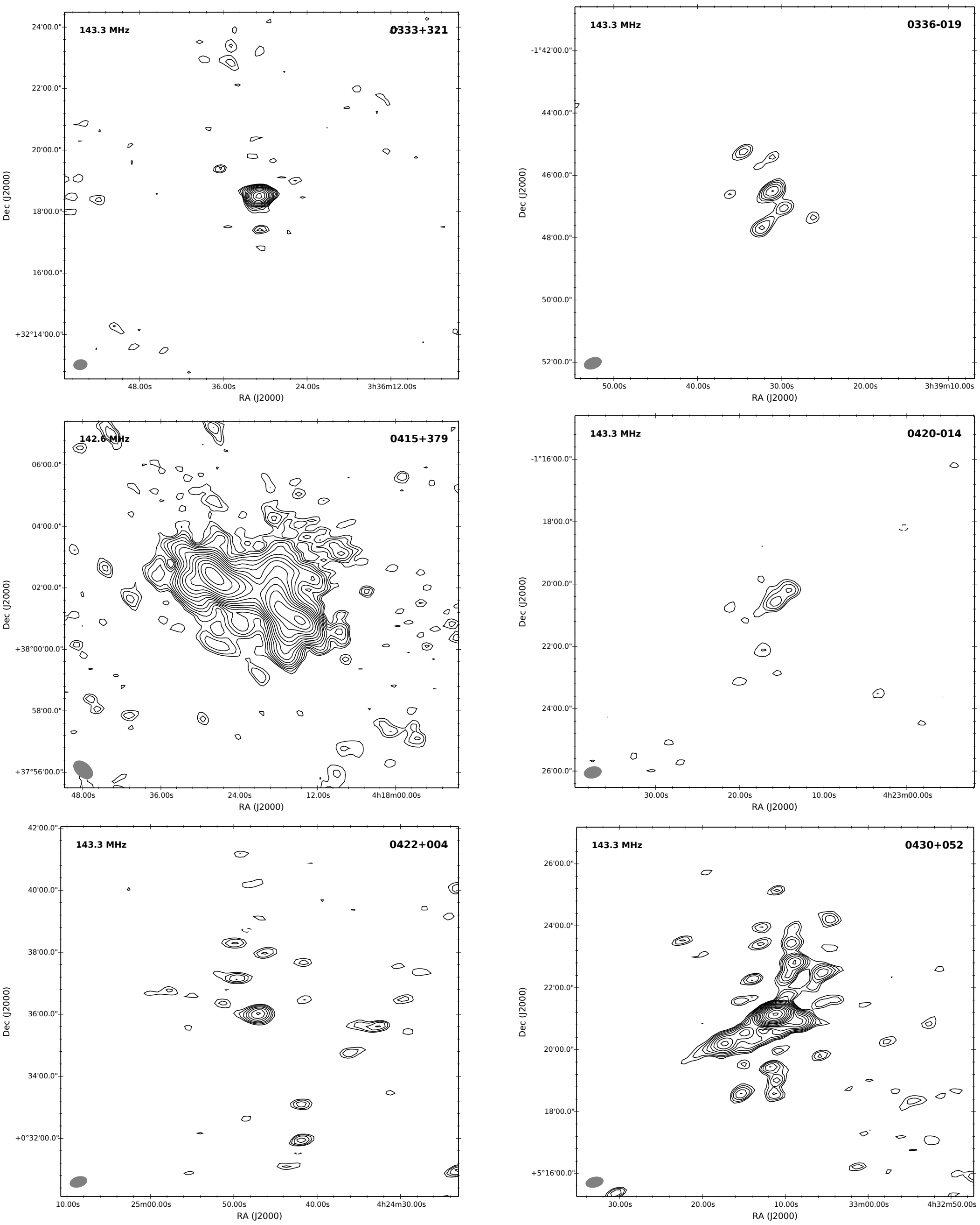

Figure B.20.: Single band reimaging result of 0333+321, 0336-019, 0415+379, 0420-014, 0422+004 and 0430+052. Imaging parameters are given in table B.3.

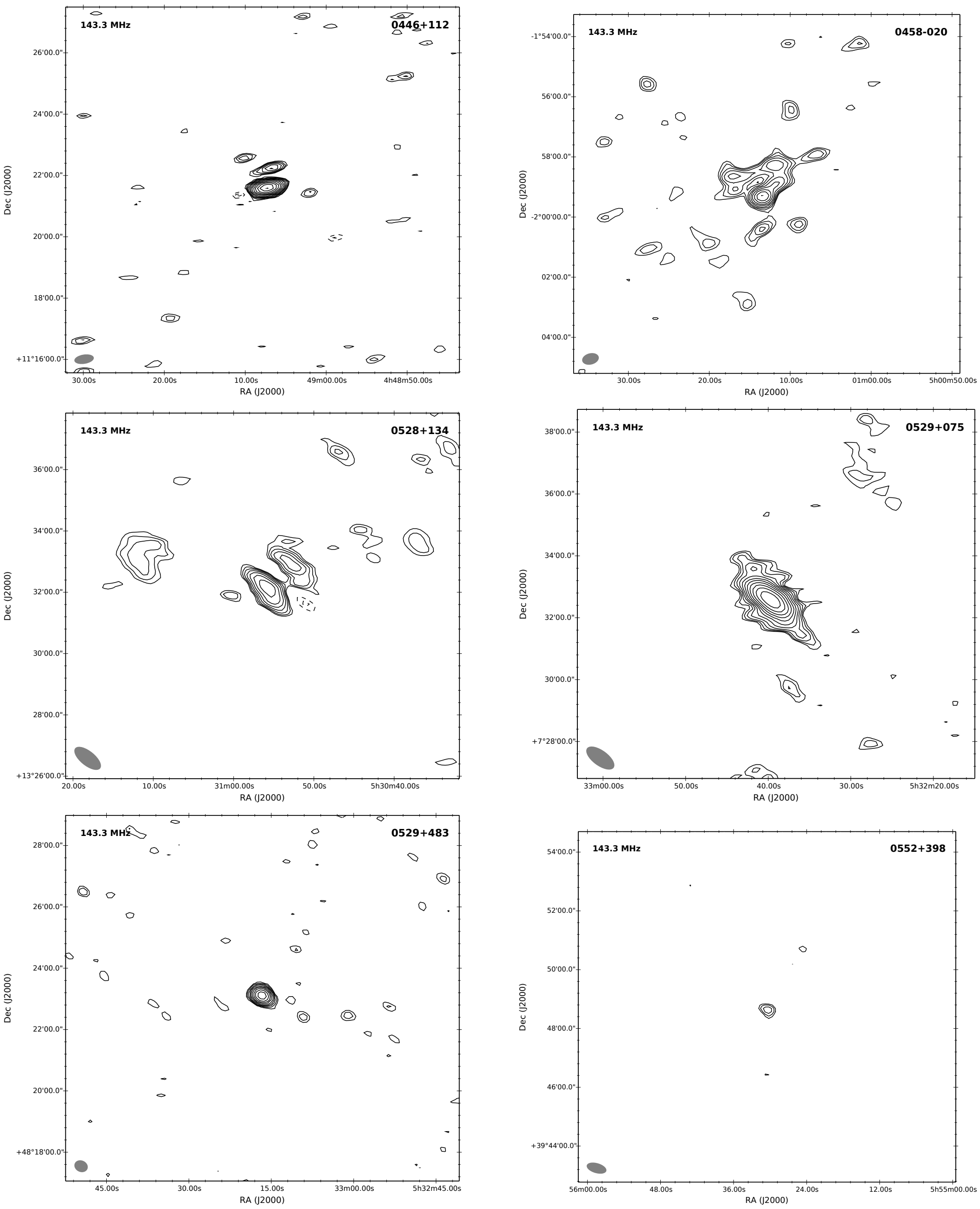

Figure B.21.: Single band reimaging result of 0446+112, 0458-020, 0528+134, 0529+075, 0529+483 and 0552+398. Imaging parameters are given in table B.3.

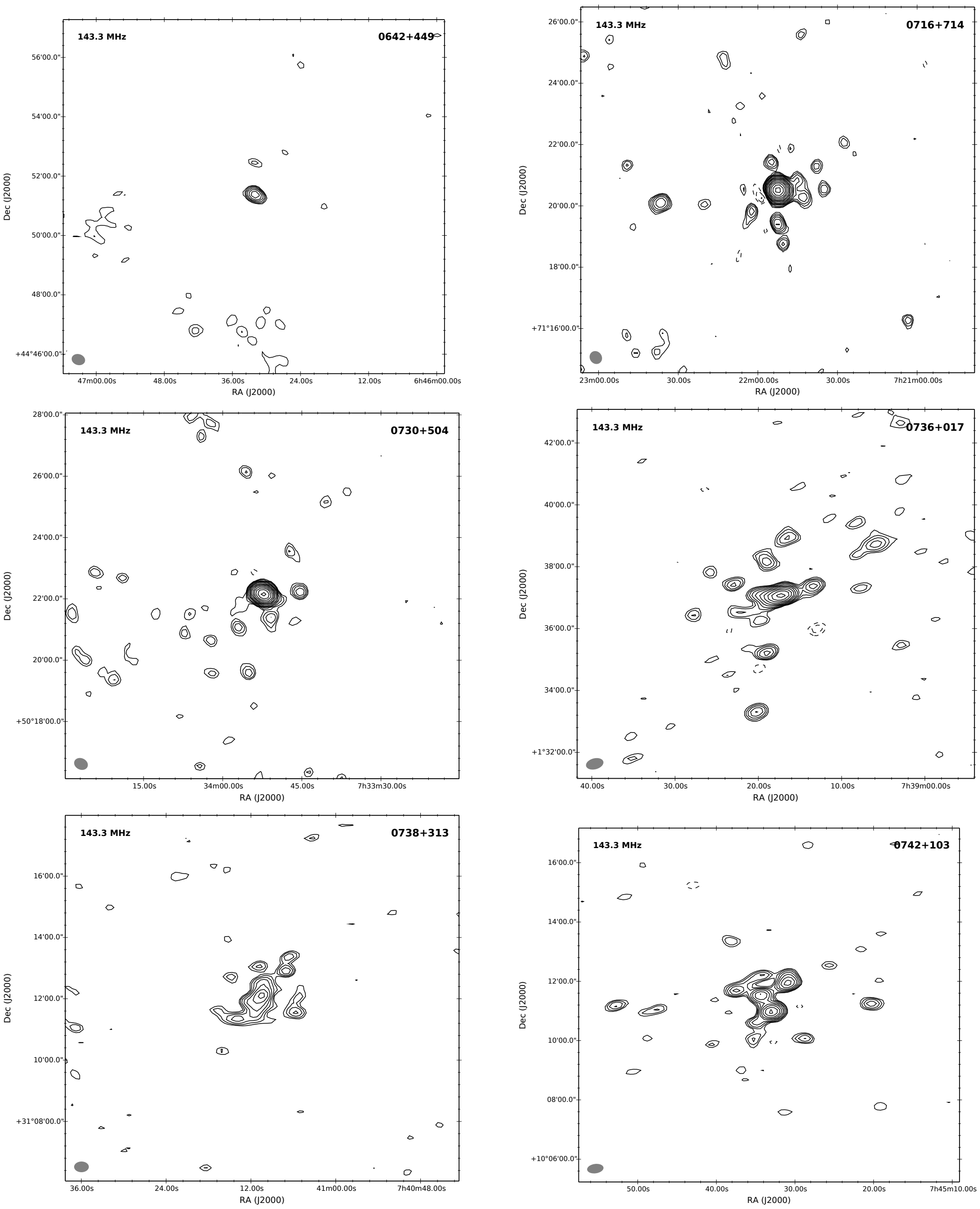

Figure B.22.: Single band reimaging result of 0642+449, 0716+714, 0730+504, 0736+017, 0738+313 and 0742+103. Imaging parameters are given in table B.3.

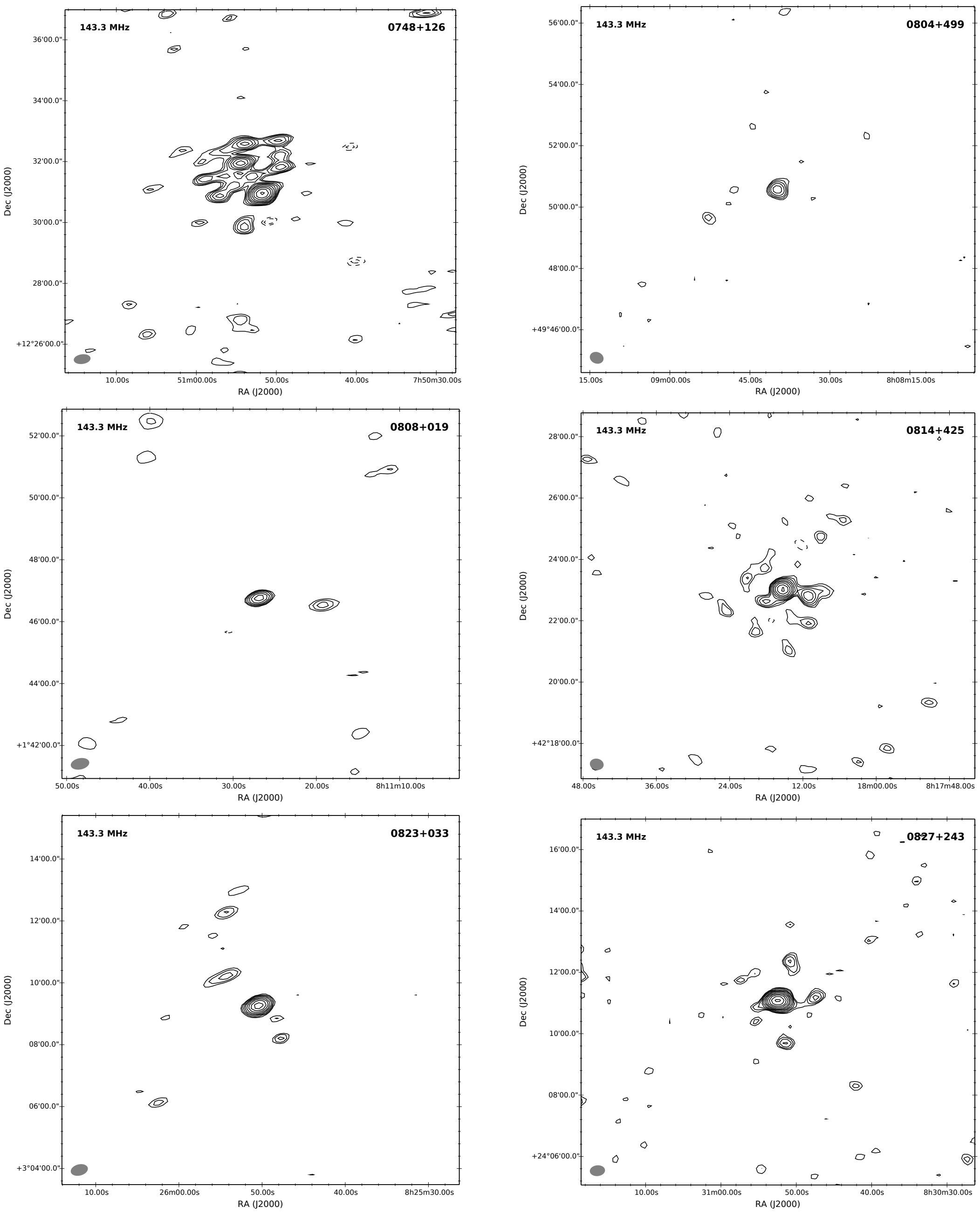

Figure B.23.: Single band reimaging result of 0748+126, 0804+499, 0808+019, 0814+425, 0823+033 and 0827+243. Imaging parameters are given in table B.3.

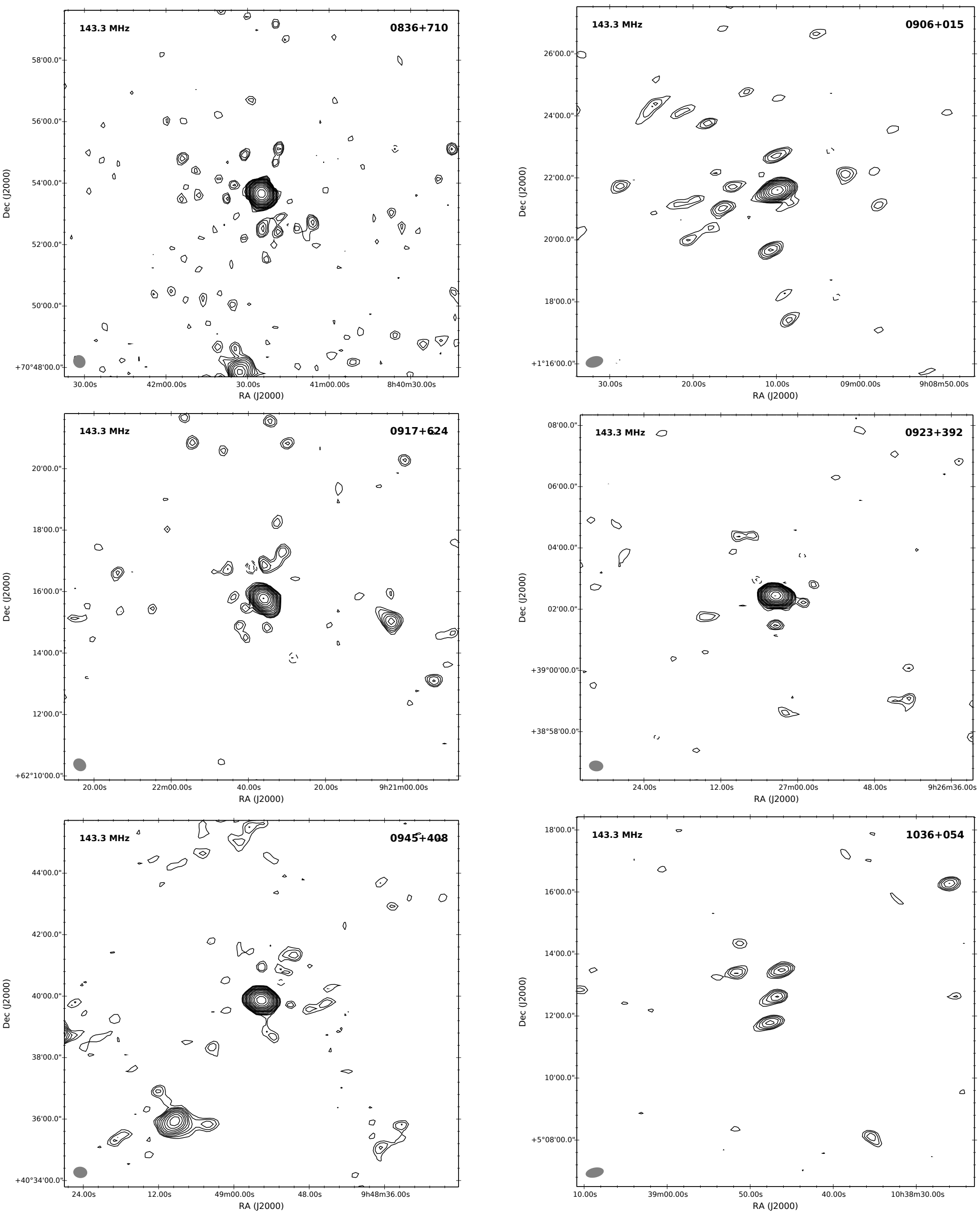

Figure B.24.: Single band reimaging result of 0836+710, 0906+015, 0917+624, 0923+392, 0945+408 and 1036+054. Imaging parameters are given in table B.3.

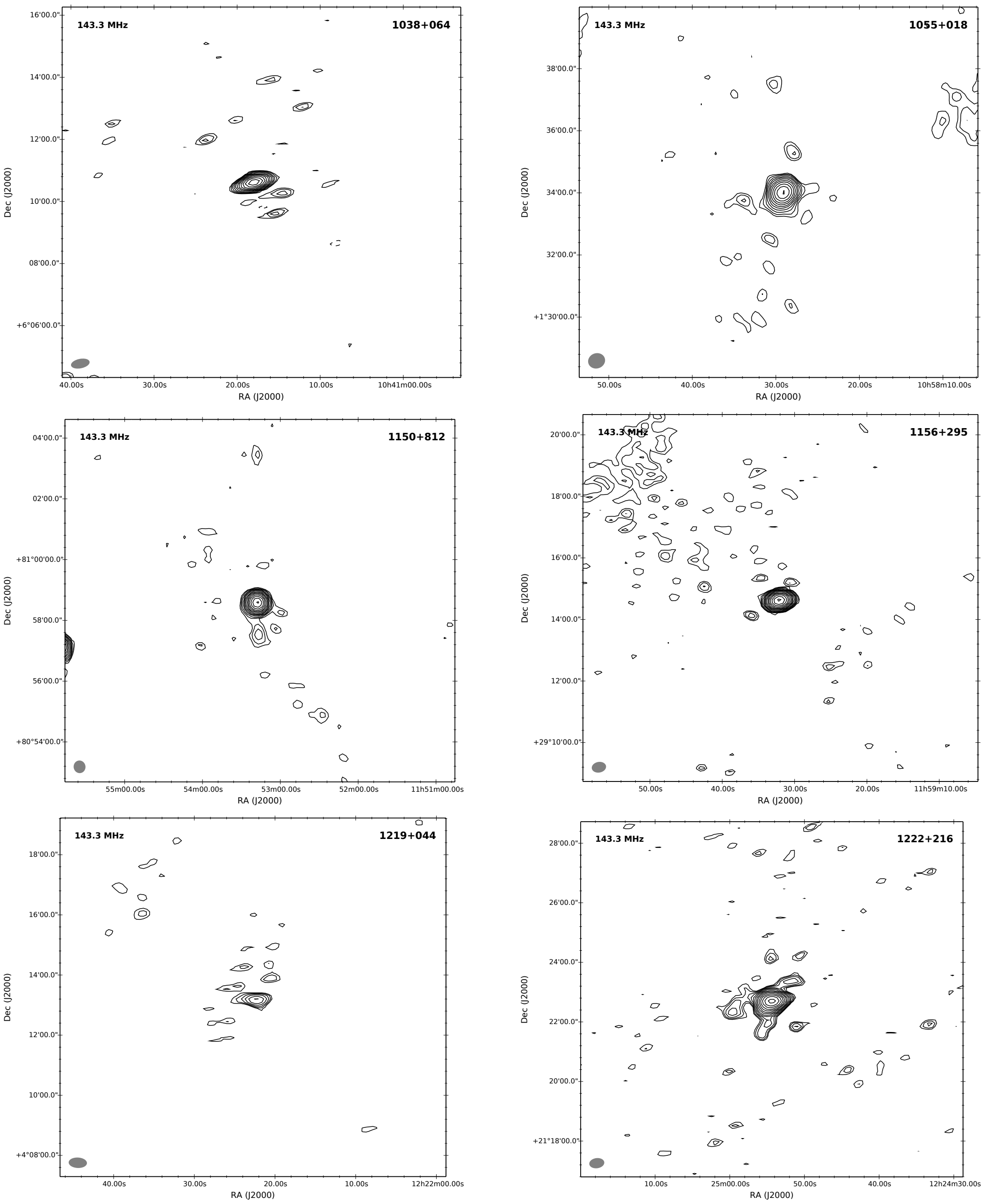

Figure B.25.: Single band reimaging result of 1038+064, 1055+018, 1150+812, 1156+295, 1219+044 and 1222+216. Imaging parameters are given in table B.3.

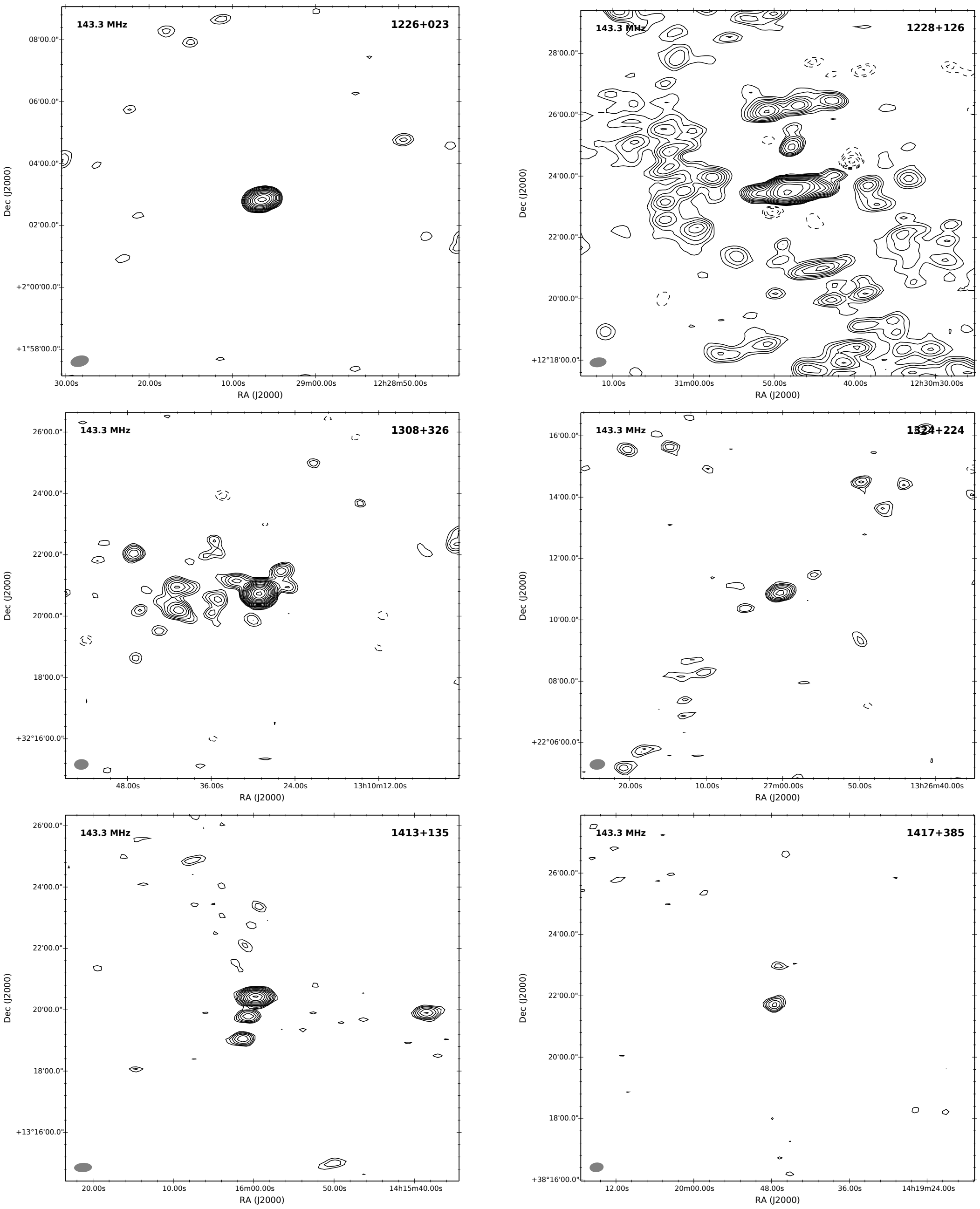

Figure B.26.: Single band reimaging result of 1226+023, 1228+126, 1308+326, 1324+224, 1413+135 and 1417+385. Imaging parameters are given in table B.3.

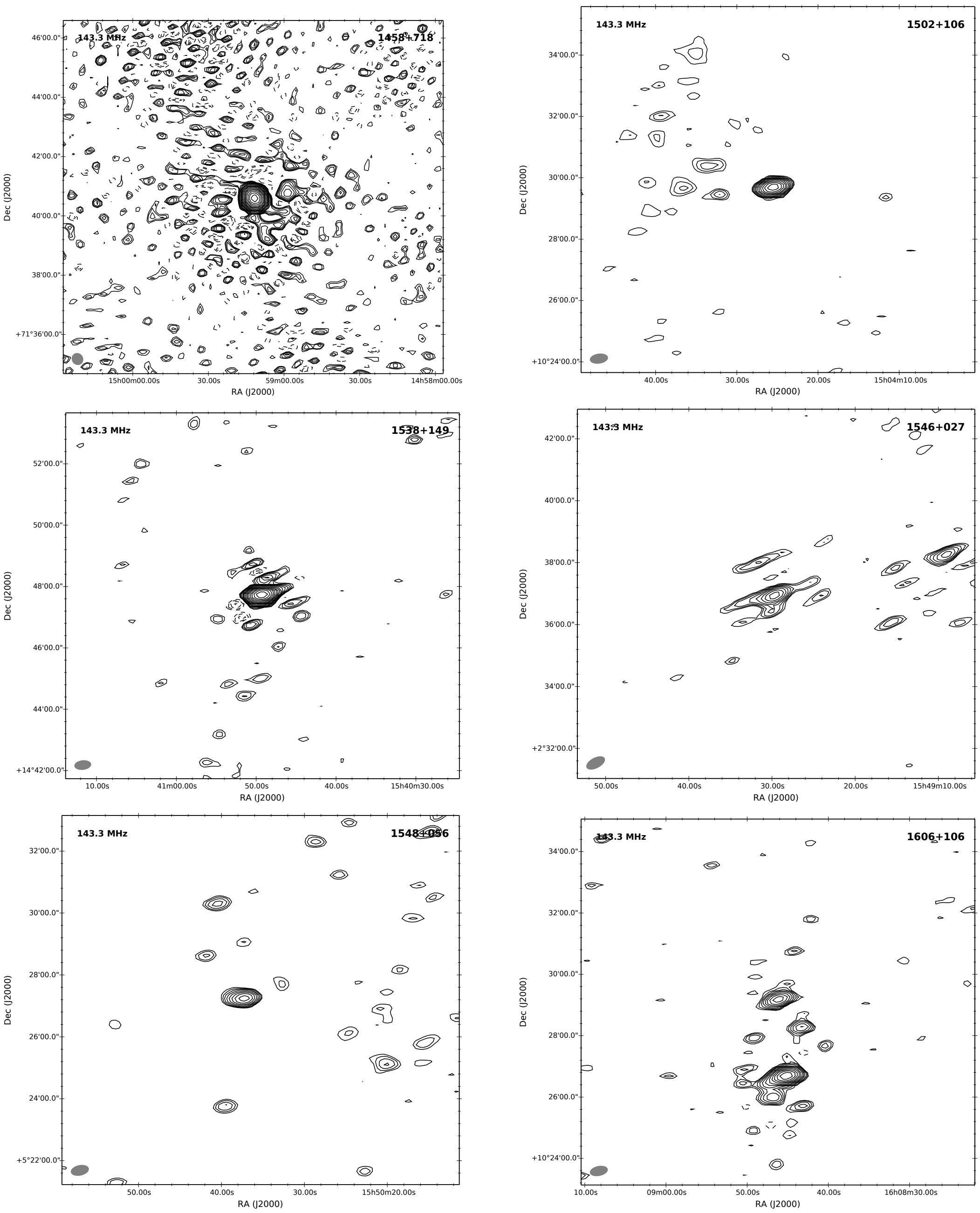

Figure B.27.: Single band reimaging result of 1458+718, 1502+106, 1538+149, 1546+027, 1548+096 and 1606+106. Imaging parameters are given in table B.3.

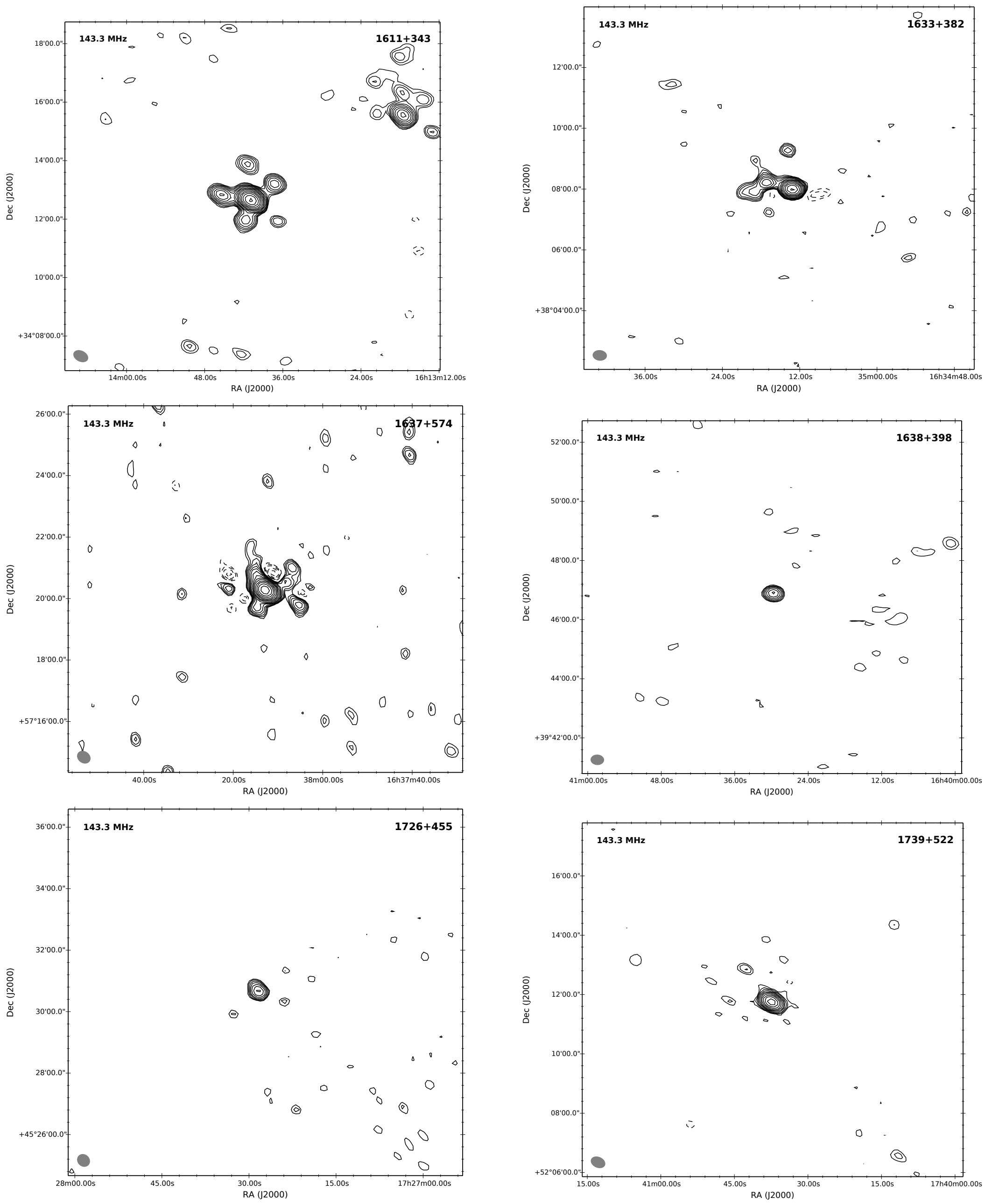

Figure B.28.: Single band reimaging result of 1611+343, 1633+382, 1637+574, 1638+398, 1726+455 and 1739+522. Imaging parameters are given in table B.3.

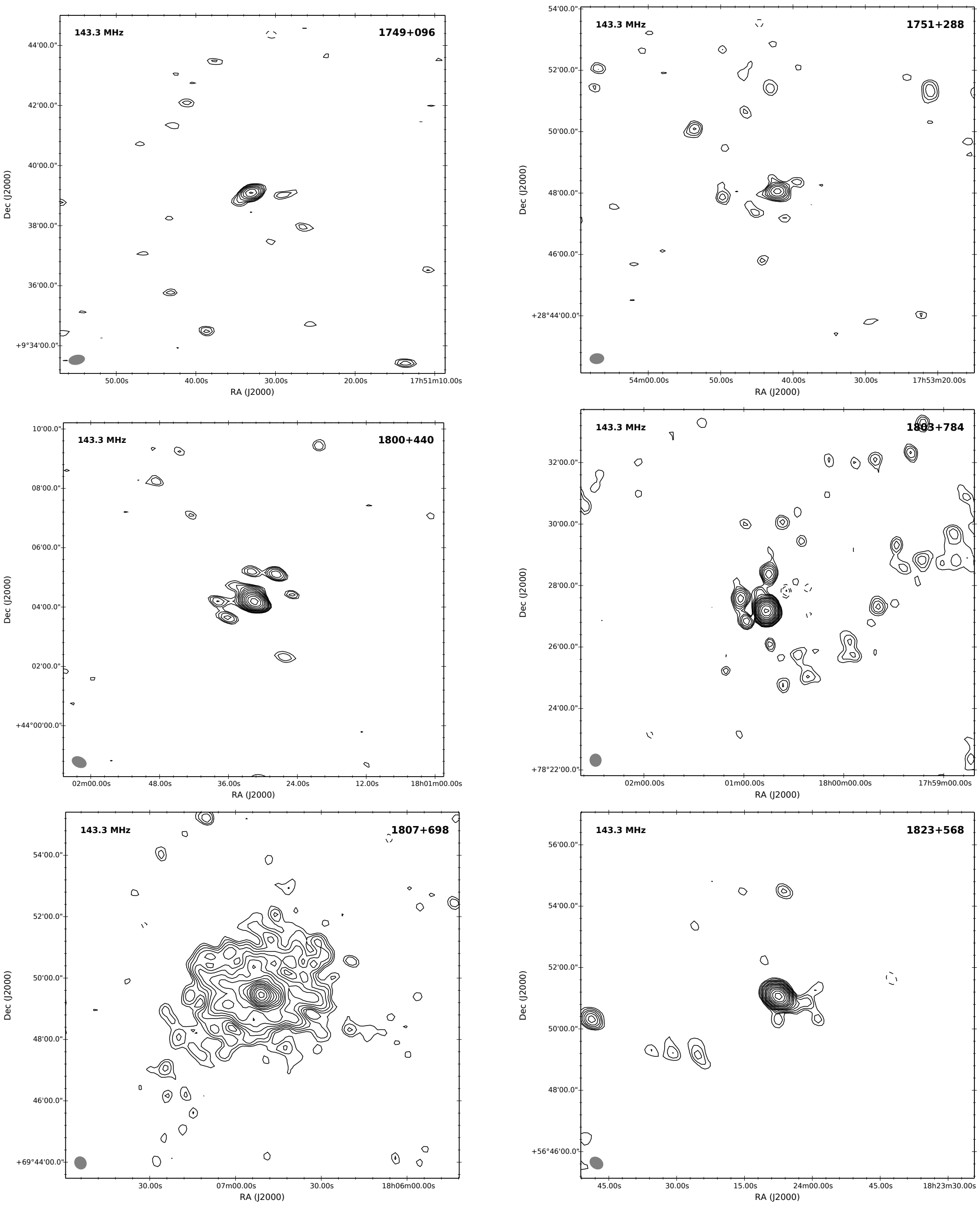

Figure B.29.: Single band reimaging result of 1749+096, 1751+288, 1800+440, 1803+784, 1807+698 and 1823+568. Imaging parameters are given in table B.3.

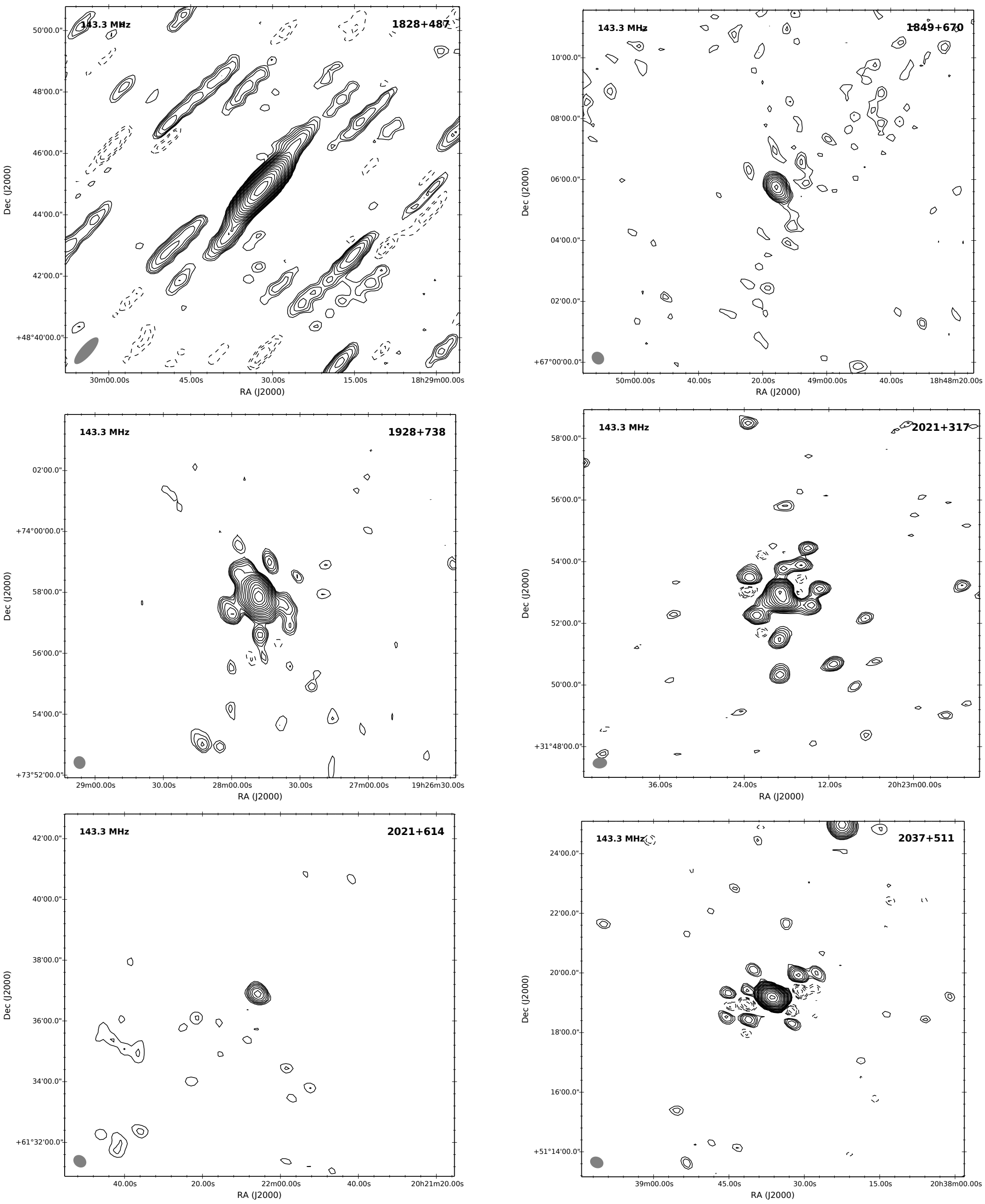

Figure B.30.: Single band reimaging result of 1828+487, 1849+670, 1928+738, 2021+317, 2021+614 and 2037+511. Imaging parameters are given in table B.3.

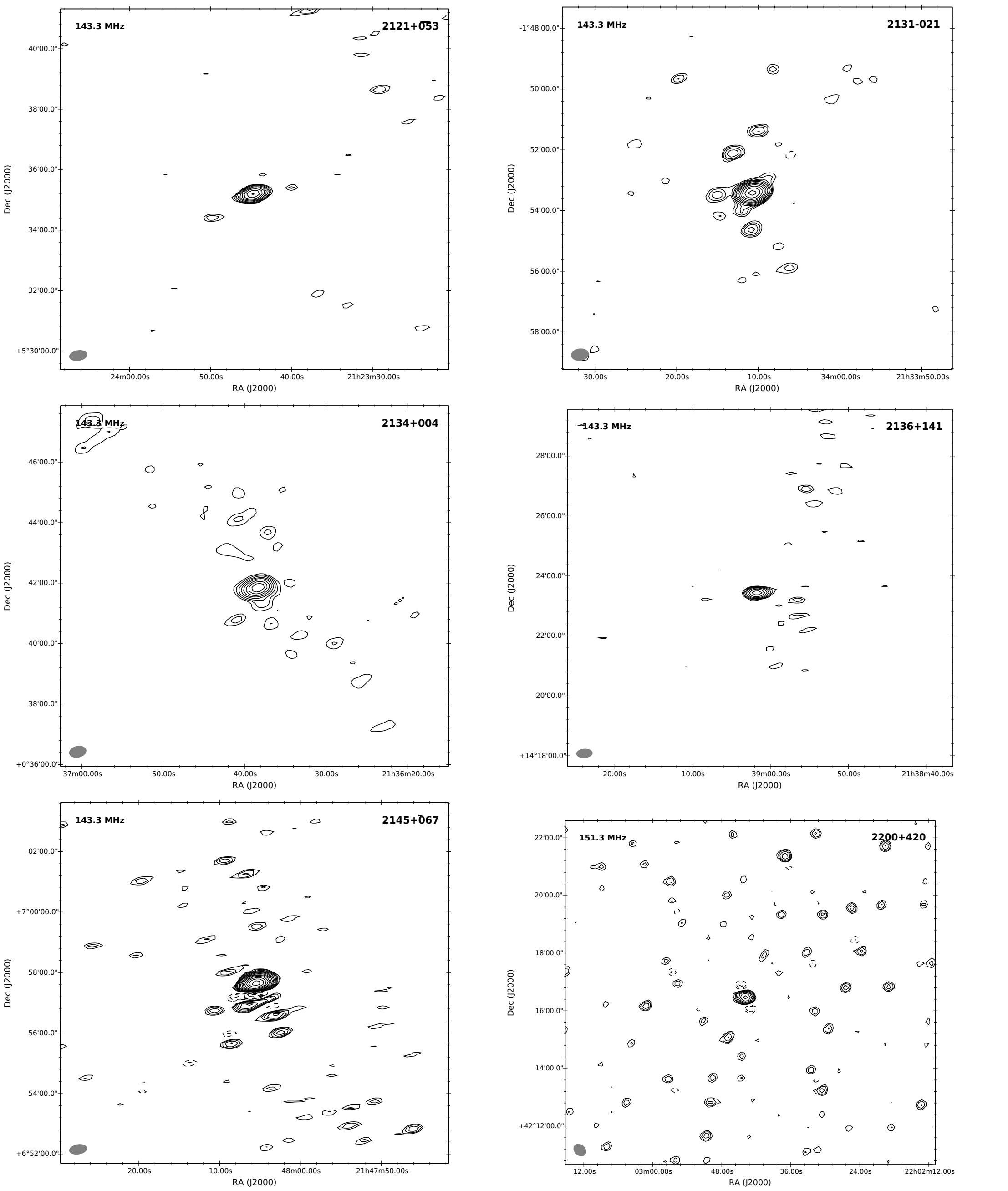

Figure B.31.: Single band reimaging result of 2121+053, 2131-021, 2134+004, 2136+141, 2145+067 and 2200+420. Imaging parameters are given in table B.3.

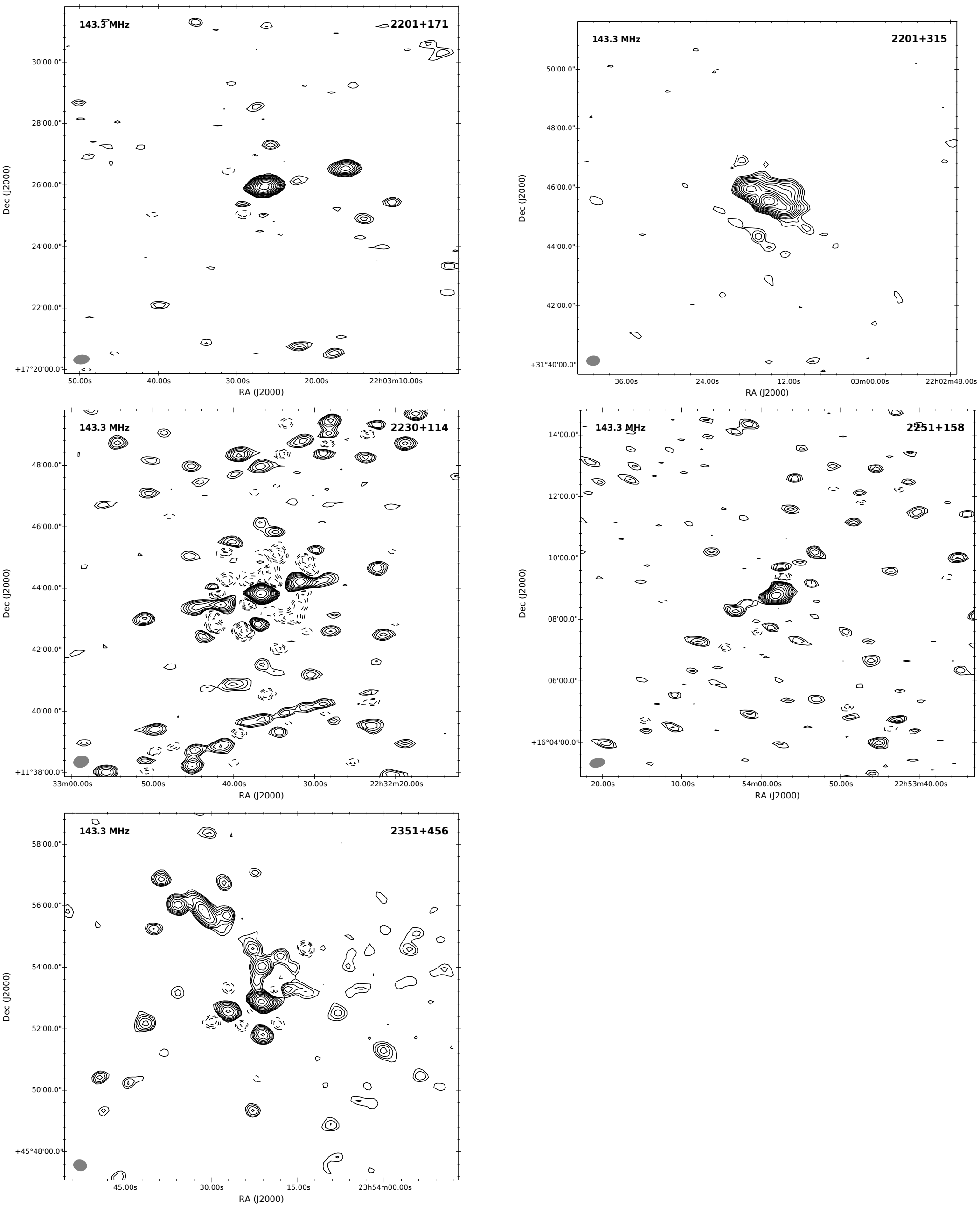

Figure B.32.: Single band reimaging result of 2201+171, 2201+315, 2230+114, 2251+158 and 2351+456. Imaging parameters are given in table B.3.

Table B.3.: Image parameter of the single band reimaging of MSSS. However the absolute flux scale is not corrected, which is why the images are only used for morphological studies.

Source	Frequency (MHz)	S_{Peak} (Jy beam^{-1})	S_{RMS} (mJy beam^{-1})	beam$_{maj}$ (arcsec)	beam$_{min}$ (arcsec)	beam$_{p.a.}$ (°)
0007+106	143.3	2.36	5.53	31.6	17.9	-74.6
0016+731	143.3	2.32	4.38	23.6	20.4	15.6
0059+581	143.3	3.71	5.58	24.6	20.5	41.0
0106+013	143.3	3.65	28.95	32.5	19.9	-75.0
0109+224	143.3	1.49	2.74	27.0	19.2	97.6
0119+115	156.7	1.10	5.05	26.8	18.3	-75.0
0133+476	143.3	3.45	3.03	25.4	20.9	57.8
0202+149	143.3	4.35	8.74	28.7	17.3	97.0
0202+319	143.3	1.92	5.60	25.1	19.4	-87.8
0212+735	143.3	3.17	4.58	23.7	20.5	-167.3
0215+015	143.3	4.97	9.18	33.1	20.3	-77.4
0224+671	143.3	1.57	5.99	24.1	20.5	22.4
0234+285	143.3	5.93	25.95	25.1	19.9	102.0
0235+164	143.3	1.96	10.75	28.7	17.2	-83.2
0300+470	143.3	3.17	10.59	23.8	21.3	59.2
0316+413	143.3	16.65	15.00	24.0	20.1	80.6
0333+321	143.3	3.53	11.16	24.6	19.6	100.3
0336-019	143.3	4.81	11.00	32.3	20.8	-67.8
0415+379	142.6	9.59	28.10	41.7	26.2	44.5
0420-014	143.3	6.99	8.42	31.3	21.6	-75.5
0422+004	143.3	3.00	10.25	31.2	19.7	-72.6
0430+052	143.3	4.26	7.68	31.8	19.4	104.3
0446+112	143.3	2.67	4.91	34.5	16.7	-79.9
0458-020	143.3	2.45	12.24	30.3	20.9	-72.9
0528+134	143.3	2.17	9.24	58.8	26.4	-131.9
0529+075	143.3	10.22	11.84	59.6	27.6	50.8
0529+483	143.3	50.37	9.11	24.2	20.7	54.8
0552+398	143.3	1.45	16.07	37.5	18.8	72.0
0642+449	143.3	3.51	7.27	24.6	20.5	66.2
0716+714	143.3	10.39	5.75	24.4	20.8	22.9
0730+504	143.3	4.76	3.61	24.9	20.5	56.5
0736+017	143.3	4.44	6.73	30.9	19.7	-72.8
0738+313	143.3	5.99	9.95	25.5	19.5	90.4
0742+103	143.3	4.15	6.85	29.7	17.6	-81.1
0748+126	143.3	4.26	6.91	29.7	17.6	-81.1
0804+499	143.3	72.88	12.22	24.6	20.7	60.2
0808+019	143.3	4.09	13.98	32.6	20.3	-76.2
0814+425	143.3	2.66	14.13	24.1	20.5	72.1
0823+033	143.3	2.51	9.68	30.3	20.2	-72.8
0827+243	143.3	2.74	6.62	26.4	19.7	97.3
0836+710	143.3	3.60	5.53	24.2	20.7	19.5
0906+015	143.3	1.59	4.84	31.2	19.8	-72.6
0917+624	143.3	2.50	3.71	24.8	20.8	35.6
0923+392	143.3	5.55	10.23	24.9	19.6	82.2
0945+408	143.3	3.95	5.54	24.2	20.7	81.8

1036+054	143.3	4.36	7.69	32.0	17.5	-75.9
1038+064	143.3	2.28	7.19	32.7	16.8	-77.1
1055+018	143.3	3.04	32.20	29.9	27.6	-54.7
1150+812	143.3	1.91	9.20	23.5	20.4	4.9
1156+295	143.3	7.16	17.35	24.9	19.3	103.2
1219+044	143.3	2.37	46.33	32.6	19.4	86.8
1222+216	143.3	4.73	18.12	27.0	19.0	99.4
1226+023	143.3	67.45	427.34	32.4	20.0	-75.2
1228+126	143.3	32.66	167.44	29.6	17.6	-82.2
1308+326	143.3	4.23	3.02	25.0	19.3	93.8
1324+224	143.3	2.02	5.43	27.0	19.1	97.7
1413+135	143.3	2.32	7.59	31.2	16.8	-87.0
1417+385	143.3	1.03	7.19	24.2	17.3	-82.1
1458+718	143.3	24.33	12.86	23.3	20.3	17.7
1502+106	143.3	4.82	12.31	32.0	18.1	-80.8
1538+149	143.3	6.33	6.86	29.5	17.3	-82.3
1546+027	143.3	2.08	6.35	36.0	18.8	-59.3
1548+056	143.3	1.17	8.96	32.0	18.9	-76.2
1606+106	143.3	2.18	10.29	32.0	18.0	-76.5
1611+343	143.3	4.29	4.44	29.2	20.8	58.3
1633+382	143.3	15.36	12.63	25.0	19.5	82.7
1637+574	143.3	4.22	4.35	25.6	20.8	43.5
1638+398	143.3	9.17	17.82	24.3	19.8	86.3
1726+455	143.3	5.41	19.16	24.5	21.2	31.9
1739+522	143.3	3.70	7.08	27.6	20.3	60.6
1749+096	143.3	3.72	9.27	29.6	18.4	-77.4
1751+288	143.3	2.73	4.26	25.4	19.7	96.1
1800+440	143.3	3.02	9.05	28.4	20.3	59.9
1803+784	143.3	4.04	5.30	24.4	20.6	-177.5
1807+698	143.3	3.48	2.77	24.6	20.9	19.4
1823+568	143.3	4.52	9.07	26.2	20.8	45.2
1828+487	143.3	72.84	27.88	63.6	20.0	140.9
1849+670	143.3	2.60	10.87	24.6	20.6	27.4
1928+738	143.3	2.24	4.42	23.8	20.4	12.0
2021+317	143.3	16.20	5.35	24.9	19.6	97.9
2021+614	143.3	1.06	4.59	25.0	20.6	39.8
2037+511	143.3	15.18	9.10	24.9	20.7	55.6
2121+053	143.3	2.41	11.39	32.6	19.5	-79.3
2131-021	143.3	1.60	9.75	31.5	22.6	-80.8
2134+004	143.3	2.02	18.82	31.1	21.6	-75.3
2136+141	143.3	3.27	17.18	29.1	17.3	-85.8
2145+067	143.3	3.36	9.67	32.2	18.7	-79.3
2200+420	151.3	7.80	131.03	26.9	20.5	40.7
2201+171	143.3	2.17	6.62	28.6	17.3	-83.5
2201+315	143.3	5.86	8.86	25.1	19.4	95.7
2230+114	143.3	21.68	115.26	27.6	22.0	-71.3
2251+158	143.3	11.76	72.66	28.1	17.2	-76.9
2351+456	143.3	5.13	7.07	24.2	20.9	68.1

B.4. Averaged images of reprocessing

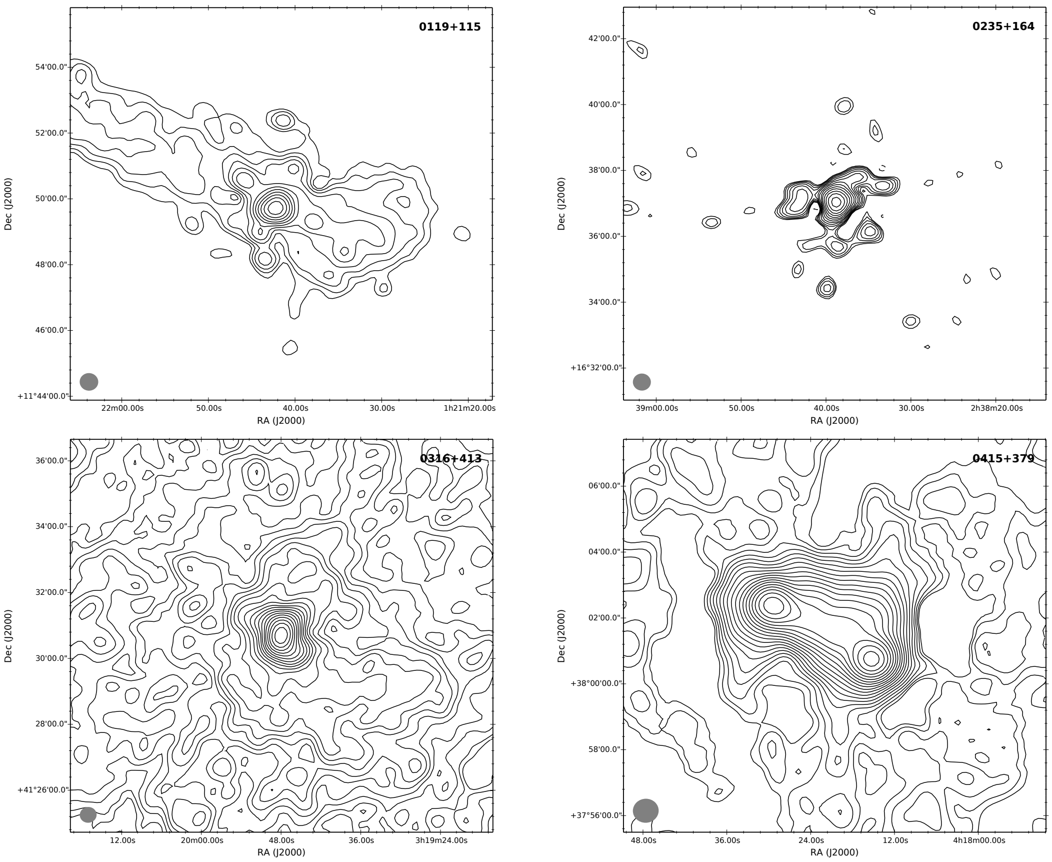

Figure B.33.: Averaged reimaging results of 0119+115, 0235+164, 0316+413 and 0415+379. Imaging parameters are given in table B.4.

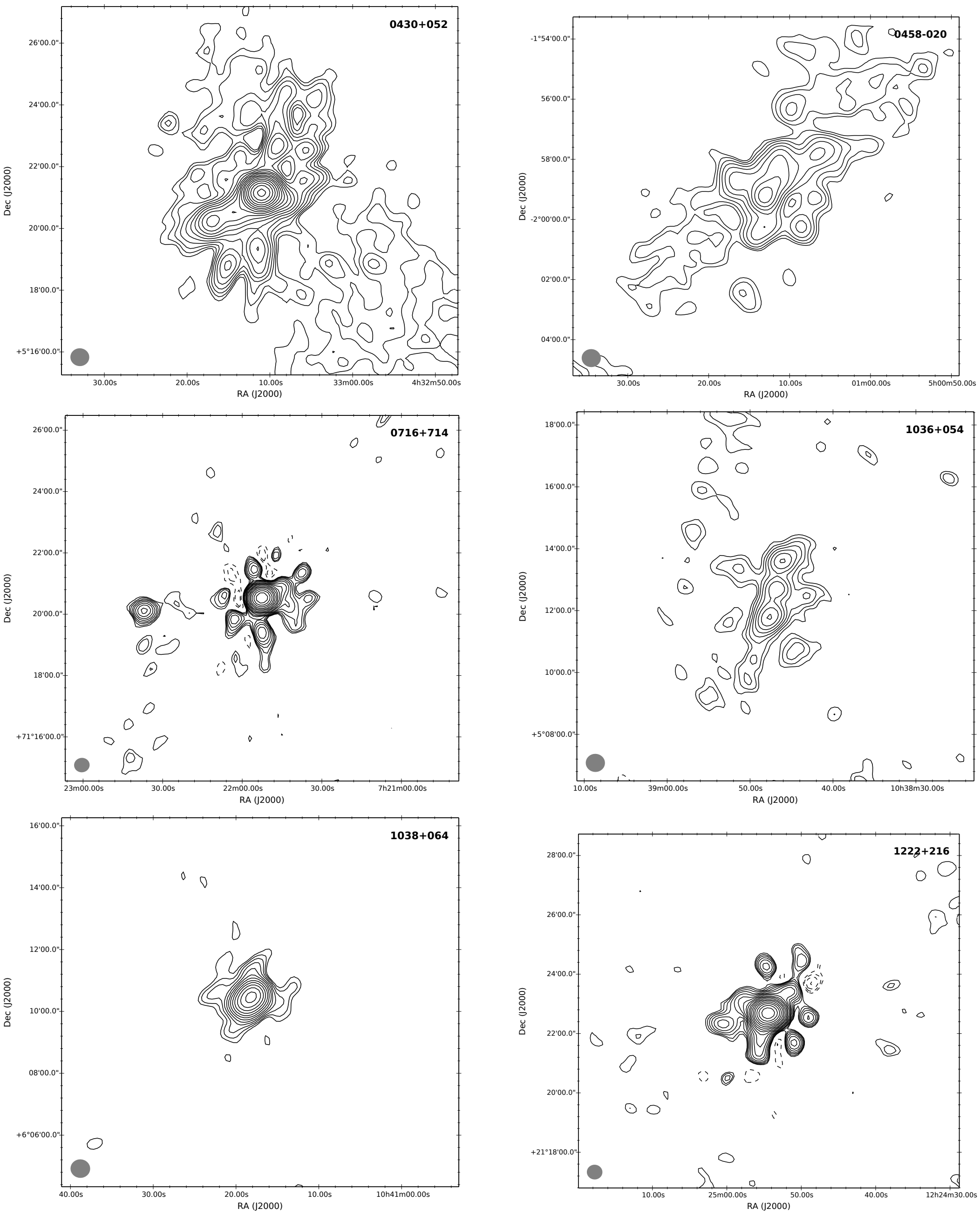

Figure B.34.: Averaged reimaging results of 0430+052, 0458-020, 0716+714, 1036+054, 1038+064 and 1222+216. Imaging parameters are given in table B.4.

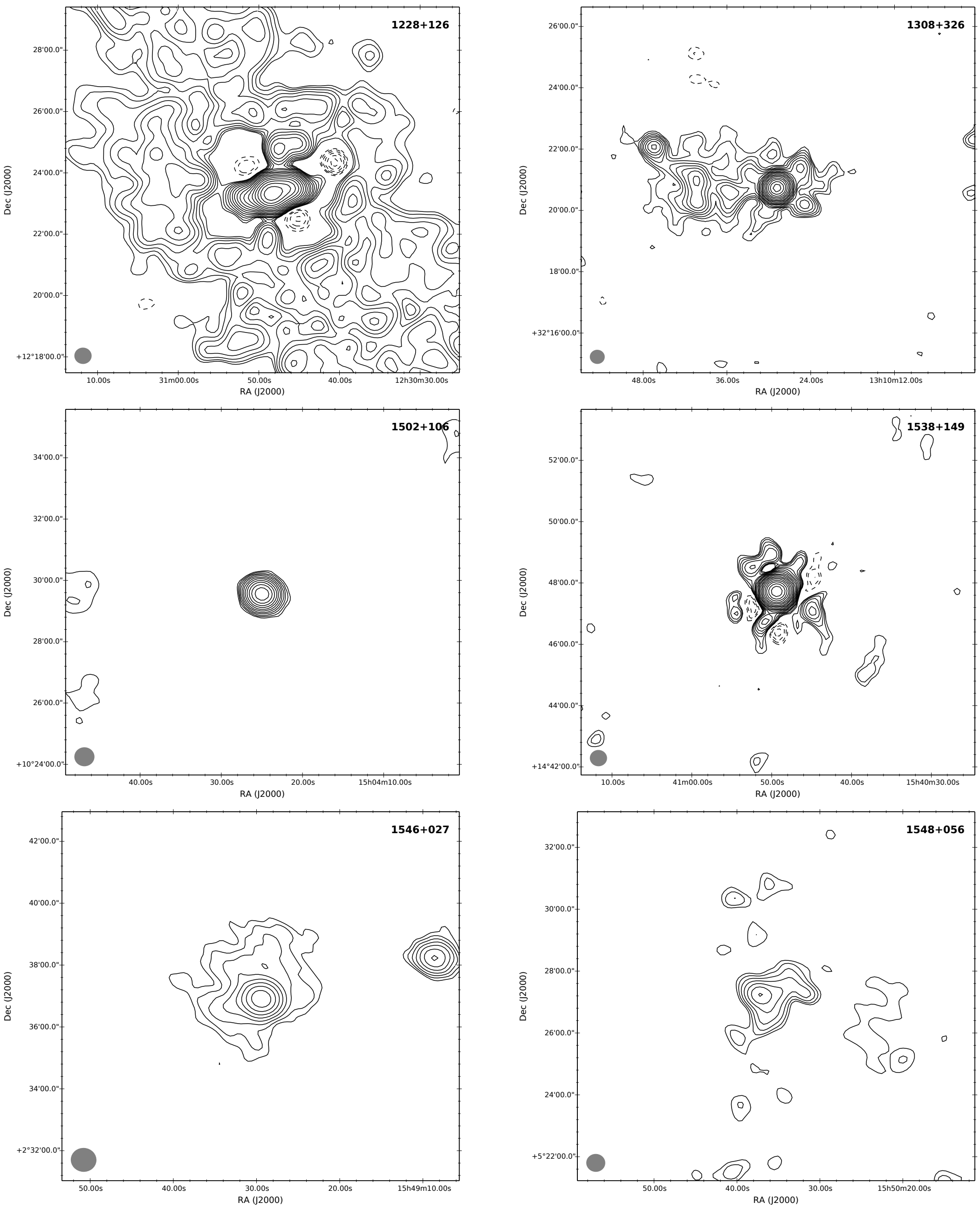

Figure B.35.: Averaged reimaging results of 1228+126, 1308+326, 1502+106, 1538+149, 1546+027 and 1548+056. Imaging parameters are given in table B.4.

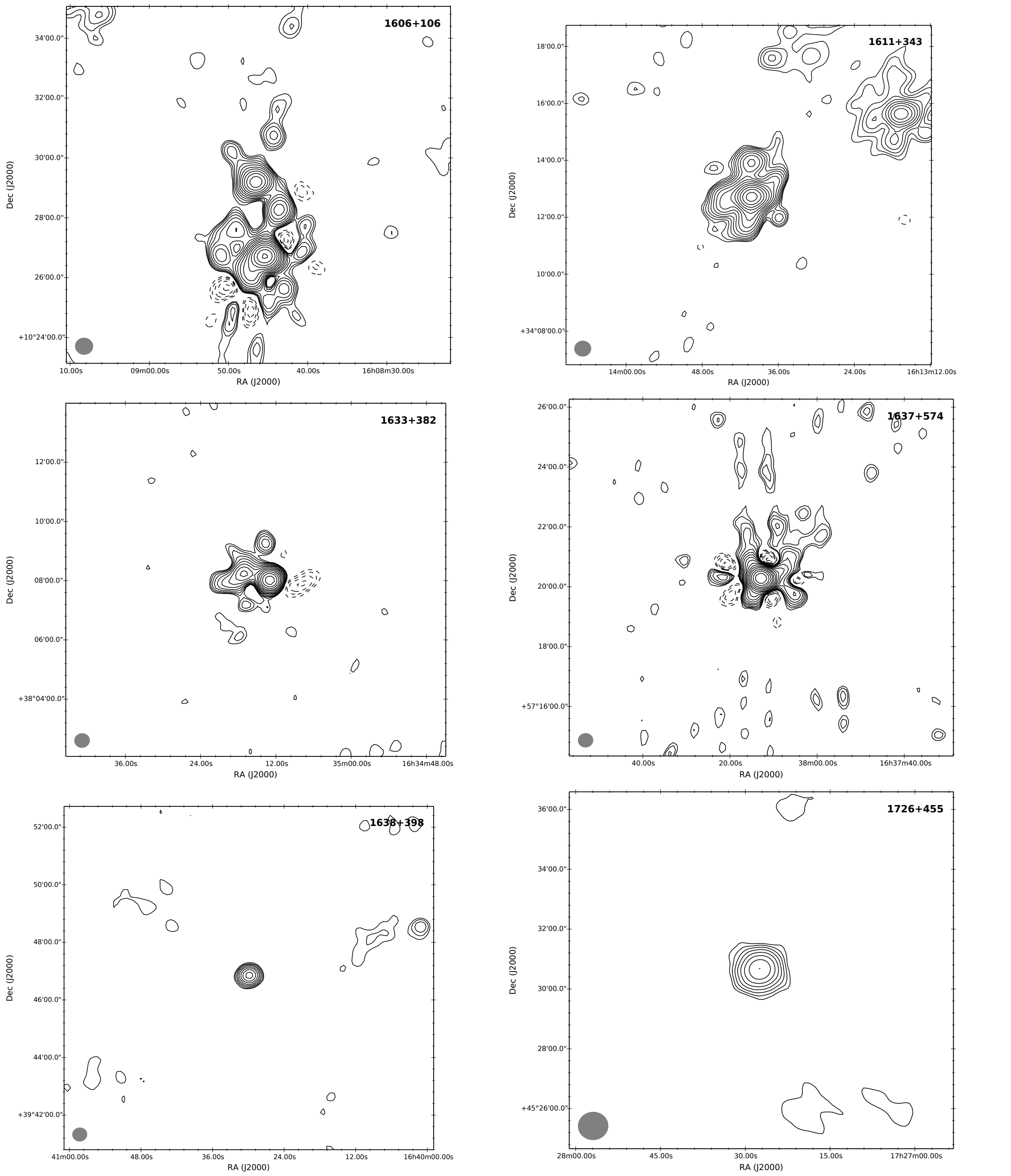

Figure B.36.: Averaged reimaging results of 1606+106, 1611+343, 1633+382, 1637+574, 1638+398 and 1726+455. Imaging parameters are given in table B.4.

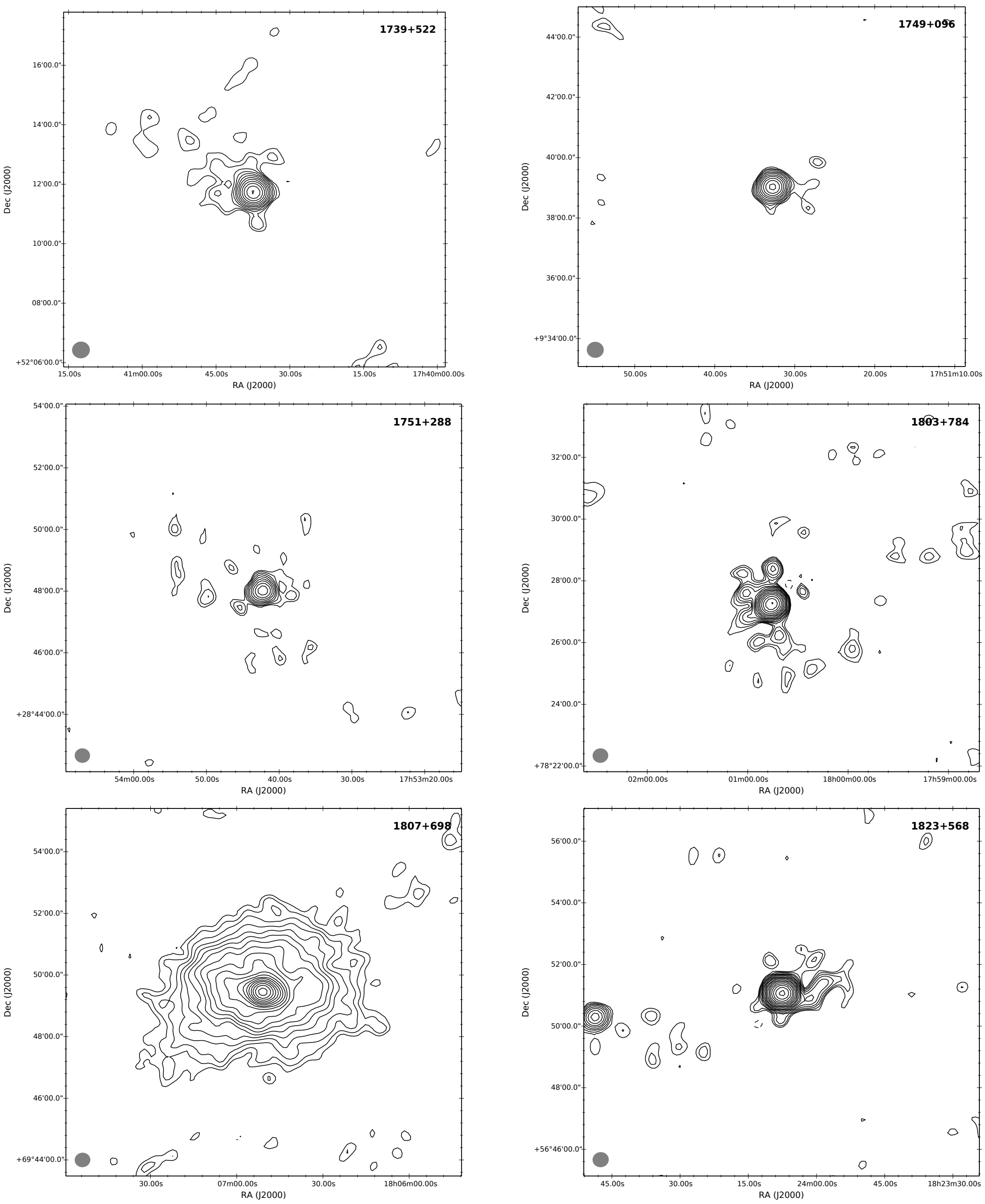

Figure B.37.: Averaged reimaging results of 1739+522, 1749+096, 1751+288, 1803+784, 1807+698 and 1823+568. Imaging parameters are given in table B.4.

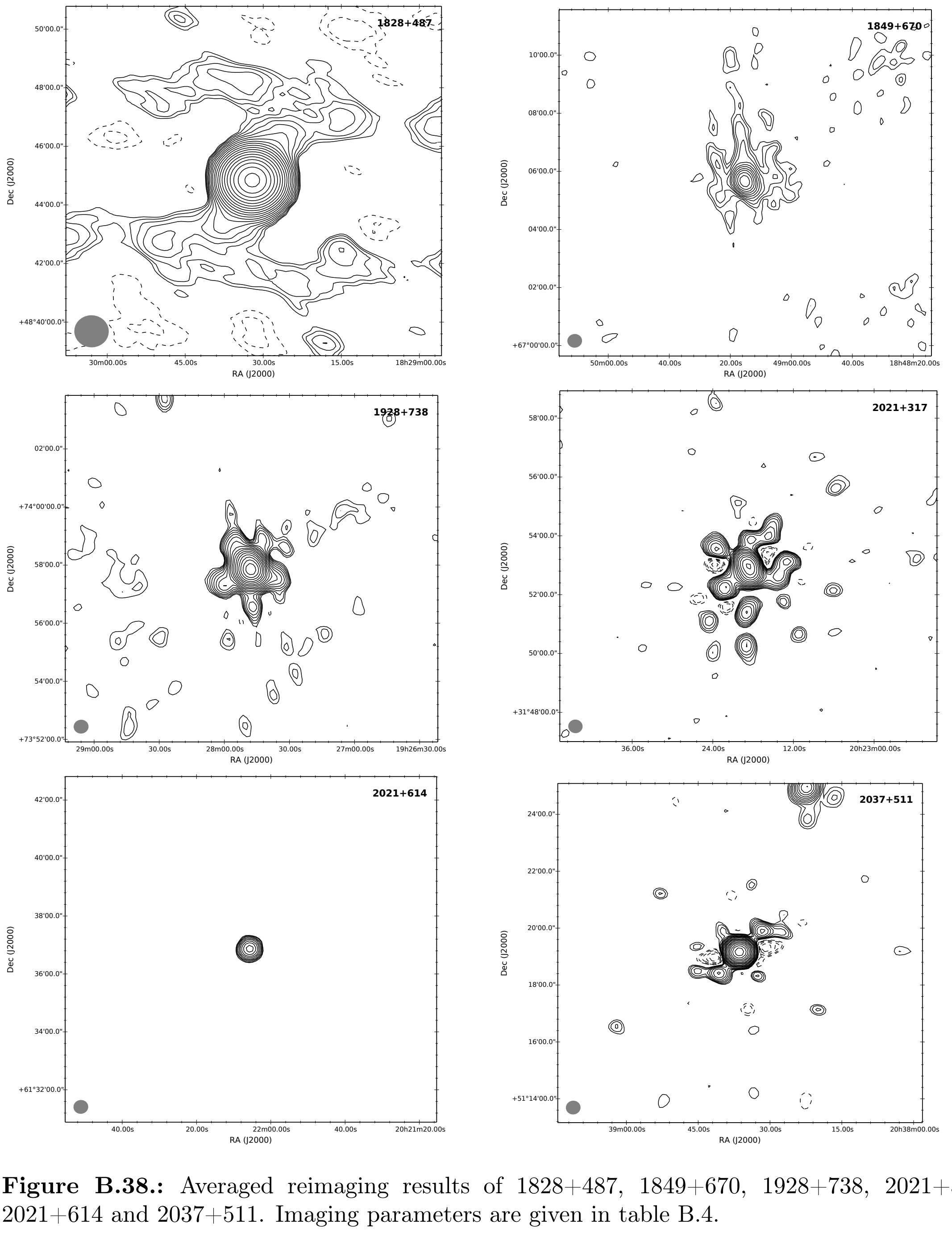

Figure B.38.: Averaged reimaging results of 1828+487, 1849+670, 1928+738, 2021+317, 2021+614 and 2037+511. Imaging parameters are given in table B.4.

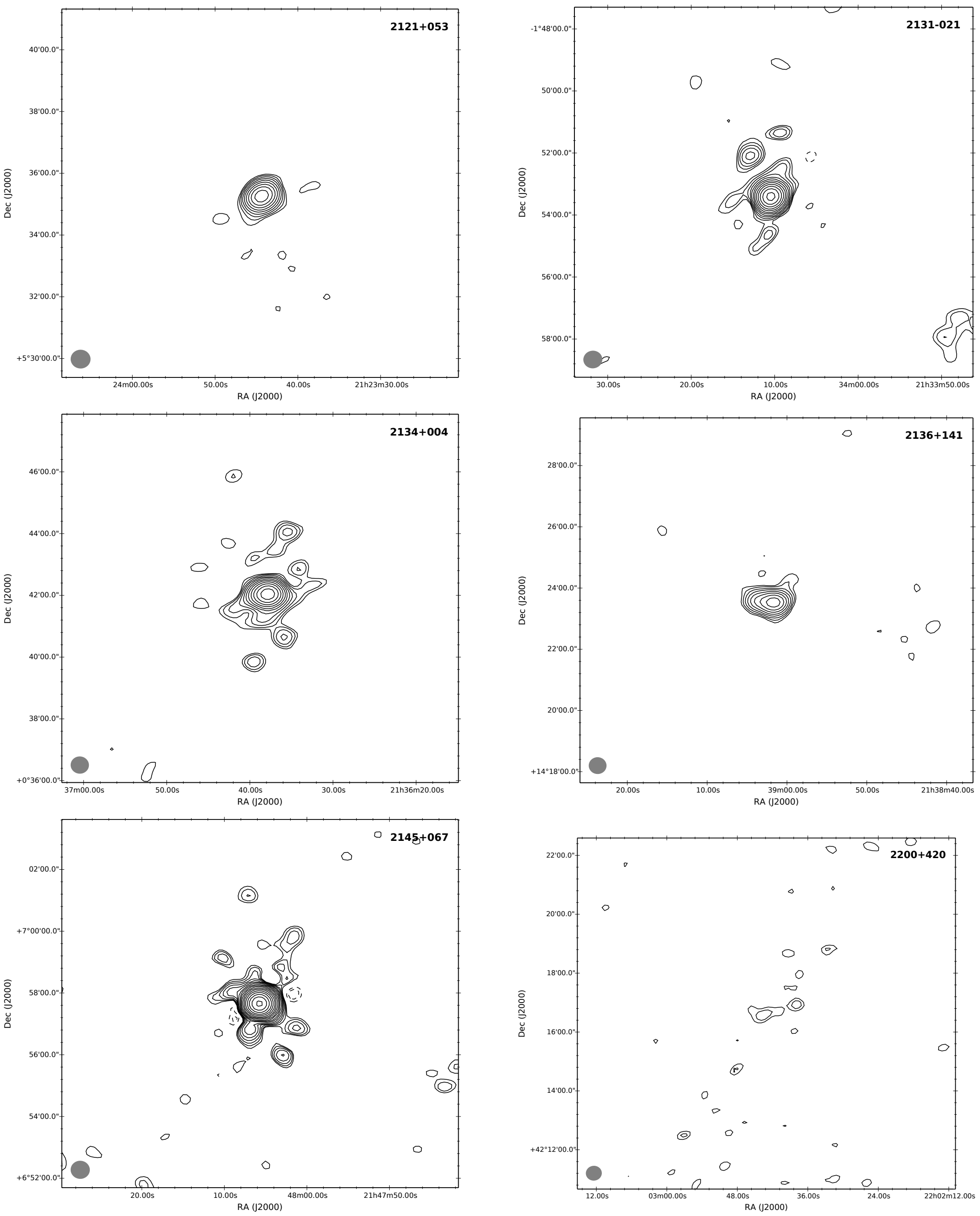

Figure B.39.: Averaged reimaging results of 2121+053, 2131-021, 2134+004, 2136+141, 2145+067 and 2200+420. Imaging parameters are given in table B.4.

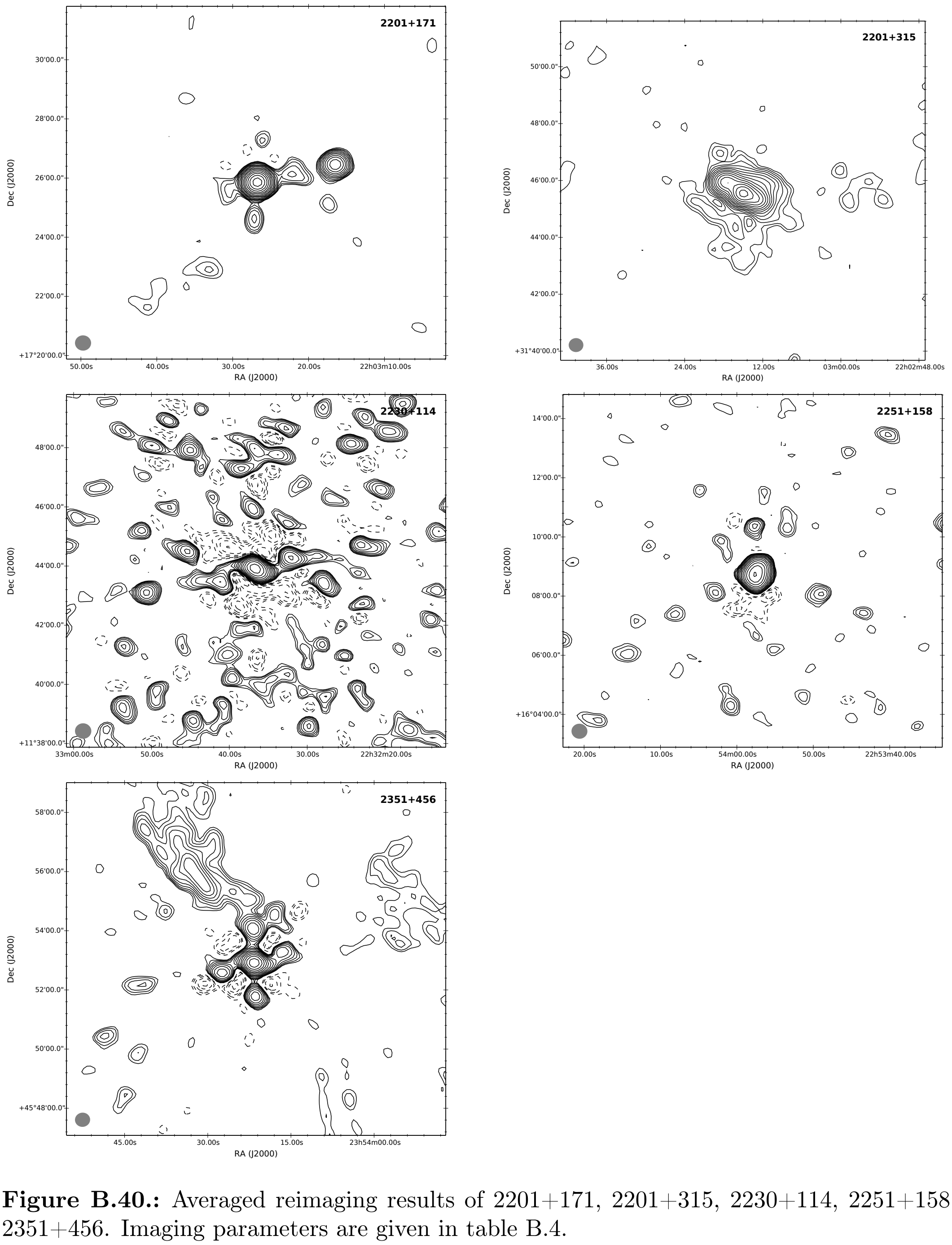

Figure B.40.: Averaged reimaging results of 2201+171, 2201+315, 2230+114, 2251+158 and 2351+456. Imaging parameters are given in table B.4.

Table B.4.: Image parameter of the averaged reimaging results of MSSS. However the absolute flux scale is not corrected, which is why the images are only used for morphological studies.

Source	S_{peak} (Jy beam^{-1})	S_{RMS} (mJy beam^{-1})	beam$_{maj}$ (arcsec)	beam$_{min}$ (arcsec)	beam$_{p.a.}$ (°)
0119+115	0.73	5.83	30.7	30.2	12.3
0235+164	1.99	2.63	29.7	29.2	6.8
0316+413	22.05	4.06	27.5	27.0	-38.3
0415+379	14.44	10.67	42.7	42.2	-45.5
0430+052	4.26	3.65	33.3	32.8	16.4
0458-020	1.90	7.35	34.6	34.1	26.6
0716+714	11.38	2.47	27.2	26.7	-51.6
1036+054	4.32	3.98	33.8	33.3	16.1
1038+064	1.50	3.93	34.6	34.1	15.5
1222+216	4.46	3.95	28.4	27.9	11.3
1228+126	59.75	83.66	30.6	30.1	7.8
1308+326	3.98	1.39	26.3	25.8	10.3
1502+106	4.43	9.59	35.8	35.3	1.4
1538+149	6.52	2.52	30.5	30.0	7.7
1546+027	2.71	6.70	45.2	44.7	40.5
1548+056	0.60	6.54	33.4	32.9	15.0
1606+106	2.39	3.04	33.0	32.5	13.6
1611+343	4.45	2.98	32.3	31.8	-32.1
1633+382	18.98	7.55	28.5	28.0	-39.9
1637+574	4.23	2.09	27.6	27.1	-43.9
1638+398	8.61	9.01	28.0	27.5	-39.8
1726+455	5.93	12.68	55.7	55.2	-52.1
1739+522	3.73	4.22	32.5	32.0	-27.3
1749+096	4.05	3.64	30.6	30.1	12.6
1751+288	2.70	2.32	26.9	26.4	14.8
1803+784	3.16	3.40	27.2	26.7	-60.6
1807+698	3.40	1.39	27.2	26.7	-52.9
1823+568	4.31	3.44	28.3	27.8	-43.7
1828+487	73.40	44.12	64.6	64.1	50.9
1849+670	2.21	5.53	27.2	26.7	-49.4
1928+738	2.35	2.48	27.5	27.0	-53.0
2021+317	18.23	2.94	26.4	25.9	21.0
2021+614	1.08	2.27	27.5	27.0	-43.7
2037+511	15.43	8.23	27.8	27.3	-38.2
2121+053	1.70	6.64	35.1	34.6	7.0
2131-021	1.48	5.71	33.1	32.6	-47.4
2134+004	2.83	6.23	32.2	31.7	19.4
2136+141	1.88	6.93	31.6	31.1	7.8
2145+067	3.21	3.60	33.8	33.3	13.4
2200+420	1.65	16.84	29.1	28.6	-51.8
2201+171	2.34	3.28	29.6	29.1	6.6
2201+315	5.67	5.48	28.1	27.6	-4.2
2230+114	13.79	41.79	30.0	29.5	14.8
2251+158	9.16	24.23	29.2	28.7	18.9
2351+456	4.97	3.29	27.6	27.1	-35.8

C. Appendix: LOFAR international observations

C.1. High resolution brightness distributions of single frequency bands

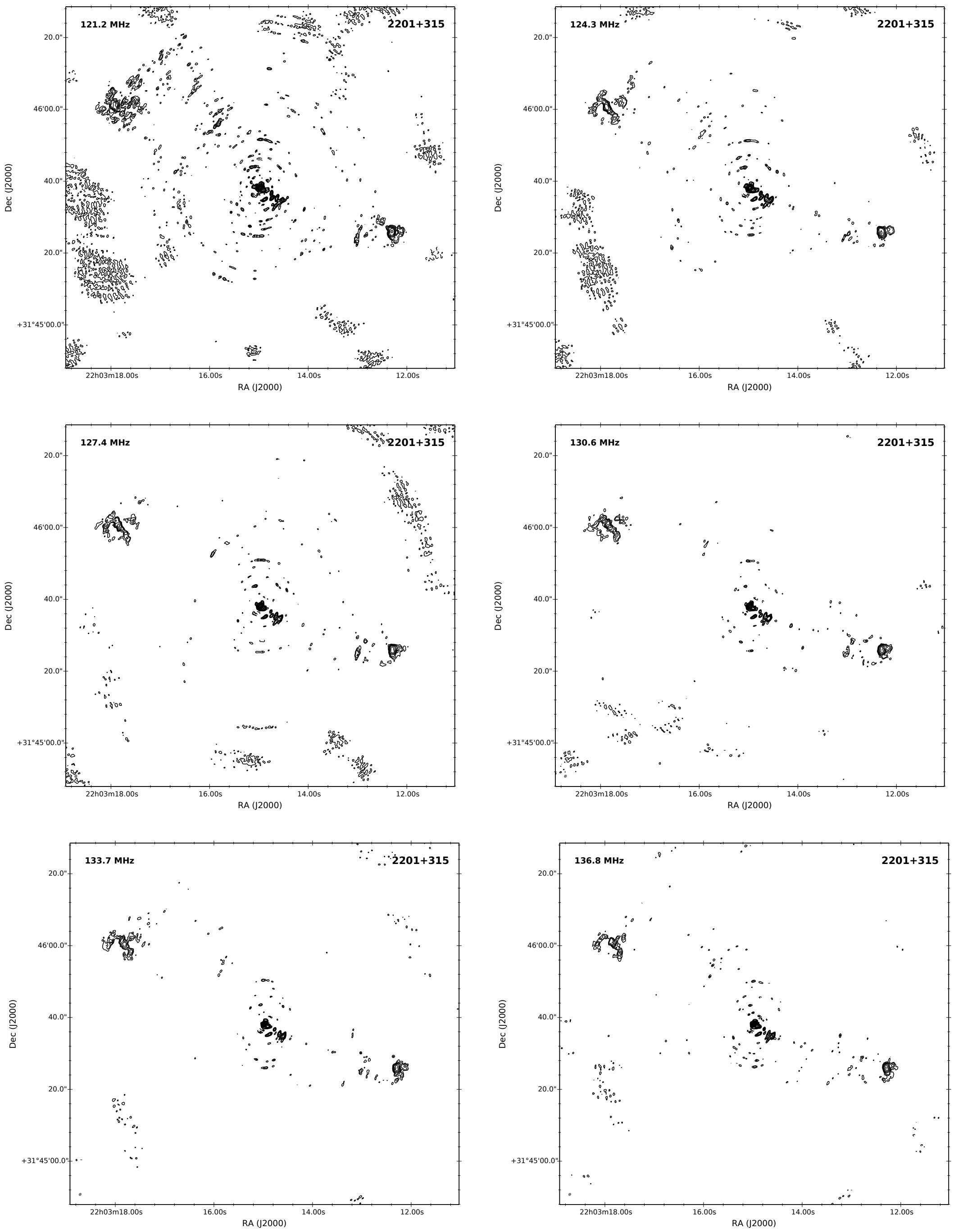

Figure C.1.: Brightness distributions of 2201+315 imaged with natural weighting. The lowest contour level corresponds to 3.5 mJy beam^{-1} with increase of a factor $\sqrt{2}$ to the peak flux density S$_{peak}$. The image parameters are found in table 5.2.

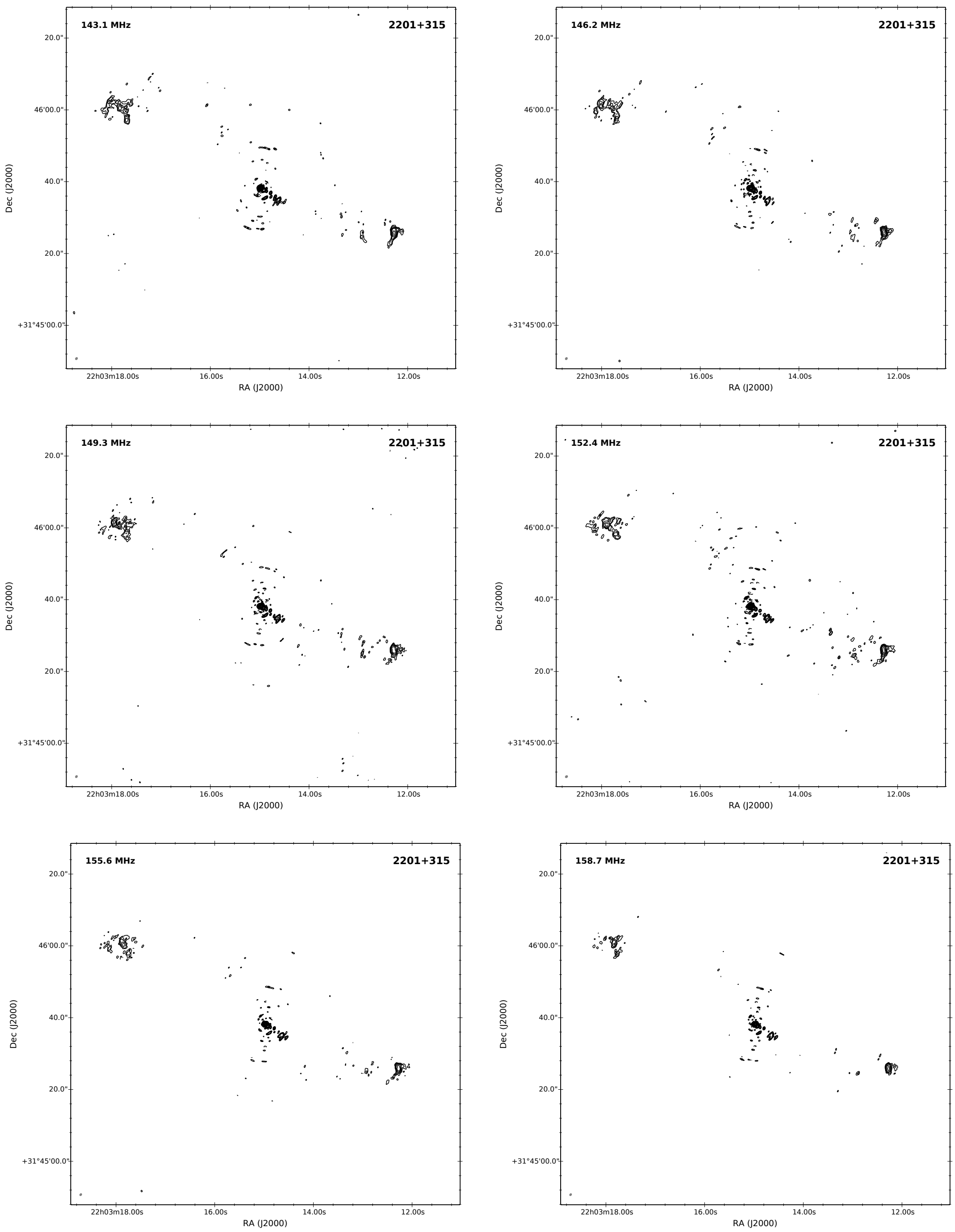

Figure C.2.: *Continue of Figure C.1.*

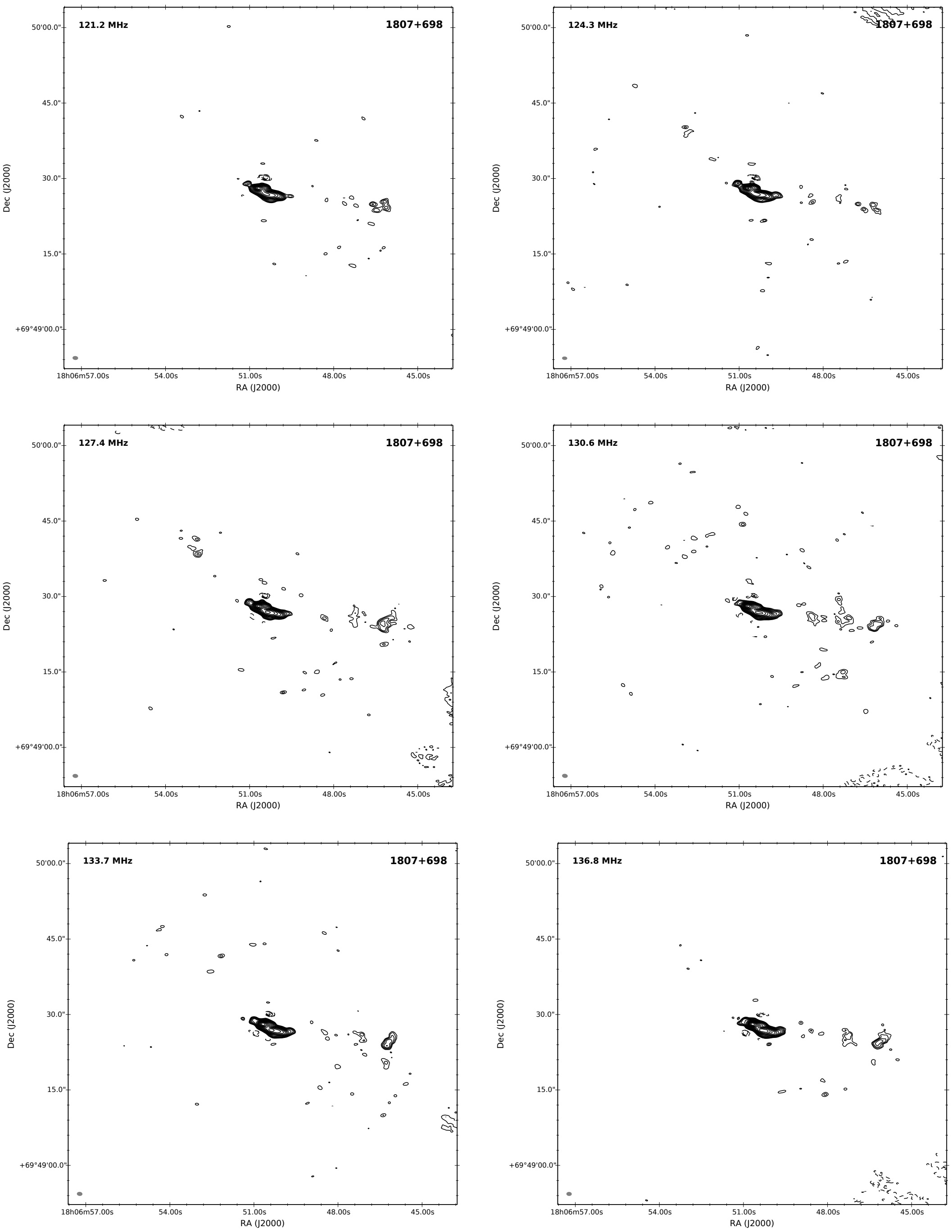

Figure C.3.: Brightness distributions of 1807+698 imaged with natural weighting. The lowest contour level corresponds to 3.0 mJy beam^{-1} with increase of a factor $\sqrt{2}$ to the peak flux density S$_{peak}$. The image parameters are found in table 5.5.

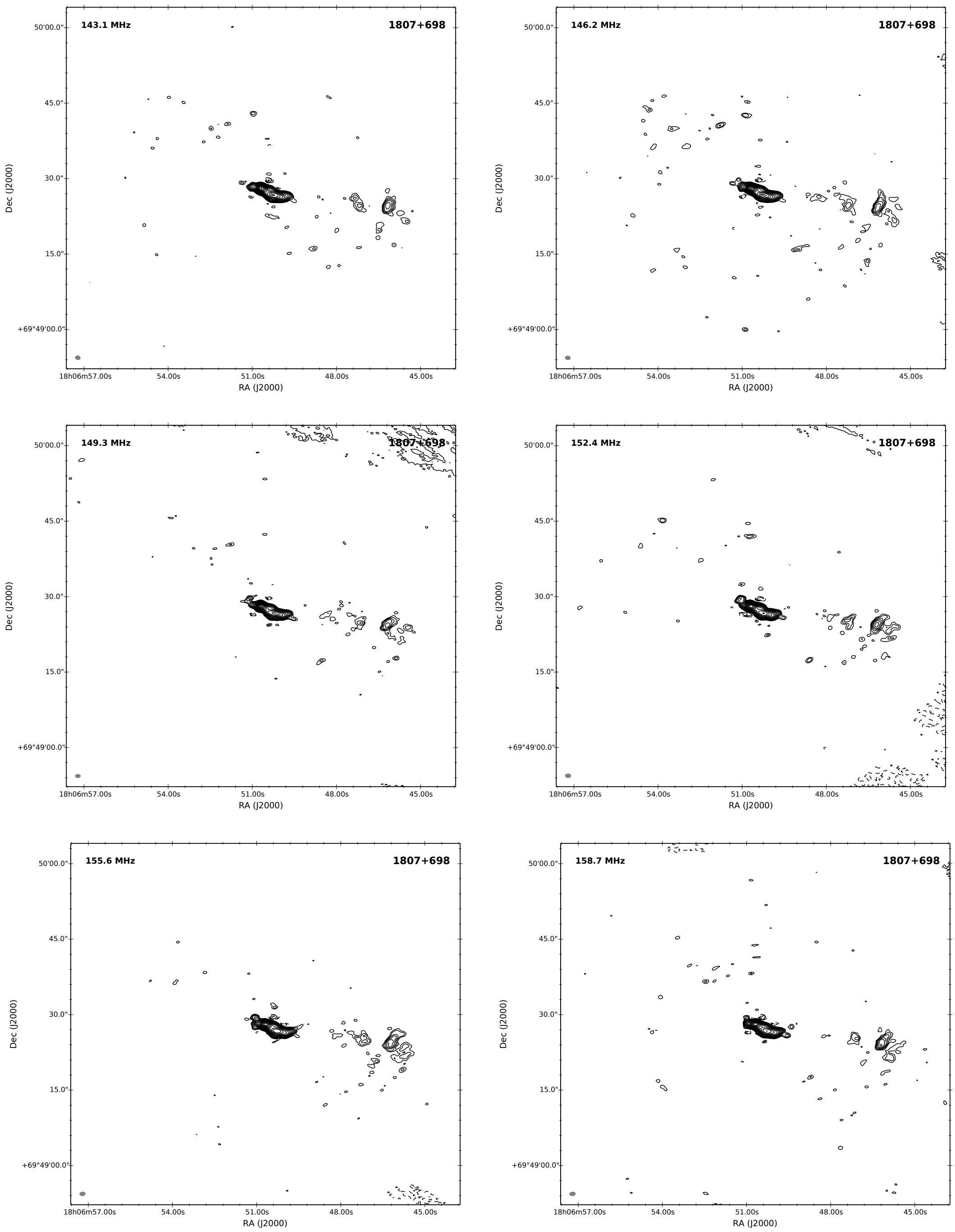

Figure C.4.: *Continue of Figure C.3.*

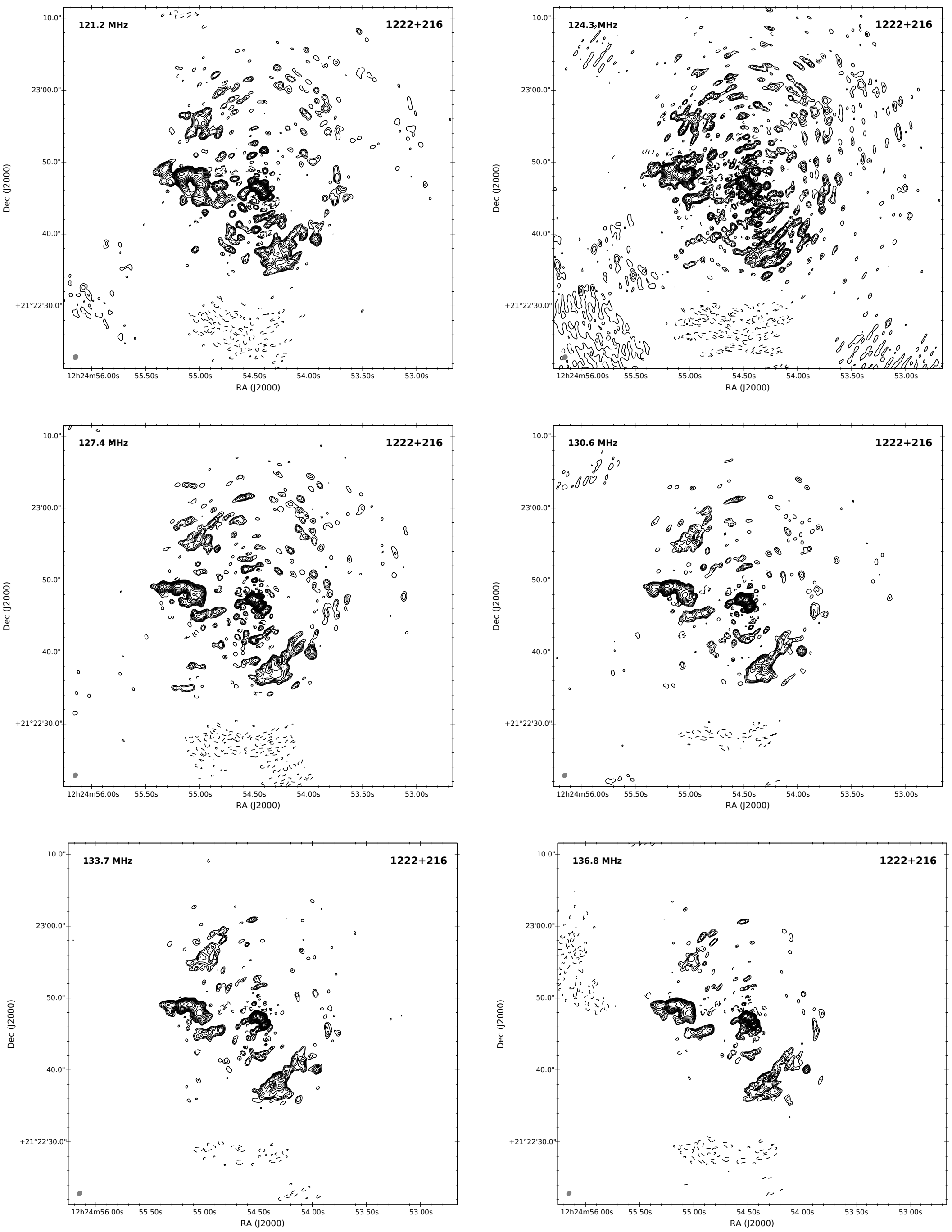

Figure C.5.: Brightness distributions of 1222+216 imaged with natural weighting. The lowest contour level corresponds to 6.0 mJy beam^{-1} with increase of a factor $\sqrt{2}$ to the peak flux density S$_{peak}$. The image parameters are found in table 5.8.

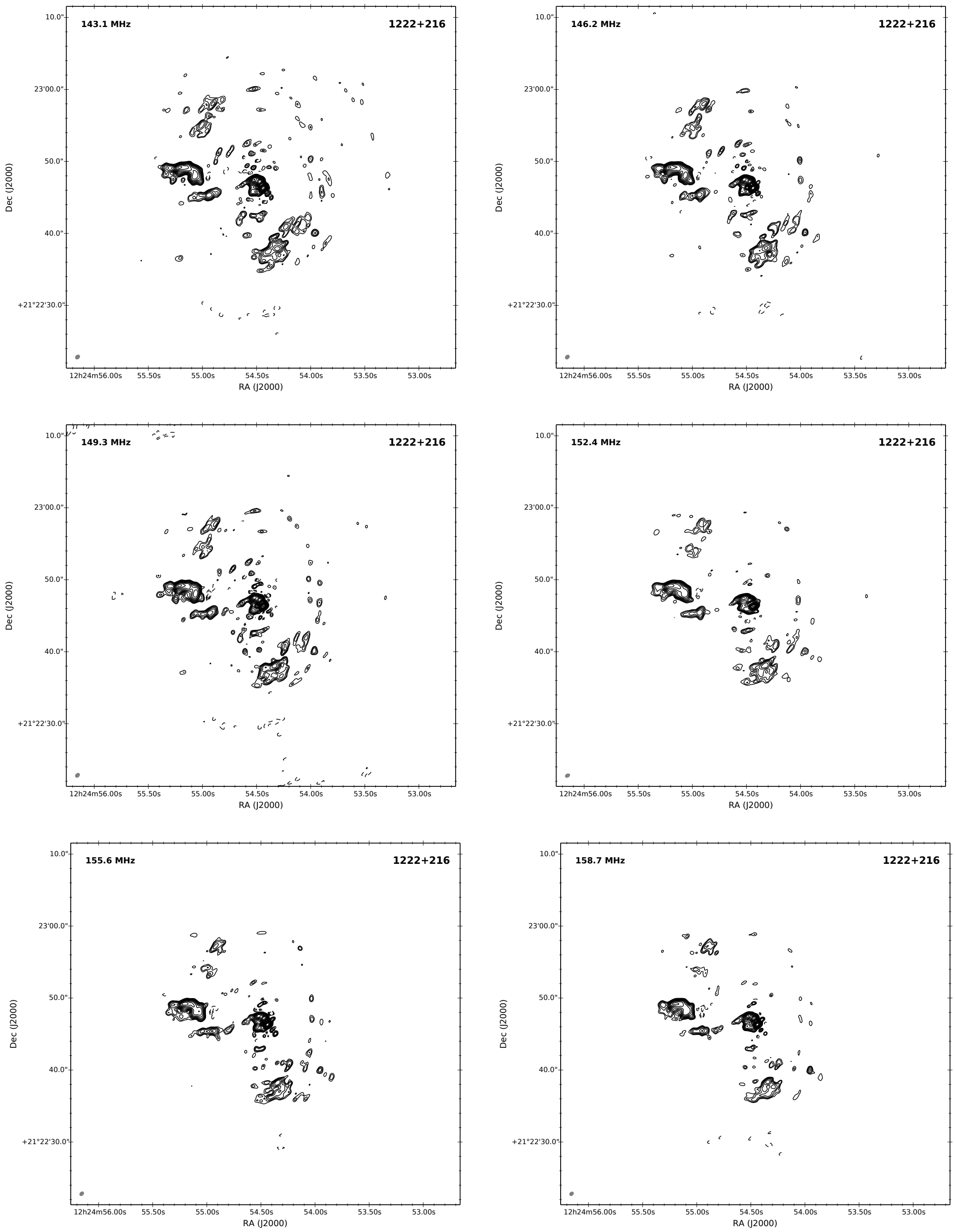

Figure C.6.: *Continue of Figure C.5.*

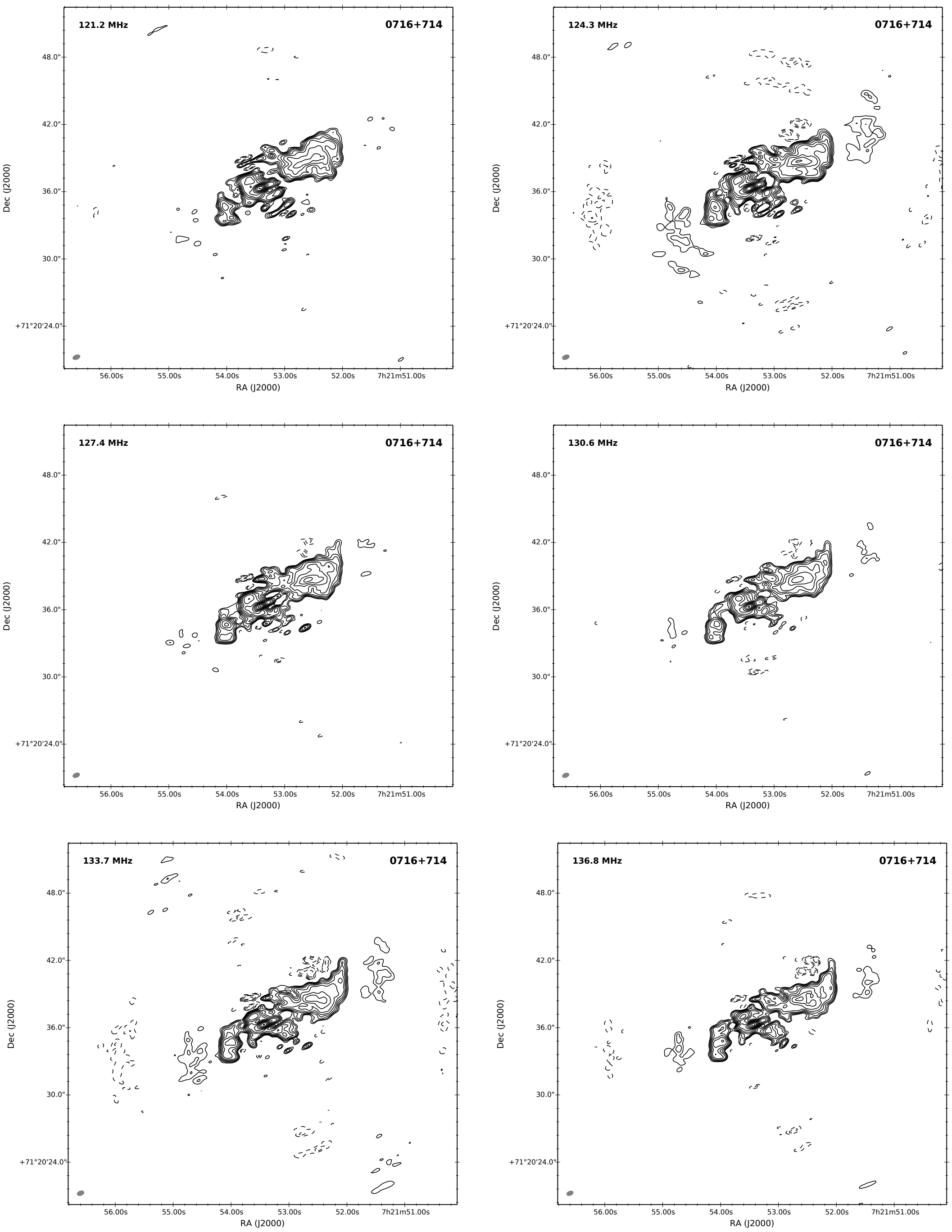

Figure C.7.: Brightness distributions of 0716+714 imaged with natural weighting. The lowest contour level corresponds to 4.0 mJy beam^{-1} with increase of a factor $\sqrt{2}$ to the peak flux density S$_{peak}$. The image parameters are found in table 5.11.

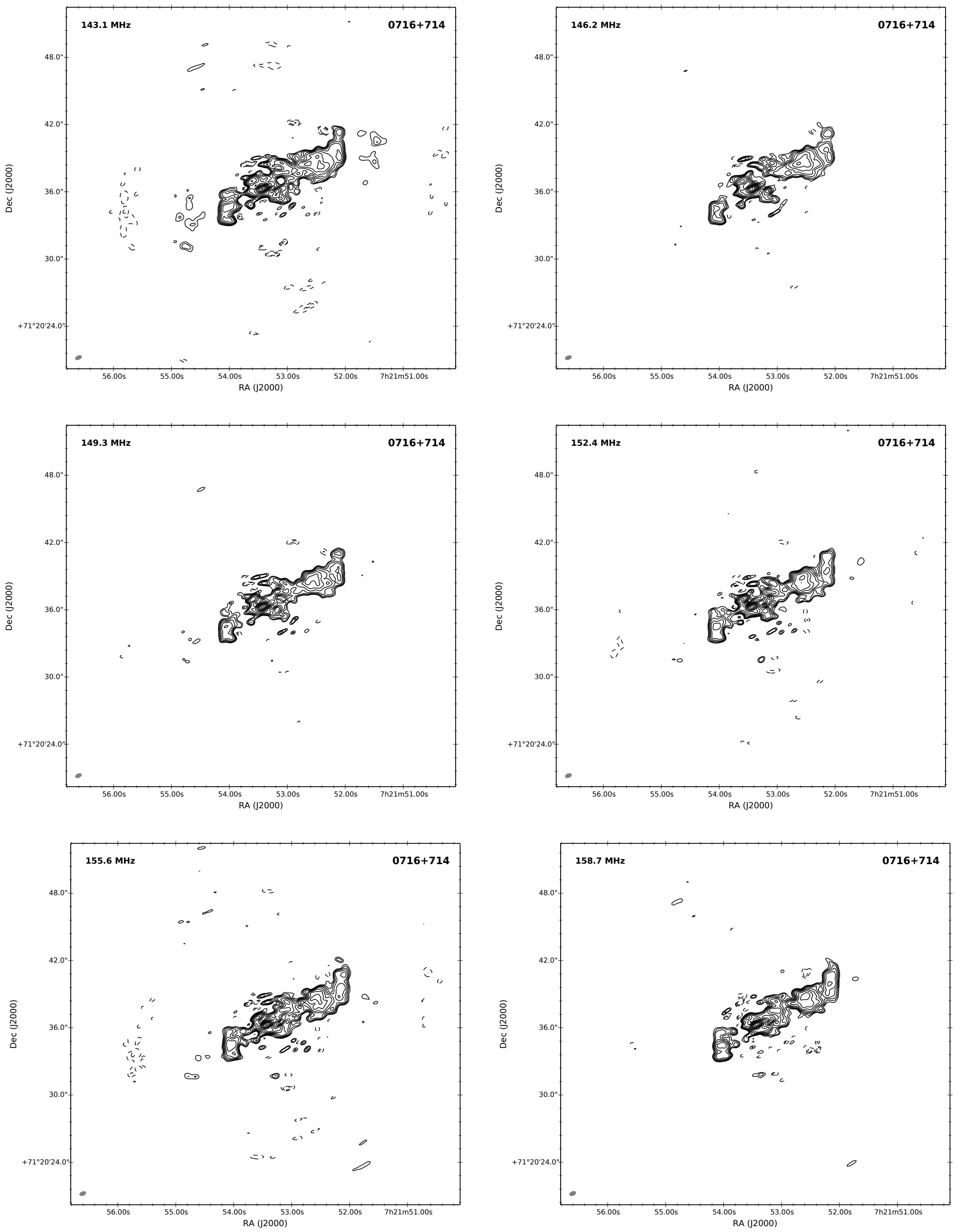

Figure C.8.: *Continue of Figure C.7.*

C.2. Tapered brightness distributions of single frequency bands

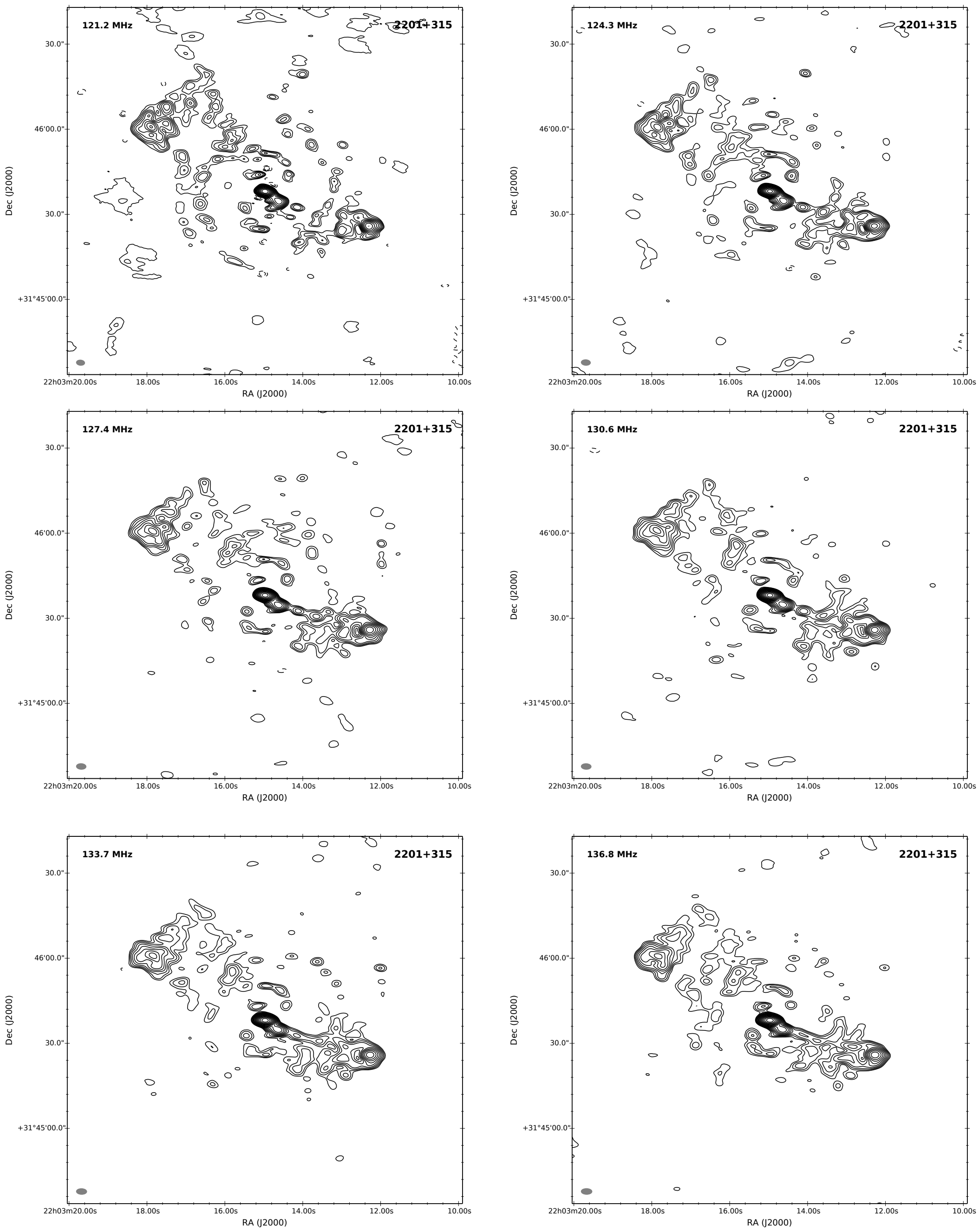

Figure C.9.: Brightness distributions of 2201+315 imaged with natural weighting and a (u, v)-taper to use only the visibilities to a range of 200 kλ. The lowest contour level corresponds to 7.0 mJy beam^{-1} with increase of a factor $\sqrt{2}$ to the peak flux density S$_{peak}$. The image parameters are found in table 5.3.

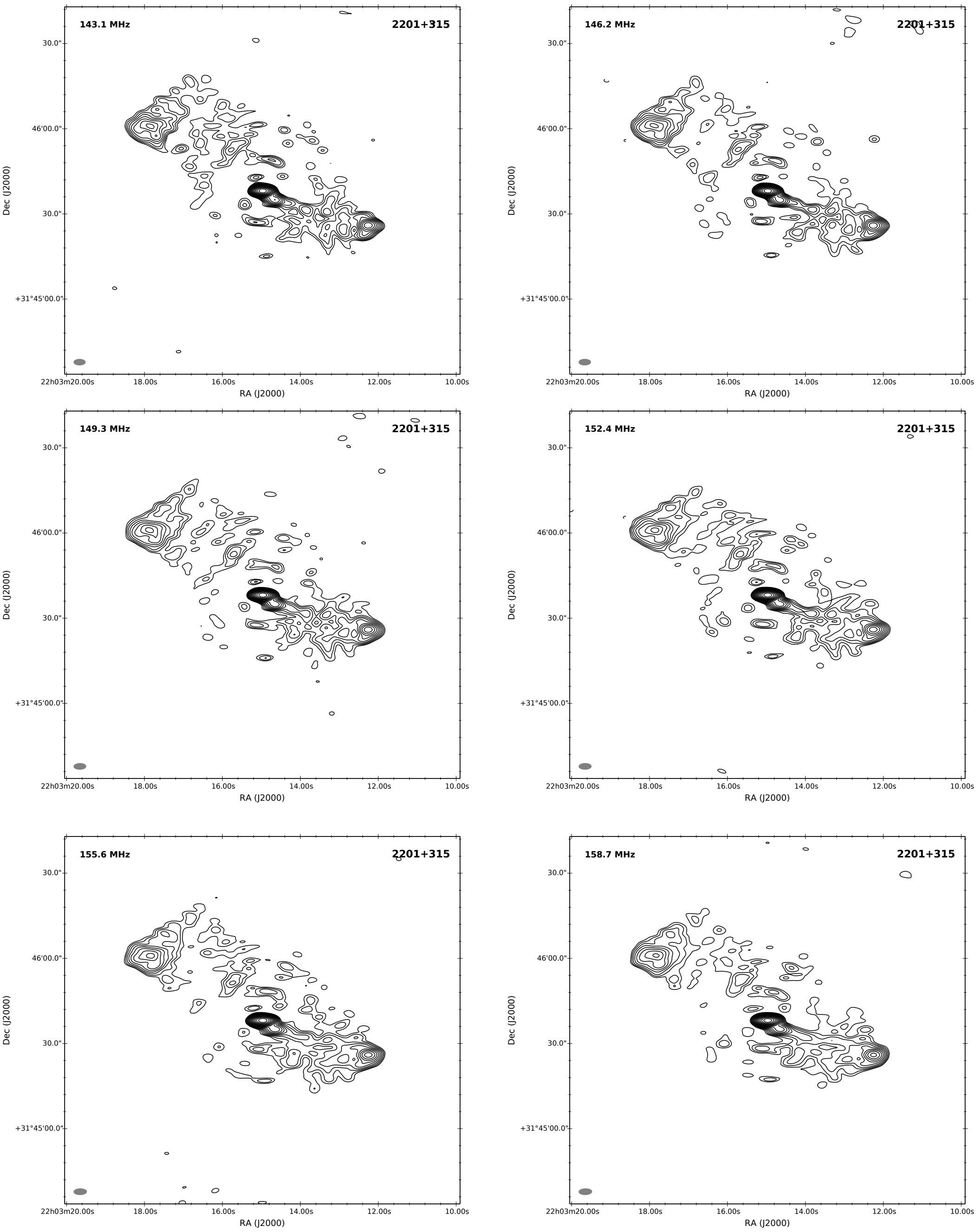

Figure C.10.: *Continue of Figure C.9.*

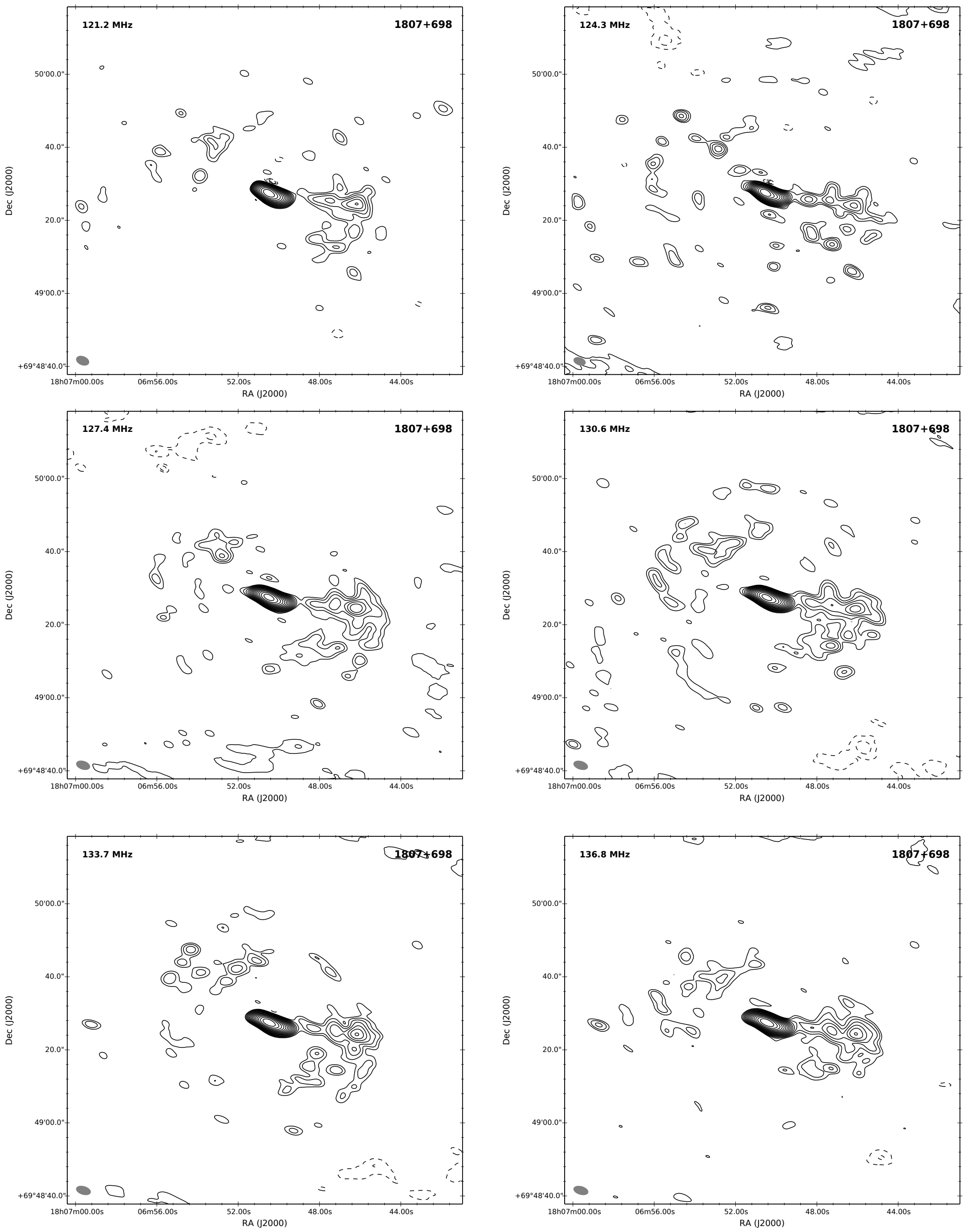

Figure C.11.: Brightness distributions of 1807+698 imaged with natural weighting and a (u, v)-taper to use only the visibilities to a range of 200 kλ. The lowest contour level corresponds to 6.0 mJy beam^{-1} with increase of a factor $\sqrt{2}$ to the peak flux density S$_{peak}$. The image parameters are found in table 5.6.

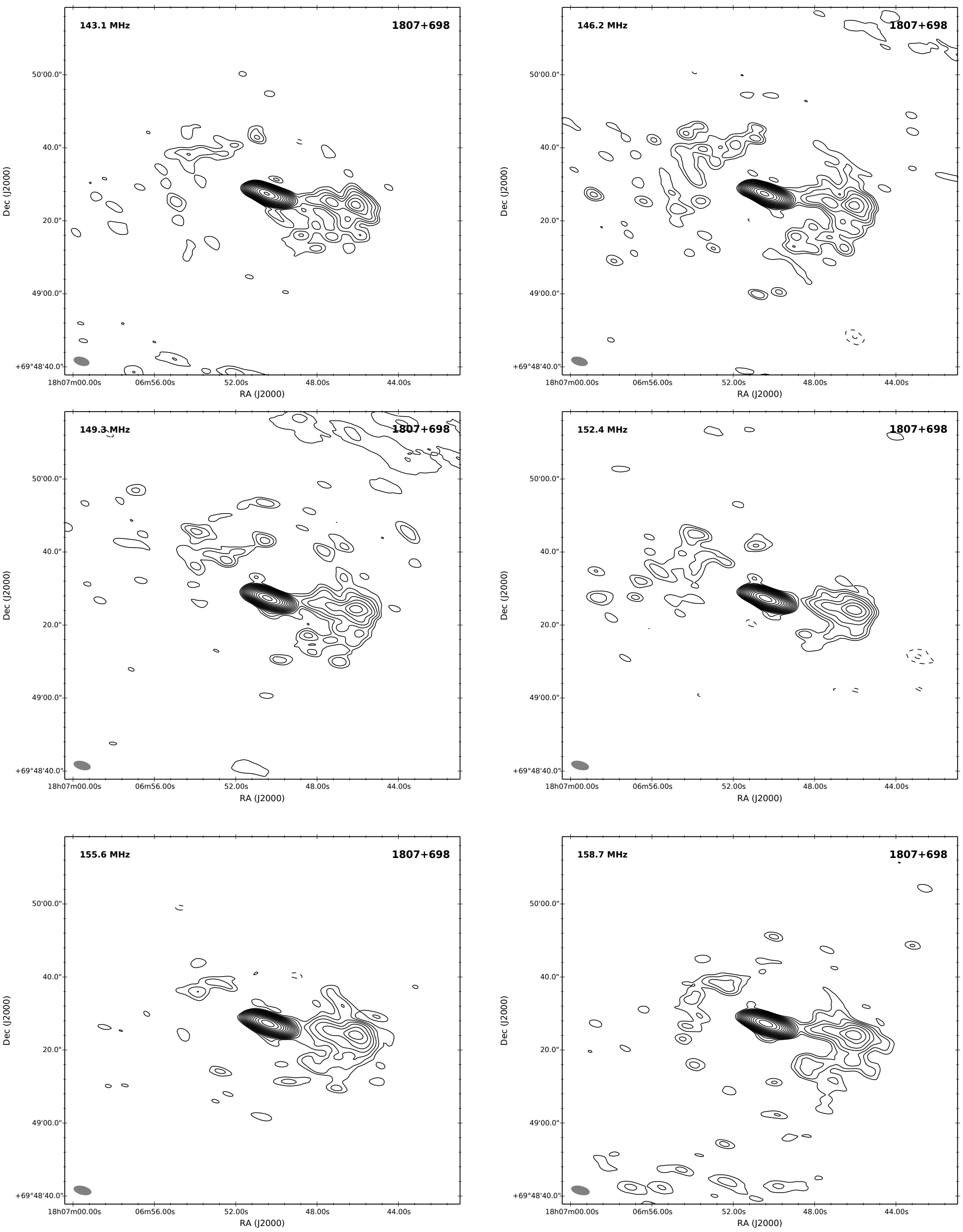

Figure C.12.: *Continue of Figure C.11.*

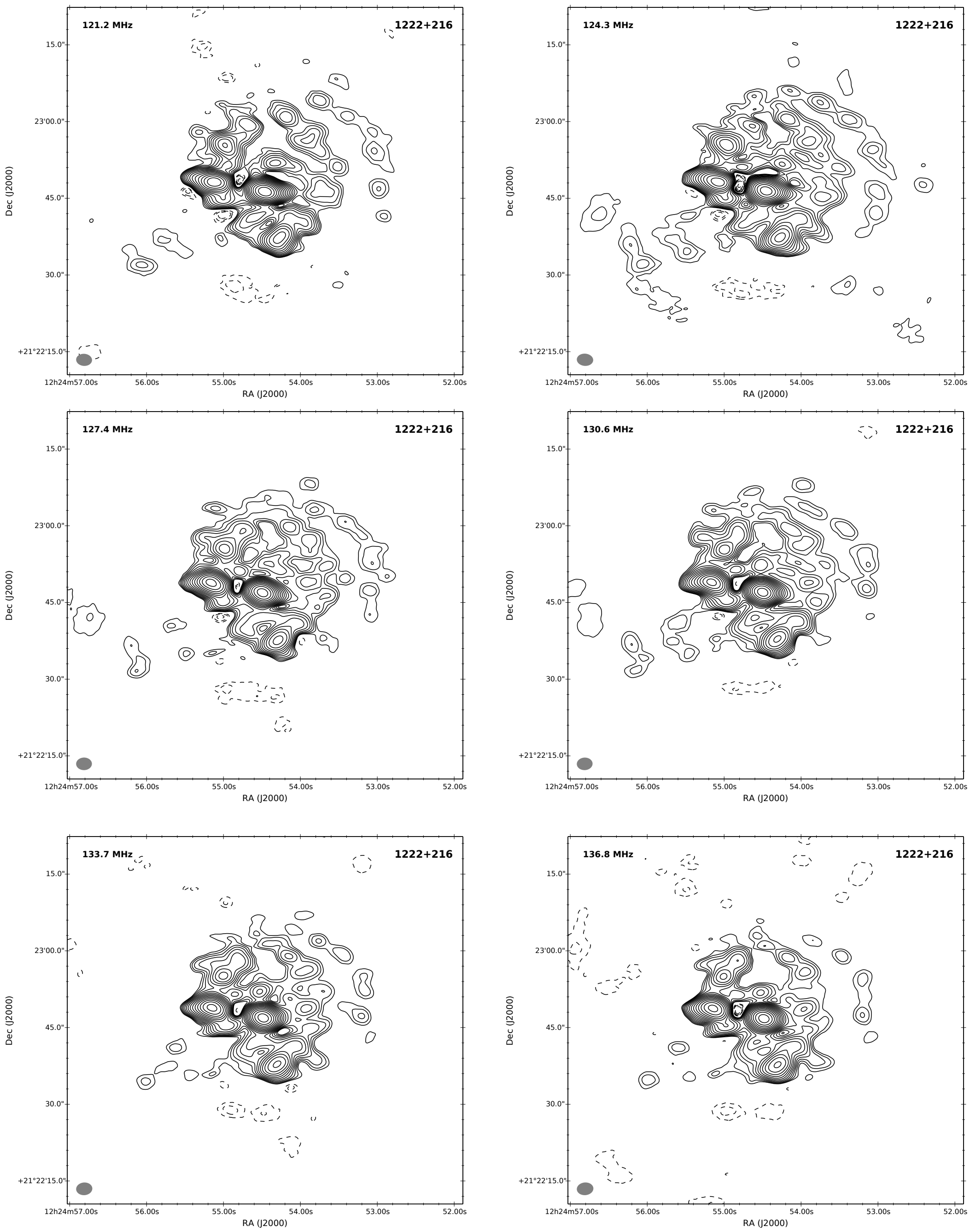

Figure C.13.: Brightness distributions of 1222+216 imaged with natural weighting and a (u, v)-taper to use only the visibilities to a range of 200 kλ. The lowest contour level corresponds to 12.0 mJy beam^{-1} with increase of a factor $\sqrt{2}$ to the peak flux density S$_{peak}$. The image parameters are found in table 5.9.

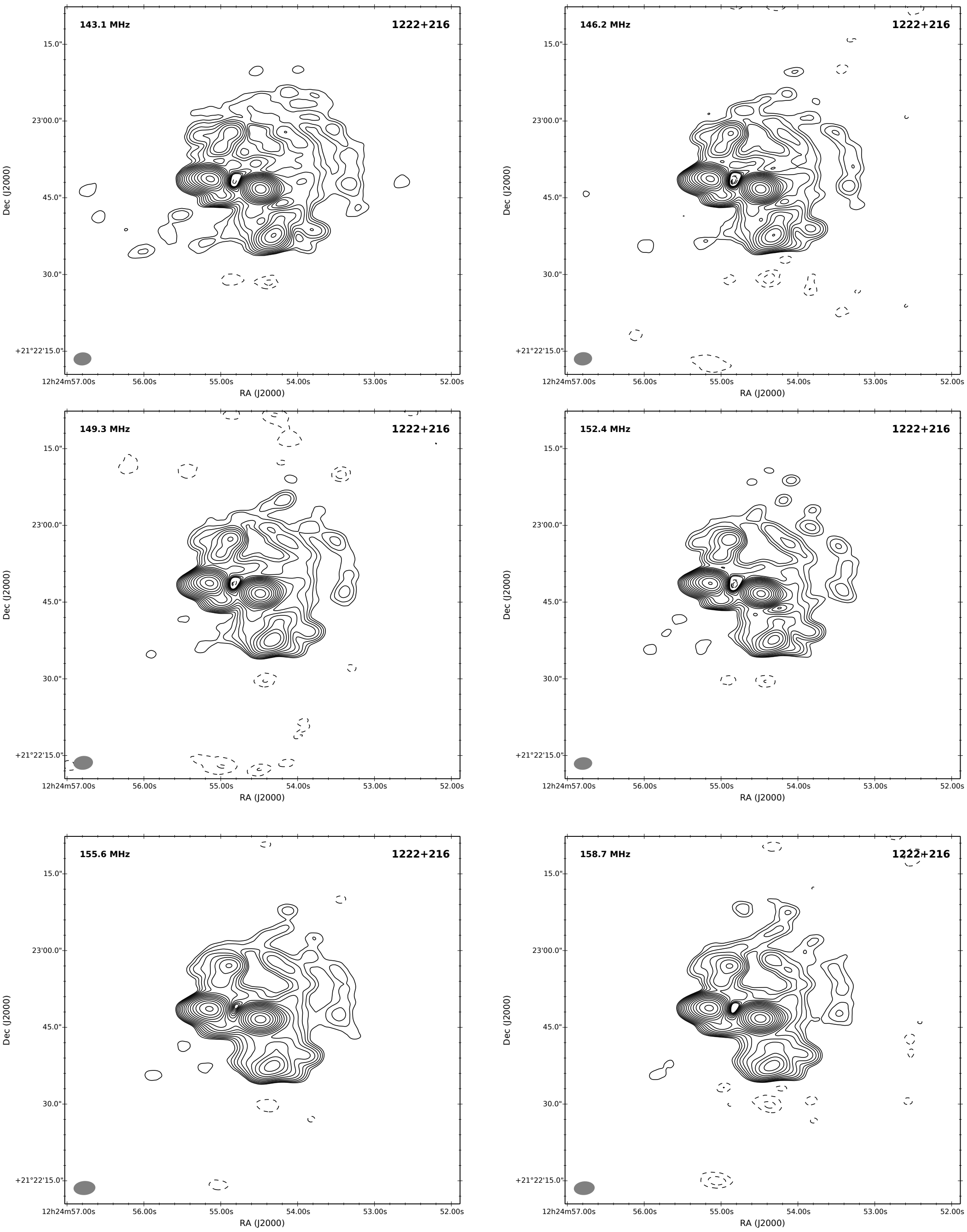

Figure C.14.: *Continue of Figure C.13.*

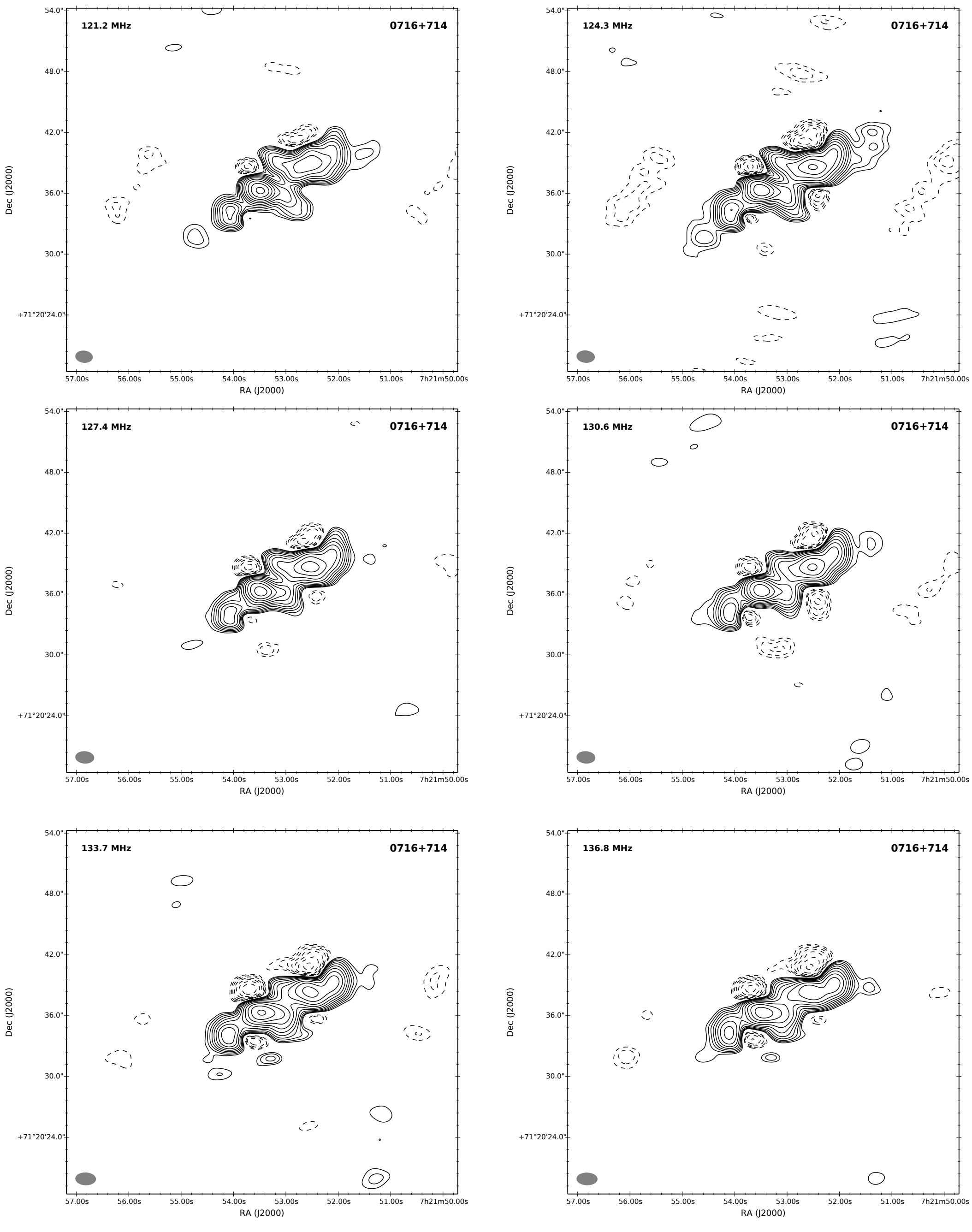

Figure C.15.: Brightness distributions of 0716+714 imaged with natural weighting and a (u, v)-taper to use only the visibilities to a range of 200 kλ. The lowest contour level corresponds to 15.0 mJy beam^{-1} with increase of a factor $\sqrt{2}$ to the peak flux density S$_{peak}$. The image parameters are found in table 5.12.

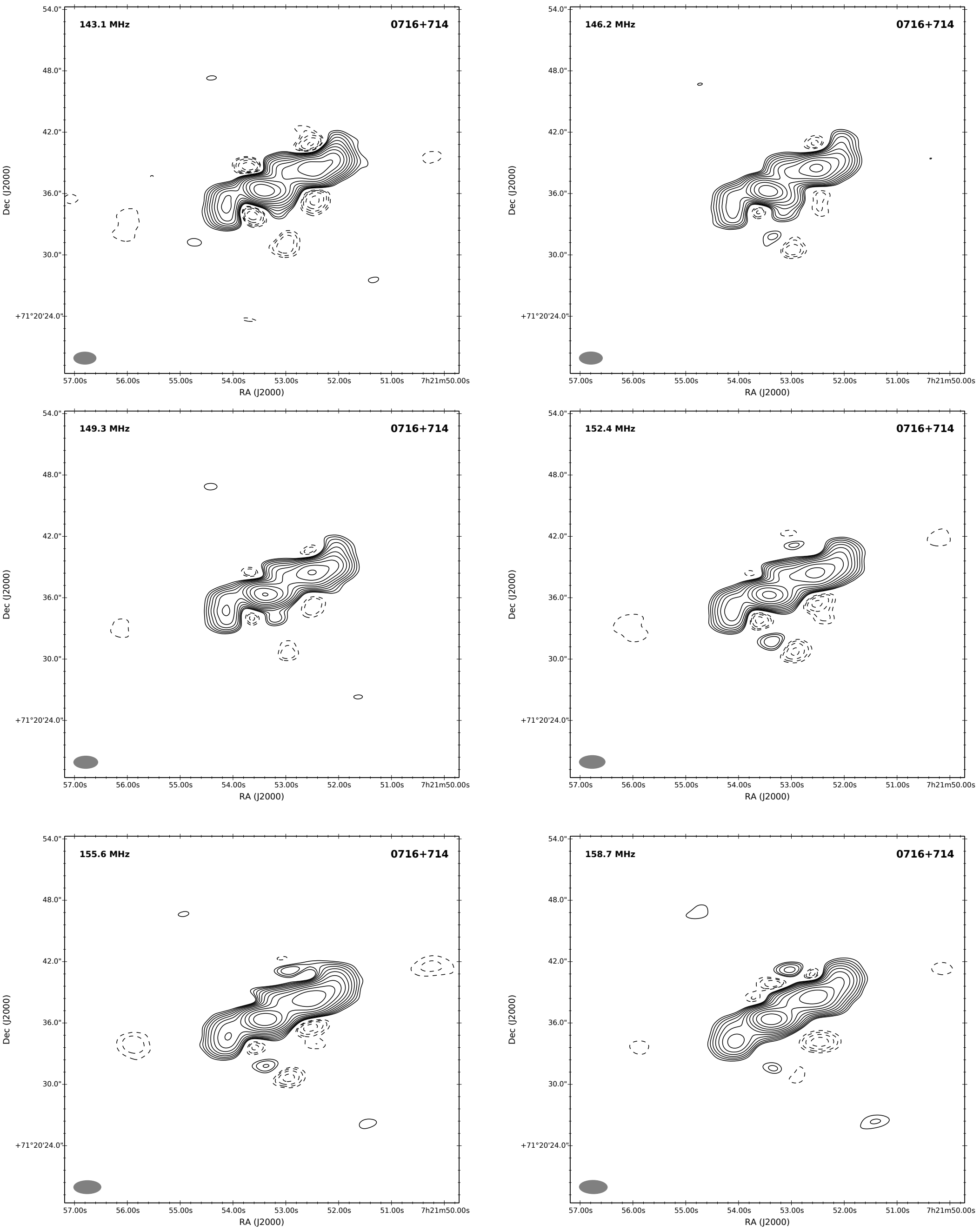

Figure C.16.: *Continue of Figure C.15.*

C.3. Example: AIPS script

```
procedure SCRIPTRUN()
    for i=1 to 39 $ to max catalogue id
        task 'FITLD'; default;
     if (i=1) then; DATAIN 'DATA:LC3_027/1807+698/1807+698-BAND0.FITS';
outname '1807-BAND0';end;
if (i=4) then; DATAIN 'DATA:LC3_027/1807+698/1807+698-BAND1.FITS';
outname '1807-BAND1';end;
if (i=7) then; DATAIN 'DATA:LC3_027/1807+698/1807+698-BAND2.FITS';
outname '1807-BAND2';end;
     if (i=10) then; DATAIN 'DATA:LC3_027/1807+698/1807+698-BAND3.FITS';
outname '1807-BAND3';end;
     if (i=13) then; DATAIN 'DATA:LC3_027/1807+698/1807+698-BAND4.FITS';
outname '1807-BAND4';end;
     if (i=16) then; DATAIN 'DATA:LC3_027/1807+698/1807+698-BAND5.FITS';
outname '1807-BAND5';end;
     if (i=19) then; DATAIN 'DATA:LC3_027/1807+698/1807+698-BAND6.FITS';
outname '1807-BAND6';end;
     if (i=22) then; DATAIN 'DATA:LC3_027/1807+698/1807+698-BAND7.FITS';
outname '1807-BAND7';end;
     if (i=25) then; DATAIN 'DATA:LC3_027/1807+698/1807+698-BAND8.FITS';
outname '1807-BAND8';end;
     if (i=28) then; DATAIN 'DATA:LC3_027/1807+698/1807+698-BAND9.FITS';
outname '1807-BAND9';end;
     if (i=31) then; DATAIN 'DATA:LC3_027/1807+698/1807+698-BAND10.FITS';
outname '1807-BAND10';end;
     if (i=34) then; DATAIN 'DATA:LC3_027/1807+698/1807+698-BAND11.FITS';
outname '1807-BAND11';end;
     if (i=37) then; DATAIN 'DATA:LC3_027/1807+698/1807+698-BAND12.FITS';
outname '1807-BAND12';end;
     douvcomp -1; digicor -1; ERROR -1; BIF 0; EIF 0; DIGICOR -1; OPCODE ' ';
     go; wait;
     task 'indxr'; default;
     getn i; cparm(3) 0.167;
go;wait;
task 'clcor'; default; getn i; antennas 15,16,17,18,19,20,21;
     opcode 'gain'; clcorprm 0.1,0; gainuse 2; gainver 1;
     go; wait;
     task 'fixwt'; default; getn i; DOUVCOMP -1; SOLINT 5;
     go; wait;
     tget 'indxr'; i= i+1; getn i;
     go; wait;
     task 'fring'; default ; getn i; ANTENNAS 0; UVRANGE 10,0;
DOCALIB 2; GAINUSE 2; CMETHOD 'DFT'; REFANT 22; SOLINT 1;
DPARM 0,3000,90,0;
     go; wait;
     task 'snsmo'; default; getn i; samptype='MWF'; cparm(2)=0;
cparm(3)=0.3; cparm(4)=1.0; cparm(5)=1.0; cparm(7)=400;
cparm(8)=10; cparm(9)=100; cparm(10)=100; inver=1; outver=2;
```

```
SMOTYPE 'VLBI'; REFANT 22; DOBLANK -1;
     go; wait;
     task 'clcal'; default; getn i; ANTENNAS 0; OPCODE 'CALI';
INTERPOL 'CUBE'; BPARM 0; SMOTYPE ' '; DOBLANK 0; SNVER 2;
INVERS 0; REFANT 22; GAINVER 0; GAINUSE 0;
     go; wait;
     task 'split'; default; getn i; DOCALIB 2; GAINUSE 3;
DOUVCOMP -1; APARM 2,0;
     go; wait;
     task 'fittp'; default; i=i+1; getn i; INTYPE 'UV';
     if (i=3) then; DATAOUT 'DATA:LC3_027/1807+698/1807+698-BAND0.UVFITS';end;
     if (i=6) then; DATAOUT 'DATA:LC3_027/1807+698/1807+698-BAND1.UVFITS';end;
     if (i=9) then; DATAOUT 'DATA:LC3_027/1807+698/1807+698-BAND2.UVFITS';end;
     if (i=12) then; DATAOUT 'DATA:LC3_027/1807+698/1807+698-BAND3.UVFITS';end;
     if (i=15) then; DATAOUT 'DATA:LC3_027/1807+698/1807+698-BAND4.UVFITS';end;
     if (i=18) then; DATAOUT 'DATA:LC3_027/1807+698/1807+698-BAND5.UVFITS';end;
     if (i=21) then; DATAOUT 'DATA:LC3_027/1807+698/1807+698-BAND6.UVFITS';end;
     if (i=24) then; DATAOUT 'DATA:LC3_027/1807+698/1807+698-BAND7.UVFITS';end;
     if (i=27) then; DATAOUT 'DATA:LC3_027/1807+698/1807+698-BAND8.UVFITS';end;
     if (i=30) then; DATAOUT 'DATA:LC3_027/1807+698/1807+698-BAND9.UVFITS';end;
     if (i=33) then; DATAOUT 'DATA:LC3_027/1807+698/1807+698-BAND10.UVFITS';end;
     if (i=36) then; DATAOUT 'DATA:LC3_027/1807+698/1807+698-BAND11.UVFITS';end;
     if (i=39) then; DATAOUT 'DATA:LC3_027/1807+698/1807+698-BAND12.UVFITS';end;
     go; wait;
    end
finish
```

Bibliography

Aartsen, M. G., Abbasi, R., Abdou, Y., et al. 2013, Physical Review Letters, 111, 021103
Aartsen, M. G., Ackermann, M., Adams, J., et al. 2014, Physical Review Letters, 113, 101101
Abazajian, K. N., Adelman-McCarthy, J. K., Agüeros, M. A., et al. 2009, ApJS, 182, 543
Abdo, A. A., Ackermann, M., Ajello, M., et al. 2010, ApJS, 188, 405
Acero, F., Ackermann, M., Ajello, M., et al. 2015, ApJS, 218, 23
Ackermann, M., Ajello, M., Allafort, A., et al. 2011, ApJ, 743, 171
Ackermann, M., Ajello, M., Atwood, W. B., et al. 2015, ApJ, 810, 14
Adgie, R. L., Gent, H., Slee, O. B., et al. 1965, Nature, 208, 275
Ageron, M., Aguilar, J. A., Al Samarai, I., et al. 2011, Nuclear Instruments and Methods in Physics Research A, 656, 11
Agudo, I., Gómez, J. L., Casadio, C., Cawthorne, T. V., & Roca-Sogorb, M. 2012, ApJ, 752, 92
Aharonian, F., Arshakian, T. G., Allen, B., et al. 2013, ArXiv:1301.4124
Antonucci, R. 1993, ARA&A, 31, 473
Antonucci, R. R. J., Hickson, P., Olszewski, E. W., & Miller, J. S. 1986, AJ, 92, 1
Antonucci, R. R. J. & Miller, J. S. 1985, ApJ, 297, 621
Antonucci, R. R. J. & Ulvestad, J. S. 1985, ApJ, 294, 158
Arshakian, T. G., Torrealba, J., Chavushyan, V. H., et al. 2010, A&A, 520, A62
Atwood, W. B., Abdo, A. A., Ackermann, M., et al. 2009, ApJ, 697, 1071
Barber, D. 1966, Nature, 209, 753
Baum, S. A., Zirbel, E. L., & O'Dea, C. P. 1995, ApJ, 451, 88
Becker, R. H., White, R. L., & Helfand, D. J. 1995, ApJ, 450, 559
Bhatnagar, S., Cornwell, T. J., Golap, K., & Uson, J. M. 2008, A&A, 487, 419
Blandford, R. D. & Königl, A. 1979, ApJ, 232, 34
Blandford, R. D. & Payne, D. G. 1982, MNRAS, 199, 883
Blandford, R. D. & Znajek, R. L. 1977, MNRAS, 179, 433
Bloom, S. D., Fromm, C. M., & Ros, E. 2013, AJ, 145, 12
Böck, M., Kadler, M., Müller, C., et al. 2016, A&A, 590, A40
Bridle, A. H. & Perley, R. A. 1984, ARA&A, 22, 319
Briggs, D. S. 1995, in Bulletin of the American Astronomical Society, Vol. 27, American Astronomical Society Meeting Abstracts, 1444
Burbidge, G. R. & Burbidge, E. M. 1957, ApJ, 125, 1
Burke, B. F. & Graham-Smith, F. 2010, An Introduction to Radio Astronomy (Cambridge University Press)
Burrows, D. N., Hill, J. E., Nousek, J. A., et al. 2005, Space Sci. Rev., 120, 165
Cara, M. & Lister, M. L. 2008, ApJ, 674, 111
Carilli, C. L. & Rawlings, S. 2004, New A Rev., 48, 979
Chen, Y., Zhang, X., Zhang, H., et al. 2015, Ap&SS, 357, 100

Cohen, A. S., Lane, W. M., Cotton, W. D., et al. 2007a, AJ, 134, 1245
Cohen, M. H., Lister, M. L., Homan, D. C., et al. 2007b, ApJ, 658, 232
Condon, J. J., Cotton, W. D., Greisen, E. W., et al. 1998, AJ, 115, 1693
Cooper, N. J., Lister, M. L., & Kochanczyk, M. D. 2007, ApJS, 171, 376
Cornwell, T. J. 2008, IEEE Journal of Selected Topics in Signal Processing, 2, 793
Cornwell, T. J., Golap, K., & Bhatnagar, S. 2008, IEEE Journal of Selected Topics in Signal Processing, 2, 647
Cornwell, T. J. & Wilkinson, P. N. 1981, MNRAS, 196, 1067
Cotton, W. D. 1995, in Astronomical Society of the Pacific Conference Series, Vol. 82, Very Long Baseline Interferometry and the VLBA, ed. J. A. Zensus, P. J. Diamond, & P. J. Napier, 189
Davies, J. G., Anderson, B., & Morison, I. 1980, Nature, 288, 64
de Gasperin, F., Orrú, E., Murgia, M., et al. 2012, A&A, 547, A56
de Grijp, M. H. K., Keel, W. C., Miley, G. K., Goudfrooij, P., & Lub, J. 1992, A&AS, 96, 389
Diamond, P. J. 1995, in Astronomical Society of the Pacific Conference Series, Vol. 82, Very Long Baseline Interferometry and the VLBA, ed. J. A. Zensus, P. J. Diamond, & P. J. Napier, 227
Doeleman, S. 2008, Journal of Physics Conference Series, 131, 012055
Eckart, A. & Genzel, R. 1996, Nature, 383, 415
Ellingson, S. W., Clarke, T. E., Cohen, A., et al. 2009, IEEE Proceedings, 97, 1421
Ellingson, S. W., Taylor, G. B., Craig, J., et al. 2013, IEEE Transactions on Antennas and Propagation, 61, 2540
Ewen, H. I. & Purcell, E. M. 1951, Nature, 168, 356
Fanaroff, B. L. & Riley, J. M. 1974a, MNRAS, 167, 31P
Fanaroff, B. L. & Riley, J. M. 1974b, MNRAS, 167, 31P
Fermi, E. 1949, Physical Review, 75, 1169
Foschini, L., Berton, M., Caccianiga, A., et al. 2015, A&A, 575, A13
Ghisellini, G. & Celotti, A. 2001, A&A, 379, L1
Ghisellini, G., Tavecchio, F., Foschini, L., & Ghirlanda, G. 2011, MNRAS, 414, 2674
Gillessen, S., Eisenhauer, F., Trippe, S., et al. 2009, ApJ, 692, 1075
Giroletti, M., Giovannini, G., Taylor, G. B., & Falomo, R. 2004, ApJ, 613, 752
Giroletti, M., Giovannini, G., Taylor, G. B., & Falomo, R. 2006, ApJ, 646, 801
Goldoni, P., Pita, S., Boisson, C., et al. 2016, A&A, 586, L2
Gopal-Krishna & Wiita, P. J. 2000, A&A, 363, 507
Gower, A. C. & Hutchings, J. B. 1984, AJ, 89, 1658
Greenstein, J. L. & Schmidt, M. 1964, ApJ, 140, 1
Greisen, E. W. 2003, Information Handling in Astronomy - Historical Vistas, 285, 109
Hales, S. E. G., Riley, J. M., Waldram, E. M., Warner, P. J., & Baldwin, J. E. 2007, MNRAS, 382, 1639
Hales, S. E. G., Waldram, E. M., Rees, N., & Warner, P. J. 1995, MNRAS, 274, 447
Hamaker, J. P. 2000, A&AS, 143, 515
Hamaker, J. P. 2006, A&A, 456, 395
Hamaker, J. P. & Bregman, J. D. 1996, A&AS, 117, 161
Hamaker, J. P., Bregman, J. D., & Sault, R. J. 1996, A&AS, 117, 137

Harris, G. L. H., Rejkuba, M., & Harris, W. E. 2010, PASA, 27, 457
Hartman, R. C., Bertsch, D. L., Fichtel, C. E., et al. 1992, ApJ, 385, L1
Heald, G., McKean, J., Pizzo, R., et al. 2010, in ISKAF2010 Science Meeting, 57
Heald, G. H., Pizzo, R. F., Orrú, E., et al. 2015, A&A, 582, A123
Heywood, I., Blundell, K. M., & Rawlings, S. 2007, MNRAS, 381, 1093
Hoffmeister, C. 1929, Astronomische Nachrichten, 236, 233
Högbom, J. A. 1974, A&AS, 15, 417
Homan, D. C., Kadler, M., Kellermann, K. I., et al. 2009, ApJ, 706, 1253
Homan, D. C. & Lister, M. L. 2006, AJ, 131, 1262
Homan, D. C., Lister, M. L., Kovalev, Y. Y., et al. 2015, ApJ, 798, 134
Hopkins, A. M., Miller, C. J., Connolly, A. J., et al. 2002, AJ, 123, 1086
Hovatta, T., Aller, M. F., Aller, H. D., et al. 2014, AJ, 147, 143
Hovatta, T., Lister, M. L., Aller, M. F., et al. 2012, AJ, 144, 105
Hovatta, T., Lister, M. L., Kovalev, Y. Y., Pushkarev, A. B., & Savolainen, T. 2010, International Journal of Modern Physics D, 19, 943
Hurley-Walker, N., Morgan, J., Wayth, R. B., et al. 2014, PASA, 31, e045
IceCube Collaboration. 2013, Science, 342, 1242856
Intema, H. T., Jagannathan, P., Mooley, K. P., & Frail, D. A. 2016, in press, ArXiv:1603.04368
Jansen, F., Lumb, D., Altieri, B., et al. 2001, A&A, 365, L1
Jansky, K. G. 1933, Nature, 132, 66
Kadler, M., Eisenacher, D., Ros, E., et al. 2012, A&A, 538, L1
Kadler, M., Krauß, F., Mannheim, K., et al. 2016, Nat Phys, advance online publication, article
Kadler, M., Ojha, R., & TANAMI Collaboration. 2015, Astronomische Nachrichten, 336, 499
Kellermann, K. I., Kovalev, Y. Y., Lister, M. L., et al. 2007, Ap&SS, 311, 231
Kellermann, K. I., Lister, M. L., Homan, D. C., et al. 2004, ApJ, 609, 539
Kellermann, K. I. & Moran, J. M. 2001, ARA&A, 39, 457
Kellermann, K. I. & Pauliny-Toth, I. I. K. 1969, ApJ, 155, L71
Kellermann, K. I., Sramek, R., Schmidt, M., Shaffer, D. B., & Green, R. 1989, AJ, 98, 1195
Kellermann, K. I., Vermeulen, R. C., Zensus, J. A., & Cohen, M. H. 1998, AJ, 115, 1295
Kettenis, M., van Langevelde, H. J., Reynolds, C., & Cotton, B. 2006, in Astronomical Society of the Pacific Conference Series, Vol. 351, Astronomical Data Analysis Software and Systems XV, ed. C. Gabriel, C. Arviset, D. Ponz, & S. Enrique, 497
Khachikyan, É. Y. & Weedman, D. W. 1971, Astrophysics, 7, 231
Kharb, P., Lister, M. L., & Cooper, N. J. 2010, ApJ, 710, 764
Komossa, S., Voges, W., Xu, D., et al. 2006, AJ, 132, 531
Krauß, F., Kadler, M., Mannheim, K., et al. 2014, A&A, 566, L7
Kreikenbohm, A., Schulz, R., Kadler, M., et al. 2016, A&A, 585, A91
Krolik, J. H. 1999, Active galactic nuclei : from the central black hole to the galactic environment (Princeton University Press)
Landt, H. & Bignall, H. E. 2008, MNRAS, 391, 967
Landt, H., Perlman, E. S., & Padovani, P. 2006, ApJ, 637, 183

Lane, W. M., Cotton, W. D., Helmboldt, J. F., & Kassim, N. E. 2012, Radio Science, 47, RS0K04

Lawrence, A. 1987, PASP, 99, 309

Ledlow, M. J. & Owen, F. N. 1996, AJ, 112, 9

Levenberg, K. 1944, Quarterly of Applied Mathematics 2, 164

Lind, K. R. & Blandford, R. D. 1985, ApJ, 295, 358

Lister, M. L. 2003, ApJ, 599, 105

Lister, M. L., Aller, M., Aller, H., et al. 2011, ApJ, 742, 27

Lister, M. L., Aller, M. F., Aller, H. D., et al. 2013, AJ, 146, 120

Lister, M. L., Aller, M. F., Aller, H. D., et al. 2016, AJ, 152, 12

Lister, M. L., Cohen, M. H., Homan, D. C., et al. 2009, AJ, 138, 1874

Lister, M. L. & Homan, D. C. 2005, AJ, 130, 1389

Longair, M. S. 2011, High Energy Astrophysics (Cambridge University Press)

Lonsdale, C. J., Cappallo, R. J., Morales, M. F., et al. 2009, IEEE Proceedings, 97, 1497

Marscher, A. P. 2009, ArXiv:0909.2576

Marziani, P., Sulentic, J. W., Dultzin-Hacyan, D., Calvani, M., & Moles, M. 1996, ApJS, 104, 37

Massaro, F., Giroletti, M., Paggi, A., et al. 2013, ApJS, 208, 15

McMullin, J. P., Waters, B., Schiebel, D., Young, W., & Golap, K. 2007, in Astronomical Society of the Pacific Conference Series, Vol. 376, Astronomical Data Analysis Software and Systems XVI, ed. R. A. Shaw, F. Hill, & D. J. Bell, 127

Miller, J. S. 1994, in Astronomical Society of the Pacific Conference Series, Vol. 54, The Physics of Active Galaxies, ed. G. V. Bicknell, M. A. Dopita, & P. J. Quinn, 149

Müller, C., Kadler, M., Ojha, R., et al. 2014a, A&A, 562, A4

Müller, C., Kadler, M., Ojha, R., et al. 2014b, A&A, 569, A115

Müller, C., Kadler, M., Ojha, R., et al. 2011, A&A, 530, L11

Müller, C., Krauß, F., Dauser, T., et al. 2015, A&A, 574, A117

Nolan, P. L., Abdo, A. A., Ackermann, M., et al. 2012, ApJS, 199, 31

Ojha, R., Kadler, M., Böck, M., et al. 2010, A&A, 519, A45

Osterbrock, D. E. & Mathews, W. G. 1986, ARA&A, 24, 171

Palmer, H. P., Rowson, B., Anderson, B., Donaldson, W., & Miley, G. K. 1967, Nature, 213, 789

Peacock, J. A., Miller, L., & Longair, M. S. 1986, MNRAS, 218, 265

Penzias, A. A. & Wilson, R. W. 1965, ApJ, 142, 419

Perley, R. A., Dreher, J. W., & Cowan, J. J. 1984, ApJ, 285, L35

Peterson, B. M. 1997, An Introduction to Active Galactic Nuclei (Cambridge, New York Cambridge University Press)

Price, R., Gower, A. C., Hutchings, J. B., et al. 1993, ApJS, 86, 365

Rector, T. A. & Stocke, J. T. 2001, AJ, 122, 565

Rees, N. 1990, MNRAS, 244, 233

Rengelink, R. B., Tang, Y., de Bruyn, A. G., et al. 1997, A&AS, 124

Richards, J. L., Hovatta, T., Max-Moerbeck, W., et al. 2014, MNRAS, 438, 3058

Richards, J. L., Max-Moerbeck, W., Pavlidou, V., et al. 2011, ApJS, 194, 29

Rybicki, G. B. & Lightman, A. P. 1979, Radiative processes in astrophysics (New York,

Wiley-Interscience)
Sambruna, R. M., Donato, D., Tavecchio, F., et al. 2007, ApJ, 670, 74
Sandage, A. 1965, ApJ, 141, 1560
Sault, R. J., Hamaker, J. P., & Bregman, J. D. 1996, A&AS, 117, 149
Scaife, A. M. M. & Heald, G. H. 2012, MNRAS, 423, L30
Schmidt, M. 1963, Nature, 197, 1040
Schmitt, J. L. 1968, Nature, 218, 663
Schneider, P. 2008, Einführung in die extragalaktische Astronomie und Kosmologie (Springer Berlin)
Schulz, R., Kreikenbohm, A., Kadler, M., et al. 2016, A&A, 588, A146
Schwab, F. R. & Cotton, W. D. 1983, AJ, 88, 688
Seyfert, C. K. 1943, ApJ, 97, 28
Shakura, N. I. & Sunyaev, R. A. 1973, A&A, 24, 337
Shepherd, M. C. 1997, in Astronomical Society of the Pacific Conference Series, Vol. 125, Astronomical Data Analysis Software and Systems VI, ed. G. Hunt & H. Payne, 77
Smirnov, O. M. 2011, A&A, 527, A106
Stadnik, M. & Romani, R. W. 2014, ApJ, 784, 151
Stein, W. A., Odell, S. L., & Strittmatter, P. A. 1976, ARA&A, 14, 173
Stickel, M., Meisenheimer, K., & Kuehr, H. 1994, A&AS, 105
Sulentic, J. W., Marziani, P., & Dultzin-Hacyan, D. 2000, ARA&A, 38, 521
Tasse, C., van der Tol, S., van Zwieten, J., van Diepen, G., & Bhatnagar, S. 2013, A&A, 553, A105
Taylor, G. B., Carilli, C. L., & Perley, R. A., eds. 1999, Astronomical Society of the Pacific Conference Series, Vol. 180, Synthesis Imaging in Radio Astronomy II
Tchekhovskoy, A., Narayan, R., & McKinney, J. C. 2010, ApJ, 711, 50
Thompson, A. R., Moran, J. M., & Swenson, Jr., G. W. 2001, Interferometry and Synthesis in Radio Astronomy, 2nd Edition (New York : Wiley)
Tingay, S. J., Goeke, R., Bowman, J. D., et al. 2013, PASA, 30, e007
Trüstedt, J., Kadler, M., Brüggen, M., et al. 2014, in Proceedings of the 12th European VLBI Network Symposium and Users Meeting (EVN 2014). 7-10 October 2014. Cagliari, Italy. Online at http://pos.sissa.it/cgi-bin/reader/conf.cgi?confid=230, id.43, 43
Urry, C. M. & Padovani, P. 1995, PASP, 107, 803
van de Hulst, H. C., Muller, C. A., & Oort, J. H. 1954, Bull. Astron. Inst. Netherlands, 12, 117
van Haarlem, M. P., Wise, M. W., Gunst, A. W., et al. 2013, A&A, 556, A2
van Weeren, R. J., Röttgering, H. J. A., Rafferty, D. A., et al. 2012, A&A, 543, A43
Wayth, R. B., Lenc, E., Bell, M. E., et al. 2015, PASA, 32, e025
Weisskopf, M. C., Brinkman, B., Canizares, C., et al. 2002, PASP, 114, 1
Wijnholds, S., van der Tol, S., Nijboer, R., & van der Veen, A.-J. 2010, IEEE Signal Processing Magazine, 27, 30
Wijnholds, S. J. & van der Veen, A.-J. 2009, IEEE Transactions on Signal Processing, 57, 3512
Wijnholds, S. J. & van der Veen, A. J. 2009, in 2009 17th European Signal Processing Conference, 1146–1150

Williams, R. E., Blacker, B., Dickinson, M., et al. 1996, AJ, 112, 1335
Wrobel, J. M. & Lind, K. R. 1990, ApJ, 348, 135
Yao, S., Yuan, W., Zhou, H., et al. 2015, MNRAS, 454, L16
Zensus, J. A., Ros, E., Kellermann, K. I., et al. 2002, AJ, 124, 662

List of Figures

List of Tables

Acknowledgement

First of all, I would like to thank my advisor Prof. Dr. Matthias Kadler, who gave me the opportunity to do my PhD in his group at Würzburg University. Thank you for the feedback, support and the possibilities to present my work at conferences and meetings. With the time working on my Master and my PhD thesis I could learn what it is like to be involved in science besides of only data reduction. I enjoyed working with him over the past years and being a part of his group.
For his great help in getting me started in the LOFAR collaboration I thank Prof. Dr. Marcus Brüggen for his great help. In the month I spend in Hamburg at the observatory I learned much of the basics of LOFAR data reduction.
I want to thank further Dr. George Heald for introducing me into the MSSS team, inviting me to ASTRON in Dwingeloo and the involvement in the data reduction and quality control of the MSSS efforts. For support in finding the right strategies for the calibration of international LOFAR observations I thank the LOFAR longbaseline group, especially, Adam Deller, Neal Jackson, Javier Moldon and Eskil Varenius.
My thanks also go to Prof. Dr. Karl Mannheim as the Chair of Astronomy at Würzburg University for his support since the start of my Master thesis.
My biggest thanks go to my radio astronomy colleagues Robert Schulz, Dr. Cornelia Müller and Alexander Kappes, who not only helped a lot with discussion and ideas but also read parts of this thesis to look for errors.
Many of my scripts and their problems would not work without the help of Sebastian Ohlmann, Kai Marquardt, Cedric Schreiner and Dr. Christoph Großberger. Thank you for the help with my questions and bugs over the last years.
I thank further all the other people from our group for the good atmosphere at work. Especially, my colleagues Till Steinbring, Katha Leiter, Annika Kreikenbohm and Marcus Langejahn , who were in the group for the same time since I started at the Chair of Astronomy.
Besides, I thank my parents for their confidence and support. Further my biggest thanks go to Melanie for being my partner since more than 5 years. Thank you for being patient with me and for always being there for me.